Molecular mechanisms of crystal nucleation and growth at ferritin/oxide interfaces: a theoretical investigation

Vom Fachbereich Produktionstechnik
der
UNIVERSITÄT BREMEN

zur Erlangung des Grades
Doktor-Ingenieur
genehmigte

Dissertation

von
M. Sc. Steffen Lid

Gutachter: Professor Dr.-Ing. Lucio Colombi Ciacchi
Zweitgutachter: Professor Dr. Dominik Horinek (Universität Regensburg)

Tag der mündlichen Prüfung: 24.08.2018

Für Cataleya und Mino.

Contents

Preface

This thesis describes the results obtained during my time as a PhD-student from December 2013 until September 2017 at the University of Bremen in the Hybrid Material Interfaces (HMI) Group under the supervision of Prof. Dr. Lucio Colombi Ciacchi. The thesis contains only my own research, if not explicitly stated otherwise, apart from chapter 1 which provides an overview of the current state of knowledge, and chapter 2 which gives a brief overview of the used methods.
Parts of this thesis have been published as follows:

Chapter 3:

Steffen Lid, Susan Köppen and Lucio Colombi Ciacchi, *Creation of Models and Parametrization of a Classical Force Field for Amorphous Al_2O_3/Water Interfaces Based on Density Functional Theory*, Comp. Mat. Sci., 140, 307 (2017)

Daniel Carmona, Laura Treccani, Monika Michaelis, **Steffen Lid**, Christian Debus, Lucio Colombi Ciacchi, Kurosch Rezwan and Michael Maas, *Mineralization of Iron Oxide Induced by Ferritin Subunits Immobilized on Silica Nanoparticles*, submitted (2018)

Chapter 4:

Julen Larrucea, **Steffen Lid**, Lucio Colombi Ciacchi, *Parametrization of a classical force field for iron oxyhydroxide/water interfaces based on Density Functional Theory calculations*, Comp. Mat. Sci., 92, 343 (2014)

Steffen Lid, Daniel Carmona, Michael Maas, Laura Treccani and Lucio Colombi Ciacchi, *Anchoring of Iron Oxyhydroxide Clusters at H and L Ferritin Subunits*, ACS Biomater. Sci. Eng., 4, 483 (2018)

A publication of the results presented in chapter 5 is currently in preparation.

Zusammenfassung

Das Ziel dieser Arbeit ist die theoretische Untersuchung der Nukleation und des Wachstums von Eisenoxid(-hydroxid) an Untereinheiten des Proteins Ferritin.

Die biomimetische Herstellung von Mikro- und Nanostrukturen aus magnetischen Materialien ist ein geeigneter Weg um die konventionellen Methoden durch eine umweltfreundliche und nachhaltige Lösung zu ersetzen. Biomineralisierung ist die von der Natur bereitgestellte Art der Synthese von anorganischen Materialien durch lebende Organismen. Eines der bekanntesten Vertreter ist das Protein Ferritin, welches in vielen Organismen und Gewebearten vorkommt und als Eisenspeicher dient. Ferritin besteht aus insgesamt 24 Untereinheiten, welche in Form einer hohlen Kugel angeordnet sind, in dem Eisen in Form von Eisenoxidhydroxid biomineralisiert wird. Diese Untereinheiten wurden in dieser theoretischen Arbeit und unterstützenden Experimenten verwendet, um magnetische Schichten von Eisenoxidhydroxid ohne räumliche Beschränkungen wachsen zu lassen.

Zu Beginn wurde die mögliche Immobilisierung der Ferritin Untereinheiten auf amorphen Metalloxidoberflächen untersucht. Modelle und Kraftfeldparameter für Ferritin und Siliziumoxid konnten aus anderen Arbeiten entnommen werden. Ein realistisches Strukturmodell von amorphen Aluminiumoxid samt Oberflächenterminierung wurde in dieser Arbeit erstellt und validiert. Das Modell diente anschließend der Parametrisierung eines klassischen Kraftfelds für die Al_2O_3/Protein/Wasser Grenzfläche auf Basis der Dichtefunktionaltheorie. Daraufhin wurden die Energieprofile von Ferritin Untereinheiten in verschiedenen Orientierungen über Aluminium- und Siliziumoxidoberflächen berechnet. Auf diese Weise konnte die Notwendigkeit der kovalenten Immobilisierung von Ferritin auf besagten Oberflächen vorhergesagt werden, und durch Experimente bestätigt werden.

Um Einblicke in die atomaren Mechanismen der Ferritin gestützten Nukleation zu erhalten, wurden Aminosäuren gesucht, welche als Ankerpunkte für Eisenoxidhydroxid dienen. Hierzu wurden fehlende klassische Kraftfeldparameter für Eisenoxidhydroxid ermittelt und es wurden Goethit und Ferrihydrit-Nanopartikel erstellt. Diese Partikel wur-

den in Molekulardynamiksimulationen in Kontakt mit verschiedenen Anordnungen von Ferritin Untereinheiten gebracht. So wurden, wie aus der Literatur bekannt, negative Aminosäuren ermittelt, die den Fe(III) Nanopartikeln als Ankerpunkte dienten. Allerdings konnte hier auch eine hohe Beteiligung von positiv- und ungeladenen Aminosäuren wie beispielsweise Arginin und Lysin beobachtet werden, im Einklang mit häufig vorkommenden Aminosäuren in Eisenbindenden Peptiden.

Für die Untersuchung des Wachstums von Eisenoxidhydroxid und die Nukleation von elementaren Bausteinen und nicht vordefinierten Partikeln wurden im Anschluss fortgeschrittene Simulationstechniken eingeführt. Durch diese konnte der enorme Zeitaufwand, der für die Diffusion der elementaren Bausteine zum Aggregat oder Protein benötigt wird, auf ein Minimum reduziert werden. Dies ermöglichte die Simulation von Kristallwachstum in klassischen Molekulardynamiksimulationen.

Weiterhin war es möglich Protonentransferreaktionen auf Basis der Dichtefunktionaltheorie in diese klassischen Simulationen einzubinden. Simulationen vom Wachstum in Wasser und an Ferritin offenbarten das Problem der Identifikation der jeweiligen Kristallstruktur, aufgrund der hohen Ähnlichkeit der Koordinierung der Eisenatome in verschiedensten Fe(III) Strukturen. Zur Identifikation wurde ein Verfahren entwickelt, welches auf dem "Average local bond order parameter" basiert und die zweite Lage an Nachbarn mit einschließt. Hierbei wurde ein 10-dimensionaler Deskriptor entwickelt, der es in Kombination mit der Wahrscheinlichkeitsdichtefunktion in Form eines "Gaussian Mixture Models" ermöglicht, zwischen verschiedenen Eisenoxidhydroxidstrukturen zu unterscheiden.

Chapter 1

Introduction

In this chapter, the motivation of this thesis and general knowledge about biomineralization, and crystal nucleation and growth theories are presented. This is followed by a short review about the function, occurrence and current knowledge of the Ferritin protein and its mineralization capability. Afterward, the two most important phases of iron oxyhydroxide for this thesis are introduced, concerning occurrence, bulk and surface structures, and properties. Finally, the overall aims of this thesis are summarized.

1.1 Motivation

The fabrication of microstructures and nanostructures made of magnetic materials has become of large importance for several emerging applications such as catalytic supports [1–3], electronic storage devices [1, 4], templates for biological studies in living cells [5], lab on a chip [6], in-flow sorting of biological entities [7], stimuli-responsive drug delivery systems [1], biodetection [2] or micro-electromechanical systems (MEMS) [8]. Conventional methods for the fabrication are sol-gel deposition [4], scanning ion microscopy lithography [1, 9], electroplating [5] or chemical/physical vapor deposition. The main drawback of these techniques is that they generally require expensive equipment, specialized laboratories and that they are rather time-consuming. This may constitute a limit to their application potential [10] and pushes towards the search for alternatives. These alternatives should be more sustainable, still enabling a high control over material properties such as morphology and chemical composition. Furthermore, no drastic processing regimes such as high temperature, pH, and harmful compounds should be required [1, 3, 4].

A straightforward fabrication approach and one of the most remarkable and fascinating examples of precisely controlled and highly selective (nano)material synthesis is the formation of magnetic inorganic materials in living organisms, called biomineralization. Here, sophisticated and surprisingly complex systems, which can be modified and organized in precisely assembled multidimensional functional structures, are created by a bottom-up approach using a small set of building blocks. The two main advantages compared to conventional methods are the facts that magnetic biominerals often surpass physicochemical properties of synthetically engineered materials [11] and the synthesis of magnetic materials by biological processes or biological templates takes place at mild conditions (ambient temperature/pressure and near-neutral pH). Two of the most prominent examples of biominerals are ferromagnetic nanoparticles that grow in the form of self-assembled chains in several bacterial species [1, 7] and ferrimagnetic iron oxide nanocrystals formed within the major iron-storage protein ferritin (Fn) [12]. Fn is formed by 24 helical subunits which can self-assemble in a spherical shape with a diameter of about 12 nm around a hollow cavity in which iron oxyhydroxide crystals are mineralized up to 8 nm size [13]. Fn subunits are either H (heavy) or L (light) chains, which are structurally nearly identical and their amino acid sequences have about 55% homology. The H/L ratio in the hetero-24mers depends on organism and tissue [14], and several studies report that L chain enhances the stability of the mineral core [15], while H chain conserves enzymatic activity (ferroxidase site) and catalyzes Fe(II) oxidation. However, assembled L-chains also seem to accelerate the demineralization of ferritin [16].

As template for biomimetic material synthesis of various metal and metal oxide nanoparticles [14], biomedical assays [17], energy storage devices [18] and 2D nanoarrays [19], whole cages of Fn, demineralized Fn (apo-Fn) or engineered Fn homopolymers consisting of only H or L chains have been widely used. This enables a high control over particle uniformity but imposes strict spatial restrictions and only discontinuous mineral assemblies can be fabricated. The usage of single and separated Fn subunits as bio-templates for the biomineralization could overcome these restrictions to the growth of structures, leading to discrete and continuous multidimensional iron oxide structures with tunable properties. This would enable the growth of extended 2D and 3D structures with control over the composition and physical properties of the mineral phases which will open new possibilities for technological applications as active catalysts, magnetic materials, and electrodes [14, 20]. Additionally, the mineralization reaction in whole Fn is not strictly

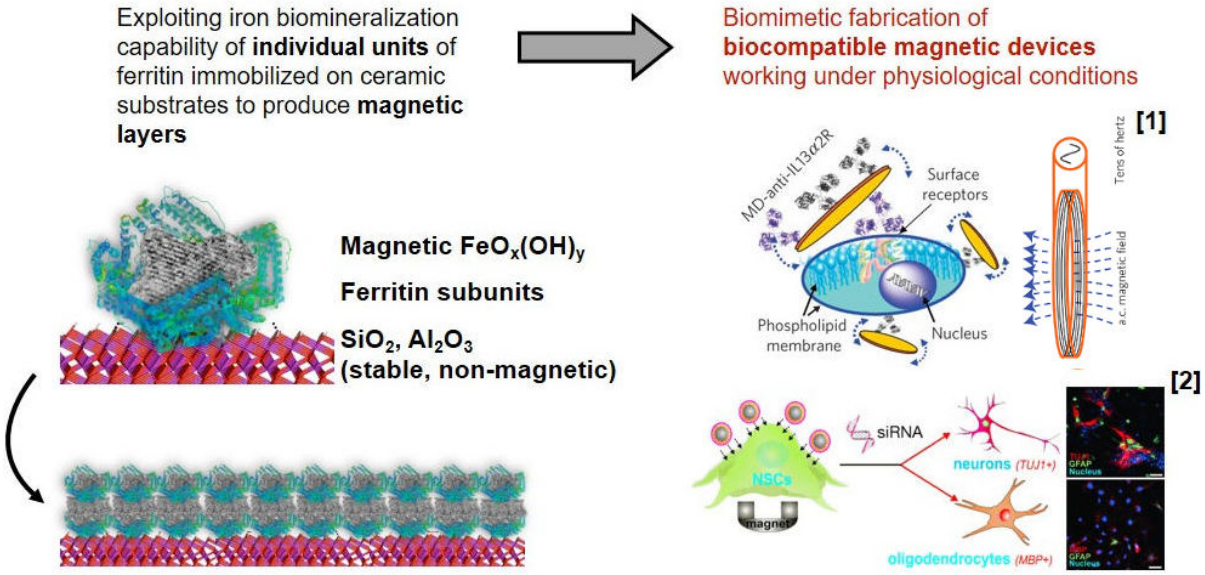

Figure 1.1: Schematic overview of the overall aim. On the upper left-hand side, the mineralization of a ferritin template on a stable material surface is shown which is in the upper one immobilized for the biomimetic growth of multilayered iron oxide film. The upper right figure shows biofunctionalized microdiscs specifically targeting cancer cells (taken from Kim et al. [21]). These magnetic microdiscs oscillate by applying an alternating magnetic field and initiate spin-vortex-mediated programmed cell death. The lower right figure is taken from the publication of Shah et al. [22], which used magnetically facilitated delivery of magnetic core-shell nanoparticles to control the differentiation of stem cells.

specific for iron [14] and the access to the catalytic oxidation site of ions different from Fe(II) including electroactive materials such as Co, Ni, Cr, Mn, Cd. may be facilitated. A schematic overview of the overall aim is displayed in Fig. 1.1. On the upper left-hand side, the mineralization of a ferritin template on a stable material surface is shown and on the lower left side the biomimetically grown multilayered iron oxide film. On the right-hand side, two possible applications are shown. The upper figure is taken from Kim et al. [21], in which biofunctionalized microdiscs are specifically targeting cancer cells. This magnetic microdiscs oscillate by applying an alternating magnetic field and initiate spin-vortex-mediated programmed cell death. The figure at the bottom is taken from a publication of Shah et al. [22], who used magnetically facilitated delivery of magnetic core-shell nanoparticles to control the differentiation of stem cells.

For the controlled fabrication of microstructures and nanostructures made of magnetic materials by single and separated Fn subunits, a novel biomimetic strategy is needed.

To create a knowledge-based fabrication protocol, rather than the traditional trial-and-error loop, a profound understanding of the mechanisms is necessary. The present work contributes to this, by the introduction of simulation tools to study the mechanisms on the atomistic level to explain experimental results and to suggest the optimal next steps. The following sections contain introductions to biomineralization, crystal nucleation and growth, the ferritin protein and iron oxyhydroxides, followed by an overview of the main goals of this thesis.

1.2 Biomineralization

Various living organisms are well known for a genetic program that enables the controlled formation of a wide range of specially designed organic-inorganic hybrid materials such as bone, teeth, and shells. This process is termed biomineralization, and the purely inorganic or composite (inorganic-organic mixture) materials are named biominerals. These nature-drawn strategies are exploited to produce materials for biomedical, industrial, and technological applications. These biomimetic approaches enable a high level of control over the composition, structure, size, and morphology of the resulting biominerals which often surpass those of synthetic analogs [23].

A class of minerals which is commonly produced by organisms are iron oxides. Besides the formation in ferritin, which is described in detail in section 1.4, iron oxide minerals are also formed in magnetotactic bacteria, limpets, and chitons, to name a few. The iron oxides are used for different functions such as stretching of tissues, iron storage, hardening of teeth, navigation, and sensing of magnetic fields [23]. For example, to navigate through the Earth's magnetic field along chemical gradients, magnetotactic bacteria produce nanoparticles of magnetite (Fe_3O_4) or greigite (Fe_3S_4) [24] as shown in Fig. 1.2. Other well-studied prominent representatives are biosilicifying organisms, such as diatoms and radiolarians, which are unicellular algae [23]. Furthermore, the most abundant crystalline biogenic minerals in nature are based on calcium carbonate. These minerals are present in freshwater and marine organisms. The variety of functions ranges from the shell of mollusks, protection as in sea urchin spines, structural purposes in coral skeletons, gravity sensors in marine and land animals [23] and functions in the photosensory organ in brittlestars [25].

These examples are only a small fraction of the diversity of biominerals. For the synthe-

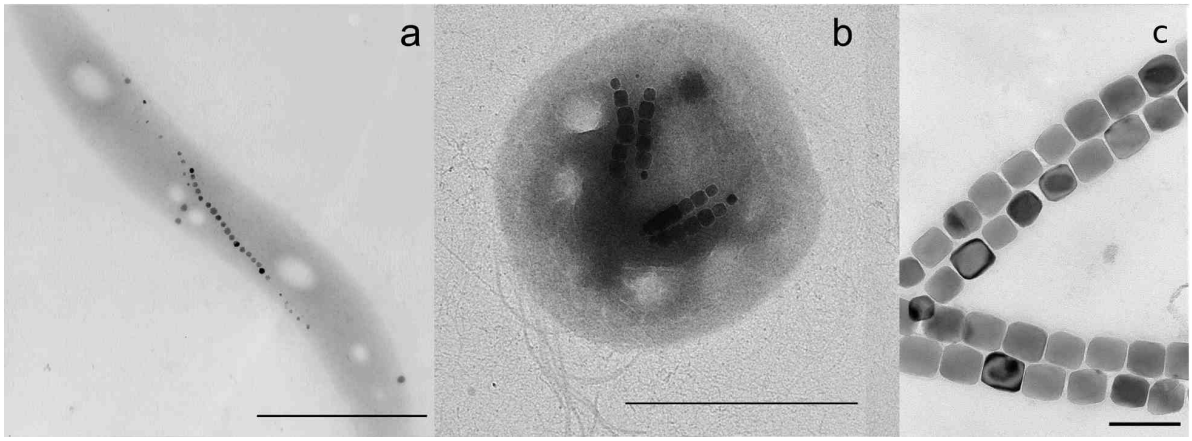

Figure 1.2: Electron micrographs of magnetotactic bacteria and magnetosome chains were taken from ref. [24]. (a) a spirillum with a single chain of cubooctahedral magnetosomes, (b) a coccus with two double chains of slightly elongated prismatic magnetosomes and (c) chain from a similar type of magnetotactic bacteria as in part (b). Scale bars are 1 μm in (a) and (b) and 100 nm in (c).

sis of novel materials in medicine, industrial and technological processes, these biominerals are sources of inspiration for many chemists, physicists, and materials scientists. However, profound fundamental knowledge of the mechanisms is required to control the structure and the morphology of these inorganic or composite materials artificially. Unfortunately, it is impossible to understand the different specific mechanisms that lead to the formation of every particular biomineral. Nevertheless, some basic strategies for controlling mineralization seem to be common to many organisms as discussed by Mann [26]. These strategies involve spatial, morphological, structural, constructional and chemical control. Spatial control comes about by mineral formation in an enclosed space into which ions and molecules are selectively transported. Morphological control relates to the shaping of biominerals into the complex morphologies, where control is based on precipitating the mineral within an enclosed space. The provided boundaries direct crystal growth along specific directions, and amorphous phases are often formed as precursors to the crystalline materials [27–30]. For structural control, active chemical groups template the mineral formation on the organic scaffold to force the nucleation of the crystal along a preferential face or axis [30]. Constructional control is the assembly of mineral-based building blocks to hierarchical architectures and occurs from the nanometer to the macroscopic level. In chemical control, physicochemical factors such as solubility and supersaturation are con-

trolled by the ionic composition of the medium, and specialized macromolecules are used to promote or inhibit the nucleation, growth, and phase transformation [31–34].

All these strategies are possible ways to control crystallization experimentally. However, the most fundamental step is nucleation, thus the formation of the first mineral nuclei. The control of crystallization, in principle, requires accurate nucleation control. In general, biomineralization does not follow classical nucleation pathways. They are nevertheless described in detail in the following section, as a reference and useful starting point for more specific studies.

1.3 Crystal nucleation and growth

For biomineralization, elements in the form of atoms, ions or molecules are taken from the environment and transported by active biologically driven processes or passive diffusion to the inner part of the cell. If the concentration of this element exceeds the equilibrium solubility, a monomer-by-monomer nucleation-and-growth pathway starts, as assumed by the Classical Nucleation Theory (CNT) [35]. This classical model of nucleation is based on a thermodynamic competition between energy gain through the crystallization of the bulk structure, and energy loss through by an increase of the resulting surface area [36], as described in the following.

In CNT, crystals form via the spontaneous assembly of elements in a stable, ordered crystalline form, if the concentration of a dissolved constituent exceeds the equilibrium solubility. CNT assumes a critical nucleus, which is formed at the beginning, with the same structure as the macroscopic bulk material. The resulting phase interface, and arising interfacial tension, hinders crystal growth up to a so-called critical size, at which the bulk energy starts to balance out the energy which is necessary to generate the phase interface. This can be explained by the fact that the bulk energy scales with the cube, while the unfavorable surface energy scales with the square of the radius [37], as shown in Fig. 1.3. By summing up these two curves, the critical size of the nuclei is shown by a maximum point, as visualized in Fig. 1.3. The change in free energy for the formation of nuclei smaller than this critical size is positive. Hence, they are thermodynamically unstable and dissolve, while nuclei bigger than the critical size grow without limit. Therefore, only thermal (random) density fluctuations on microscopic length-scales can lead to the formation of nuclei, and (pre-)critical nuclei are rare species [38]. During growth, the

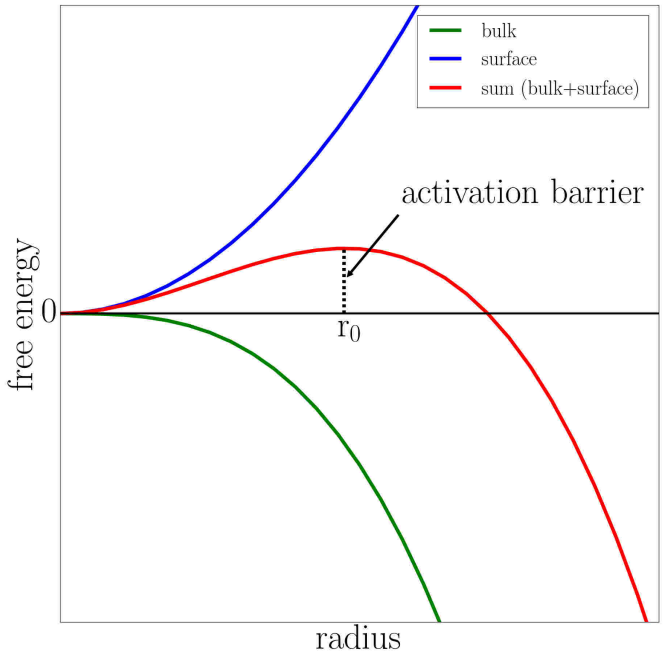

Figure 1.3: Dependence of the free energy of the nuclei on their radius, as assumed in Classical Nucleation Theory. The surface energy (blue) scales with square while the bulk energy (green) scales with cube. The sum of both curves (red) represents the competition between energy gain and loss. Up to a critical size (r_0), the nuclei are thermodynamically unstable and dissolve. Only nuclei bigger than the critical size grow without limit.

nucleus is then simply enlarged by further attachment of the basic monomers which can be atoms, ions or molecules. With the CNT critical size of the nucleus and the associated activation energy, nucleation rate and its dependence on supersaturation can be predicted. This means that CNT is a very powerful concept for the qualitative comprehension of nucleation phenomena in general, but limited by a number of assumptions and simplifications. In particular, structure and composition of the nucleus are considered to be the same as the bulk crystalline phase, and structural changes in the bulk or at the surface are neglected. However, in case of iron oxyhydroxides, phase transformations are often observed, see ref. [39] and references therein. Furthermore, multistep assembly of large unit-cell structures and the formation of subcritical supramolecular clusters or complexes are not considered [40] in CNT.

To overcome these limitations of CNT and to describe more complex crystal-formation

processes, non-classical nucleation pathways have been proposed.

One non-classical pathway to describe the formation of biomineral crystals is based on pre-nucleation clusters, which are solutes with a molecular character in aqueous solution [41, 42]. These prenucleation clusters are considered to be thermodynamically stable solutes, and therefore, probably larger than the classical pre-critical nuclei. The formation of these clusters is an endothermic process. Hence the driving force must be entropic [43], perhaps based on the release of ion hydration water similar to the formation of micelles [37]. In contrast to CNT, the structures of these aggregates probably do not relate to the macroscopic bulk structures [44], and the prenucleation species do not have a phase interface and no interfacial tension [37].

Furthermore, particle-mediated processes assume nanoparticles as monomers, leading to the formation of mesoscopically structured crystals, mentioned as "mesocrystals" [45–49]. The formation of such mesocrystals in case of biominerals is often observed within an amorphous precursor phase [48, 50–52].

Another non-classical nucleation pathway considers, in contrast to CNT, the nucleation of crystallites by at least two steps. In the first step, a stable disordered cluster or mesocrystal is formed, followed by nucleation of the final crystalline phase within the cluster by structural rearrangements [53–57]. The first metastable phase that has been nucleated is probably the phase with the lowest energy barrier, following Ostwald's step rule [58]. The final crystal phase, based on a second nucleation event, is formed via solid-solid phase transitions stepwise to the most stable phase. This pathway and the classical nucleation pathway are schematically shown in Fig. 1.4.

Theoretical investigations reveal that crystallization of iron oxyhydroxides can occur through classical or non-classical scenarios where phase-transformation are often observed [39, 59]. In this thesis, the two-step nucleation and growth pathway, based on the approach of Kawska and Zahn [60], is used to simulate the mineralization process of iron oxyhydroxide in water and at the Fn protein. Here, an iterative docking scheme is used to simulate the formation of aggregates which contains as the first step the diffusion of particles to an aggregate, followed by the docking process and reorganization or transformation of the resulting structure. A detailed description of the Kawska-Zahn approach and the implementation can be found in chapter 5, and an overview about the current knowledge of the ferritin protein and its biomineralization capability can be found in the following section.

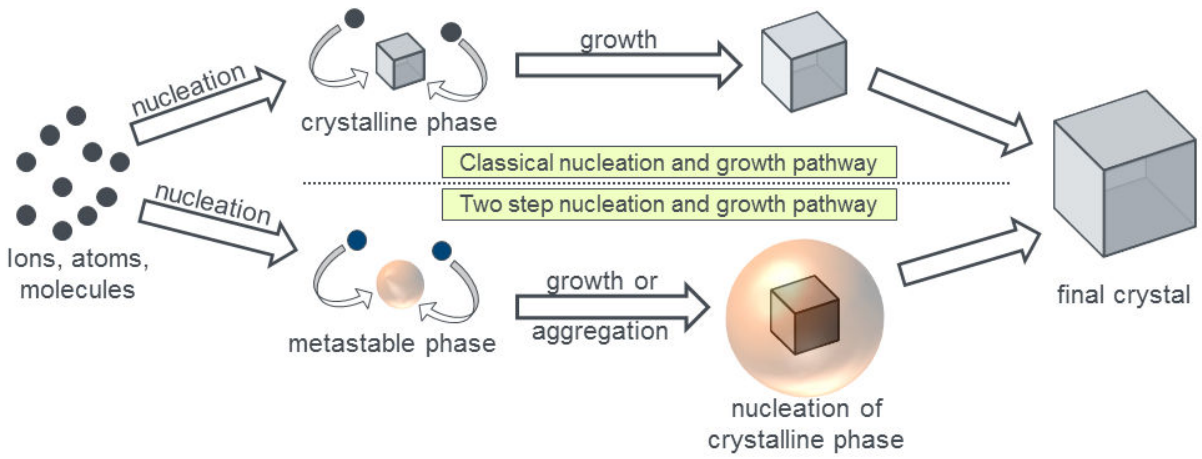

Figure 1.4: The upper pathway shows crystal growth based on Classical Nucleation Theory (CNT) [35] and the pathway on the bottom the two-step nucleation and growth pathway, following Ostwald's step rule [58].

1.4 The Ferritin protein

Ferritin (Fn) is the major intracellular iron storage protein [61] in all organisms and, as such, it is relatively easy to isolate and produce [62]. The primary task of Fn is to protect cells from the potentially toxic effects of free iron, by the uptake of iron in a mineralized form within the protein nanocage for later use by the cell in the synthesis of heme. Along with the classic ferritin, the DNA-binding protein from starved cells called mini-ferritin is found in many bacteria and some archaea [63, 64] with its primary role to protect the bacterial chromosome from oxidative damage [65]. Furthermore, heme-containing bacterioferritins occur in some bacteria and archaea and differ from Fn by the incorporation of twelve b-type heme groups between subunits, which are introduced in the following, in a twofold symmetric binding site [66]. The similarities between species of a specific chain are high, with 80%-90% identity between human, rat, chicken and horse proteins [67]. On the contrary, heme-containing bacterioferritins exhibit only 18%-21% identity with human, horse and chicken and even less identity (14%) to the ferritin-like protein isolated from E. coli [67–69].

Fn is probably the best-studied biomineralization scaffold, whereby the most extensively studied ferritin is that of horse spleen, traditionally considered as the model of mammalian ferritin. It is composed of 24 polypeptide chains of apoferritin (iron-free ferritin) which are self-assembled in a highly symmetrical octahedral symmetry [70] as presented in Fig. 1.5 a. The hollow apoferritin shells with outer diameters of roughly 12 nm and inner diameters

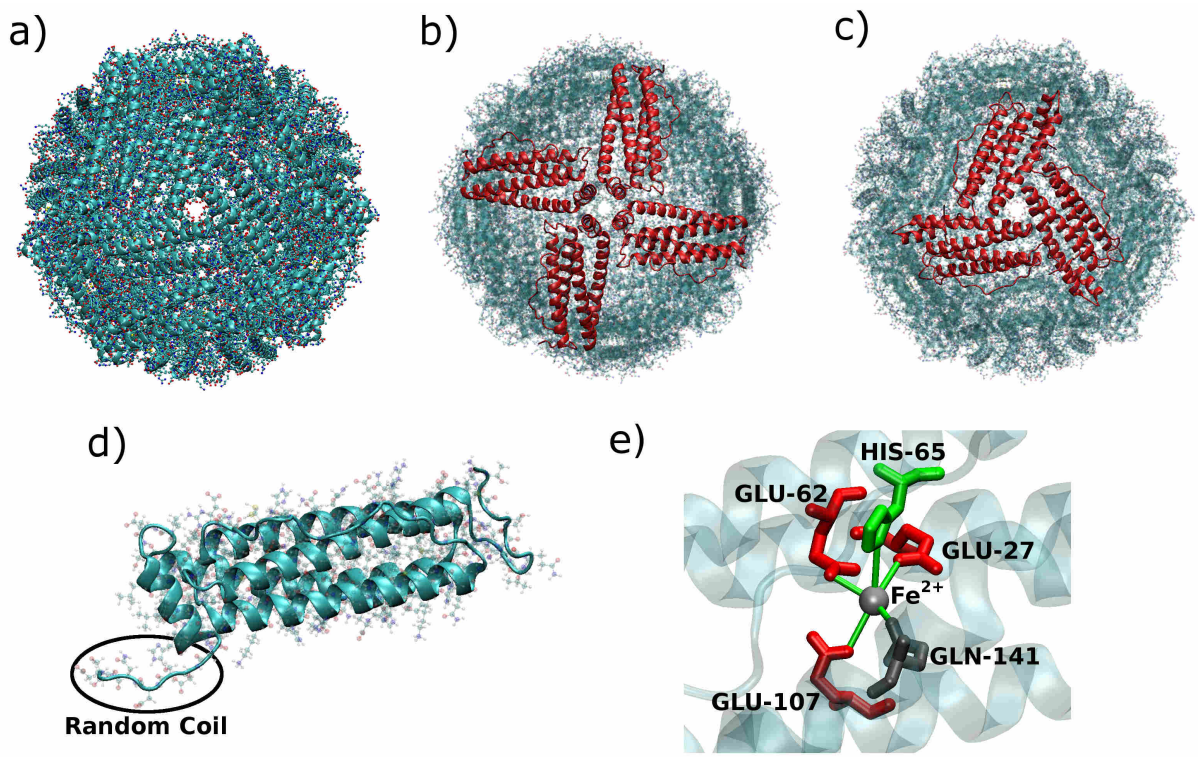

Figure 1.5: Representation of the Ferritin protein, (*a*) full Fn protein composed of light (L) subunits, (*b*) Fn protein with highlighted fourfold symmetry axes, (*c*) Fn protein with highlighted threefold symmetry axes, (*d*) single H-subunit of the Fn protein, (*e*) ferroxidase center of the H-subunit.

of 8 nm [71] are remarkably stable to temperature and pH changes [72, 73]. The heteropolymers consist of heavy subunits (H-chain - 21 kDa) and light subunits (L-chain - 19 kDa) [74] where the H/L ratio depends on organism and tissue [14].

Both types of ferritin subunits are closely related in terms of primary (around 55% protein sequence identity) and tertiary structure [75, 76], and the polypeptides spontaneously fold into Four-α-helix bundles completed by a short C-terminal helix [77, 78]. In case of the H subunit, this C-terminal helix is extended by a short random coil which consists of five amino acids. The structure of the Ferritin H-chain is taken from the protein database (2FHA.pdb) and visualized in Fig. 1.5 d. A single ferritin protein is capable of accommodating up to 4500 iron (III) atoms within the large central cavity [79–81]. All 24mer ferritins have negatively charged pores at the eight fourfold (Fig. 1.5 b) and six threefold (Fig. 1.5 c) symmetry axes. These pores are about 2 nm long, connecting the inner cavity

with the protein's external environment [78, 82, 83] to allow the entry and exit of cations during mineralization and demineralization [84].

L rich proteins are predominant in iron storage organs such as the liver and spleen, and they are involved in iron nucleation, mineralization, and long-term storage of Fe(III) [85, 86]. In contrast, H rich ferritin proteins are mostly found in organs of low iron content including the heart and pancreas, due to their major role in rapid detoxification of iron and intracellular iron transport. In the most widely accepted model, Fe^{2+} ions enter the cage through pores between the assembled subunits at three-fold symmetry axes, while oxygen is believed to enter either through pores at fourfold-symmetry axes [87] or via narrow hydrophobic channels in direct correspondence of the ferroxidase sites [88]. Fe(II) moves through those hydrophilic channels until reaching a catalytic site known as ferroxidase center, which is located in the middle of each H-subunit [74]. This ferroxidase center (see Fig. 1.5 e) has conserved glutamic acid, glutamine and histidine residues that coordinate iron and promotes the oxidation of Fe(II) to Fe (III) in the presence of oxygen or peroxide [75, 89–91]. The resulting Fe (III) ions are transferred to the central cavity where they form microcrystals and mineralize as Fe (III) hydrates [62, 92]. An additional pathway in mammalian ferritins is based on a reaction on the mineral surface, which allows simultaneously iron oxidation and nucleation steps [93, 94] after Fe(II) migrates through the 3-fold channels [82]. The resulting Fe(III) mineral is traditionally described as ferrihydrite (formula unit $Fe_{10}O_{16}H_2$) [12, 61, 93] which is consistent with a single defect-rich hexagonal phase with $P6_3mc$ space-group symmetry and contains, in its ideal form, 20% tetrahedrally and 80% octahedrally coordinated iron(III) [95]. A high-resolution scanning transmission electron microscopy image of the ferritin iron core is presented in Fig. 1.6. General information about ferrihydrite is summarized in the following section, while other iron oxyhydroxides are introduced in section 5.5.

1.5 Iron oxyhydroxides (FeO(OH))

In the following, the two iron oxyhydroxide structures mainly studied in this thesis are introduced. They are, on the one hand side, goethite, which is very well studied and contains a relatively simple unit cell, and on the other hand ferrihydrite which is, as already mentioned, a phase forming in the Fn core.

Goethite (α-FeO(OH), as presented in Fig. 1.7 a) represents the most stable coarse

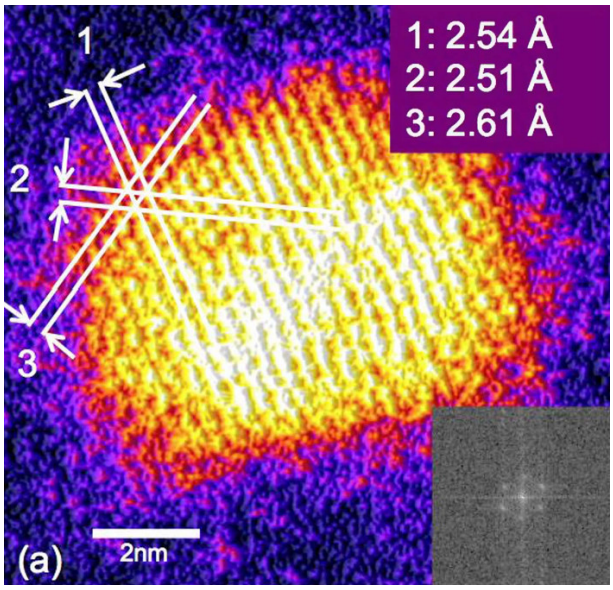

Figure 1.6: High-resolution STEM image of the ferritin iron core taken from ref. [96]. The presented d-spacing and angles (interplanar angles of 61.1°, 59.06°, and 60.05°) are consistent with the ferrihydrite crystal structure [97], and the inset on the lower right contains the corresponding FFT (Fast Fourier Transformation).

polymorph of iron oxyhydroxide [98] and the only stable phase with respect to hematite and liquid water at ambient temperature and pressure conditions [99]. Goethite naturally occurs as needle-like nanoparticles in sediments as a result of weathering of other iron-based minerals [100, 101]. Goethite plays an essential role in environmental science and technology due to the capability to control the mobility of heavy metals [102]. The magnetic ordering of the iron ions is antiferromagnetic, whereby theoretical investigations reveal the $+-+-$ alternation of the spin directions in the primitive cell is the most stable one [102]. The electronic and structural properties of goethite have been studied previously by a number of contributors, including our group [102–105]. The needle-shaped goethite crystals display two relevant surfaces in water solution, which lie on the (110) and (021) crystallographic planes [103] as shown in Fig. 1.7 b/c. The termination and energetics of the surfaces of goethite were studied in detail in ref. [103] from where it is known that water molecules adsorb dissociatively on the (110) surface while both dissociated and molecularly adsorbed molecules are found on the (021) surface.

The structure of ferrihydrite (formula unit $Fe_{10}O_{16}H_2$) is traditionally used to describe the mineral phase of the Fn core [61, 93]. In nature, ferrihydrite particles are very small,

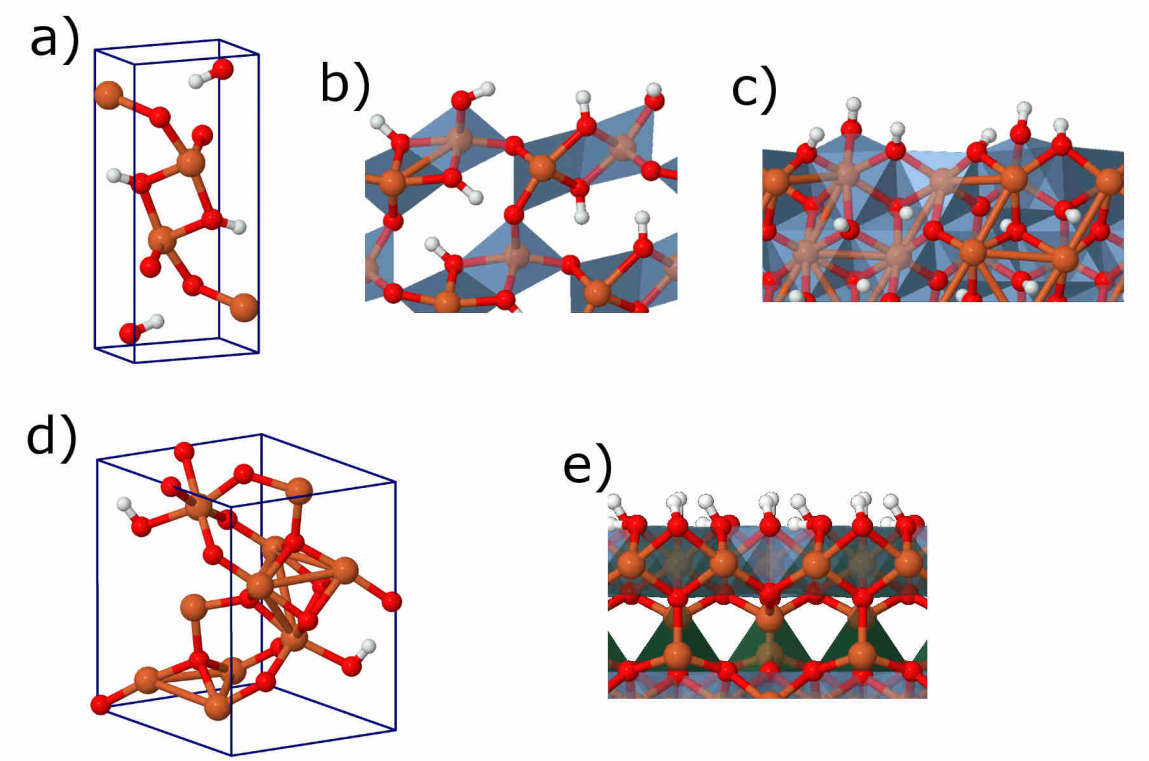

Figure 1.7: Representations of the bulk primitive unit cell of goethite (*a*) together with the surface unit cells corresponding to the (110) (*b*), and the (021) (*c*) planes. (*d*) represents the most stable unit cell and corresponding surface (*e*) of ferrihydrite, as studied in ref. [105].

in order of 2-3 nm [106, 107], and the structure is particle-size dependent with different degrees of crystallinity [108]. Several experimental [95, 109, 110] and computational [111, 112] studies focus on the structure of ferrihydrite and here, for the creation of particles and surfaces, the hexagonal bulk unit cell with $P6_3mc$ space-group symmetry [95], as displayed in Fig. 1.7 d, is used. The missing information about the position of the H atoms in the unit cell, due to X-ray scattering experiments, are determined by comparing the total DFT based energies of different possible positions, see ref. [95, 105]. The lowest energy and therefore the most stable structure is obtained when the H atoms are bound to the edges of O coordination octahedra around Fe atoms, in different cavities and pointing in the same direction with respect to the cell *c* axis. Based on the obtained unit cell, the found most stable surface is used, which is the basal (0001) plane terminated with OH groups, in correspondence of octahedrally coordinated Fe atoms. The surface is presented in Fig. 1.7 e. Here, all Fe ions are in the 3+ oxidation state which is in agreement with

experimental conclusions of Hiemstra [110]. Detailed information about other possible terminations and stability of different possible surfaces can be found in ref. [105].

1.6 Goals

This thesis investigates the atomistic mechanisms of the ferritin-promoted nucleation and growth process of iron oxyhydroxide. Different immobilization strategies for Fn on two oxide surfaces are investigated, as well as the initial anchoring of nascent nuclei at the ferritin subunits' mineralization sites. Furthermore, advanced simulation methods are implemented for realistic simulation of nucleation behavior as well as for simulations of growth of iron oxyhydroxide structures. New analysis techniques are developed for the automatic, unbiased identification of crystal structures.

Despite the success of cryogenic transmission electron microscopy (cryo-TEM), which has proven to be a powerful tool to analyze classical and non-classical nucleation and crystallization phenomena [113, 114], insights at the atomic scale in the process of nucleation and of the very early stages of crystal growth are barely accessible to current experimental methods. Theoretical investigations, such as computer simulations, are necessary to enable detailed insights to understand the underlying atomistic mechanisms. Due to the size of the systems, in case of the simulations of the ferritin-promoted growth process, classical force-field potentials and advanced molecular dynamic simulation technique will be used.

For the formation of a homogeneous layer of Fn subunits on oxide surfaces, the immobilization of Fn subunits to stable material surfaces will be investigated in the first step. This is a fundamental step, as it may alter the properties of the biomolecules and have a significant influence on the properties of the magnetic structures after mineralization. In the case of single and separated subunits, to fabricate continuous and extended 2D and 3D structures, the orientation of the Fn subunits attached to the surface is important. Thus the accessibility of the inner side, which is responsible for its mineralization activity, is essential, and the question of preferred orientations of the Fn subunits above the respective surface will be answered. Here, the putative preferential protein orientation for initial adsorption at a given pH will be predicted following the procedure of Hildebrand et al. [115]. A snapshot of the MD simulation of the heavy Fn subunit above the amorphous alumina surface is shown in Fig. 1.8. Furthermore, physisorption, which presents the

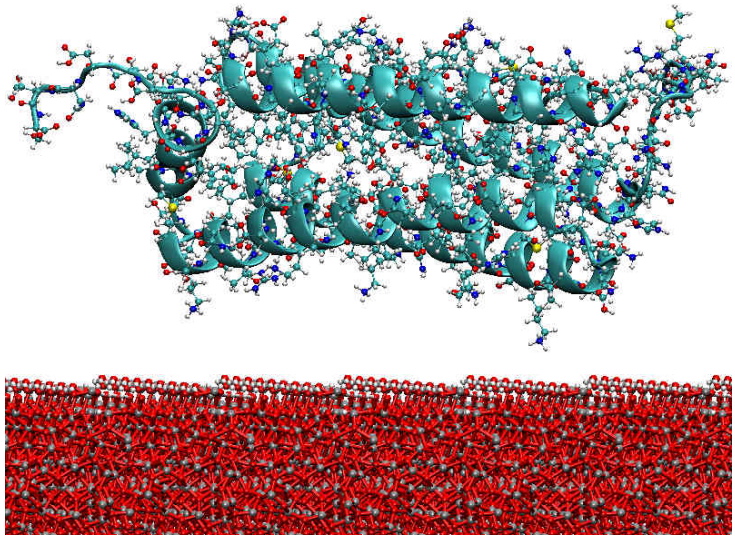

Figure 1.8: Snapshots of the MD simulation of the Fn H subunit above a pseudo-amorphous alumina surface to find putative preferential protein orientation for initial adsorption. Here, the inner side (with reference to their assembly in hollow Fn spheres) is pointing to the surface (see chapter 3).

easiest solution for immobilization, will be investigated to reveal the stability of this non-covalent immobilization strategy. For that, the driving forces towards the non-covalent adsorption of Fn subunits to the amorphous Al_2O_3 (alumina) and SiO_2 (silica) will be investigated.

Models and classical force field parameters for the amorphous SiO_2 surface are available in literature [116] and models of the Fn subunits will be taken from the protein database and described by the AMBER-99SB 25 force field [117]. Anyway, due to the amorphous layer which is found on alumina particles even with a crystalline core [118, 119], amorphous alumina models as well as a suitable classical force field potential are needed but missing in literature so far. These missing parameters could be fitted to Density Functional Theory (DFT) reference calculations based on the successful previous works for the case of the SiO_x/water/protein [116, 120, 121] and TiO_x/water/protein [122] interfaces. To enable this fitting and all subsequent investigations, surface and particle models have to be generated which guarantees chemical stability and realistic termination. For that, bulk amorphous structures and surfaces will be generated taking into account the chemical termination with hydroxyl groups and chemisorbed water molecules at the full quantum level.

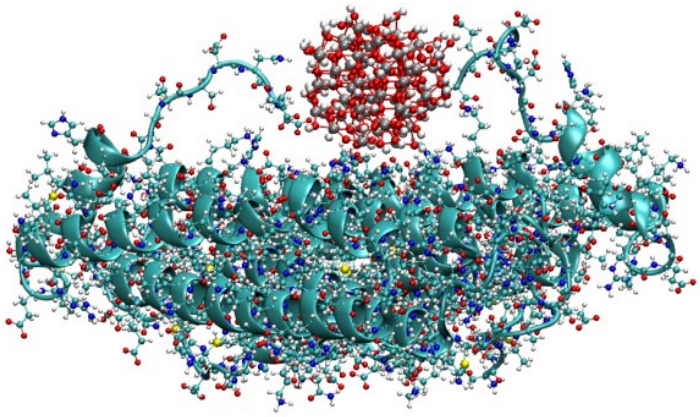

Figure 1.9: Docking of a small goethite nanoparticle model to a twofold-symmetric ferritin subunit arrangement to investigate the anchoring sites of Fe(III) oxyhydroxides clusters on ferritin subunit assemblies.

After that, the different roles in iron uptake and mineralization of H (heavy) and L (light) subunits will be investigated, since the different functions are still not clear but maybe a key to tune and control mineral synthesis. Realistic models of goethite and ferrihydrite nanoparticles will be created based on the classical force field for iron oxyhydroxide in a water environment [105] which will be extended in this work to describe Fe-O-Fe interactions within solid Fe(III) phases. Based on these models and classical force field parameters, a series of molecular dynamics simulations will be performed to investigate the anchoring sites for Fe(III) clusters on Fn subunit assemblies. A snapshot as an example of the performed docking simulations for the case of a small iron oxyhydroxide particle above a twofold-symmetric ferritin subunit arrangement is shown in Fig. 1.9. The distribution of anchoring sites for Fe(III) nuclei in ferritin will be analyzed to answer some fundamental questions for a precise understanding of this early nucleation step. Are there differences of the distribution of anchoring sites between heavy (H) and light (L) Fn subunits or between the inner part of the subunits and the outer part (with reference to their assembly in hollow Fn spheres)? According to the current understanding, L subunits are primarily responsible for promoting or at least assisting iron nucleation and anchoring, mineralization, and long-term storage of Fe(III) [85, 86]. H subunits play instead a major role in the catalytic oxidation of Fe^{2+} ions to Fe^{3+} at the so-called ferroxidase site as already described and shown in section 1.4. Furthermore, the question of similarities between the residues of the anchoring sites and residues in iron oxide binding peptide

sequences [123, 124] will be addressed.

Finally, the molecular mechanisms of crystal nucleation and growth of iron oxide in water and at the ferritin/oxide interfaces will be investigated starting from an accurate analysis of the formed iron oxide phases. To this aim, the Kawska-Zahn approach [60] will be used to simulate the nucleation and crystal growth of iron oxyhydroxide. This approach will be implemented and tested for the case of crystal growth of iron oxyhydroxide in water. Furthermore, the possibility of describing proton-transfer reactions, following the idea of ripening reactions, will be investigated. The inclusion of different kinds of proton transfer reactions during the simulation could answer the question if different types of proton transfer reactions can influence the final crystal structure.

Moreover, it is known that iron oxyhydroxide forms either α or γ-FeOOH (goethite or lepidocrocite) in water, while ferrihydrite is formed in the ferritin shell under identical conditions [125]. An understanding of the structure-function relationship of the organic matrix/mineral composite is very important for the development of bio-inspired materials. Furthermore, the interaction between the organic and inorganic phases also plays an important role in determining the material properties of the biominerals. Therefore, it is essential to investigate and answer the question of structural differences between the phases which are grown in water and on Fn subunits based on classical force fields.

Standard methods such as radial distribution function (see section 3.1.1), coordination number [126] or motif recognition [127] are hardly applicable to investigate such structural differences for iron oxyhydroxides, due to the fact that these structures consist mainly of four and six-fold coordinated iron atoms. Therefore, machine-learning-based methods of phase recognition, which are not dissimilar in essence from the well-known face-recognition techniques, will be applied.

Chapter 2

Methods

This chapter contains a short introduction of the simulation techniques used in this thesis. First, classical force fields and classical molecular dynamic simulations are introduced, followed by an advanced sampling method which is employed to calculate interaction free energies at protein/mineral interfaces. Afterward, quantum mechanical simulations within Density Functional Theory are presented together with corrections and approximations for accelerated ab-initio molecular dynamics simulations. A more in-depth look at each technique can be found in the standard literature of the respective method. The technical details of all simulations can be found in the appendix, as referenced in the respective chapters.

2.1 Classical force fields

A very important tool to investigate structure, dynamic and thermodynamic of biological systems are Molecular Dynamic (MD) simulations on the basis of classical force fields (FF). These classical force fields are necessary to integrate Newton's equation of motion, in which atoms are described as particles with mass m:

$$\vec{F} = m \cdot \vec{a} \tag{2.1}$$

where $\vec{F}$ is the force which acts on a particle, producing an acceleration $\vec{a}$. This force can be expressed as a gradient of the potential energy V which act on the particle at position $\vec{x}$:

$$\vec{F} = -\nabla V(\vec{x}) \tag{2.2}$$

This potential is approximated by classical force fields. In this work, the AMBER force field [128] is used, in which the potential is divided into bonded and non-bonded interactions. Bonded interactions consist of contributions of bond lengths, angles, and dihedrals:

$$V_{bonded} = \overbrace{\sum_{1-2pairs} K_r(r-r_0)^2}^{bond} + \overbrace{\sum_{1-3pairs} K_\theta(\theta-\theta_0)^2}^{angle} + \overbrace{\sum_{1-4pairs} \frac{V_n}{2}[1+cos(n\ \Phi)-\delta]}^{dihedral} \tag{2.3}$$

The directly bonded potential is defined by a harmonic potential with the length r, the equilibrium length r_0, and the spring constant K_r. The harmonic three direct neighboring atom potential is based on the angle θ, the equilibrium angle θ_0, and the spring constant K_θ. The non-harmonic dihedral part describes the rotation of four bonded atoms. It is described by a periodic cosine function with the maximum energy difference V_n of the respective conformation by rotation around the dihedral Φ. Here, n is the number of the periodicity and δ the phase shift with respect to the equilibrium angle.

The non-bonded interactions consist of a Coulomb and a van-der-Waals part, here in the form of the Lennard-Jones-12-6-Potential, as implemented in the 'Large-scale Atomic/Molecular Massively Parallel Simulator' (LAMMPS) [129].

$$V_{non-bonded} = \overbrace{\sum_{ij} 4\varepsilon_{ij}\left[\left(\frac{\sigma_{ij}}{r_{ij}}\right)^{12} - \left(\frac{\sigma_{ij}}{r_{ij}}\right)^{6}\right]}^{Lennard-Jones} + \overbrace{\sum_{ij}\left(\frac{Cq_iq_j}{\epsilon r_{ij}}\right)}^{Coulomb}. \tag{2.4}$$

Here σ_{ij} and ε_{ij} are calculated via straightforward combination rules [130, 131] $\sigma_{ij} = (\sigma_i + \sigma_j)/2$ and $\varepsilon_{ij} = \sqrt{\varepsilon_i \varepsilon_j}$, for atoms i and j separated by a distance r_{ij}. C is an energy-conversion constant, q_i and q_j are the charges of the two atoms and ϵ is the dielectric constant of the medium in which the particles are embedded. The Lennard-Jones-Potential describes the attractive and repulsive interactions between two atoms as long as the distance between the two atoms is smaller than a selected cutoff radius ($r_{ij} < r_c$).

To start a calculation, a randomly chosen velocity of the Maxwell-Boltzmann-velocity-distribution is applied to every atom depending on the selected temperature (T).

$$p(v) = \frac{m}{2\pi k_B T} exp\left(\frac{-mv^2}{k_B T}\right) \tag{2.5}$$

Where k_B is the Boltzmann constant and m and v the mass and velocity of the atom. For the MD simulation, Newton's equation of motion has to be integrated for all atoms of the system at the same time. Since this is not possible, numerical methods based on Taylor expansions are used to solve this problem. Here, a timestep δt is chosen and the equations of motions are evaluated at each step, iteratively. For the calculation of position and velocity at the next step $t + \delta t$, the 'Velocity-Verlet' algorithm [132] is used, which considers Taylor expansion up to the third term:

$$x(t + \delta t) = x(t) + v(t)\delta t + \frac{1}{2}a(t)\delta t^2 \tag{2.6}$$

$$a(t + \delta t) = -\frac{1}{m}\frac{\delta V(x(t + \delta t))}{\delta t} \tag{2.7}$$

$$v(t + \delta t) = v(t) + \frac{1}{2}[a(t) + a(t + \delta t)]\delta t \tag{2.8}$$

Most of the MD simulations in this thesis are performed in the NVT ensemble. An ensemble is the statistical population of a large number of physically similar systems. The canonical NVT ensemble represents a closed system, where the number of atoms (N), the volume of the system (V) and the temperature (T) are constant. A thermostat is used for the regulation of the temperature during the calculation. The simplest way to control the temperature is to adjust the velocities of the atoms, since:

$$\langle E_{kin} \rangle = \frac{1}{N}\sum_{i=1}^{N}\frac{1}{2}m_i v_i^2 = \frac{3}{2}k_B T \tag{2.9}$$

with the mass m of an atom with the velocity v and the Boltzmann constant k_B. The difference between selected and current temperature is known, and the velocities of the atoms are multiplied by a factor which is proportional to this temperature difference. One problem with this approach is that it does not allow fluctuations in temperature which are present in the canonical ensemble. Therefore, the Nosé-Hoover thermostat [133, 134] is used, which was originally developed by Nosé and further improved by Hoover. In this

approach, an additional reservoir is introduced with an own potential and kinetic energy. The coupling to the real system influences the temperature fluctuations which conserves the canonical ensemble of the original system. Therefore, the temperature is not fixed, rather tends to the target value.

Extensive sampling is required to overcome energy barriers of a few k_BT in these standard MD simulations. Unfortunately, this does normally not happen in typically short simulation times of ~100 ns. Therefore, standard MD simulations are often trapped in local minima of the energy landscape. To overcome this limitation more advanced MD simulation techniques are needed. One of these techniques is presented in the following section, which includes additional bias potentials on top of the unbiased force field potential to compensate the poor sampling of a standard MD simulation

2.1.1 RESTmetaD simulations

The advanced molecular dynamic simulation method called RESTmetaD combines Replica Exchange Solute Tempering (REST) with Metadynamics (meta), which complement each other in an ideal way.

By using this technique, it is possible to overcome energy barriers and thus escape from local minima of the potential energy. This enables the scan of the whole conformational phase space and by that, for example, calculate the free energy of adsorption of a peptide. As a consequence, this technique allows comparing results based on a classical force field with experimental values.

In Metadynamics simulations, the system starts in an unbiased state. During the simulation, an additional bias, chosen a priori, is added to the force field potential to accelerate the sampling along a chosen collective variable (CV). A CV is a function of the coordinates, such as the distance between two atoms, which is adapted to its height during the simulation. The repulsive bias potential, typically with the shape of a Gaussian, is added after a selected period of time to the current position of the CV. Here, the applied bias potential is given by [135, 136]:

$$V(s(q),t) = \sum_{k\tau<t} W(k\tau) exp\left(-\sum_{i=1}^{d} \frac{[s_i - s_i(q(k\tau))]^2}{2\sigma_i^2}\right) \tag{2.10}$$

with the height and width of the Gaussian W(kτ) and σ_i respectively, the natural number

k, the deposition stride of the Gaussians τ and d, which is the total number of the collectives variables s_i. Over time, more and more bias is added, and the native potential energy is compensated by the increasing bias potential. As a result, it can be demonstrated that the added bias potential converges towards the systems free energy landscape plus an offset constant [135, 136]:

$$V(s(q), t \to \infty)_{bias} = -F(s(q)) + C. \tag{2.11}$$

In the REST method, the usage of several replicas of the system at different temperatures is used to overcome the limitations of a standard MD simulation. Here, a base replica at 300K is used, which exchanges the atom coordinates $\vec{x}$ after a particular simulation time with replicas at higher temperatures and thus reduced energy barriers. It must be ensured that the conditions of each replica branch stay constant by exchange of the atom coordinates $\vec{x}$, and the ground replica must be still in a canonic ensemble, even though after exchanges with other branches [137, 138]. For that, the potential energy of the system is divided in a central group (here the protein p), and the bath (here water w) and the total potential energy of replica m becomes [139, 140]:

$$E_m = E_{pp} + \left[\frac{\beta_0}{\beta_m}\right] E_{ww} + \left[\frac{\beta_0 + \beta_m}{2\beta_m}\right] E_{pw} \tag{2.12}$$

with the internal interactions of the protein E_{pp}, the internal interactions of water E_{ww} and the interaction between both systems E_{pw}. $\beta_0 = 1/k_B T_0$ with the temperature T_0 of the base replica and $\beta_m = 1/k_B T_m$ with the temperature T_m of the replicas of higher temperatures. By this division, it is possible to keep the bath (solvent) cold and only expose the solute to higher temperatures, therefore this method is called replica exchange with solute tempering

While the temperature in the REST method typically ranges from 270-695 K [141], the bias due to the added potential of metaD effective CV temperature is typically around 3000 K [142, 143]. The combination of these two methods thus significantly improve the sampling potential of either the REST or the metaD methods alone. In conclusion, metadynamics samples very efficiently along a selected CV while slow degrees of freedom not reached by the chosen CV can partly be compensated by the solute tempering.

2.2 Density Functional Theory (DFT)

The equation of motion in many body systems in quantum mechanics is given by the time-dependent Schrödinger equation:

$$\hat{H}\Psi = i\hbar\frac{\partial}{\partial t}\Psi \tag{2.13}$$

Where Ψ is the wave function, i is the imaginary unit, $\hbar$ is the reduced Planck constant ($\hbar = \frac{h}{2\pi}$) and $\hat{H}$ the Hamilton operator. Schrödinger's equation for systems with more than a pair of atoms is not solvable analytically. A first approach to reduce this problem is the separation of atomic nuclei and electron motion, due to the huge difference in mass and the high velocity of the electron. This concept is at the basis of the Born-Oppenheimer-Approximation [144]. It means the motion of electrons is taking place on a different time scale and the electrons follow the motion of core nuclei instantly while remaining in their groundstate. By this separation, it is possible to handle the motion of core nuclei classically, and the original problem is reduced to identifying the electron groundstate. One way to accomplish this is via Density Functional Theory (DFT), which leads to the determination of the quantum mechanical groundstate of a system on the basis of the electron density alone. DFT roots on the first Hohenberg-Kohn theorem, which demonstrates that for a system of interacting electrons, the ground state to an external potential V_{ext} is uniquely defined by the ground state density $n(r)$ [145]. By the second Hohenberg-Kohn theorem, the energy functional of an arbitrary density n is bigger or equal the electronic ground state energy [145]. This allows, under observation of the density n as a variable, to solve the many-body problem by minimization of the energy functional $E[n]$. The energy functional of the overall system reads as follows:

$$E[n] = T[n] + V_{int}[n] + V_{ext}[n] = F_{HK}[n] + \int n(r)V_{ext}(r)dr \tag{2.14}$$

with the kinetic energy functional T and the intern potential of the electron-electron-interaction V_{int}. The terms in the functional $F_{HK} = T[n] + V_{int}[n]$ includes all known many-body quantum effects. The approximation of Kohn and Sham [146] divide the terms of this functional in a functional of a non-interacting system of particles and an unknown functional E_{XC}. This contains all unknown parts of the interacting many-body system, whereby XC are the abbreviations of eXchange and Correlation. Additionally,

the term of the non-interacting system is divided into a kinetic and Hartree part, where the Hartree part is represented by Coulomb-Interactions of two charged clouds given by:

$$E_{Hartree}[n] = \frac{1}{2}\int\int \frac{n(r_i)n(r_j)}{|r_i - r_j|} dr_i dr_j \tag{2.15}$$

The kinetic energy part is split into contributions of non-interacting electrons $T_0[n]$ and an additional, unknown contribution $T_c[n]$:

$$T[n] = T_0[n] + T_c[n] \tag{2.16}$$

whereby $T_c[n]$ is a part of the unknown functional E_{XC}. Based on the assumptions of Kohn and Sham [146], the overall expression of the energy functional of a system is:

$$E[n] = T_0[n] + \int n(r)V_{ext}(r)dr + E_{Hartree}[n] + E_{XC}[n] \tag{2.17}$$

The base of this idea is the possibility to chose the effective potential of the non-interacting system in a way that the density of one-electron wavefunctions Ψ_i corresponds to the sought density. This leads to N independent equations for the description of electron motion in an effective Kohn-Sham potential, which includes the complex many-body interactions:

$$\hat{H}\Psi_i(r) = \left[-\frac{1}{2}\nabla^2 + V_{ext}(r) + V_{Hartree}(r) + V_{XC}(r)\right]\Psi_i(r) = E_i\Psi_i(r) \tag{2.18}$$

The only unknown part is the Exchange-Correlation-Potential, for which already simple approximations deliver sufficient accuracy for practical applications. The Local Density Approximation (LDA) is based on the assumption that the exchange-correlation energy of a varying charge density at a point is equal to the energy of a homogeneous electron gas with the same charge density. This simple assumptions already provides adequate results in many cases. In this work, the Generalized Gradient Approximation (GGA) is used for the exchange-correlation potential, which considers, next to the location-dependent density, also the gradient of the density.

$$E_{XC}^{GGA}[n] = \int n(r)\epsilon_{XC}^{GGA}(n(r), \nabla(r))dr \tag{2.19}$$

with ϵ_{XC}^{GGA} being the exchange-correlation energy of an homogeneous electron gas. Several forms of this approximation are available. In this work, the procedure of Perdew, Burke, and Ernzerhof (PBE) [147] is used. Furthermore, some calculations are performed spin-polarised, wherefore up and downspin are not necessarily in the same spatial orbital. Here, the kinetic and exchange-correlation parts are calculated separately for each spin, and the Hartree part and the external potential for the overall density. For the DFT based calculations, the Vienna Ab initio simulation package" (VASP) [148–151] is used. The technical details for each chapter can be found in the respective appendix.

To solve the Kohn-Sham equation numerically, a set of start-wavefunction have to be chosen at the first step. In this thesis, the plane wave Ansatz is used as the basis for the calculations, where the wave function is represented by linear combinations of plane waves. An important parameter becomes the energy cut off, which describes the maximum kinetic energy up to which plane waves are included in the basis set. The higher the cutoff, the more plane waves are included, but the longer the respective calculations. The higher the cutoff, the better the result, since plane waves with higher kinetic energy imply a higher frequency and lead therefore to a higher resolution. However, with the plane wave ansatz, all electrons are treated in the same way, independently of their distance to the core, but only the valence electrons with the highest distance to the core are mainly responsible for the chemical behavior and physical properties. Therefore, so-called pseudopotentials are used to approximate electrons near the core by an effective potential and reduce the calculation time. These pseudopotentials match the true core's Coulomb potential after a defined radius and describe therefore the valence electrons correctly. Inside this radius, the potentials are preferably smooth to overcome problems of oscillations of the valence functions near the core, since they have to be orthogonal to all the core states. Another possibility offers the projector augmented wave (PAW) method of Blöchl [152], which combines pseudopotentials with the linear augmented plane wave (LAPW) method. This combination provides the possibility of retaining calculation efficiency of pseudopotentials by simultaneously improving the description of valence orbitals near the core. For that, the wavefunction is divided into a part for electrons near the core and a part to describe the valence electrons. Here, the true wavefunction is transformed to a pseudo-wavefunction, whereby, in contrast to the pseudopotential method, the true wavefunction is accessible by a transformation operator. Furthermore, auxiliary functions are introduced, which are created with multiple angular-momentum components up to a defined radius, by linear

combinations of solutions of the radial equation of Schrödinger of isolated atoms. Outside the radius, they change over to the true wavefunction. The transformation operator is defined by true wavefunctions, the auxiliary functions and the so-called projection functions, which are the sum of normalized, free choosable function approximation.

Especially for larger systems, it is much more efficient to perform DFT based calculations in reciprocal space. For that, Bloch's theorem is used. It states that wavefunctions can be described by a plane wave multiplied by a periodic factor. Furthermore, this periodic factor can be expanded by Fourier transformation over reciprocal lattice vectors. For determination of energy or density, it is necessary to integrate over the first Brillouin-zone, which is described by $\vec{k}$-points. In calculations, the method of special-k-points [153] is used to substitute integrals of the Brillouin-zone by a weighted discrete sum. For these system dependent calculation parameters, it is important to find the minimum required number of k-points, to reduce the needed time of calculation, by simultaneous approximate the integral as best as possible. For that, the Monkhorst-Pack-scheme [154] is used, which systematically improves the approximation of the integral with a number of k-points by using the k-points as linear combinations of reciprocal lattice vectors.

2.2.1 Corrections in DFT based calculations

DFT is an exact theory, but for its application, approximations are necessary due to the not accessible exact form of the exchange-correlation potential. In the following, two types of corrections are introduced, which are used to overcome known weaknesses in DFT based calculations.

2.2.1.1 Hubbard-U correction

The isolating behavior of many oxides of transition metals cannot or is only defectively described by standard LDA or GGA methods. Here, not only the band-gap but also the ground state is qualitatively false determined. To correct this error, Anisomov et al. [155–157] added an additional on-site Hubbard-like interaction term E_{Hub} to the energy functional results in:

$$E_{GGA+U}[n(r)] = E_{GGA}[n(r)] + E_{Hub}[n_m^{I\sigma}] - E_{DC}[n^{I\sigma}] \tag{2.20}$$

With the electron density n, the atom orbital occupation $n_m^{I\sigma}$ of the atom I with the spin σ which is considered in the correction. E_{Hub} is the term that contains electron-electron interactions as modeled by the Hubbard Hamiltonian. The index m determine the spatial orbital of the corresponding azimuthal quantum number. For example, the d-orbtial with azimuthal quantum number $l = 2$ gives five $(2l + 1)$ possible spatial orbitals. The last term $E_{DC}[n^{I\sigma}]$ is subtracted to prevent double counting of the energy contribution of the orbital, which occurs in E_{Hub} and $E_{GGA}[n(r)]$. In the rotational-invariant approximation of Cococcioni et al. [158], as implemented in VASP and used in this thesis, the Hubbard-U correction results in:

$$\begin{aligned} E_U[n_{mm}^{I\sigma}] &= E_{Hub}[n_{mm}^{I\sigma}] - E_{DC}[n^{I\sigma}] \\ &= \frac{U}{2} \sum_I \sum_{m,\sigma} \left(n_{mm}^{I\sigma} - \sum_{m'} n_{mm'}^{I\sigma} n_{m'm}^{I\sigma} \right) \\ &= \frac{U}{2} \sum_{I,\sigma} Tr[n^{I\sigma}(1 - n^{I\sigma})] \end{aligned} \tag{2.21}$$

By this, the correction is optimized to the system by a free choosable correction value U for the curvature found in the total energy for non-integer occupation numbers, due to the self-interaction of latter. In this thesis, for iron, a U value of 4.3 eV is used, which leads in a previous work with similar systems to reasonable results [158].

Fig. 2.1 contains the density of states (DOS), means the number of states within an energy interval, for the iron and oxygen atoms of the goethite unit cell. Here, the band gap is of special interest. It describes the energy range between the valence and conduction band where no electron states can exist. Goethite as an isolator presents band gap values between 2.1 eV and 2.5 eV [101]. Standard GGA calculations basically underestimate the band gap, and here a value of 0.294 eV is obtained (see Fig. 2.1 left). By including the Hubbard-U correction with the mentioned U value of 4.3 eV the area between valence and conduction band is widened and the band gap climbs to a value of 1.662 eV (see Fig. 2.1 right). Furthermore, the energy levels are shifted, and is was already proven that results based on these shifts lead to better accordances with experiments both for goethite and other iron oxyhydroxides (see ref [159]).

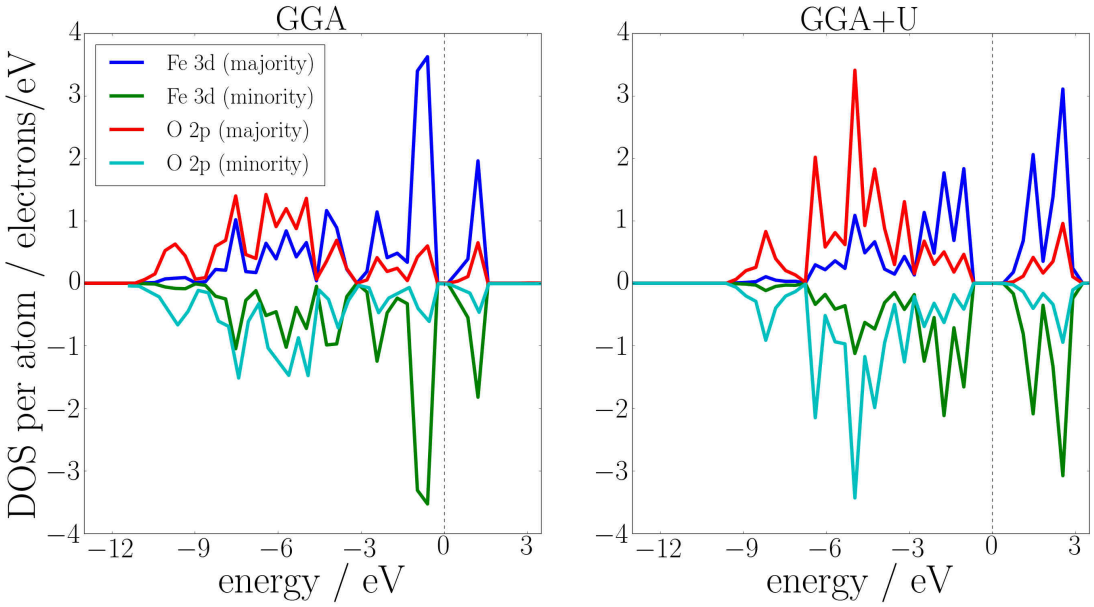

Figure 2.1: Projected density of states of the iron and oxygen atoms of the goethite unit cell obtained with and without the inclusion of the Hubbard-U correction.

2.2.1.2 vdw-DF2 correction

The van-der-Waals interaction is a quantum mechanical phenomenon, which describes the interactions of charge distributions of an atomic system through electrodynamic correlation with charge distribution of another system. As explained above, DFT is exact and contains this interaction in the exchange-correlation potential. But due to the approximations of this potential, long-range interactions such as van-der-Waals interactions are not described by local approximation as LDA and GGA. As a correction for this missing information, the second order van-der-Waals correction (vdw-DF2) is used. This correction has been proven as reliable for systems similar to this studied in this thesis [105, 160]. The basis for the van-der-Waals correction is supplied by the approach to divide the correlation energy into two parts, one for the local and one for the non-local interactions. While the local part can correctly be described by LDA or GGA, the non-local part is estimated by several approximations [161]. The general form of the non-local correlation energy (E_c^{nl}) is in the original vdw-DF correction [161] as in the optimized vdw-DF2 correction [162] given by:

$$E_c^{nl}[\delta n] = \int d^3 r_i \int d^3 r_j \delta n(r_i) \phi(r_i, r_j) \delta n(r_j) \tag{2.22}$$

with δn, the deviation of the charge density to a homogeneous system at the points r_i and r_j and the kernel function ϕ. This kernel function depends on $Rf(r_i)$ and $Rf(r_j)$, where $R = |r_i - r_j|$ and $f(r)$ is a function of $\delta n(r)$ and the gradient $\nabla\delta n(r)$. The vdw-DF2 correction of Lee et al. [162], which is used in this thesis, is based on the original vdw-DF correction of Andersson et al. [161] and is improved with regard to equilibrium distances and the strength of hydrogen bonds. This happened, among others, by replacing the revPBE [163] by the PW86 [164] exchange potential, because revPBE was shown to be too repulsive close to the equilibrium distance.

2.2.2 Car-Parrinello molecular dynamics

In this thesis, the correct surface termination of an amorphous alumina surface is investigated by means of first-principles molecular dynamics simulation of the amorphous alumina surface in contact with water. Since standard DFT based calculations are time-consuming, especially DFT based molecular dynamic simulations of bigger systems, it is advisable to use other concepts. In the following, the Car-Parrinello molecular dynamics [165] is used, which is based on the idea to avoid the time effort involved in optimizing the wavefunction at every timestep.

The CPMD combines Ehrenfest and Born-Oppenheimer molecular dynamics. In the Ehrenfest molecular dynamics the wavefunction is optimized only once, and during the further simulation, it should be ensured that the electrons remain in the ground state, despite the motion of the core. Thus, the timestep of the simulation is determined by the electronic motion. In the Born-Oppenheimer molecular dynamics, instead, the wavefunction of the electrons is minimized after every change of configuration. In this way, the timestep of the simulation is defined by the core motion. CPMD tries to combine the benefits of both methods using a timestep which is defined by the core motion and a one-time minimization of the electronic wavefunction. The introduction of a fictional mass for the electron wavefunction μ, which is much higher than the real electron mass, is essential to maintain adiabaticity of the electronic degrees of freedom. Thus, the electrons remain in their groundstate during the simulation, and the wavefunction does not have to be minimized after every step. The motion of the atom cores is adjusted to the physical temperature, which is proportional to the kinetic energy, while the electrons move according to a fictional temperature, which is proportional to the fictional kinetic energy of the orbitals. Additionally, with the implementation of the fictional mass of the

electrons, adiabatic separation is assumed, therefore consideration of separated electron- and core-systems without energy transfer between the two systems. The CP equation of the core motion reads as follows [166]:

$$M_I \ddot{R}_I(t) = -\frac{\partial}{\partial R_I} \left(< \Psi_0 | H_e | \Psi_0 > + constraints \right) \tag{2.23}$$

and accordingly for the electrons:

$$\mu_i \ddot{\Psi}_i(t) = -\frac{\partial}{\partial \Psi_i^*} \left(< \Psi_0 | H_e | \Psi_0 > + constraints \right) \tag{2.24}$$

With the mass of the core M_I, the position of the core R_I, the groundstate wavefunction Ψ_0, the hamiltonian H_e and the fictional mass of the wavefunction μ. The constraints are the sum of all necessary conditions of the system such as orthonormality of the wavefunction. To ensure adiabatic separation, the phonon and electron spectra must not overlap. This is guaranteed by a frequency gap (ω_{ij}) dependent upon the energy gap between occupied (i) and unoccupied (j) states with related eigenvalues ε_i and ε_j [166]:

$$\omega_{ij} = \sqrt{\frac{2\left(\epsilon_i - \epsilon_j\right)}{\mu}}. \tag{2.25}$$

Corrections to the original CP formulation are available to guarantee adiabaticity even in the case of systems with small or zero gaps, such as metals.

Chapter 3

Interfaces between Ferritin and Al_2O_3/SiO_2

The immobilization of Ferritin subunits is of fundamental importance for the fabrication of continuous and extended 2D and 3D structures on stable material surfaces. In particular, the engineering of extended metal oxide structures on stable material surfaces via bio-inspired crystal nucleation and growth, based on the possibility of immobilization of Fn subunits while retaining their mineralization activity.

Two different oxide surfaces are chosen as versatile templates for the immobilization of Fn subunits. Alumina (Al_2O_3) is readily available as a cheap particulate material with a large surface area. Moreover, TEM supports can be prepared from alumina crystals, enabling characterization of the growing magnetic films with atomic-level resolution (see Fig. 3.2). Additionally, Silica (SiO_2) particles are used, which can be easily modified, and are perfectly spherical. Here the growth can be visualized by TEM images, and examples are presented in Fig. 3.1.

The most straightforward method for biomolecule immobilization is the physisorption from a concentrated protein solution. It was already proven that sufficiently stable adsorbed protein layers can be obtained while retaining the enzymatic activity in the adsorbed state [169, 170]. The main objective of this chapter is the investigation of the preferred protein adsorption orientation on the Al_2O_3 and SiO_2 surfaces. Thus, the accessibility of the site of the subunit which is responsible for its mineralization activity, as well as the strength of the forces between the subunits and the surfaces at different pH values are studied. This investigation is performed following the procedure of a previous work [115], in which static single-point calculations of the proteins are performed at different protein-surface heights, where the protein is at every height rotated around its

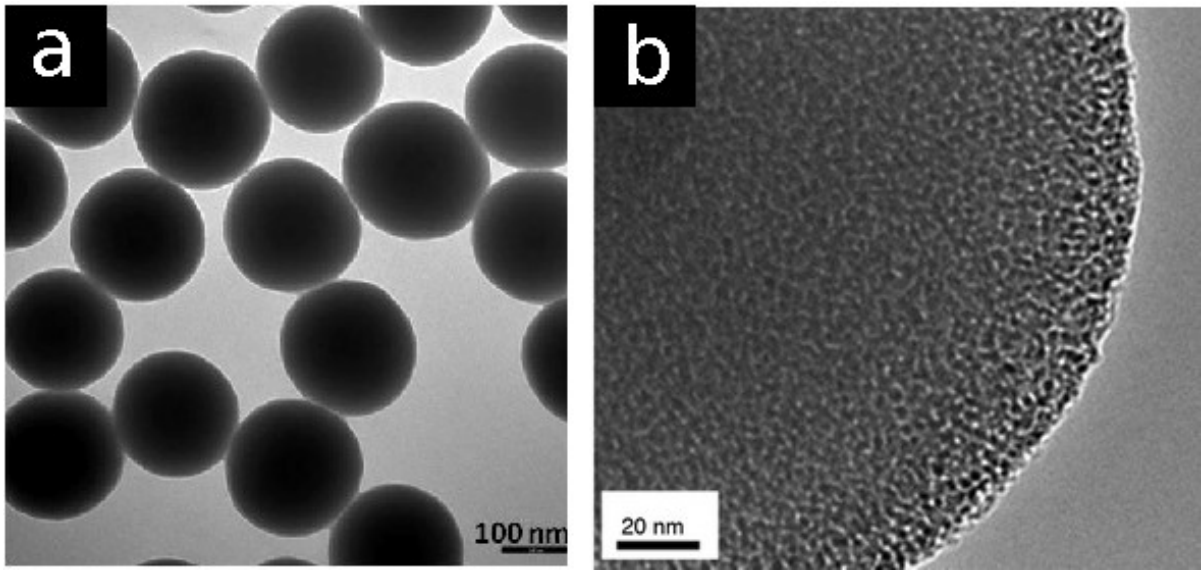

Figure 3.1: TEM images (a) of the silica nanoparticles (150 nm) taken from ref. [167] and HR-TEM images (b) of silica nanoparticles taken from ref. [168].

geometrical center. In order to achieve this goal, classical force-field potentials and realistic surface models for alumina and silica are needed, and the general procedure to obtain these is explained in the following by taking the example of alumina. The models and parameters for silica were determined following a similar strategy in a previous work in our group [116]. Here, realistic models of amorphous alumina/water interfaces are created taking into account the chemical termination with hydroxyl groups and chemisorbed water molecules, as predicted by Density Functional Theory (DFT) based MD simulations. On the basis of these models, we parametrize a fixed-charges force field to describe the interactions within alumina and across the alumina/water interface, which can be seamlessly combined with biomolecular force fields via straightforward combination rules. All newly determined force field parameters are fitted to reference calculations at the level of dispersion-corrected DFT (see section 2.2). The accuracy of our force field parametrization is tested by comparing the heat of immersion of the surface computed in molecular dynamics simulations with available experimental values. The ability of our models and force field to predict experimental observables is demonstrated by unbiased calculations of the adsorption free energy of glutathione disulfide on alumina in comparison with experimental data. All technical details to the creation of surface models and force field parameters are presented in Lid et al. [171]. Further technical details of the setup of the simulations regarding physisorption (section 3.3) as well as the supporting experimental

results are taken from ref [167].

3.1 Amorphous Al_2O_3 bulk structures and surfaces

As far as atomistic simulations are concerned, most of the available work on alumina/water interfaces has so far employed ideally crystalline surface models [172, 173]. However, it is well established that even particles with a crystalline core (e.g., α-Al_2O_3) present a few nm thick amorphous layers of aluminum oxyhydroxide at their outmost surfaces [118, 119]. This calls for the development of new realistic models of interfaces between amorphous alumina and large molecules, such as organic drugs or proteins, in water solutions. Scanning electron microscopic (SEM), transmission electron microscopic images (TEM) and high-resolution transmission electron microscopy (HR-TEM) images of the alumina core and an amorphous layer at the surface are presented in Fig. 3.2.

In this section, the strategy for the creation of amorphous alumina surfaces structures including the correct surface termination is introduced and validated. In line with a previous work of Adiga et al. [174], we describe the interactions within the alumina bulk and the terminal hydroxyl group by means of a Buckingham-Coulomb potential of the form:

$$V(r_{ij}) = A_{ij}e^{-\frac{r_{ij}}{\rho_{ij}}} - \frac{C_{ij}}{r_{ij}^6} + \frac{q_i q_j}{r_{ij}} \tag{3.1}$$

in which the atoms i and j are separated by a distance r_{ij} and the assigned parameters A_{ij}, ρ_{ij} and C_{ij} are reported in Table 3.1. As an exception, Al-H and H-H atom pairs only interact through the Coulomb term.

In the original reference [174], the surface hydroxylation was modeled empirically, upon replacement of Al with H atoms in amorphous bulk structures before surface creation and MD annealing. We follow here a different strategy, in which relatively small models of bulk amorphous structures and dry surfaces are first created with the classical force field, and then allowed to react with bulk water in DFT-based first-principles MD simulations. This allows the chemisorption process of water on reactive surface sites to be described at the full quantum level.

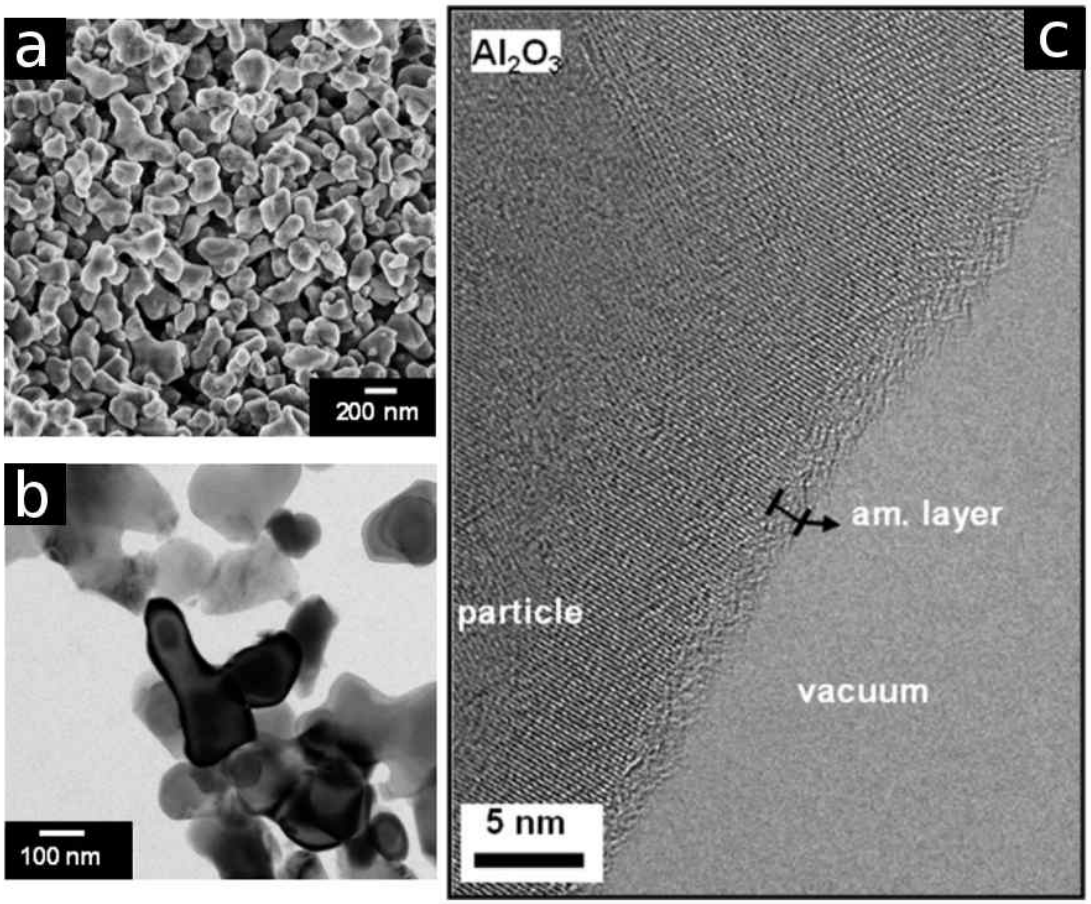

Figure 3.2: SEM (a) and TEM (b) images of alumina nanoparticles taken from ref. [172] and HR-TEM images (c) of the alumina particle crystal structure of the core and an amorphous layer on the surface taken from ref. [118].

Table 3.1: Potential parameters parameter from Matsui [175] and Adiga et al. [174]. Al-H and H-H atom pairs interact only via the Coulomb term. The charges are q_{Al} = 1.4175 e, q_O = -0.945 e and q_H = 0.4725 e.

	A_{ij}/eV	ρ_{ij}/Å	C_{ij}/eV^6
Al-Al	31570921	0.068	14.05
Al-O	28476	0.172	34.58
O-O	6462	0.276	85.09
O-H	9871	0.113	0.71

3.1.1 Amorphous bulk structures

Amorphous bulk structures are created with a hybrid 'melt and quench' technique following the scheme of Chagarov et al. [176]. Namely, Al and O atoms are randomly placed in the correct stoichiometry in a simulation box at the very low density of 0.9 g/cm^3. The system is first annealed at 5000K for 500 ps at constant volume, and then the density is gradually increased to 3.2 g/cm^3 over 350 ps. After a further 400 ps equilibration, the system is cooled down to 300 K in 100 ps and further equilibrated for 1 ns. The strategy is applied to four different systems with increasing number of atoms (100, 200, 1000 and 2000 atoms).

In order to compare the obtained structures with other theoretical and experimental data, we calculate the radial distribution function (RDF) $g_{i,j}$ between pairs of atoms i and j as

$$g_{i,j}(r) = \frac{\langle n_{i,j}\,(r, r+\Delta r)\rangle}{\rho_j 4\pi r^2 \Delta r}\ , \tag{3.2}$$

where ρ_j is the bulk density of species j and Δr is a chosen step width (0.1 Å in our case). From $g_{i,j}$ we can compute the average first-neighbor distance $d_{i,j}$, corresponding to the position of the first peak's maximum, as well as the average nearest-neighbor number $n_{i,j}$. The latter is obtained by integrating $g_{i,j}$ up to the radius $R_{i,j}$ corresponding to the minimum after the first RDF peak:

$$n_{i,j}(R) = 4\pi\rho_j \int_0^{R_{i,j}} g_{i,j}(r) r^2 dr\ . \tag{3.3}$$

In Table 3.2 we list the values of d and n for the different atom pairs, with $R_{Al-Al} = 3.7$ Å, $R_{Al-O} = 2.2$ Å, and $R_{O-O} = 3.2$ Å, in comparison with literature data of simulations [176, 177] and experiments [178]. The results are nearly independent on the number of atoms, with the exception of the smallest system (100 atoms), in which the average Al–Al distance is significantly smaller and the O–O distance larger than in the other cases. Our results are in good agreement with literature data obtained with the same Matsui interatomic potential, except for the smaller value of n_{Al-Al} predicted by Chagarov [176]. In comparison with available experimental data, the first-neighbor distances are reasonably well reproduced or slightly underestimated. However, for all atom pairs, the number of coordination neighbors predicted by the Matsui potential is larger than in the experi-

Table 3.2: Positions of the RDF peak maxima d and average nearest neighbor numbers n for our systems including different number of atoms (100, 200, 1000, 2000) in comparison with literature data of simulations (sim) and experiments (exp).

	Al-Al		Al-O		O-O	
System	d	n	d	n	d	n
100	2.95	8.50	1.75	4.24	2.83	10.16
200	3.10	8.24	1.76	4.31	2.77	10.00
1000	3.10	8.46	1.75	4.28	2.78	9.98
2000	3.07	8.51	1.75	4.32	2.75	10.00
sim [176]	3.07	6.98	1.77	4.23	2.82	10.66
sim [177]	3.12	8.26	1.76	4.25	2.75	9.47
exp [178]	3.2	6.0	1.8	4.1	2.8	8.5

ments, which is seemingly inconsistent with the good agreement regarding the atom-atom distances. A possibility to reconcile this discrepancy would be that the experimental samples investigated in ref. [178] contains a large number of defects such as vacancies, pores or grain boundaries, leading to an effective undercoordination of the atoms with respect to defect-free bulk.

In the following, we use the system containing 200 atoms as the basis for the construction of surface models in DFT simulations. To ensure that the chosen system size is sufficiently large, in Fig. 3.3 we display the RDF as well as the distribution of bond angles of this system in comparison with the MD simulations of Gutierrez et al. [177] (1800 atoms). While our data present fluctuations due to the small number of atoms, overall the agreement with the larger system regarding these structural details is very good. Similar comparisons with the data of Adiga et al. [179] (21375 atoms) and Chagarov et al. [176] (100 atoms) are presented in the Appendix in Fig. A1.

3.1.2 Surface termination predicted by Car-Parrinello molecular dynamics

In order to create a model of amorphous alumina surfaces in contact with liquid water, we start from the bulk amorphous structure composed of 200 Al and O atom described in the previous section. After cleaving the bulk crystal by increasing the periodic cell size along the z direction by 18 Å, the system is fully relaxed in a DFT simulation, and the free space between the top and bottom surfaces of the alumina slab is filled with 64 water

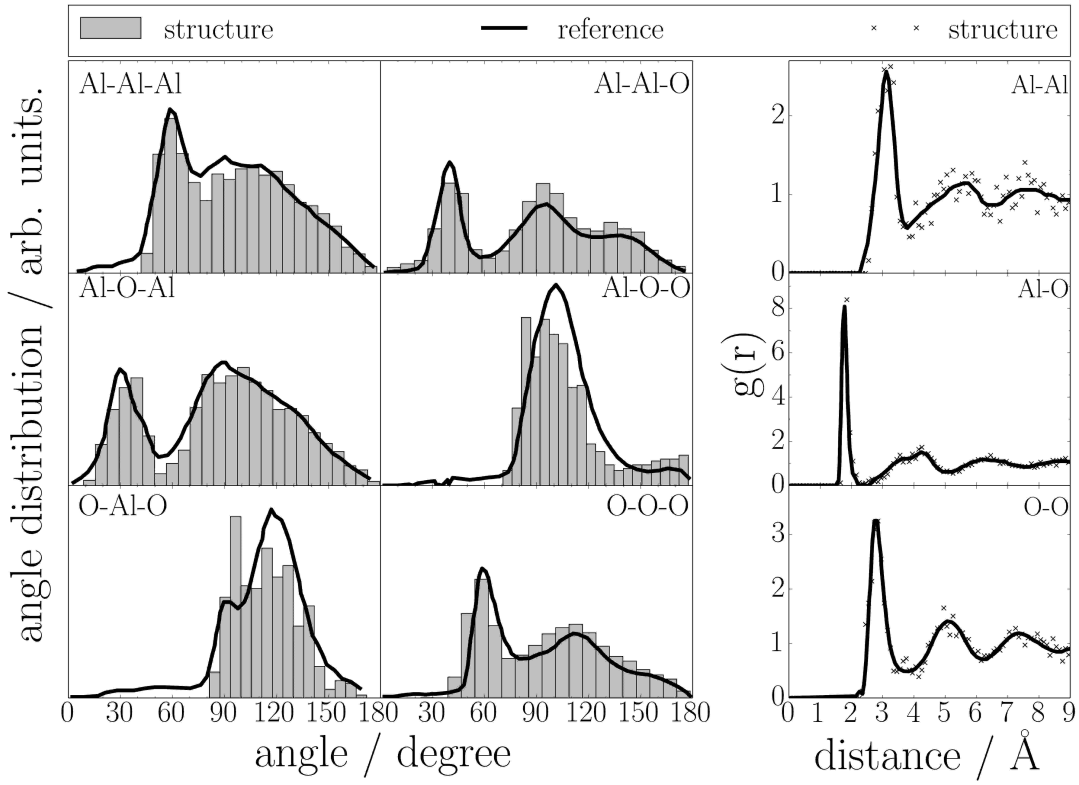

Figure 3.3: Angle and radial distribution function (g(r)) of an amorphous alumina structure, created by a melt and quench method described in the text, including 200 atoms in stoichiometric Al_2O_3 ratio, in comparison to simulations of Gutierrez [177].

molecules, which roughly correspond to the correct water density.

A DFT-based, Car-Parrinello MD simulation (see section 2.2.2) is then started, during which the water molecules react with the dangling bonds of both the top and bottom surfaces of the alumina slab. Especially in the first few picoseconds of the simulation, several water molecules bind to undercoordinated Al atoms and immediately dissociate leaving a terminal OH group at the adsorption site and, in almost all cases, a proton on an O atom in fourth-neighbour position with respect to the terminal hydroxyl group. This dissociative adsorption mechanism is in perfect agreement with results of refs. [180, 181], where the 1-4 dissociation of water onto the (0001) surface of α-Al_2O_3 has been found to be kinetically strongly favored over the competing 1-2 dissociation. In a few cases, upon dissociation, the proton jumps to a much farther adsorption site via a Grotthuss proton-transfer chain along the hydrogen bond network of the liquid water.

Later in the simulation, two water molecules are observed to adsorb in molecular form

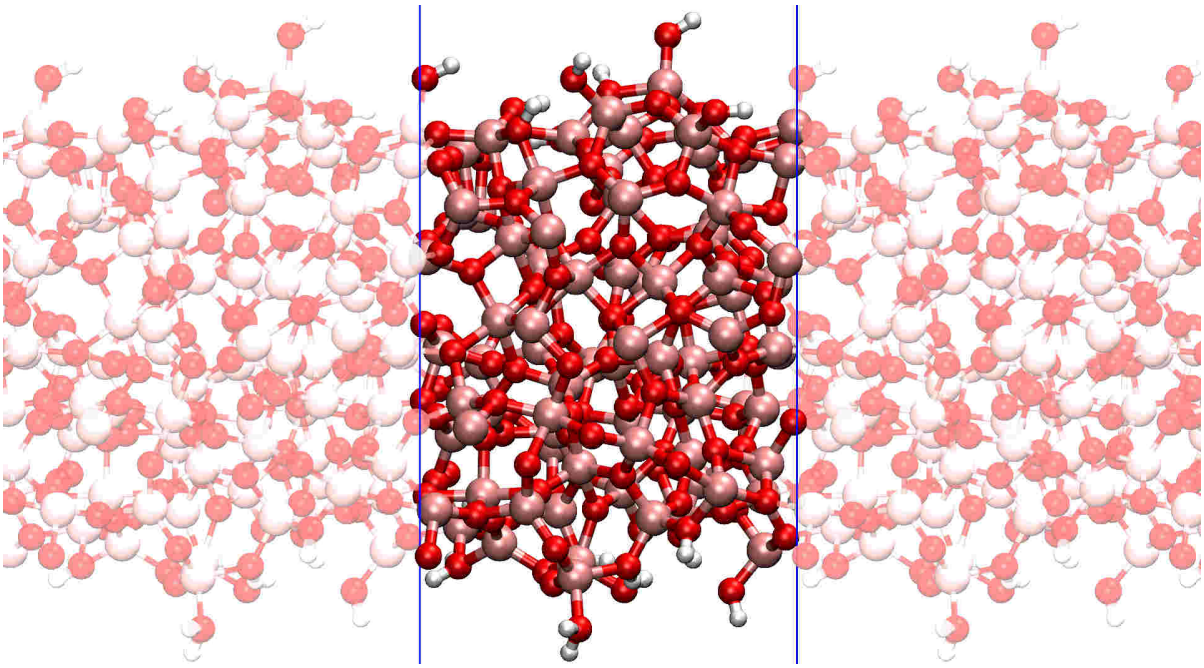

Figure 3.4: Protonated amorphous alumina surface after 10ps Car-Parinello molecular dynamic simulation.

and not to dissociate immediately. Overall, all adsorption events take place within 6 ps, with no further chemical interaction except for the eventual dissociation of one of the molecularly adsorbed molecules occurring in the following 4 ps, after which the simulation is stopped and the system fully relaxed to 0 K. The finally obtained terminated top and bottom slab surfaces are displayed in Fig. 3.4. The resulting OH density of 6.8 nm^{-2} is well within the wide range of experimental values lying between 3 to 15 OH/nm^2, depending on the pre-treatment temperature of the alumina powders used in the experiments [182].

3.2 A Force Field for the Al_2O_3/water/protein interface

On the basis of created models, we parametrize a fixed-charges force field to describe the interactions across the alumina/water/protein interface, which can be seamlessly combined with biomolecular force fields via straightforward combination rules.

Classical force fields describing the interactions in alumina bulk and dry surfaces are already available, either based on fixed charges [183, 184] or including polarizability [185] and charge transfer schemes [186]. Potentials mapping the interactions between the surface and its surrounding environment have also been presented, for instance, general oxide force fields [187], or parametrized for special cases such as crystalline alumina surfaces [173] or small molecule/small cluster interactions [188]. Moreover, a reactive force field of the 'ReaxFF' type has been developed for alumina/water systems [189], but to date, it has not been extended to include also the interaction with organic or biological molecules.

Here, we present a simple fixed-charges potential and its parameter optimization, enabling molecular dynamics simulations of amorphous alumina surfaces in contact with water and dissolved biomolecules.

3.2.1 Parameter fitting

In order to optimize the parameters of the interaction potential between the amorphous alumina surface and water solutions, we follow the approach already successfully employed in previous works for the case of the FeO(OH)/water/protein [105], SiO_x/water/protein [116, 120, 121], and TiO_x/water/protein [122] interfaces.

To ensure compatibility with standard biomolecular force fields such as AMBER [128], CHARMM [190] or OPLS [191], we map the true surface/molecule interactions onto a pairwise potential composed of a Coulomb and a 12-6 Lennard-Jones (LJ) term:

$$V(r_{ij}) = \frac{q_i q_j}{r_{ij}} + 4\varepsilon_{ij}\left[\left(\frac{\sigma_{ij}}{r_{ij}}\right)^{12} - \left(\frac{\sigma_{ij}}{r_{ij}}\right)^{6}\right] , \tag{3.4}$$

where r_{ij} is the distance between two atoms i and j with associated point charges q_i and q_j. The LJ pair parameters σ_{ij} and ε_{ij} are constructed from atom-specific parameters via Lorentz-Berthelot combination rules [130, 131] as $\sigma_{ij} = (\sigma_i + \sigma_j)/2$ and $\varepsilon_{ij} = \sqrt{\varepsilon_i \varepsilon_j}$.

In biomolecular force fields, the atomic point charges are often computed by fitting the electrostatic potential obtained from first-principle calculations (ESP charges). Interest-

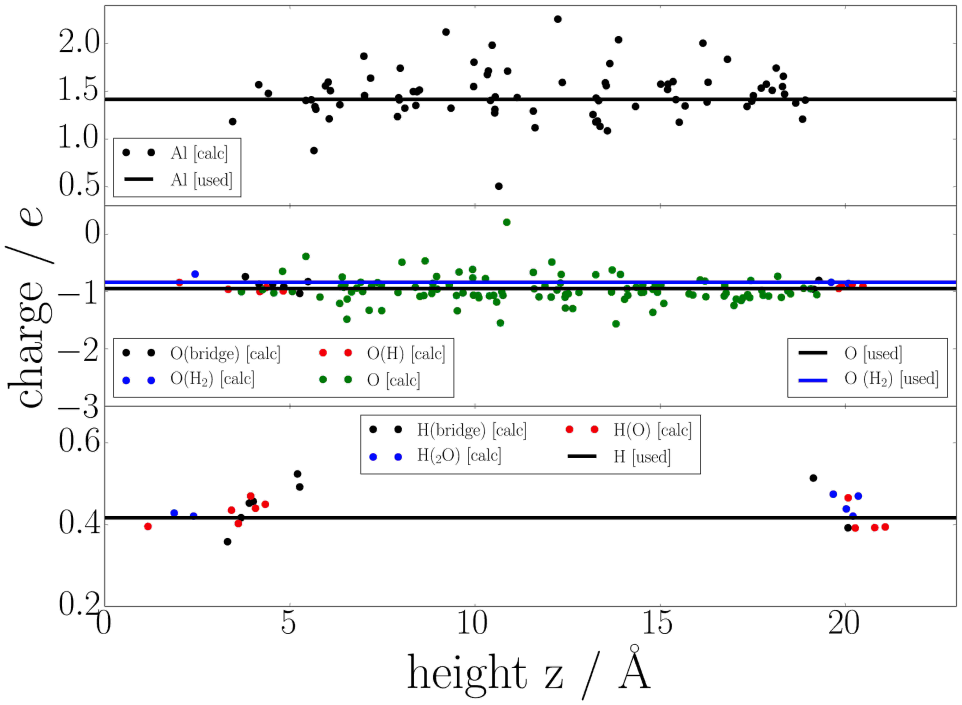

Figure 3.5: ESP charges calculated by the REPEAT Code [192] for all different atom types existing in the created amorphous alumina surface. The straight lines represent the charges which are used in our classical force field calculated by Matsui [175].

ingly, for our surface slab, the average ESP charges of all Al and O atoms computed with the REPEAT method [192] differ no more than 0.03 e from the atomic point charges used in the Matsui potential (see Fig. 3.5), which is within the error of the method. This allows us to use exactly the same point charges for the Coulomb interactions both within the alumina an across the alumina/water/biomolecule interfaces.

The LJ atomic parameters σ and ε are adjusted to best-fit the potential energy profiles computed with dispersion-corrected DFT for single water molecules in three different orientations at twelve different positions above the alumina surfaces. The three different water orientations correspond to the hydrogen atoms directed towards the surface (*down*), away from the surface (*up*) and in the unbiased orientation obtained after DFT relaxation at a given position (*relax*). The variation of the total energy of the system while the water is moved along the z coordinate perpendicular to the surface keeping all other atoms fixed is computed for each orientation and starting position. Representative examples for one position are shown in Fig. 3.6; all other energy profiles are reported in the Appendix

Table 3.3: Atomic specific charges and Lennard-Jones parameters to describe the interactions between amorphous Alumina and water.

element	q / e	σ / Å	ε / eV
Al	1.4175	1.29	0.08
O	-0.945	3.07	0.02
H	0.4725	0.52	0.004

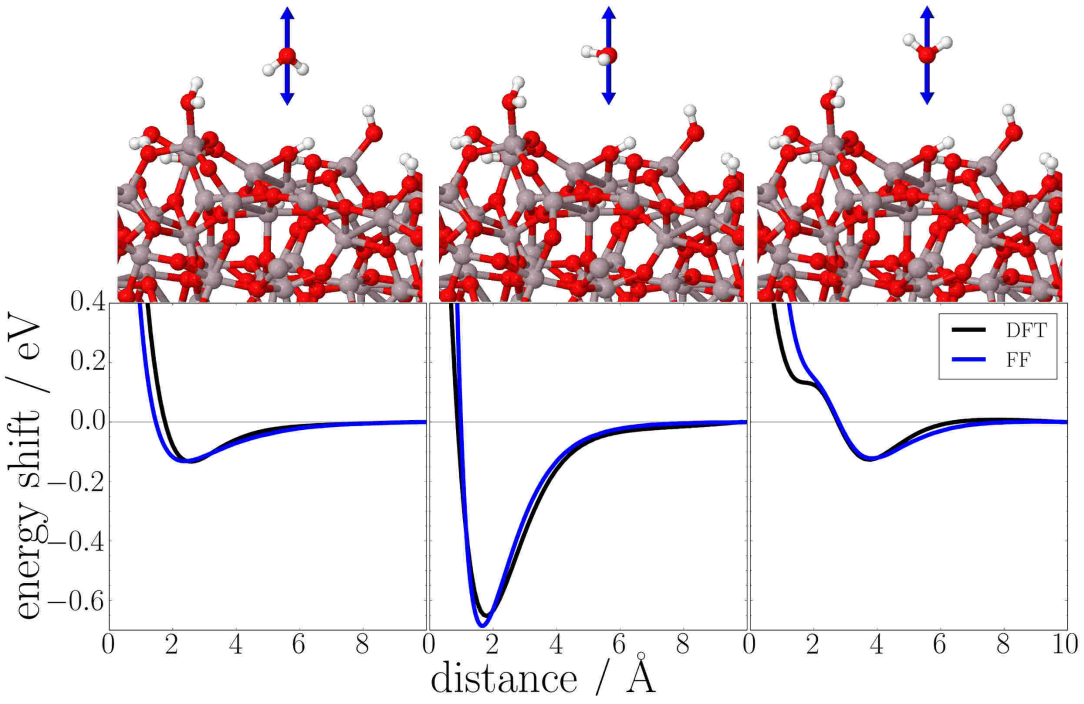

Figure 3.6: Potential energy profiles of water molecules at different orientations above an amorphous alumina surface computed with DFT (black lines) and our force field (FF, blue lines) with the optimized parameters listed in Table 3.3. The height over the surface is relative to an arbitrary initial position at 0 Å.

(Fig. A2 and A3). In the figures, the black lines are the DFT reference profiles, whereas the blue lines are the profiles calculated with the TIP3P water model and our force field (FF), using the parameters σ and ε obtained by a least-square fit to all 36 references via the General Utility Lattice Program (GULP) [193] (Table 3.3). We note that the fitting procedure leads to a good agreement between the DFT and the FF curves in all considered cases.

Before demonstrating that the so-obtained parameter set also guarantees good transferability to other (organic) molecules and consistency with experimental data, we conclude this section checking whether the interactions between the alumina surface and the water

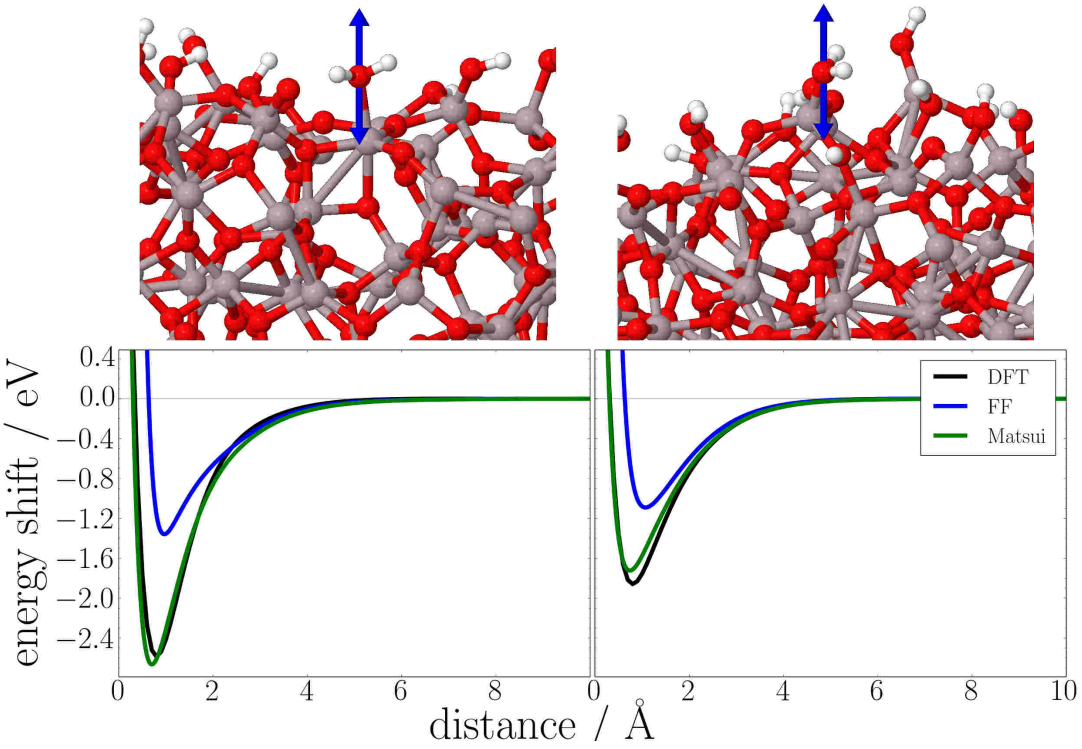

Figure 3.7: Potential energy profiles of molecularly adsorbed water molecules at undercoordinated surface aluminum atoms based on our classical intermolecular force field (blue), the intramolecular force field of Matsui [175] (green) and DFT (black).

molecules directly bound to Al atoms are better described by the original Matsui Buckingham potential or our newly parametrized Coulomb/Lennard-Jones potential. The variations in energy when the two strongly adsorbed molecules move along the z coordinate perpendicular to the surface are computed both with DFT and the two potentials. It is immediately visible from the results in Fig. 3.7 that the Matsui potential reproduces almost perfectly the strong chemisorption interactions, which are instead severely underestimated by the Coulomb/Lennard-Jones potential. We also note that the strength of the interaction (-1.8 and -2.5 eV in the two considered cases) would not allow a frequent desorption of these molecules from the surface at room temperature. Therefore, it is perfectly legitimate to consider them as part of the surface and treat the Al-O interactions as chemical bonds indistinguishable from those within the alumina bulk.

3.2.2 Transferability to amino acid side chains

As a first test of the transferability of our force field parametrization to biomolecular systems, we compute the potential energy profiles between the amorphous alumina surface and a set of small organic molecules as representative analogs of typical amino acid side chains, both at the DFT and FF levels. In these calculations, the force field parameters for the organic molecules are taken either from the AMBER-99SB force field, or, if not available, from the generalized amber force field (GAFF) [194]. The profiles of formic acid (HCOOH) and ammonia (NH_3) are computed for two different orientations over six different positions above the surfaces (see Fig. 3.8 and Appendix Fig. A4 and A5). Profiles for carboxamide, sulfhydryl, phenyl and hydroxyl groups bound to CH_3, representative of the side chain terminal groups of asparagine, cysteine, phenylalanine, and serine, are computed for two different positions each (Fig. 3.8 and Appendix, Fig. A6).

Remarkably, without further adjustment of the parameters optimized in the previous section for the case of pure water, all FF profiles reproduce with a very high degree of fidelity the features of the DFT references. This holds both for relatively strong interactions of the order of -0.4 eV (e.g., formic acid with carbonyl towards the surface, phenylalanine) and for weak interactions between -0.1 and -0.2 eV (serine, cysteine). Even in the case of purely repulsive interactions (formic acid with OH towards the surface) or non-monotonous profiles (ammonia, N towards the surface) is the agreement excellent. Obviously, some discrepancies are still present; for instance, the position of the potential energy minimum of cysteine is 0.4 Å off the DFT reference. However, given the simplicity of the potential, these small discrepancies are more than acceptable.

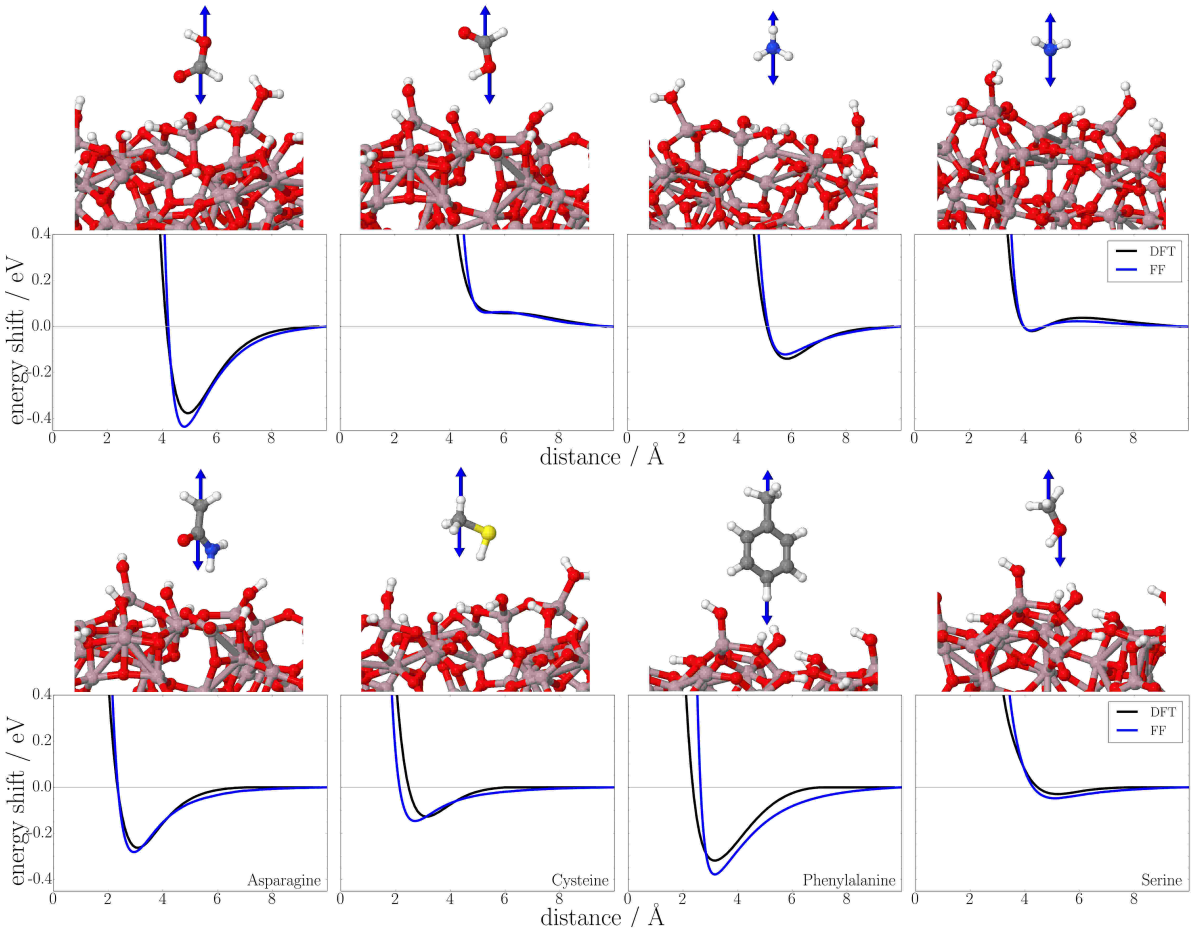

Figure 3.8: DFT (black lines) and force field based (blue lines) energy profiles for two different orientations of formic acid and ammonia, and four different amino acid side chains above the amorphous alumina surface.

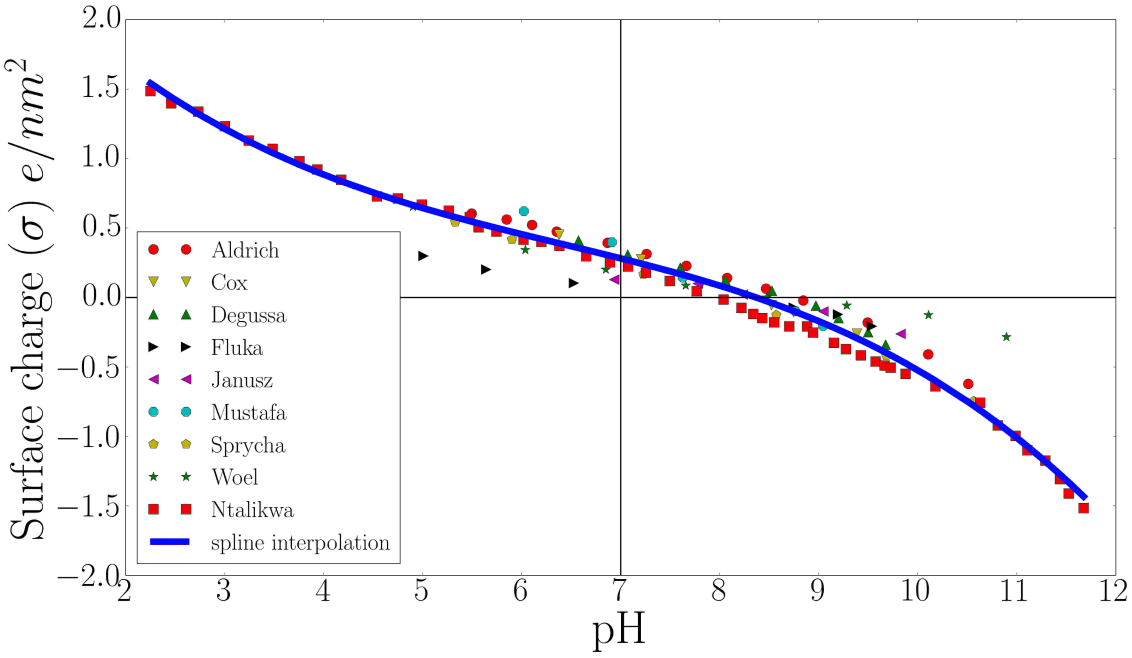

Figure 3.9: Results of surface charge density measurements taken from refs. [195, 196], interpolated with a single spline.

3.2.3 Consideration of surface charges

The variation of the surface charge density of alumina particles with the pH of the solution in which they are immersed depends on the particle synthesis method and pre-treatment. In Fig. 3.9 we summarise literature results for surface charge density measurements of ten different Al_2O_3 powders, taken from ref. [195] and ref. [196]. Interpolation with a single spline gives an average point of zero charge (pzc) for alumina at pH 8.4. At the pzc, the surface presents an equal amount of protonated and deprotonated sites, at an estimated density of 0.54 nm^{-2}. This value based on the assumption that at pH values less than 5.4 and higher than 11.4 (pzc $\pm$ 3) all negative sites are protonated, and all positive sites are deprotonated, respectively.

We can now use this information to create surface models presenting the correct protonation/deprotonation state at any given pH. Following the procedure developed in ref. [116], upon removal of a proton from a bridging OH group or addition of a proton to a surface O atom, the charges of the first and second neighboring atoms need to be adjusted in order to obtain sites with net charges of $\pm 1\,e$, because of the non-integer proton charge

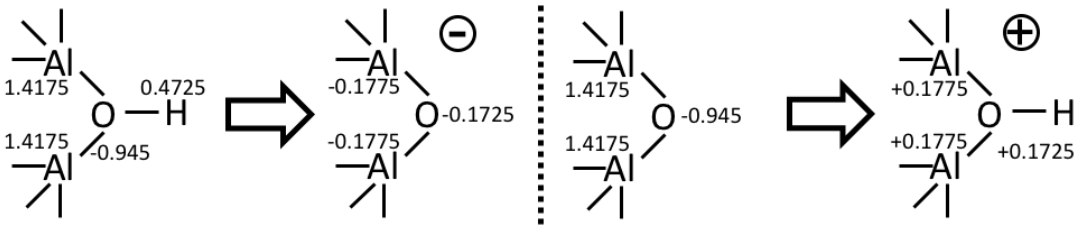

Figure 3.10: Summary of the differences of the atomic point charges assigned to the positive and negative surface sites at the amorphous alumina surface

of 0.4725 e. The choice of protonating/deprotonating only bridge O/OH sites and not terminal OH or OH_2 groups is motivated by the fact that terminal O^- groups are less stable, and that adsorbed H_2O or H_2O^+ groups possess a very strong tendency to dissociate and leave a proton on a bridging oxygen atom nearby. A summary of the atomic point charges assigned to the positive and negative surface sites is reported in Fig. 3.10.

3.2.4 Heat of immersion

In order to validate our new force field parametrization against experimental observables, in this section we compute the heat of immersion (E_{im}) of the amorphous alumina surface model at pH 8.4 (overall neutral but zwitterionic). This can be compared with available measurements of the enthalpy gain per unit of surface area after immersion of dry alumina powder in water. E_{im} is the difference between the averaged potential energies of the interface system including water and surface ($E_{Al_2O_3/wat}$), the dry surface in vacuum ($E_{Al_2O_3}$) and a water box containing the same number of water molecules as the interface system (E_{wat}), divided by the total surface area ($2A$, considering both the top and the bottom sides of the surface slab):

$$E_{im} = \frac{E_{Al2O3} + E_{wat} - E_{Al_2O_3/wat}}{2A} \, . \tag{3.5}$$

For these calculations we use a surface slab model with periodically repeated lateral dimensions, wherefore the surface slab model is only pseudo-amorphous, in the xy plane of 38.5×37.7 Å^2 and thickness along z of 21.07 Å, placed in a periodically repeated cell with an initial height of 102 Å. The empty volume is filled with 7212 TIP3P water molecules. Periodically repeated cells of same lateral dimensions are used for the pure water and dry surface systems. Each separate system is simulated for 10 ns in MD simulations in the

NVT ensemble, after a short equilibration period in which the water density is adjusted to the bulk TIP3P equilibrium value of 0.979 g/cm^3 [197].

The energy values along the three simulations are collected in distributions which can be fitted with Gaussian functions, from which the average values are readily obtained. Our predicted value $E_{im} = 441 \pm 18$ mJ/m^2 lies in the lower range of the experimental values measured for amorphous alumina powders. These span a broad window between 379 mJ/m^2 and 792 mJ/m^2 [198–201], depending on the powder surface area and thermochemical pretreatments.

3.2.5 Free energy of adsorption of GSSG

In this final section, we employ our FF to compute the free energy of adsorption of glutathione disulfide (GSSG) on the amorphous alumina surface by means of RESTmetaD, and compare the results to available experimental values [172, 202]. GSSG consists of two glutathionyl (GS) moieties connected by a disulfide bridge. The simulations are performed with the same repeated surface slab model as for the calculations of E_{im}. All oxygen atoms of the surface are constrained close to their equilibrium positions via a weak harmonic constraint with a spring constant of 2.17 eV/Å. This is important to keep intact the structure of the surface in the (fictitious) high-temperature replicas. At 300 K our potential, although constructed via non-bonded terms, preserves the surface structure without additional constraints. Two simulations are performed for surfaces at pH 8.4 (pzc) and 5.4. At both pH values, GSSG carries a charge of -2 e [118]. At pH 5.4 the surface charge density is +0.54 e/nm^2, corresponding to a total of 16 positive net charges on the top and bottom sides of the slab. The resulting charge excess is compensated by the addition of 14 Cl^- ions to the 3141 water molecules modeling the solution environment.

Free energy profiles are computed along the z component of the center of mass of GSSG, which acts as the collective variable in the RESTmetaD scheme. From the Boltzmann integration of these profiles in regions assigned to the adsorbed and desorbed state of the molecule, we are able to compute the experimentally measured free energy difference ΔG. More computational details are described in section 2.1.1 and in refs. [142, 143]. The evolution of the free energy profiles during the RESTmetaD simulations are shown in Fig. 3.11 and 3.12, while the convergence of the predicted ΔG values at the two pH values is shown in Fig. 3.13.

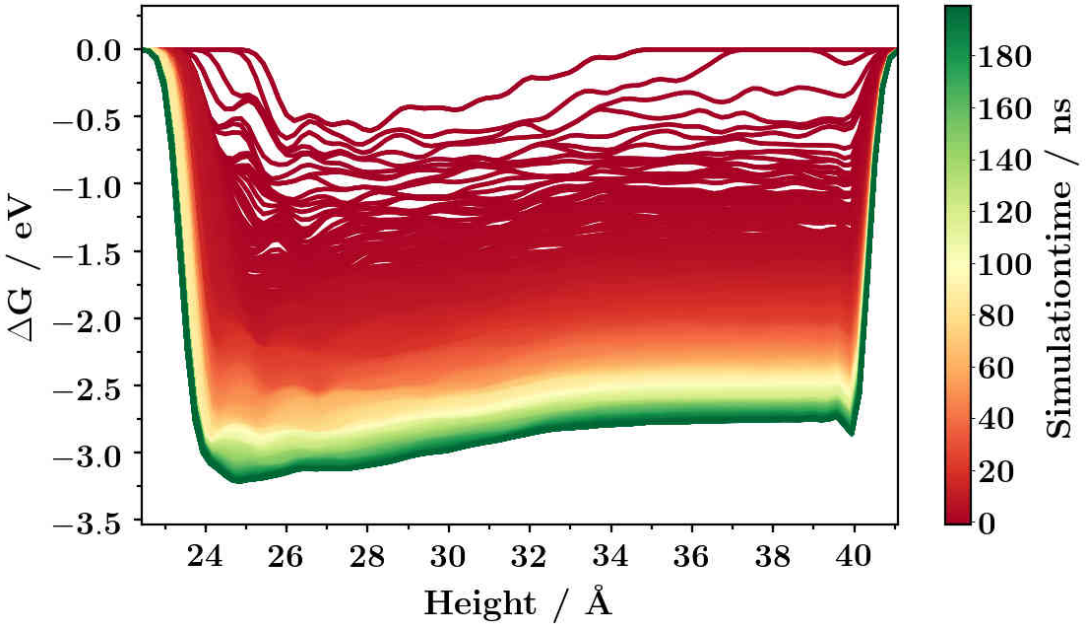

Figure 3.11: Evolution of the free energy profiles during the RESTmetaD simulations for the z-component of the center of mass of GSSG (glutathione disulfide) at the pseudo-amorphous alumina surface model at pH 8.4 (overall neutral but zwitterionic).

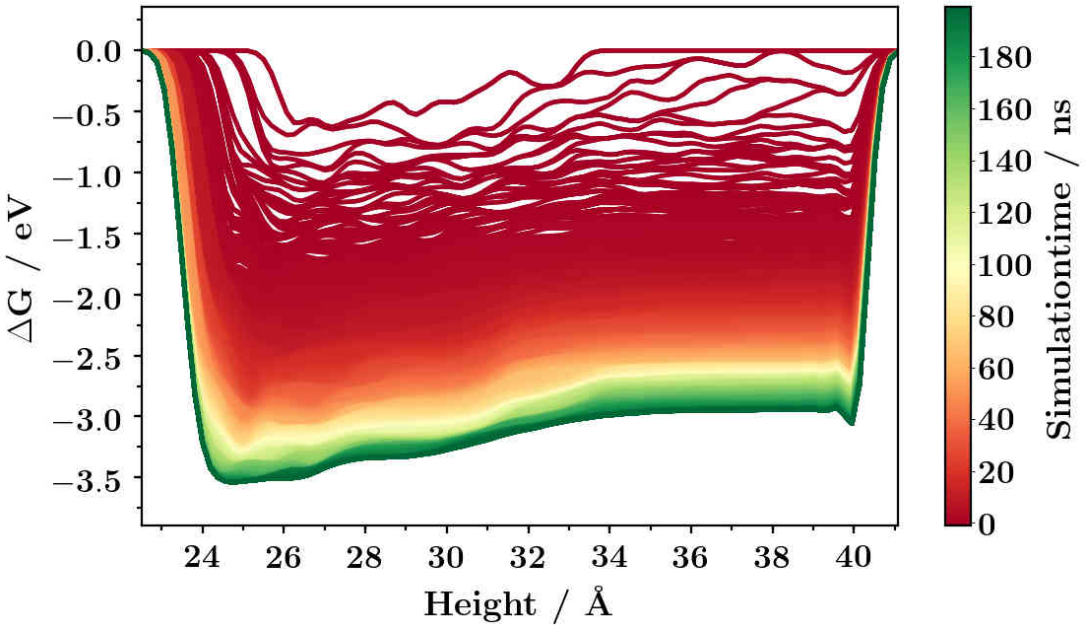

Figure 3.12: Evolution of the free energy profiles during the RESTmetaD simulations for the z-component of the center of mass of GSSG (glutathione disulfide) at the pseudo-amorphous alumina surface model at pH 5.4 with a surface charge density of 0.54 e/nm^2.

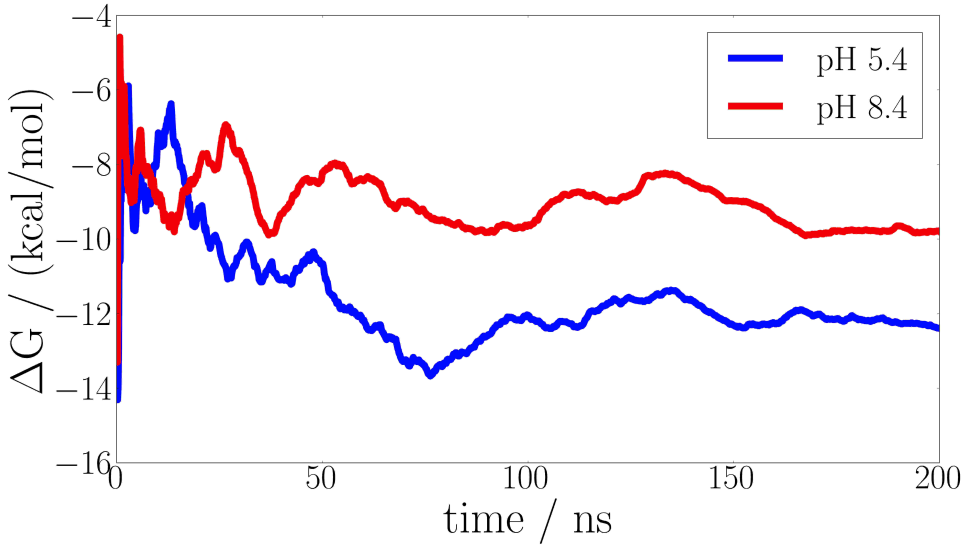

Figure 3.13: RESTMetaD convergence of the free energy of adsorption ΔG of GSSG above the pseudo-amorphous alumina surface for pH values of 5.4 and 8.4.

The finally predicted results are $\Delta G = -0.425 \pm 0.002$ eV at pH 8.4 and $\Delta G = -0.557 \pm 0.002$ eV at pH 5.4. The latter value needs to be compared with the experimental estimates of -0.360 eV at pH 5.4 [172] and -0.421 ± 0.017 eV at pH 4.8 [202]. This small deviation between computationally predicted and experimentally estimated values could be the result of many factors, among which: the assumptions made for the estimation of ΔG from experimental adsorption isotherms, the presence of surface defects or contaminants, the deviation of the surface charges from their assumed distribution, or the repulsive interaction between adsorbed and negatively charged GSSG molecules.

A possible explanation is the number of bonds between GSSG and the alumina surface. Fig. 3.14 is taken from ref. [172] and contains on the left-hand side two hypothetical binding modes of GSSG adsorbed to Al_2O_3 and on the right-hand side the amount of release glutathionyl (GS) moieties under nonreducing conditions and after treatment with dithiothreitol (DTT). By the treatment with DTT, all disulfide bonds which are exposed to the solvent will be cleaved via reduction and GSSG will be split into two GSH molecules. In case of binding mode I (scheme on the upper left side), both GS molecules are bound to the alumina nanoparticle, and the treatment with DTT should not affect the amount of bound GSH. In contrast, in case of binding mode II (scheme on the lower left side) only one GS molecule of the GSSG is bound to alumina, and after exposure to DTT,

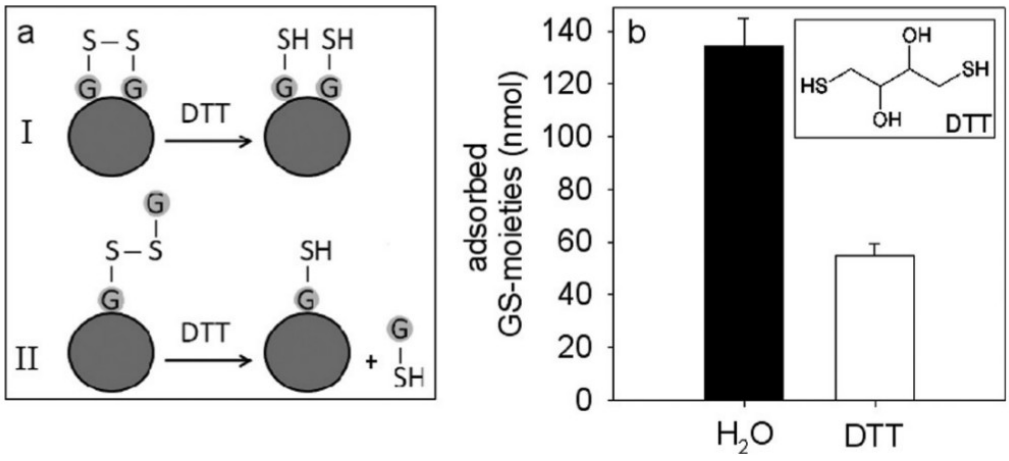

Figure 3.14: The figure is taken from ref. [172]. On the left-hand side, two hypothetical binding modes of GSSG adsorbed to Al_2O_3 is shown. On the right-hand side, the amount of released glutathionyl (GS) moieties under nonreducing conditions and after treatment with dithiothreitol (DTT) is shown.

the amount of bound GSH should decrease. In the graph on the right-hand side, the amount of adsorbed GSSG is considered to be not affected under nonreducing conditions in water. In the case of treatment with DTT, a decrease of about 50% of the detectable GSH moieties from the nanoparticles is observed. This suggests that GSSG is bound via only one of its two GS moieties to the nanoparticles, as assumed in binding mode II.

A cluster analysis of all GSSG structures pertinent to the free-energy minimum (with their COM between 24.5 and 25.1 Å along z, see Fig. 3.11), is performed with the VMD clustering tool [203], with a RMSD cutoff value of 1.0 Å. Fig. 3.15 contains the highest-population cluster (including 43% of all structures) of GSSG adsorbed over the pseudo-amorphous alumina surface. The disulfide bond is highlighted as a yellow ball and stick model. The structures in the cluster are presented as blue lines, and one exemplary structure of the cluster is presented as ball and stick model for better visualization. This highest population cluster, in contrast to the experimental findings, coincides with binding mode I. Nevertheless, the interactions between GSSG and alumina are primarily mediated via the oxygen atoms of the carboxylate groups (Fig. 3.15). Moreover, in 89.6% of the minimum-energy structures, the disulfide bond is not involved in the surface binding, but well exposed to the solvent. This is in perfect agreement with the early prediction made via standard MD simulations in ref. [172], and consistent with the observed cleavage of the disulfide bond of adsorbed GSSG upon treatment with dithiothreitol (DTT) [172, 202].

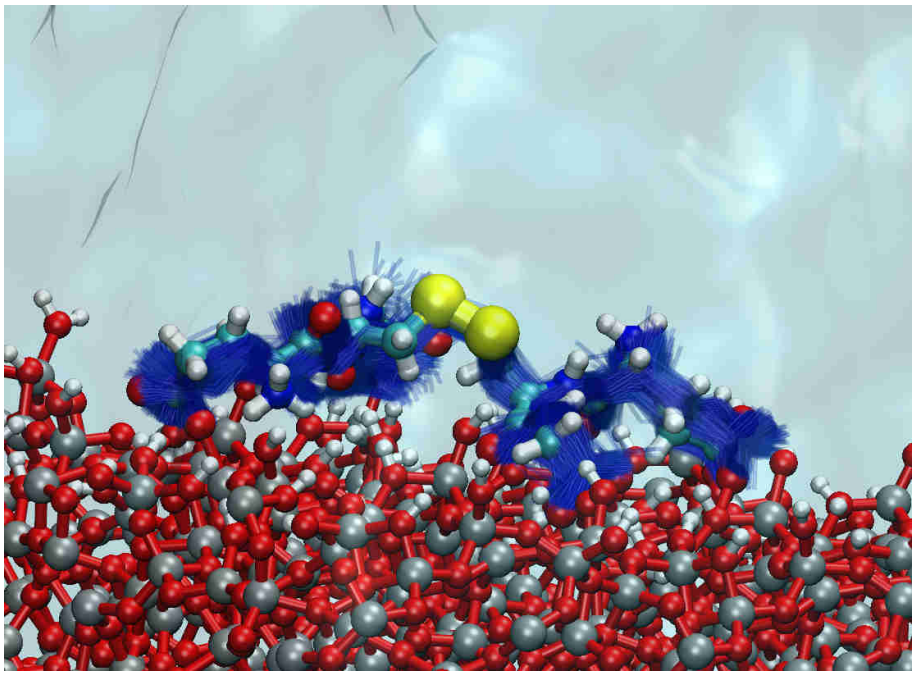

Figure 3.15: Highest-population cluster (including 43% of all structures) of GSSG adsorbed over the pseudo-amorphous alumina surface. The cluster analysis is performed with the VMD clustering tool [203], with a RMSD cutoff value of 1.0 Å. The disulfide bond is highlighted in yellow while the structures in the cluster are presented as blue lines.

Nevertheless, in the case of the highest population cluster, both GS moieties are bound to the surface, in contrast to the experimental finding. The could explain the discrepancy in the free energy of adsorption.

Additionally, it could also be due to specific features of the surface models used in our calculations. For instance, our surface models carry 6.8 OH groups per nm^2, while the correspondent experimentally estimated values in refs. [172, 202] lie between 2 and 3. Finally, the discrepancy may arise from the not perfect transferability of our potential parameters from pure alumina/water interfaces to systems containing dissolved (and charged) biomolecules.

It is worth noting that little adjustments of the surface atomic charges or LJ parameters could be performed to reproduce any available experimental observable. However, in the absence of a large quantity of well established experimental data, we restrain for now from further FF refinements. In fact, uncertainties of the order of 0.1 eV are intrinsic in both computational and experimental estimates of elusive quantities such as the free energy of adsorption of polypeptides on oxide surfaces [142].

3.3 Immobilization of Ferritin subunits at Al_2O_3 and SiO_2

In the following, the interactions between Fn subunits and amorphous alumina and silica are investigated to examine the possibility of non-covalent immobilization of Fn via physisorption. Physisorption represents the easiest solution for the immobilization of Fn because the Fn subunits only have to be added to a solution containing alumina or silica nanoparticles without further treatment. Therefore, two main questions should be answered by classical MD simulations. First, how strong are the forces between the Fn subunits and the alumina and silica particles at different pH values? Thus, are the physisorbed subunits stably attached and not washed away during subsequent purification steps before or after the mineralization of iron oxide at the subunits? Second, are there preferential orientations for the Fn subunits attached to the surface? Is the inner side of the Fn cavity, which is responsible for its mineralization activity, available for mineralization? Afterward, experimental results are presented to verify the results of the performed simulations.

3.3.1 Orientation of Ferritin subunits above Al_2O_3 and SiO_2

In order to assess the feasibility of the adsorption of Fn subunits on the amorphous Al_2O_3 and SiO_2 surfaces while retaining activity for iron oxide mineralization, we first perform atomistic simulations to estimate the driving forces towards the non-covalent adsorption of Fn subunits to the amorphous Al_2O_3 and SiO_2 surfaces. These simulations are performed in implicit solvent at the level of the Derjaguin-Landau-Verwey-Overbeek (DLVO) theory [204, 205] following the procedure of a previous work [115] and based on the previous parameterized force field for alumina and the parameter set of Butenuth et al. [116] for silica. All technical details are presented in Carmona et al. [167]. Static single-point calculations of the Protein are performed at protein-surface heights of 0 to 50 Å, in 2 Å steps. The protein-surface height is defined as the distance between the highest atom of the surface and the lowest atom of the protein in the direction perpendicular to the surface slab. For every height the protein is rotated around its geometrical center in 60°steps around the x- and y-axis, resulting in 36 different orientations per height step. In order to estimate more precisely the preferential protein orientation, the protein is additionally

placed at a height of 12 Å above the surface and rotated around its geometrical center in 5°steps around the x- and y-axis. This allowed us to predict the putative preferential protein orientation for initial adsorption at a given pH and provided an assessment of the strength of the surface-protein interactions prior to adsorption.

The amorphous Al_2O_3 surface is the same repeated surface slab model, which is therefore only pseudo-amorphous, as used for the calculation of E_{im} and the free energy of adsorption in the previous section. The forces of static single-point calculations for all heights and orientations above both surfaces are displayed on the left-hand side in Fig. 3.17 for the H subunit (a) and L subunit (b) for pH 3 and 8.4, respectively. The colored semitransparent areas symbolize the standard deviations for all resulting profiles at the given pH. Negative force values represent attractive forces onto the protein, with the zero-energy point sets to the average value at the maximum distance of 50 Å. At pH 3, as shown in Fig. 3.9, the alumina surface is positively charged, and only repulsive interactions can be observed for H and L subunits. In contrast, only attractive interactions are observed between the Ferritin subunits and the overall neutral but zwitterionic alumina surface at pH 8.4.

A snapshot of the MD simulation of the heavy Fn subunit above the pseudo-amorphous alumina surface is shown in Fig. 3.16. The computed relative energies for each protein orientation at a height of 12 Å above the surfaces are displayed as two-dimensional color maps for H and L subunits and each pH on the right-hand side in Fig. 3.17. The average interaction energy is set to zero (white) and the changes of the relative energy varied between -1.6 eV (green) for attractive interactions and +1.6 eV (red) for repulsive interactions. The color maps of the H and L subunits at pH 3 and 8.4 generally show the same results. Therefore, only repulsive interactions between alumina surface and all orientations of the protein are present at pH 3 and only attractive interactions at pH 8.4. Thus immobilization of Fn by physisorption at pH 8.4 could be in principle achieved. However, this could lead to orientations in which the inner side, which is responsible for its mineralization activity, points to the alumina surface and becomes unavailable for mineralization.

The amorphous SiO_2 surface with a slab size of 28x28nm is taken from the previous work of Cole et al. [120], whereby the protonation state of the surface terminal groups

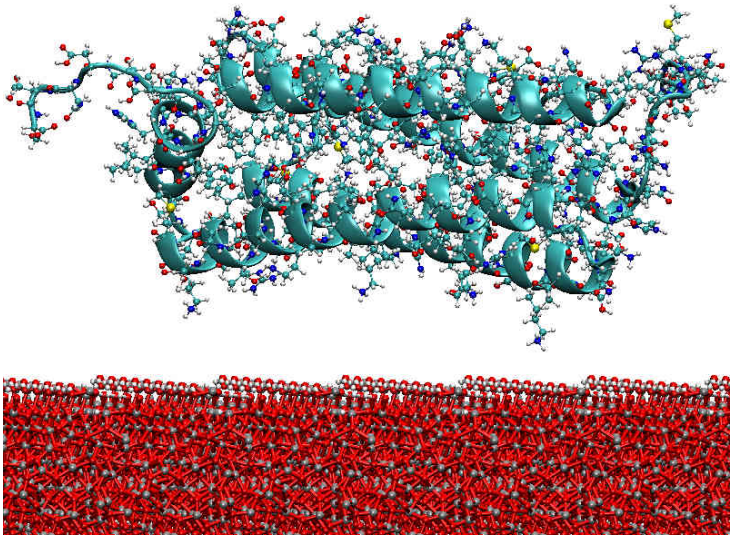

Figure 3.16: Snapshots of the MD simulation of the Fn H subunit at pH 8 above the pseudo-amorphous alumina surface to find putative preferential protein orientation for initial adsorption. Here, the inner side (with reference to their assembly in hollow Fn spheres) pointing to the surface.

at the different pH values was set to reproduce the average values of potentiometric titration experiments [206–208]. At pH 3, the surface is almost neutral and only attractive interactions can be observed for H and L subunits (see Fig. 3.18 a and b). At pH 8, the silica surface is negatively charged, and the interaction forces are either attractive or repulsive depending on the specific orientation of the subunit due to the occurrence of negatively or positively charged residues at the surface of the respective subunit (see Fig. 3.18a and b). As in case of alumina, the average interaction energy is set to zero (white) and the changes of the relative energy varied between -1.6 eV (green) for attractive interactions and +1.6 eV (red). The relative energies for each protein orientation at a height of 12 Å above the surfaces for pH 3 are displayed in the color maps for H (Fig. 3.18c) and L (Fig. 3.18e) subunits. Here, only attractive interactions between silica surface and all orientations of the protein are present. The color maps of the H (Fig. 3.18d) and L (Fig. 3.18f) subunits at pH 8 generally show the same result. Thus the rotation around the y-axis between 0 and 180°is energetically favorable in contrast to rotations around the y-axis between 180 and 360°. For rotations around the y-axis in between 0 and 180°, the outer side of the protein, i.e., the surface which is located at the outside of the whole Fn protein shell, faces towards the silica surface. Accordingly, it can be concluded that there

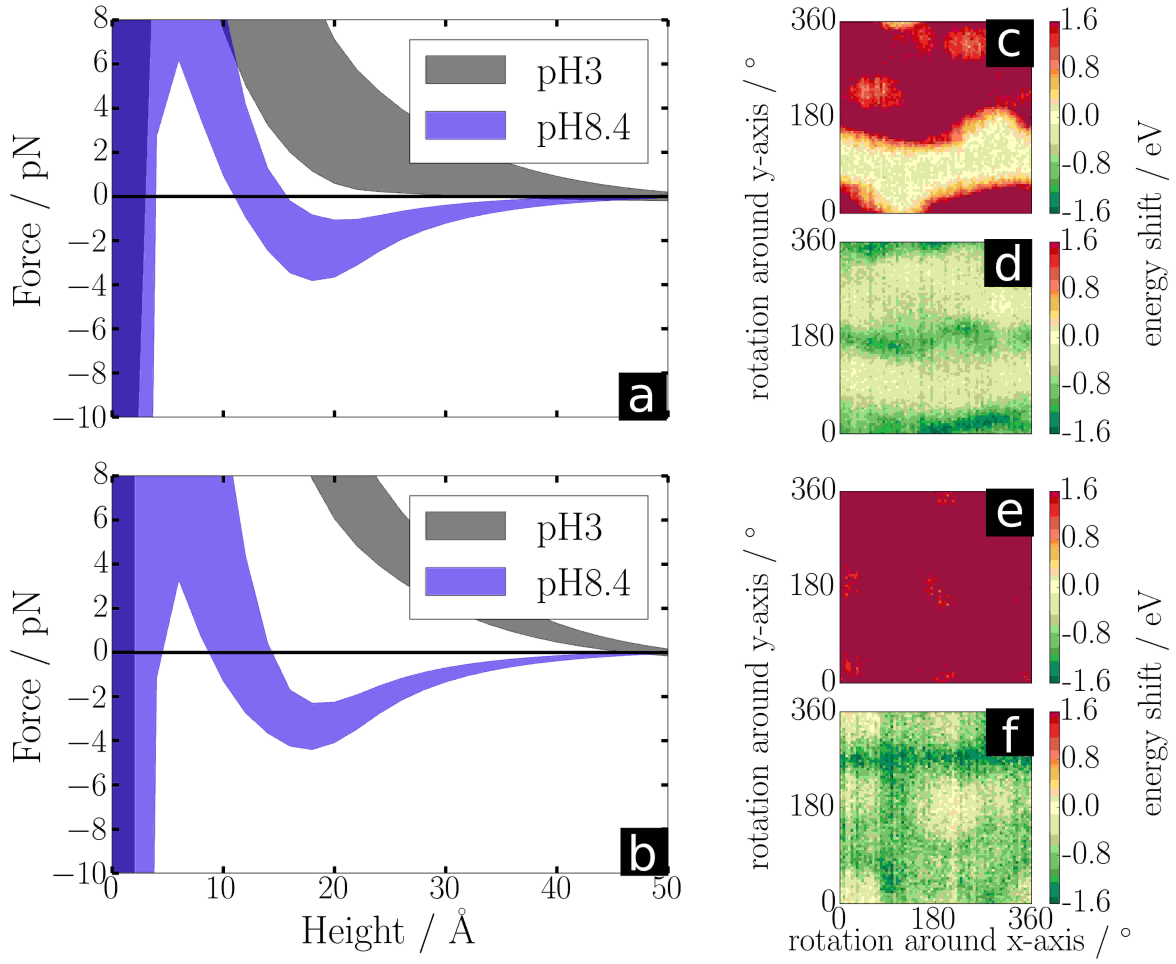

Figure 3.17: Interaction forces between H (a) and L (b) ferritin subunits with an pseudo-amorphous Al_2O_3 surface model calculated for all possible protein orientations at two pH values (3 and 8.4). The colored semitransparent areas are the standard deviations obtained from rotating the protein around the x- and y-axis. The zero-energy point is set to the average value at the maximum distance of 50 Å. The interaction energies between silica surface and proteins which are rotated at a height of 12 Å reported as color maps on the right, for the cases (H, pH 3: c), (H, pH 8.4: d), (L, pH3: e), (L, pH 8.4: f).

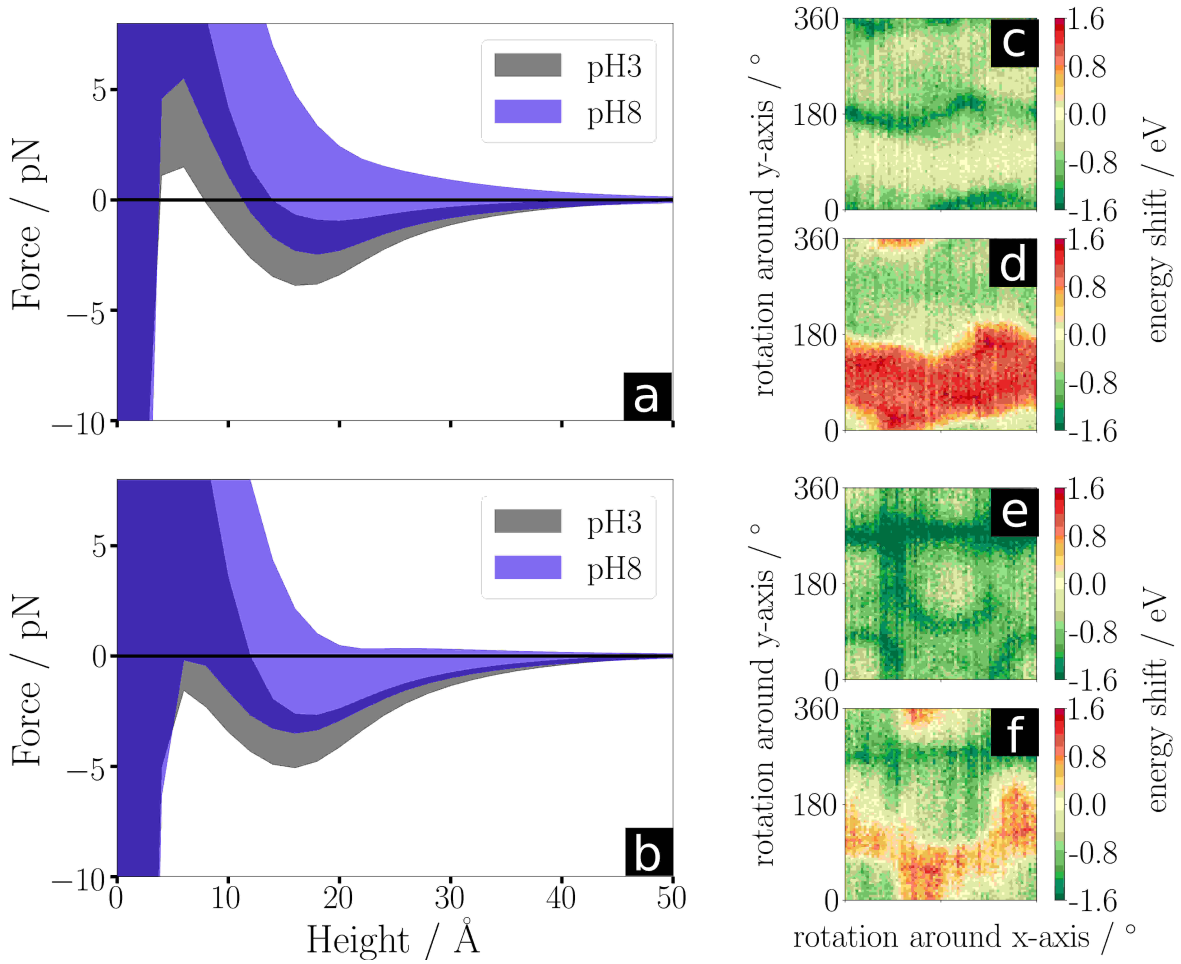

Figure 3.18: Interaction forces between H (a) and L (b) ferritin subunits with an amorphous SiO2 surface model calculated for all possible protein orientations at two pH values (3 and 8). The colored semitransparent areas are the standard deviations obtained from rotating the protein around the x- and y-axis. The zero-energy point is set to the average value at the maximum distance of 50 Å. The interaction energies between silica surface and proteins which are rotated at a height of 12 Å reported as color maps on the right, for the cases (H, pH 3: c), (H, pH 8: d), (L, pH3: e), (L, pH 8: f).

is a favorable interaction for the non-covalent anchoring of Fn subunits at pH 8 in which the inner side of the protein, which is responsible for its mineralization activity, points away from the silica surface and becomes available for mineralization. Therefore, silica is a more suitable candidate than alumina for the immobilization of Ferritin subunits by physisorption at a pH value of 8.

Further all-atom molecular dynamics simulations in explicit water solvent are performed under periodic boundary conditions to verify whether actual anchoring of the protein to the surface takes place in the orientation predicted by the implicit-solvent calculations above. The subunits are initially placed at a height of 12 Å above the surface, in orientations in which the inner or outer sides pointed to the surface. The simulations are performed in the NVT ensemble at 300 K, with a protonation state of the surface and the protein corresponding to pH 8. The resulting (negative) net charge of the simulation cell is compensated by adding an equal amount of Na^+ ions in the water-filled cells. All surface atoms except the terminal OH groups are constrained in their equilibrium position. Figure 3.19 summarizes the results for one H subunit at pH 8, with the inner (top) and outer (bottom) side pointing to the surface as the initial configuration. Snapshots of the initial configuration (left), after 15 ns (middle) and after 30 ns (right) are shown. The images displayed in Fig. 3.19 are representative for the results observed in all other simulations. The simulations predict that anchoring to the surface takes place after rotation of the units from a side-on to an end-on configuration and with formation of only a few unstable surface contacts, irrespective of the pH. In fact, as it will be shown below, physisorption experiments led to unstably bound proteins, which were washed off the surface during mineralization. This behavior can be explained by the small attractive force between Fn subunits and silica, lying in the range of -5 pN or less. In comparison, in Ref. [115] much larger attractive forces of magnitude ranging between -20 and -60 pN have been predicted to act between chymotrypsin or lysozyme and silica surfaces.

3.3.2 Immobilization Experiments

Based on the results of the previously described simulations, the following experiments are performed to investigate the possibility to retain the mineralization activity of the Fn subunits by physisorption on silica. These experiments are realized by Daniel Carmona in the Advanced Ceramics Group of Prof. K. Rezwan at the University of Bremen, and all technical details can be found in Carmona et al. [167].

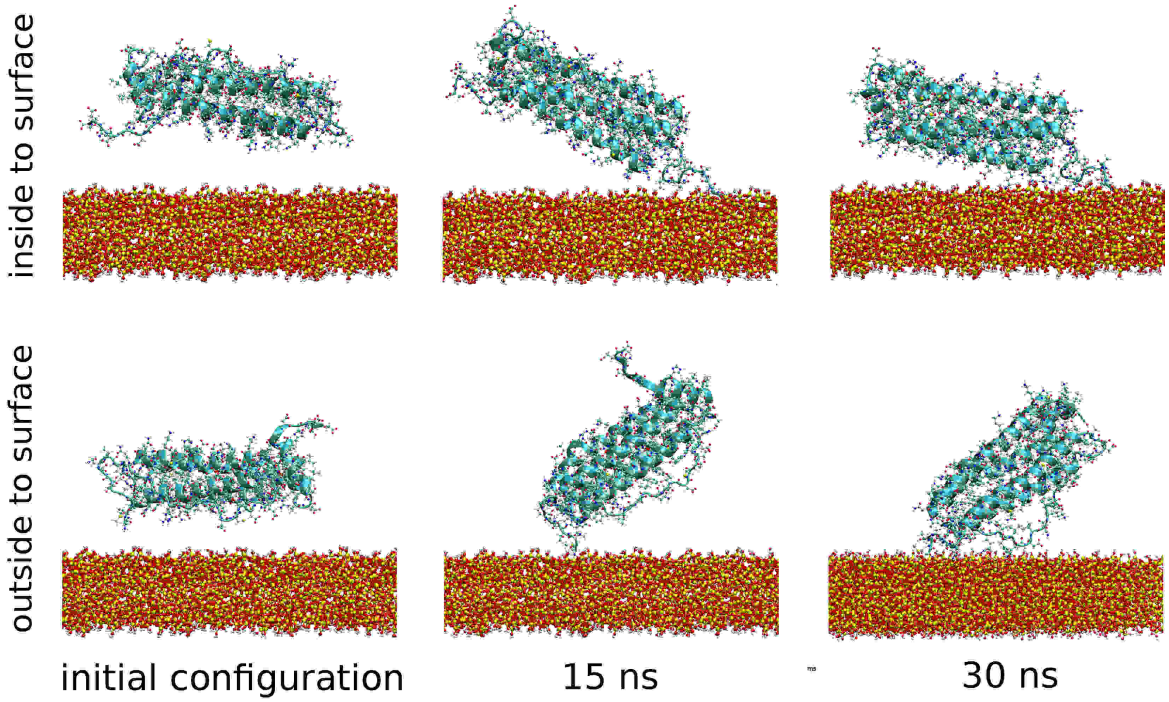

Figure 3.19: Snapshots from MD simulations of the Fn H subunit at pH 8 with the inner (top) and outer (bottom) side pointing to the surface at the initial configuration. Snapshots of the initial configuration (left), after 15 ns (middle) and after 30 ns (right).

Two type of experiments are performed, immobilization of Fn subunits by physisorption and immobilization by covalent binding of Fn to the silica particles. After the respective immobilization strategy, iron ion solution and an oxidant are added following the stepwise mineralization procedure after Mann et al. [209–211]. The TEM images of the particles after every cycle of the protocol are used to control the ability to induce nucleation and growth of iron oxide crystallites on the ferritin subunits. TEM images of the particles before and after functionalization and protein immobilization as well as the verification of no crystal growth of iron oxide on functionalized particles without Fn proteins, are described in detail in ref. [167]. The results of both immobilization strategies for the H subunits after immobilization, the first and fourth cycle of the mineralization protocol are presented in Fig. 3.20. The formation of iron oxide nuclei could be identified on particle surfaces as dark gray dots in the TEM images. In case of physisorbed H subunits, no iron oxide mineral can be observed after the first cycle of the mineralization protocol (Fig. 3.20 b). Here, only irregular crystals formed after the 4th cycle in the region between the particles as a result of adventitious mineralization (Fig. 3.20 c). In case of covalently

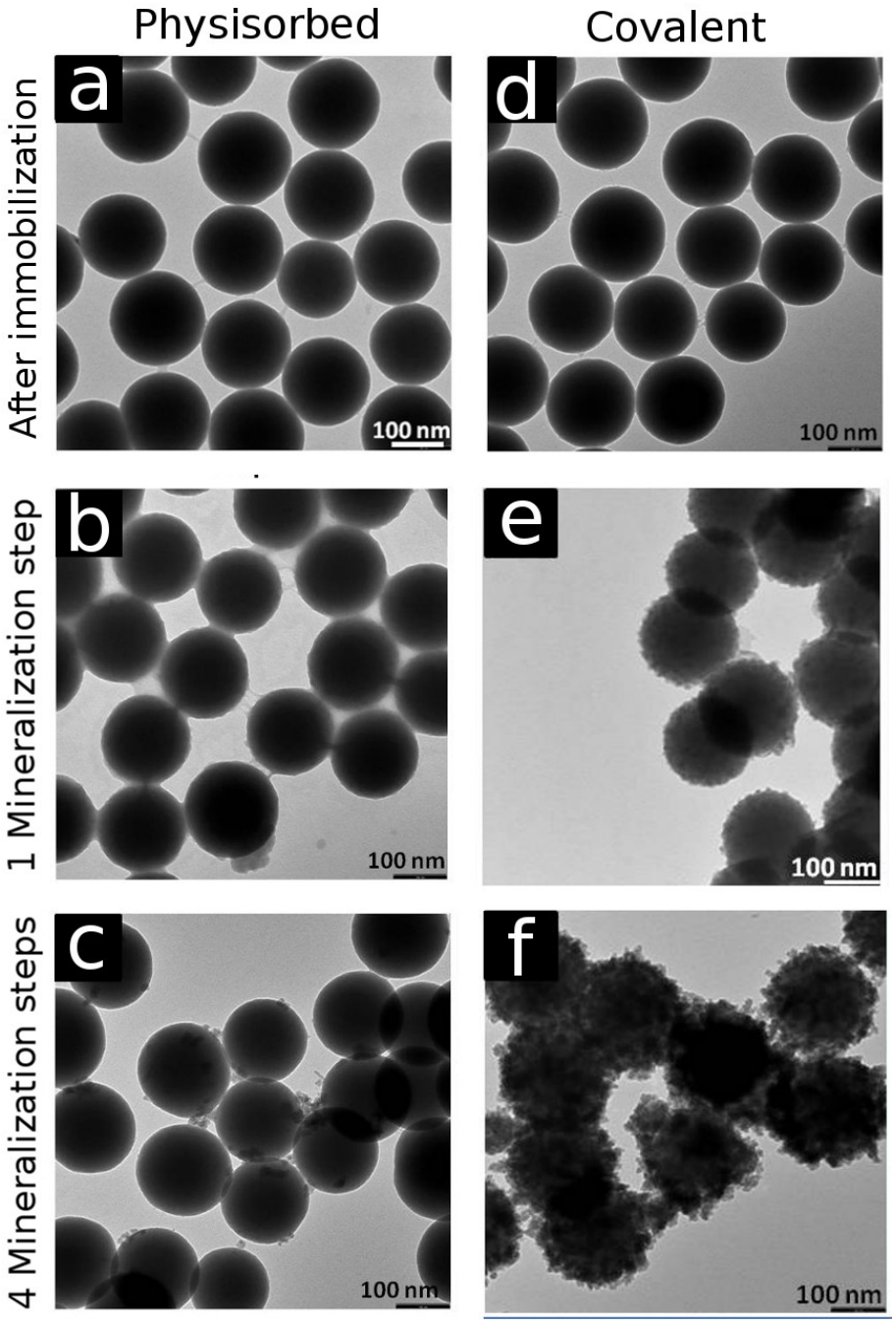

Figure 3.20: TEM images of SiO_2 particles with H subunits which are covalently immobilized and via physisorption. The images present the samples before, after 1 and 4 mineralization cycles of the mineralization protocol to observe how the iron oxide film (dark grey dots) is formed.

immobilized Fn subunits, the formation of iron oxide can be observed after the first cycle of the mineralization protocol. After 4 mineralization cycles, a thin film of iron oxide is formed in relation to the added iron salt during the different cycles.

As already mentioned, the lack of iron oxide formation on the particles, in case of physisorbed subunits, is supposedly related to the low binding affinity of the Fn subunits to the silica surface, so that the subunits are washed off the during mineralization protocol.

Chapter 4

The Ferritin/FeO(OH) interface

In order to shed light on the atomistic mechanisms of ferritin-promoted mineralization, in this section the anchoring sites for Fe(III) clusters on Fn subunit assemblies using models of goethite and ferrihydrite nanoparticles are investigated on the basis of Molecular Dynamics simulations.

Until now, many details of the iron oxide formation process are still unknown, especially the initial anchoring of nascent nuclei at the ferritin subunits' mineralization sites. Here, classical MD simulations are used to answer this fundamental question of an important biomineralization mechanism. Additionally, a precise understanding of this early nucleation step would enable a more rational approach towards utilizing the mineralization properties of ferritin subunits in bionanotechnological applications. Therefore, amino acids of ferritin, which acts as anchor points for the nanoparticles, are analyzed by a systematic docking procedure followed by short MD runs in explicit water solvent, to reveal possible differences in the H- and L-subunits. While structures for the H- and L-subunits of Fn are available in the protein database (2FHA.pdb and 2FG8.pdb respectively), realistic structures of Fe(III) nanoparticles have to be created. For that, a classical force field parameter set was created in the same way as the alumina parameter set. All technical details can be found in our publication in [105]. For the parametrization, we focus on the most common and experimentally and theoretically well-investigated phase goethite (α-FeOOH), and check the transferability afterward to ferrihydrite, which is the naturally growing iron oxyhydroxide phase in ferritin. The force field is required to describe Fe-O-Fe interactions within solid Fe(III) phases, in order to create realistic models of iron oxyhydroxide particles. After the fitting of the parameter set and subsequent validation,

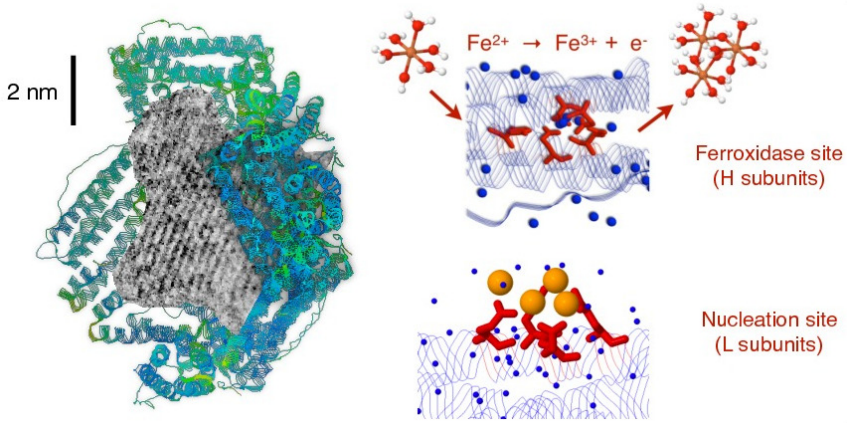

Figure 4.1: Schematic drawing of half a ferritin cage with a Fe(III) oxyhydroxide mineral particle growing in it, together with representations of the ferroxidase site in H ferritin subunits (pdb: 2FHA) and of a nucleation sites with a tri-iron cluster in L subunits (pdb: 5LG8). The blue dots represent crystallization water included in the original pdb files.

goethite and ferrihydrite nanoparticles are generated in a way that guarantees chemical stability and realistic surface termination. All technical details are described in Lid et al. [171].

4.1 Classical force fields and particle models for FeO(OH)

4.1.1 A classical force field for FeO(OH)

In line with previous works on Si, Ti and Al oxides [116, 120, 171, 212], we describe the pairwise interactions between Fe, O and H atoms in Fe oxyhydroxide crystals via a force field (FF) comprising the sum of Buckingham and Coulomb terms;

$$V(r_{ij}) = A_{ij}e^{(-\frac{r_{ij}}{\rho_{ij}})} - \frac{C_{ij}}{r_{ij}^6} + \frac{q_i q_j}{r_{ij}} \,, \tag{4.1}$$

where the fixed atomic point charges q_i are the same as in our FeO(OH)/water force field [105], namely $+1.35\,e$ for Fe, $-0.90\,e$ for O and $+0.45\,e$ for H. The Buckingham parameters A_{ij}, ρ_{ij}, C_{ij} are optimized by a least-squares fit to the volume-energy curve computed with DFT for bulk goethite crystals, including full relaxation of the atomic positions at each volume value (Fig. 4.2, left). In doing this, we consider the Fe-Fe and H-H pairs are interacting only via the Coulomb potentials, which means setting to 0.0 the

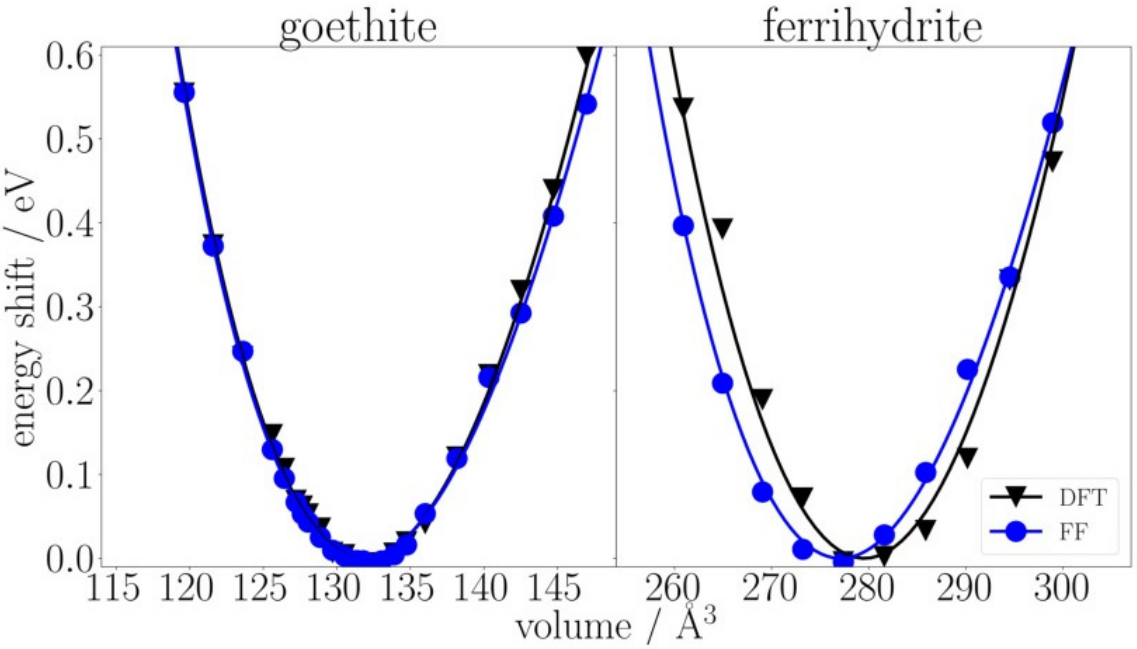

Figure 4.2: Comparison of the energy-volume curves calculated at the DFT and FF levels for goethite (our reference) and ferrihydrite.

corresponding Buckingham parameters. Moreover, we consider the O atoms in Fe-O-Fe bridges and Fe-(OH)-Fe bridges as two different species.

The results of the fit are reported in Table 4.1. The volume/energy curves are fitted with the Murnaghan's equation of state [213] to evaluate the minimum-energy volume V_0 and the bulk modulus B_0 both for the DFT reference and the FF calculations (see Table 4.2). Importantly, the latter are computed for a $4 \times 2 \times 6$ periodic supercell, in order to avoid inconsistencies with the chosen cutoff value of 12 Å. The match of the DFT and the FF calculations for goethite is almost perfect, with only a minor deviation of the estimated B_0 value, demonstrating the capability of the Buckingham/Coulomb potential to map the true interactions within the crystal.

The transferability of the so-obtained FF parametrization to the ferrihydrite phase $Fe_{10}O_{16}H_2$ is checked by comparison of similar DFT energy/volume reference values with their FF counterpart (without further parameter optimization). As shown in Fig. 4.2 (right) and Table 4.2, the FF parametrization slightly underestimates V_0 and B_0 by about 1 % and 8 %, respectively. These minor discrepancies are fully acceptable, given that DFT predictions typically deviate from the corresponding experimental values by similar amounts (see Table 4.2).

Table 4.1: Optimized Buckingham pair potential parameters

Pair	A_{ij} / eV	ρ_{ij} / Å	C_{ij} / eVÅ^6
Fe-Fe	31121	0.154	0.00
Fe-O	12078	0.187	18.42
Fe-O(H)	74700	0.175	49.86
Fe-H	0	0.000	0.00
O-O	17621	0.239	0.05
O-O(H)	15877	0.238	33.20
O(H)-O(H)	11783	0.234	32.34
O-H	17401	0.140	3.51
O(H)-H	6124	0.104	0.34
H-H	0	0.000	0.00

Table 4.2: DFT and FF bulk properties

		V_0 / Å^3	B_0 / GPa
goethite	DFT	131.9	131.7
	FF	131.8	126.2
	exp [214]	138.8	140.3
ferrihydrite	DFT	279.6	126.9
	FF	277.1	116.3
	exp [95]	277.8	–

4.1.2 Creation of goethite and ferrihydrite particle models

Models for clusters (nanoparticles) of goethite and ferrihydrite are created according to the following procedure. Two goethite particles with edge lengths of about $15\times12\times12$ Å^3 ('goethite small', Fig. 4.3a) and $19\times19\times17$ Å^3 ('goethite big', Fig. 4.3c) are carved out of an extended bulk crystal cleaved along the most stable (110) and (021) crystallographic planes [112]. Exposed Fe atoms of the surfaces (with coordination lower than 4) are then saturated with OH groups, while an equal amount of H atoms is placed on singly coordinated O atoms, according to the water termination propensity studied in detail in refs. [103, 105]. This results in particles with compositions equal to $53(FeOOH)\cdot7H_2O$ and $133(FeOOH)\cdot9H_2O$, respectively.

Further saturation of fourfold and fivefold coordinated Fe atoms is not necessary since upon immersion of the created particles in bulk water the non-bonding interaction potential [105] drives spontaneous water adsorption up to complete sixfold coordination of all Fe sites. This can be seen exemplarily in Fig. 4.3b, where fourfold and fivefold coordinated

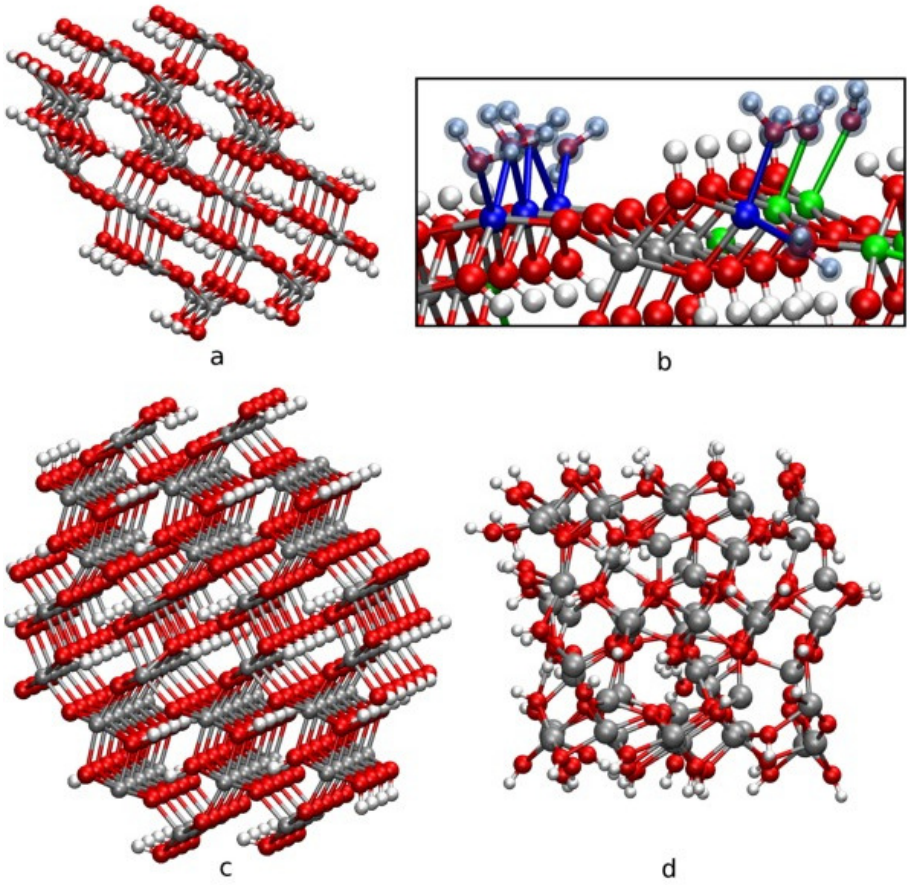

Figure 4.3: Created goethite and ferrihydrite particle models. (a) Goethite small; (c) goethite big; and (d) ferrihydrite. (b) TIP3P water molecules (marked with semitransparent blue spheres) bound to fourfold (blue) and fivefold (green) coordinated Fe atoms of the (021) goethite surface.

Fe atoms are colored green and blue, respectively, while the spontaneously adsorbed water molecules at the end of a short MD simulation are highlighted with semitransparent blue spheres. Notably, in some cases, water molecules bind in bridge positions between two surface Fe atoms, which is not uncommon in many hydrated metal oxide systems.

One ferrihydrite particle model with dimensions of $17 \times 15 \times 15$ Å^3 (Fig. 4.3d) is built taking into account the relative stability of surface Fe ions, as suggested from a number of experimental studies [108, 110, 112]. Namely, ferrihydrite contains three different Fe sites, two of which are hexa-coordinated (Fe-1 and Fe-2, with ratios of 60% and 20%, respectively) and one is tetrahedrally coordinated (Fe-3) [108]. Fe-3 tetrahedra have been suggested to dissolve very easily, while Fe-2 octahedra have lower stability with respect to Fe-1 octahedra [110]. Consistently, after carving a small particle including

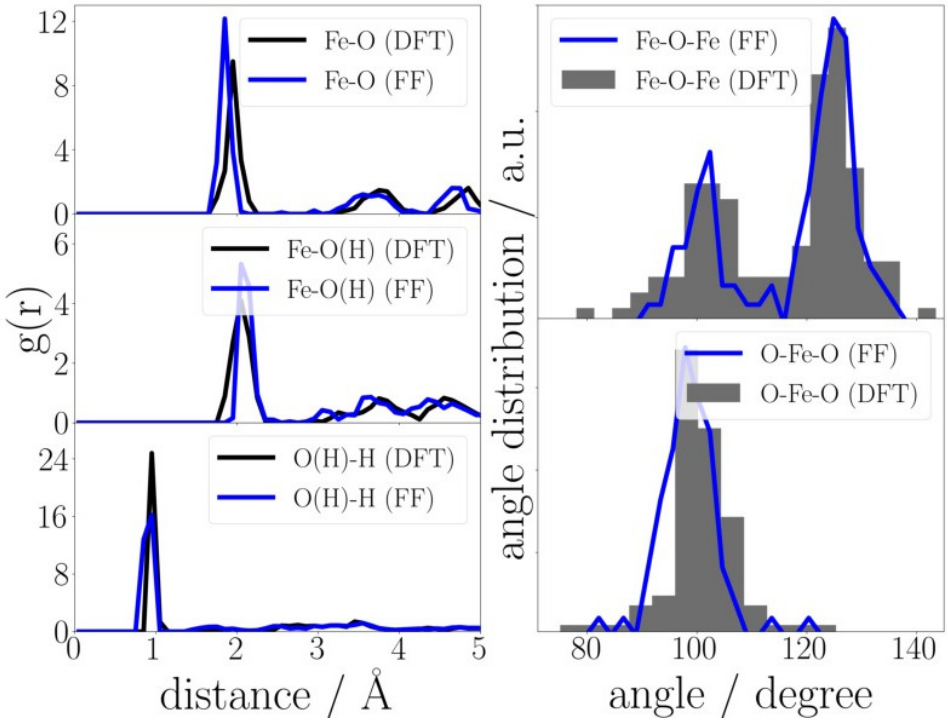

Figure 4.4: Comparison of radial distribution functions and angle distributions for the small goethite nanoparticle model relaxed using DFT and our FF.

seven formula units $Fe_{10}O_{16}H_2$ out of a bulk ferrihydrite crystal, six exposed Fe-2 and Fe-3 surface atoms are removed , the remaining Fe atoms with coordination lower than 4 are saturated with OH groups, singly coordinated O atoms are saturated with H atoms, and additional H atoms are adsorbed on bridging oxygen to compensate for the resulting odd charge stoichiometry. The resulting neutral ferrihydrite particle model with composition $Fe_{64}O_{124}H_{56}$ prior to immersion in liquid water is shown in Fig. 4.3d.

In order to ensure that the resulting nanoparticle models are chemically realistic, the stability of the smaller goethite cluster is checked with DFT. Namely, the cluster is immersed in bulk TIP3P water and a short (10 ns) MD simulation is run to terminate the exposed Fe atoms with water molecules spontaneously. After that, the water-terminated structure is relaxed in vacuum both using the classical FF and DFT. The resulting pair radial distribution functions (rdf) and angle distributions within the cluster are compared in Fig. 4.4. The agreement between the DFT and FF results is excellent, perhaps with the minor exception of the FF Fe-O rdf, which is shifted by about 0.1 Å (i.e., 4 %) toward smaller distances than the DFT reference.

4.1.3 A classical force field for the FeO(OH)/water interface

To describe the interactions of the $FeO_x(OH)_y$/water/protein interface a parameter set is optimized following the same strategy as in case of Alumina described in section 3.2. Here, all electronic structure calculations are performed within the framework of spin-polarized Density Functional Theory including the DF2 [162] dispersion correction for the treatment of the long-range interactions between small molecules and the iron oxyhydroxide surfaces. In order to improve the accuracy on the strongly correlated d electrons, the GGA+U [155–157] correction is applied (for more details see 2.2.1). Based on the results of Cococcioni *et al.* [158], the value of the Hubbard U parameter is set to 4.3 eV.

For the parameter fitting we map the true surface-molecule interactions with a potential composed by a Lennard-Jones (LJ) and a Coulomb term to guarantee compatibility of the potential with standard biomolecular force fields:

$$V_{non-bonded} = \overbrace{\sum_{ij} 4\varepsilon_{ij}\left[\left(\frac{\sigma_{ij}}{r_{ij}}\right)^{12} - \left(\frac{\sigma_{ij}}{r_{ij}}\right)^{6}\right]}^{Lennard-Jones} + \overbrace{\sum_{ij}\left(\frac{Cq_iq_j}{\epsilon r_{ij}}\right)}^{Coulomb} \tag{4.2}$$

Where the LJ pair parameters are obtained via Lorentz-Berthelot mixing rules [130, 131]. Atomic charges of goethite surfaces are computed through the REPEAT method [192], whereby the average values obtained for different atoms are used as species-specific fixed charges in our potential (see Table 4.3). The LJ potential parameters associated to the Fe, O, O(H) and H atoms are fit to best reproduce the potential energy profiles of the interactions between a TIP3P water molecule and the goethite surfaces. To this aim, we perform a series of single-point DFT total energy calculation for different orientations and positions of the TIP3P water molecule above the (110) and (021) goethite surfaces for increasing surface-molecule distances along the direction normal to the surface. The same energy profiles are then computed by means of the potential in equation 2.4 and compared to the DFT references. Here, the TIP3P water molecule is first placed randomly above the goethite surface, followed by an energy minimization of the system with fixed atomic position of the surface. The found position and orientation of the molecule is the relaxed position, while two other orientations are chosen, in which the oxygen position is the same, but the hydrogens are changed to face to the surface or away from the surface (see Fig. 4.5). The atom specific LJ parameters are varied until an acceptable agreement is

found for all calculated energy profiles and the final values of all parameters are reported in Table 4.3.

	ϵ /eV	σ /Å	charge / e^-
Fe	0.190	1.35	1.35
O	0.004	2.35	-0.90
O(H)	0.016	3.00	-0.90
H	0.005	0.45	0.45

Table 4.3: Species-specific optimum set of parameters that provide the best fit to DFT results.

Some representative energy profiles are shown in Fig. 4.5, and all underlying profiles can be found in the Appendix A7.

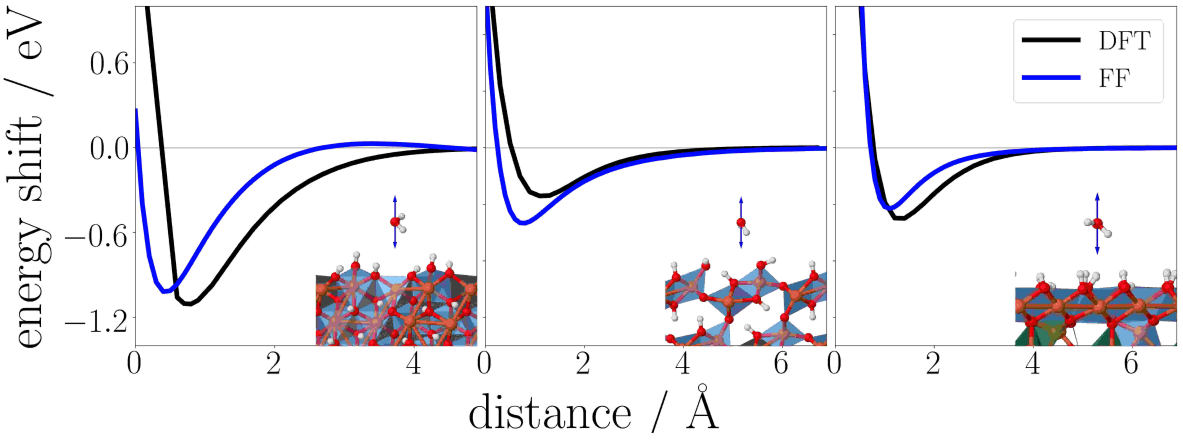

Figure 4.5: DFT and potential based energy profiles for a water molecule on the (021) surface (left), the (110) surface (middle) and above the ferrihydrite surface (right).

While energy values at the potential minima are reproduced with reasonable accuracy, an overall tendency to shorter Fe-O bond distances is obtained. The overall agreement between the results based on the parameterized classical force field and DFT can be considered acceptable, although not perfect. The parameter set reported in Table 4.3 should be thus considered as a compromise, which is able to reproduce at the same time greatly different situations such weak, dispersion-dominated interactions, repulsions (see Appendix A1.3) and strong and direct surface-molecule bonds as well. As we will present in the next section, the parameter set presents a good transferability to other iron oxyhydroxides, is capable of reproducing interactions between goethite and small organic

molecules, and, additionally, is able to reproduce available experimental literature data such as the heat of immersion of Fe(III) phases.

4.1.3.1 Validation of the parameter set

Transferability The transferability of the potential parameters presented in Table 4.3 to the case of water molecules over the ferrihydrite surface and to interactions with ammonia and formic acid is probed in this section. To this aim, potential energy profiles are computed both with DFT and with the classical potential for TIP3P water above the ferrihydrite surface, where one representative result is displayed on the right-hand side in Fig. 4.5 and all results can be found in the Appendix in Fig. A7. The overall agreement between our potential and the DFT based results suggest an acceptable transferability of the potential parameter set to other iron oxyhydroxides. The best agreement is obtained for the case of water at the equilibrium adsorption site after previous relaxation (right-hand side in Fig. 4.5) where both the equilibrium bond distance and the bond strength and are reproduced with about 0.2 Åand 0.05 eV respectively. In case of ammonia and formic acid, as two representative cases for small organic molecules, a similarly good degree of transferability is obtained over both goethite and ferrihydrite surfaces (see Figs. 4.6 and 4.7). Here, the DFT based equilibrium distances are reproduced within 0.2 Å, and the energy at the minimum is reproduced with errors smaller than 0.1 eV.

Heat of immersion Following the strategy described in section 3.2.4, the heat of immersion (E_{im}) of FeOOH predicted by our potential parameter set is compared with available experimental data. A distance of 50 Å between the upper and lower side of the goethite (021) surface is filled with 5000 TIP3P water molecules and the density profile of the system after density adjustment and 1.5ns MD equilibration at 300 K within the NVT ensemble is shown in Fig. 4.8. Evident oscillations of the water density in the interface regions are usual for water/oxide interfaces and level out and reach the expected bulk density values at distances larger than about 10 Å from the surfaces. The values of the heat of immersion are calculated similarly to Al_2O_3 by equation 3.5 for the two goethite surfaces and the ferrihydrite surface. The calculated values for the different surfaces range from 242.5 to 399.9 mJ/m^2. They are in very good agreement with experimentally measured values for FeOOH particles, which range from 180 to 440 mJ/m^2 depending on different particle synthesis methods [98, 215].

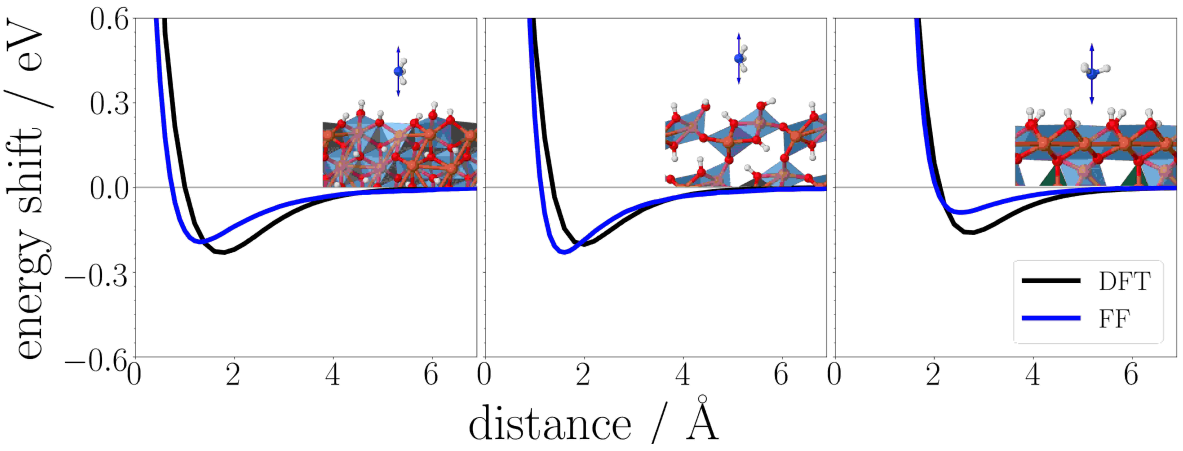

Figure 4.6: Energy profiles for an ammonia molecule above the goethite (021) and (110) surface and the surface model of ferrihydrite (from left to right) where the black line represents the DFT based result, and the blue line based on our potential. Here, in case of goethite, the H and in case of ferrihydrite the nitrogen atom faces to the surface. All energy profiles can be found in the Appendix A9.

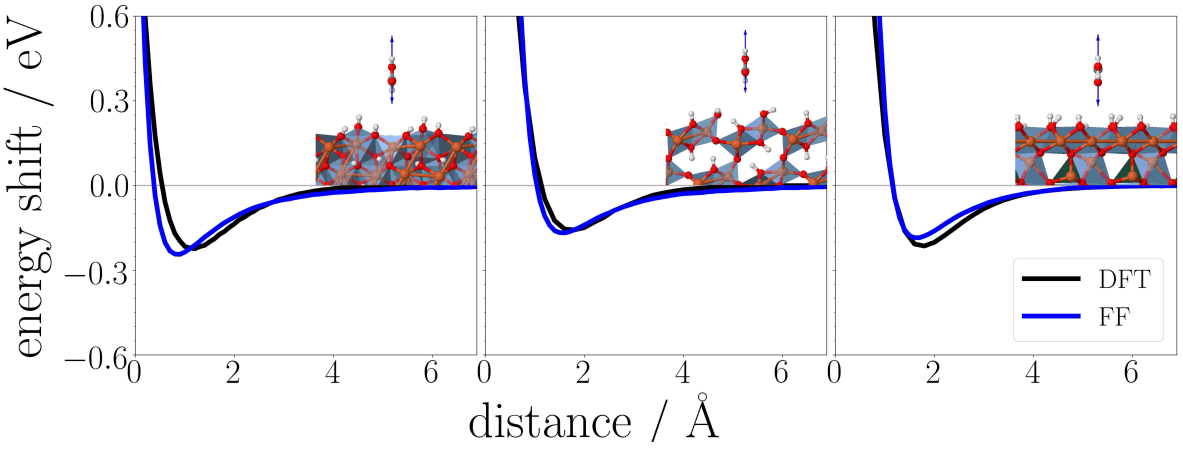

Figure 4.7: Energy profiles of a formic acid molecule above the goethite (021) and (110) surface and the surface model of ferrihydrite (from left to right) where the black line represents the DFT based result and the blue line based on our potential. Here, in case of goethite, the OH group and in case of ferrihydrite the carbon atom face to the surface. All energy profiles can be found in the Appendix A8.

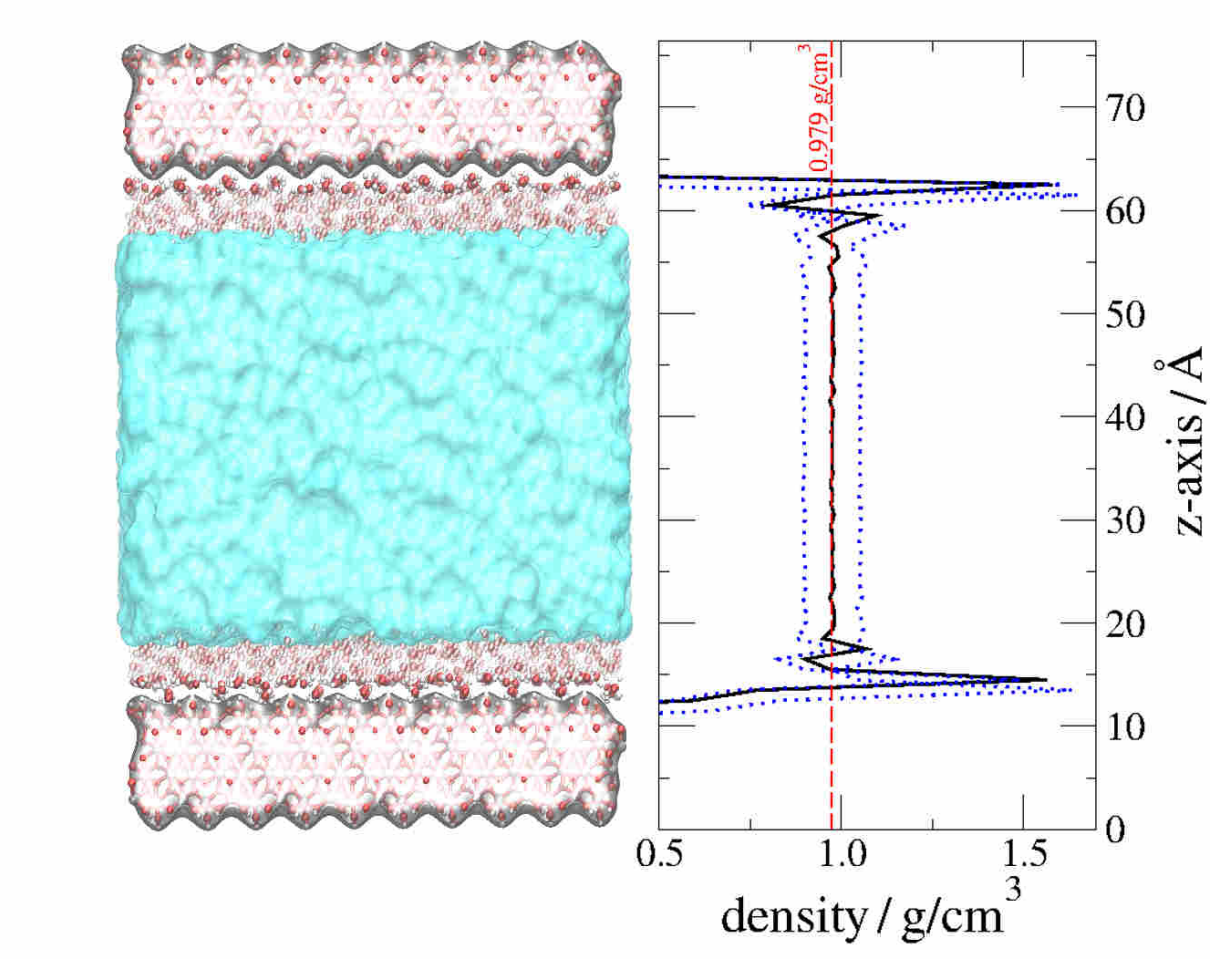

Figure 4.8: Illustration of a system containing two (021) surfaces of goethite separated by TIP3P water. The density of water molecules is represented along the vertical (z) axis on the right. The red line represents the density of bulk TIP3P water and the blue line represents the density of the interface system. The dashed blue lines depict the maximum and minimum values of the density during the optimization procedure of the cell height.

Surface	E_{im} mJ/m^2
goethite (021)	242.5
goethite (110)	399.9
ferrihydrite	333.5
experiments [98, 215]	180-440

Table 4.4: Heat of immersion values for the (021) and (110) surfaces of goethite and the surface model of ferrihydrite in contact with TIP3P water.

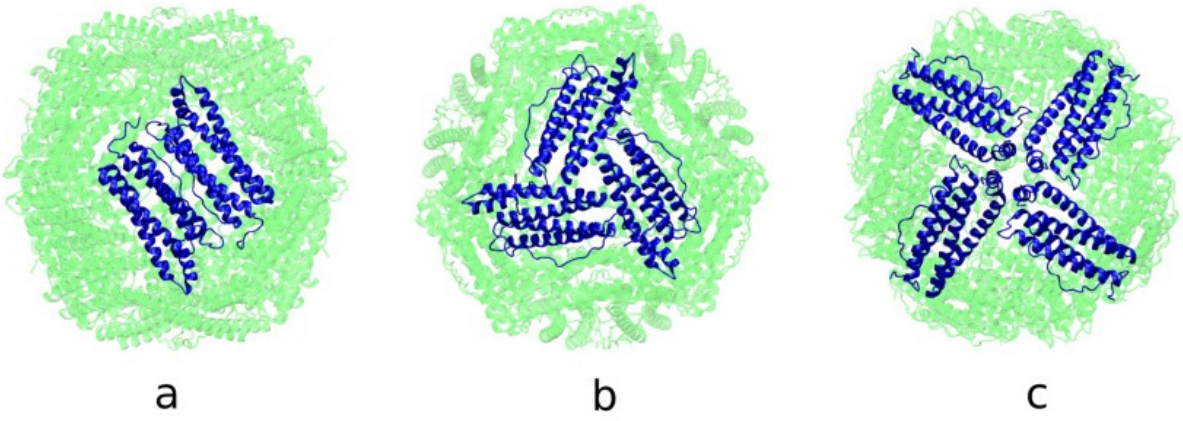

Figure 4.9: Ferritin subunit arrangements consisting of (a) two, (b) three, and (c) four subunits extracted from a complete Fn shell. The subunits are visualized in blue, and the complete shell is colored green.

4.2 Interactions between Ferritin and FeO(OH) nanoparticles

4.2.1 Theoretical investigations

The Fe(III) nanoparticles models presented above (see Fig. 4.3) are used as probes to determine the binding affinity of Fe oxyhydroxide anchoring points in several Fn subunit arrangements qualitatively. Since subunits have the natural tendency to self-assemble in water solution over a very broad range of pH [216], we consider arrangements of either H or L subunits around 2-fold (2 subunits), 3-fold (3 subunits) and 4-fold (4 subunits) symmetry axes of apo-Fn cages, as shown in Fig. 4.9.

The hydrated particles are initially placed at a distance of 10 Å from the central symmetry site of each of the Fn subunit arrangements (see Fig. 4.10a). The simulation box is then filled with TIP3P water molecules and the solvent density is adjusted in a 5 ns NPT simulation (thermalization step). Within these 5 ns, the particles spontaneously start binding to several anchoring sites at the Fn subunits, interacting mostly with amino acid side chains, and more rarely with the protein backbone (Fig. 4.10b). Some exemplary contacts to different amino acids are shown in Fig. 4.10c-f, where distances smaller than 2.7 Å are visualized by means of green bonds. For instance, the oxygen atoms of the carboxyl group of a glutamic acid form a bidentate bond to a surface Fe atom, after having displaced a molecularly adsorbed water molecule therein (Fig. 4.10c). Lysine and

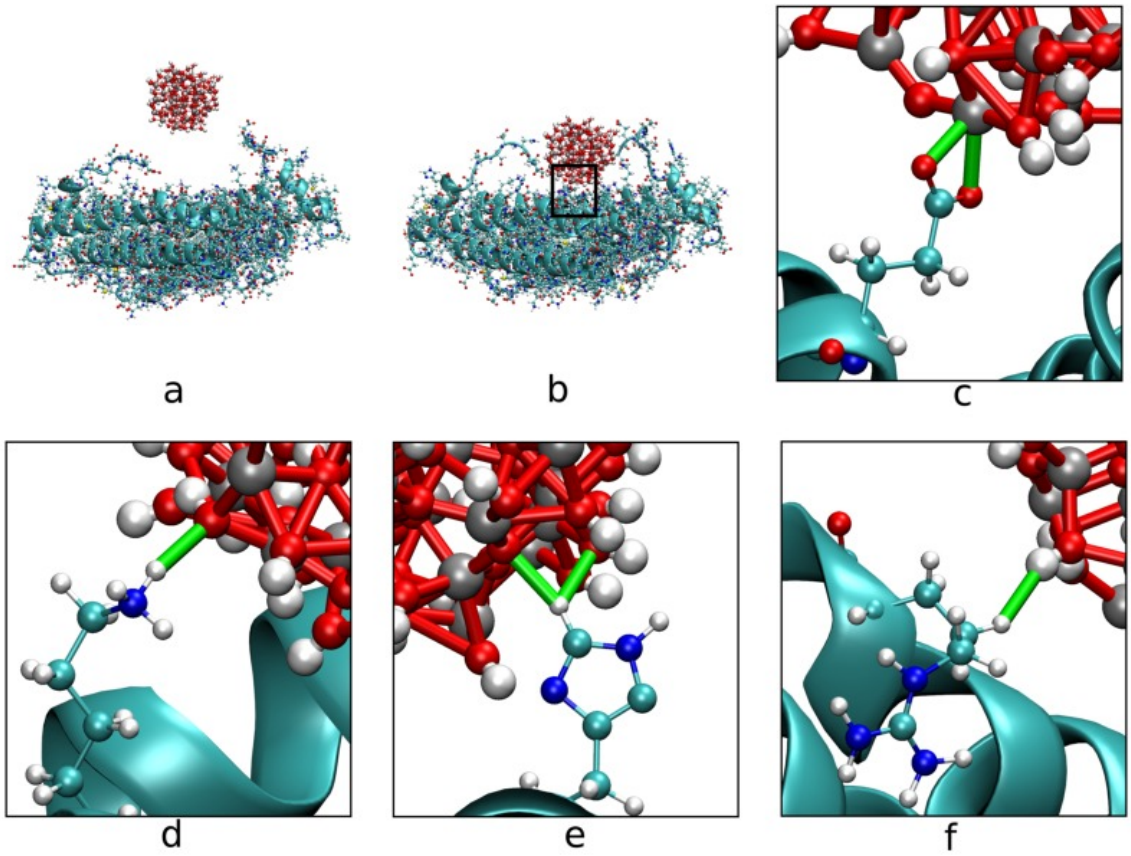

Figure 4.10: Docking of the "ferrihydrite" nanoparticle model (Fig. 4.3d) to the 2-fold symmetric Fn subunit arrangement (Fig. 4.9a, chains A and B). (a) Initial configuration. (b) Configuration after MD thermalization of 5 ns. (c-f) Exemplary anchoring points after MD of 50 ns, including Glu 65 (chain A), Lys 54 (chain B), His 58 (chain B), Arg 64 (chain B), respectively. Fn-goethite distances of $<$2.7 Å are visualized with green bonds.

histidine groups undergo another kind of interaction to the particle, via hydrogen atoms of their side chains (Fig. 4.10d,e). Even hydrophobic regions, such as the long aliphatic chain of arginine, can be brought into van-der-Waals contact to OH terminal groups of the nanoparticles (Fig. 4.10f), mostly indirectly due to stronger (polar) interactions with neighboring residues.

After the 5 ns equilibration and first contact formation, longer NVT runs lasting 50 ns each are performed to analyze the stability of the particle/protein interactions. This simulation time is sufficient to converge the time percentage of individual contacts. The results of the analysis are presented in Figs. 4.11 and 4.12 for the exemplary case of the 2 subunit arrangements (H and L). All other results are included in the Supplementary Information. Every time an amino acid comes to a distance of less than 2.7 Å from the

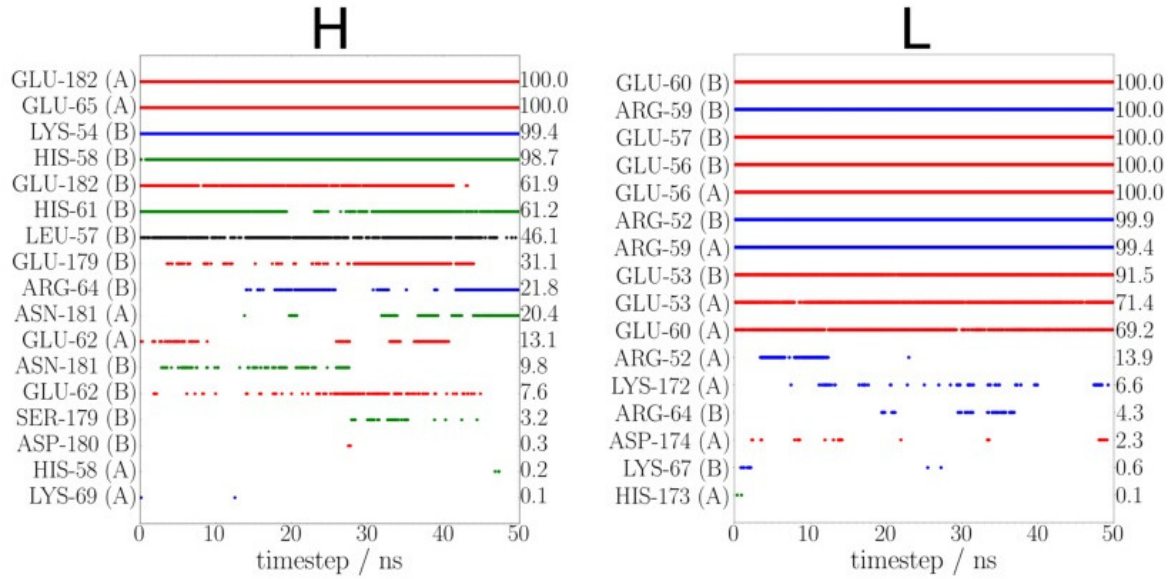

Figure 4.11: Time evolution of the anchoring sites between the 2-fold symmetric Fn subunit arrangement (composed of chains A and B) and the "ferrihydrite" particle model (Fig. 4.3d), for H (left) and L (right) subunits. Marked are all contacts with distances smaller than 2.7 Å between any atom of the Fn amino acid residues and any atom of the Fe(III) particle. The residues are labeled with their sequence position number and the chain they belong to. The time percentage in which a contact is present is shown on the right in each graphics. Contacts involving amino acids with positively charged side chains are colored blue, with negatively charged side chains red, with uncharged polar side chains green and all others colored grey.

cluster with at least one of its atoms, a contact interaction is counted and marked with a dot in the graphics in Fig. 4.11. The used color code indicates positively charged residues in blue, negatively charged residues in red, polar uncharged residues in green and all other residues in grey.

Both for H and in L subunits, the stablest contacts (present for more than 99 % of the simulation time) are formed with charged residues, especially glutamic acid and arginine, at different positions along the different Fn chains (A or B for the 2 subunit arrangements). We note in particular the great number and stability of contacts with residues 52 to 60 of the L subunit arrangements (Fig. 4.11 right). Especially the very stable contacts with the GLU residues at positions 56, 57 and 60, and (to a slightly lesser extent) 53 are striking. In a recent investigation, these very residues have been found to anchor a tri-Fe cluster and a fourth isolated Fe ion in both human and horse ferritin [217] (this is the so-called 'nucleation site' shown in Fig. 4.1). Intermittent contacts are formed in particular with

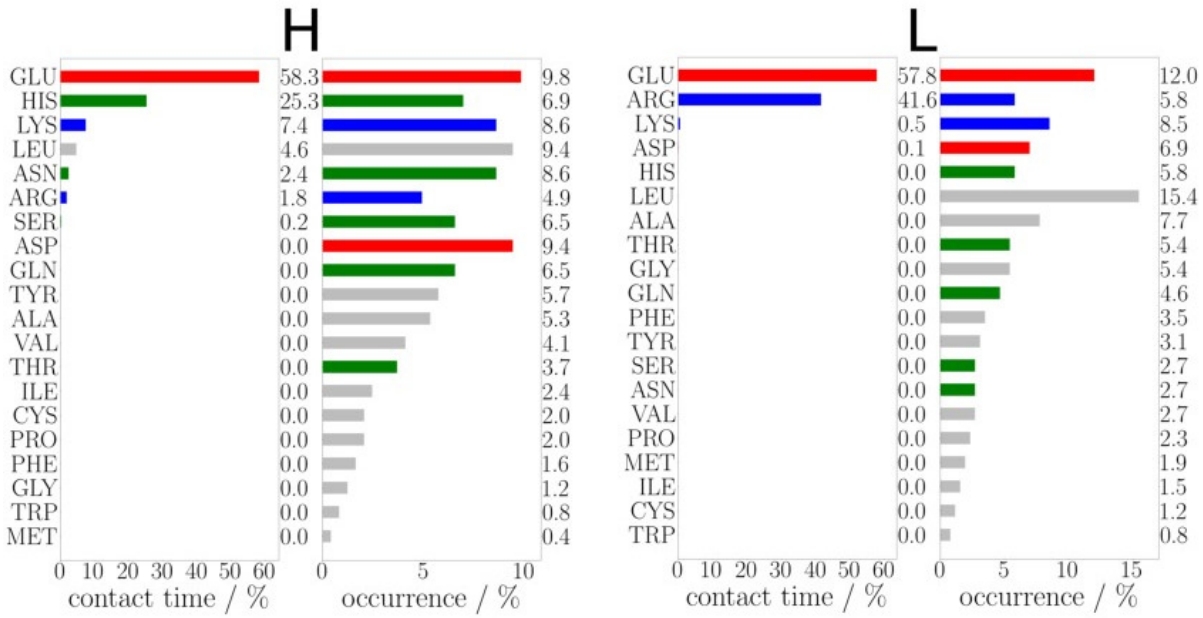

Figure 4.12: Amino-acid-residue-resolved analysis of the anchoring sites for the systems in Fig. 4.11. Shown are the percentage of contact time (left panels) and the relative residue occurrence at the solvent accessible surface of the subunits (right panels), for the case of H and L subunits (left and right, respectively). The values for each residue type are also reported on the right-hand side of each panel, for the sake of clarity. Color code as in Fig. 4.11.

residues in the terminal region (positions 172-174).

On the H subunits, stable contacts are formed with GLU 65, but only intermittent contacts with GLU 62, despite the fact that both residues are part of a similar 'nucleation site' on H subunits [61]. Interesting to mention is also the anchoring of the particle at the H subunit's C-terminal site (stably with SER 183 and GLU 182, intermittently with SER 179 and ASN 181), via the long and flexible random-coil segments shown to be interacting with the left and right sides of the goethite nanoparticle in Fig. 4.10b. This finding is again in striking agreement with former NMR-based work, in which Fe^{3+} ions have been observed to move directly from the ferroxidase site towards the C-terminus of each H subunit, where early mineral nucleation is thus expected to occur [218].

The percentage amount of formed contacts resolved by the type of amino acid is presented in Fig. 4.12. Importantly, the distributions of contacts are not, or only weakly, correlated with the distributions of residues potentially available at the solvent accessible surface of the subunits, indicated as the residue occurrences in Fig. 4.12. Unsurprisingly,

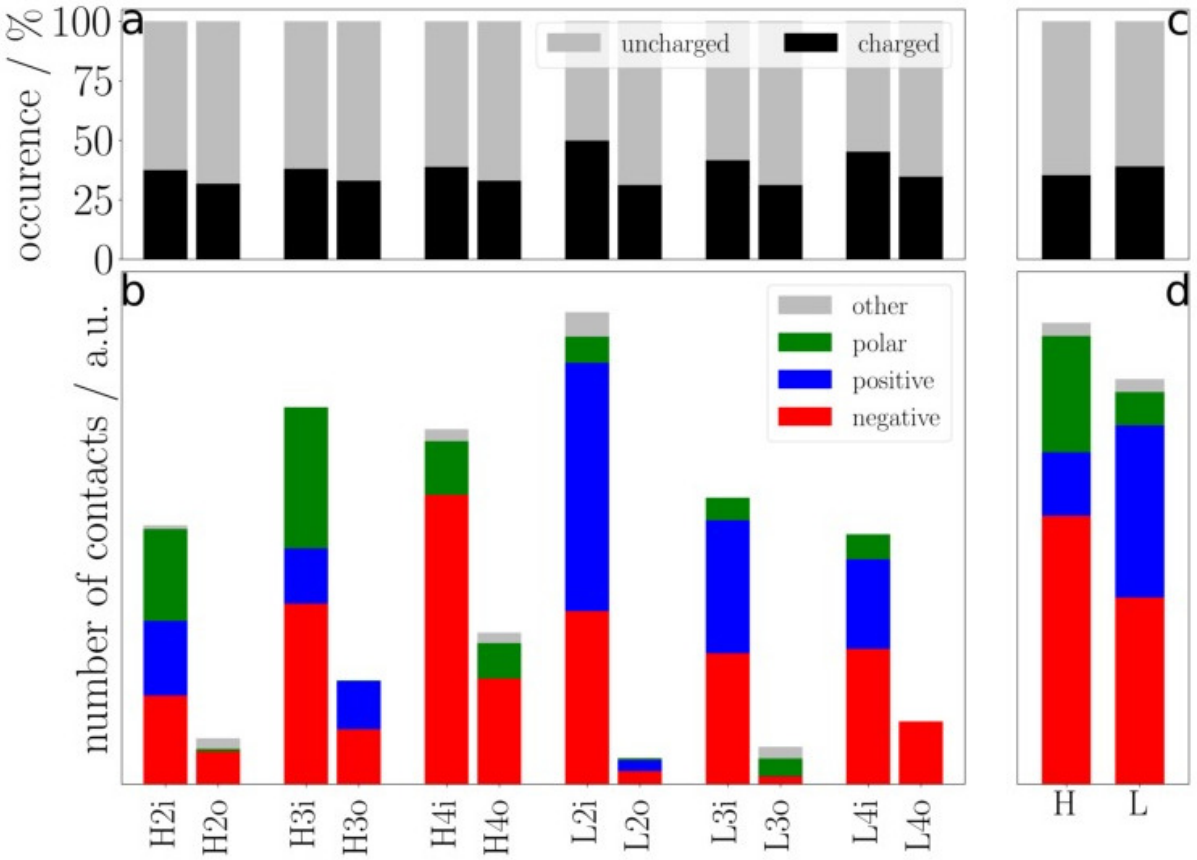

Figure 4.13: (a) Relative occurrence of charged and uncharged residues and (b) cumulative contact numbers to Fe(III) nanoparticle models on the inner (i) and outer (o) side of Fn arrangements with two, three or four subunits (H or L). (c) Total occurrences and (d) summed contact numbers for either H or L subunits are also reported.

overall the majority of contacts is formed via negatively charged residues, in particular glutamic acid. However, very frequent is also binding via positively charged residues (lysine and arginine), whose role is mostly underestimated in the literature concerning the iron oxide binding capability of native Fn. Notably, contacts via non-charged polar residues, involving mostly histidine, are frequently observed, especially for H subunits (see also the Supplementary Information for the results concerning the other Fn subunit arrangements). Finally, contact via non-polar residues is less frequent, and in large part due to neighboring effects, when a stable contact is present at a (charged or polar) site in the immediate vicinity.

In Fig. 4.13 we summarize the total number of contacts formed with the three subunit arrangements of either H or L subunits, distinguishing between the inner (i) or outer (o) side of the subunits with respect to a whole Fn cage. The upper panel reports the occurrences of charged and uncharged residues at the solvent accessible surface. These are only slightly different at the inner or outer sides of different subunits arrangements (Fig. 4.13a) and are roughly equal in either H or L subunits (Fig. 4.13c). Evident is the much larger number of contacts formed with the inner side rather than with the outer side, confirming the evolutionary engineering of the Fn sequence to firmly anchoring Fe(III) mineral particles inside its cavity. Both in the individual arrangements (Fig. 4.13b) and in the overall sums (Fig. 4.13d), the number of contacts formed with H subunits slightly exceeds the one formed with L subunits (with the exception of the twofold arrangement). More importantly, the availability of negatively charged and of neutral contact sites is significantly larger in H than in L subunits. This may point toward a larger affinity of H subunits for positively charged Fe^{2+} ions or very small Fe(III) clusters in the initial nucleation stages of Fe oxyhydroxide particles, which can be exploited in mineralization experiments (see next section). An important role in supporting the heterogeneous nucleation of particles may be especially played by the random-coil sequence segments at the C-terminal end of the H subunits, which are able to embrace the growing clusters effectively. We note that these results do not depend significantly on the size or the phase composition (goethite vs. ferrihydrite) of the probing cluster models, as highlighted in Fig. 4.14 for the case of the arrangement composed by 2 Fn subunits.

However, as a note of caution, we would like to point out two main limitations of our simulation protocols. First, the quantitatively accurate sampling of all possible protein/mineral contacts would require a much larger number of MD simulations for each

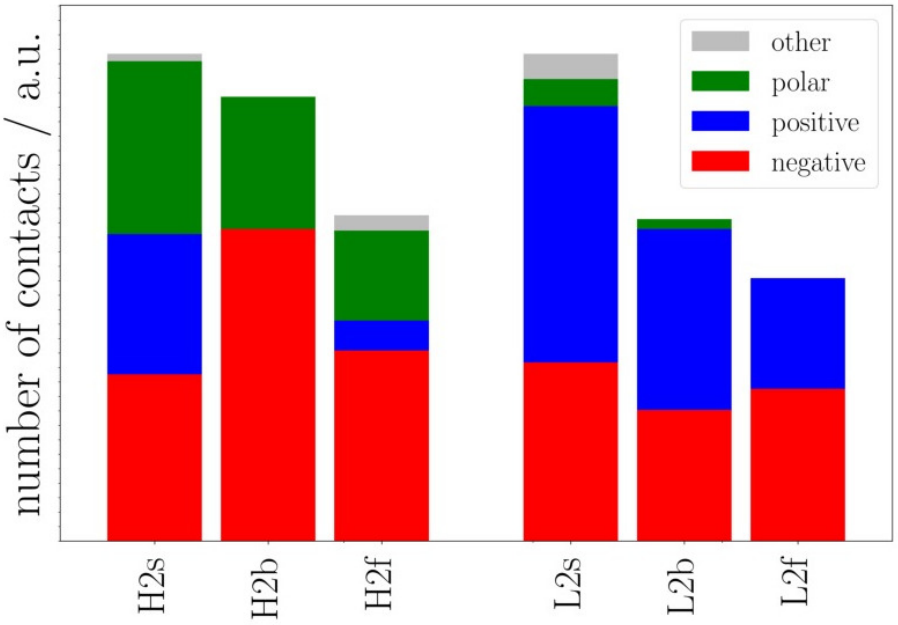

Figure 4.14: Total number of contacts for H or L subunits estimated with Fe(III) particle models of different sizes and phases (s, goethite small; b, goethite big; f, ferrihydrite), as shown in Fig. 4.3.

considered system. Here, we limit ourselves to a qualitative evaluation of the main putative anchoring sites; all presented numbers should be taken only as indicative trends. Second, the employed force fields do not allow proton exchanges to occur between the mineral and the protein, which could (and probably would) happen in reality. In particular, protonation of histidine, and possibly glutamic and aspartic acid, cannot be excluded as a result of pK_a shifts of amino acids deeply buried at the protein/mineral interface.

4.2.2 Mineralization experiments

The results presented above point towards a small, but not negligible difference between the distribution of anchoring sites for Fe^{3+} ions or nascent Fe(III) oxyhydroxide clusters at ferritin subunits, namely the larger amount of negative and neutral sites available on H rather than L subunits. In order to exploit this difference, mineralization experiments are carried out by incubating a solution of Fe^{2+} ions with either H or L subunits immobilized on silica particles for very long time (overnight, at least 14 hours) before adding the oxidation agent. During this long incubation or 'activation' step, we expect maximum loading of the negatively charged and neutral anchoring sites with positively charged

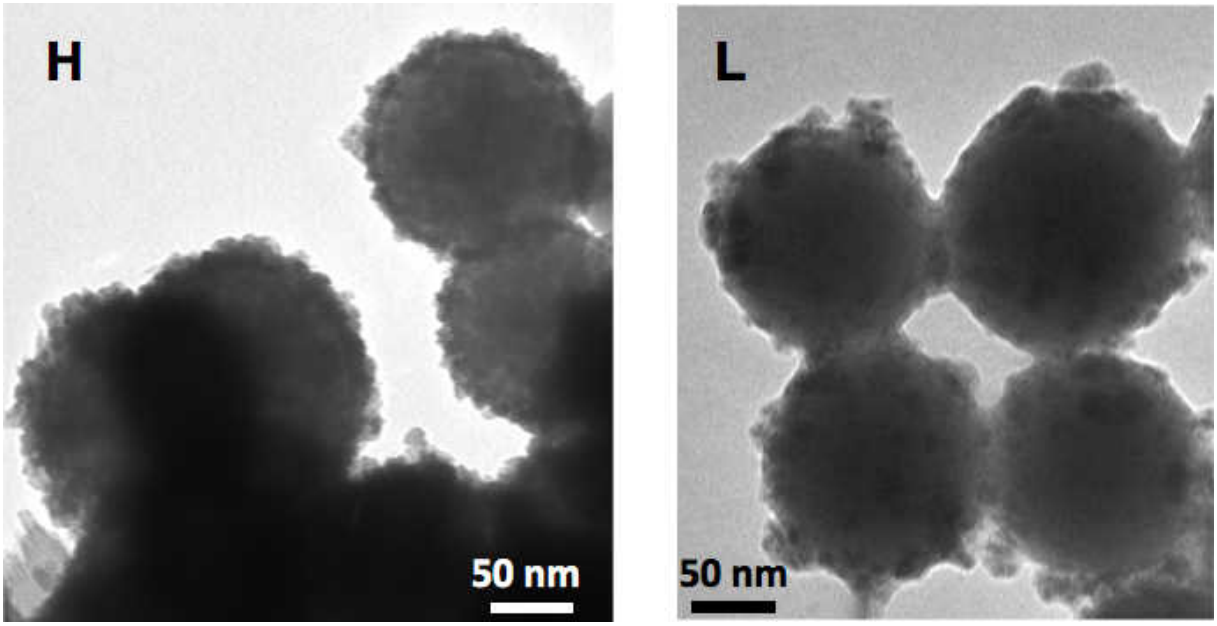

Figure 4.15: TEM images of H (left) and L (right) Fn subunits covalently immobilized on SiO_2 particles, after the Fe oxide mineralization procedure described in ref. [220].

ions. Moreover, even if the incubation is performed under nitrogen protection, partial oxidation of some of the ions via residual oxygen traces in the solution, or even by the protein themselves, could take place. Protein-bound Fe^{2+} ions and, if present, initially formed Fe(III) nuclei, would act as preferential seeds for the further Fe(III) mineral growth during the subsequent oxidation step.

This hypothesis is in line with other two-step mineralization protocols developed earlier, for instance to promote the deposition of metal nanoparticles on DNA molecules [219]. In this early work is was shown that loading of the biomolecules with charged metal ions and the formation of active nuclei for further metal growth follows very slow kinetics; hence long incubation times were necessary to promote a selectively heterogeneous metallization. In the present work, we follow the same idea, although an oxidation rather than a reduction step follows the initial activation.

In Fig. 4.15 we report examples of typical structures obtained with this mineralization protocol (for further details see Methods). According to our expectation, and in spite of the postulated physiological propensity of L subunits to stabilize the initial formation of ferrihydrite clusters in Fn cages, the Fe oxide films grown on immobilized H subunits seem to be more dense and uniform than those grown on L subunits. This observation

could be indeed explained by a faster nucleation and growth kinetics on H subunits due to the presence of a larger number of mineralization seeds formed during the activation step preceding the oxidation. However, other factors such as an active role played by the ferroxidase site in catalyzing the oxidation from Fe^{2+} to Fe^{3+} cannot be excluded.

In these experiments, the immobilization protocol of the subunits on the silica particles before mineralization is a crucial and non-trivial step. In particular, neither the average coverage nor the homogeneity of the covalently bound subunits can be readily accessed, as also discussed in depth elsewhere [167]. Since the here-employed protocol is not targeting specific amino acids but all primary amines, and given the similarity in the content of amine-bearing residues in the H and L chains, we do not expect significant differences in the amount of bound H or L subunits prior to mineralization. In any case, the findings presented here are to be considered as a first and qualitative assessment based on the visual inspection of few TEM images, and must thus be taken with care. More precise experiments based on the quantitative study of the mineralization kinetics are needed and will be performed in future studies.

Chapter 5

Nucleation and growth of $FeO_x(OH)_y$ on Ferritin

Nevertheless, the investigation made use of predefined particles. To get more insights at the atomic level in the process of nucleation and of the very early stages of ferritin-promoted crystal growth of iron oxyhydroxide, a more in-depth look is necessary. Therefore, more advanced methods are implemented for the realistic simulation of nucleation behavior as well as for simulations of growth, and structures. New analysis techniques are developed for the identification of the so-obtained mineral phases.

Based on the small dimensions of the nuclei and their transient nature, it is difficult to study the early stages of nucleation experimentally. Nevertheless, cryogenic transmission electron microscopy (cryo-TEM) has proven to be a powerful tool to analyze classical and non-classical nucleation and crystallization phenomena [113, 114]. Moreover, in some special cases, the nuclei could be investigated directly [221–225], but in general experiments reveal quantities, such as rate, crystal size or shape distribution, which are only indirectly correlated with nucleation. To get comprehensive insights, at the atomic scale, to the process of nucleation and the very early stages of crystal growth, simulation techniques are necessary.

In recent years, different techniques such as Molecular Dynamics (MD), Monte Carlo (MC) and enhanced sampling methods have been increasingly used to investigate nucleation [60, 126, 136, 226–238]. Ab initio MD simulations are maybe the most accurate way to study nucleation, but due to the computational effort, the number of atoms and the timescales are limited [239]. In classical MD simulations, simplified potentials enable

the usage of hundreds of thousands of atoms and timescales of microseconds as well as the calculation of kinetics, dynamics, and thermodynamic quantities. Nevertheless, high energy barriers and long timescales in the crystallization processes limit the number of possible efficient investigations based on classical MD simulations.

Monte Carlo simulations [240, 241] are stochastic in contrast to MD simulations which are deterministic. Here, random perturbations are applied to generate an ensemble of representative configurations. These random perturbations must be sufficiently large, energetically feasible and highly probable to ensure proper sampling. While the ensemble of configurations can be used to obtain static information and relevant thermodynamic observables, such as the free energy, kinetic or dynamical information cannot be directly obtained, since the sequential generation of configurations does not relate to the time evolution of the system.

Several enhanced sampling methods, such as metadynamics, use collective variables (CVs), which identify all relevant states in the phase transition, to enable the calculation of thermodynamic and kinetic quantities associated with rare events. For that, order parameters (OPs) are necessary which define the crystalline state based on a spatial configuration of an ensemble of atoms or molecules and the accuracy of this method depends mostly on the choice of the collection variable. In this thesis, differences between the nucleation and growth of iron oxyhydroxides in water and on the Fn protein are of interest, and enhanced sampling methods are not suitable. Instead, a combination of classical MD and MC simulation is used based on the idea of Kawska and Zahn [60]. The iterative scheme of the Kawska-Zahn approach circumvents the problem of long timescales for the diffusion of the ion to the aggregate, which occurs in systems of crystal formation of compounds with low solubility due to the low concentration. In this scheme, a Monte Carlo type part is used to identify possible adsorptions sites, followed by a classical MD simulation run after each growth step, for structural optimization of the formed aggregate and solvent, as described in section. 5.1.

For the implementation, several input functions and commands of the LAMMPS [242] packages are combined. This combination offers a fast and efficient way to perform the simulation of nucleation and growth without external scripts and therefore with few read/write processes to share information between code and scripts. After the implementation of the Kawska-Zahn approach, the nucleation and growth of $FeO_x(OH)_y$ in water will be investigated. Of special interest is the possibility to include ripening reac-

tions, by the inclusion of proton transfer reactions, into the process. It is known that iron oxyhydroxide forms either α or γ-FeOOH (goethite or lepidocrocite) in water, while ferrihydrite is formed in the ferritin shell under identical conditions [125]. Therefore, the nucleation and growth on Fn subunits will be investigated to answer the question of structural differences between the phases, which are grown in water and on Fn subunits. The obtained structures will be compared by introducing a new way of structure determination. Moreover, the obtained nucleation sites of the aggregates to the protein will be compared to the previously obtained results of docking simulations in chapter 4.

5.1 Kawska-Zahn approach and implementation

In this following section, the original Kawska-Zahn approach [60] is introduced, as well as the way of implementation in the LAMMPS code to describe the crystal growth of $FeO_x(OH)_y$. The most important parts of all necessary steps are summarized with comments in the Appendix in section A1.5.

The original Kawska-Zahn approach [60] was introduced to describe CaF_2 crystallite formation based on an iterative process, where each iteration is divided into three steps. The first steps include the random choice and placement of an ion, as well as the diffusion of it to an aggregate. Subsequently, the aggregate and the newly attached ion are placed in a box filled with solvent. After the relaxation of solvent molecules in step two, the total system is allowed to relax, in a simulated annealing process in a molecular dynamic run. The resulting structure is then taken as new starting point for the next iteration.

An overview of the general process is shown in Fig. 5.1 and described in the following. As a starting point, a single $Fe(III)(OH)_3(H_2O)_3$ complex, as presented in Fig. 5.2, is used. At the beginning of each iteration, a new complex is placed randomly in the simulation box, and it is ensured that the distance is in a selected range, thus not too near or too far away (Fig. 5.1 I.). If a complex is placed in the correct distance range, a docking simulation in NVT ensemble starts (Fig. 5.1 II.) Here, all interactions with the solvent are switched off, and only the new complex is able to move. If the complex is moved away from the aggregate, the complex is removed from the system and the iteration starts from the beginning. Otherwise, the (full) resulting system, with possible highly overlapped atoms of the new complex and TIP3P water molecules (large energies and forces), is relaxed in a multi-step procedure to push the atoms away from each other slowly. In

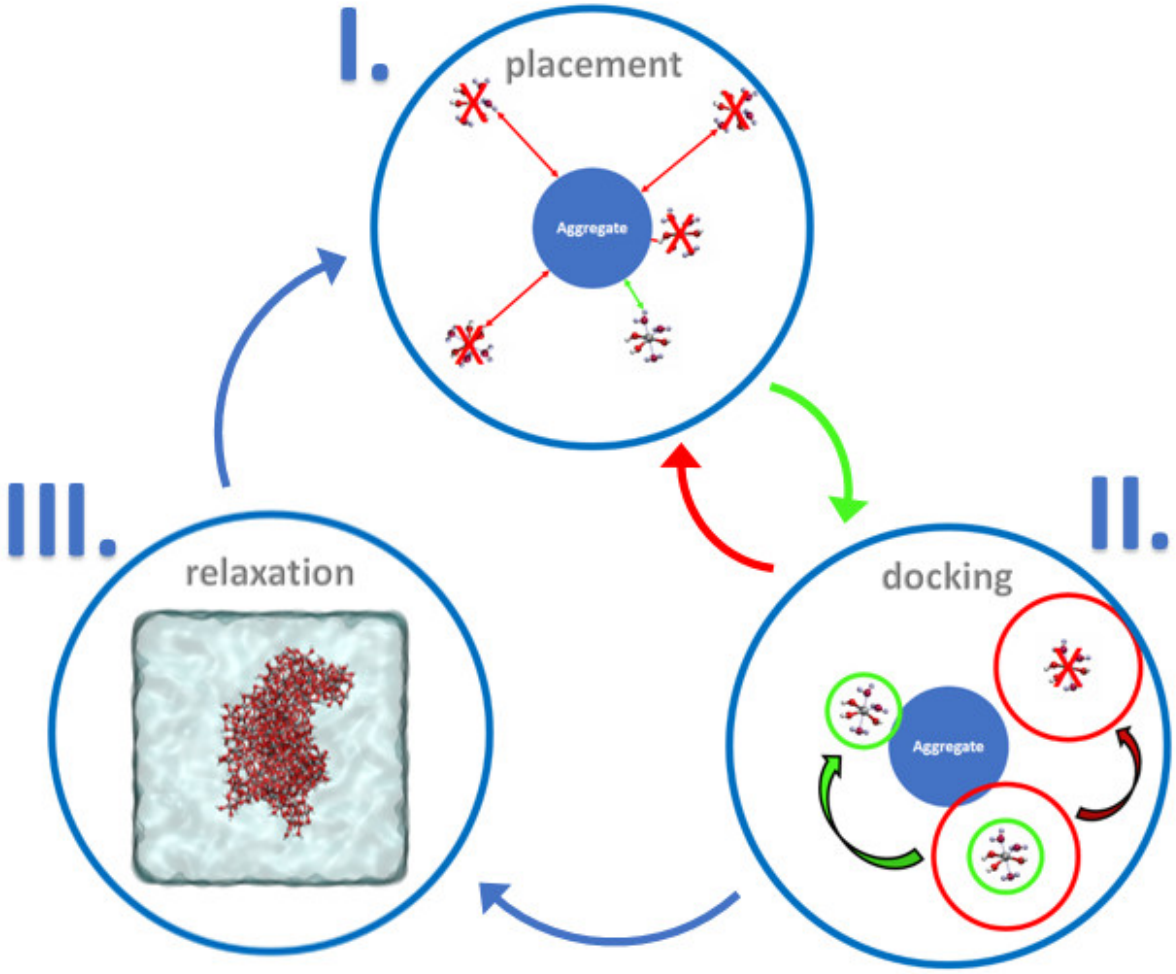

Figure 5.1: Iterative scheme for simulation the crystal growth of iron oxyhydroxide based on the Kawska-Zahn-approach [60]. I. Placement of the complex randomly in the box is only succesful if the distance between complex and existing aggregate is in a defined range. II. A docking simulation is performed by checking the distance between complex and aggregate in every step and succeeds if the complex attaches to the aggregate. If the complex moves away from the aggregate, the complex is removed from the system and step I. is repeated. III. Relaxation of the system.

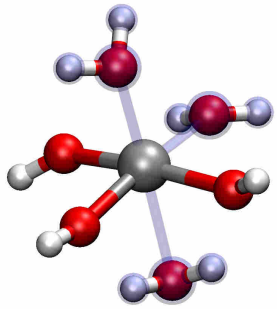

Figure 5.2: Fe(III)(OH)$_3$(H$_2$O)$_3$ complex which is the predominant species at pH 8 and added during the growth process.

this multi-step procedure, the timestep and temperature are slowly increased to ensure a suitable relaxation. Finally, a simulation in NPT ensemble is performed to adjust the correct density, since the added complexes slowly increase the size of the system (Fig. 5.1 III.)

5.2 Growth of Fe(OH)$_3$ in water

Based on the strategy described in the previous section, crystal growth simulations of iron oxyhydroxide in water are performed. The Fe(III)(OH)$_3$(H$_2$O)$_3$ complex, which is added in every step, is shown in Fig. 5.2. It consists of three OH groups and to coordinate the iron atom six-fold, three attached TIP3P water molecules. This complex is used, since Fe(OH)$_3$ is the predominant Fe(II) species at pH 8 [243, 244], at which supporting experiments are performed. First results of the obtained aggregates, after the relaxation step, are shown in Fig. 5.3. Attached water molecules of the TIP3P water model are highlighted with blue spheres and the "bonds" to the aggregate are shown in transparent blue.

It is clearly seen that OH groups act as the connection between the iron atoms of the different complexes forming an aggregate. Thus, the TIP3P water molecules of the complex (as shown in Fig. 5.2), as well as possible attached molecules from the solution are largely replaced by the OH groups, to attach the new complex to the aggregate. TIP3P water molecules are only attached to the outermost iron atoms, to complete their coordination shell. Additionally, it can be seen that iron atoms tend to be six-fold coordinated, and

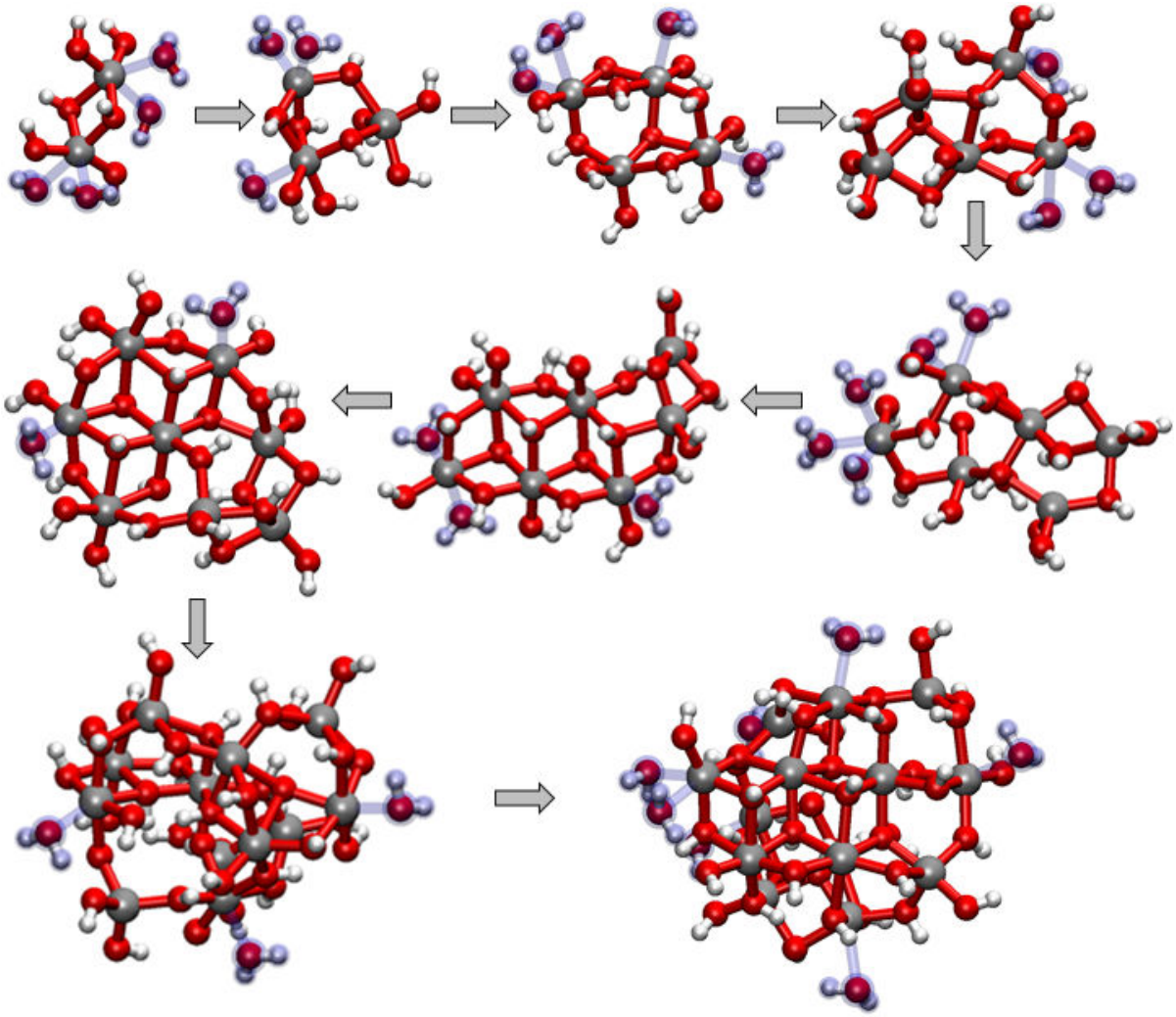

Figure 5.3: Obtained aggregates in the growth process of $Fe(OH)_3$ in water based on the process described in section 5.1. Shown are the aggregates which consists of 2 to 8, 12 and 14 iron atoms. TIP3P water molecules are highlighted by a blue sphere.

five-fold coordinated atoms are only occurring at the surface. It is supposed that these iron atoms are five-fold coordinated since the already attached TIP3P water molecules spatial hindered the attachment of other TIP3P water molecules.

Nevertheless, by the usage of this simulation strategy and due to the $Fe(OH)_3$ complex (and attached water) which is added in every step, only $Fe_x(OH)_{3\times x}$ aggregates can be obtained. To obtain $FeO_x(OH)_y$ structures and to mimic reactions which occur in nature, proton transfer reaction must be included in the simulations as introduced in the following section.

5.3 Proton transfer reactions

For a more realistic growth process, and to obtain more realistic structures, proton transfer reactions (PTR) are included in the simulations, following the idea of the ripening reactions during the crystal growth of ZnO from ethanolic Zn^{2+}/OH^- solution [245, 246]. This step is very important, since a dehydration reaction is necessary to create FeO(OH) structures from the basic complex:

$$Fe(OH)_3 \rightarrow FeO(OH) + H_2O \tag{5.1}$$

Moreover, recent studies reveal the formation of ferrihydrite based on a rapid and continuous release of H^+ [247]. Nevertheless, classical force fields are not able to describe such, or any, chemical reaction. To overcome this problem, a combined quantum/classical MD scheme will be explored to describe proton-transfer reactions. To this aim, the influence of the magnetic ordering to the stability of the aggregates, which were previously obtained, and exemplary PTRs are investigated in the first step.

DFT based reference calculations are performed for aggregates which consist of two and four iron atoms, where the structures are taken from the simulations performed in the previous section. Here, the influence of the magnetization to the stability of the aggregate, as well as the influence to the energy for exemplary PTRs are investigated. For the PTR, the hydrogen of an at least two times coordinated oxygen atom is pushed to an outer OH group and the energy of the product is subtracted from the energy of the educt:

$$\Delta E = E_{product} - E_{educt}. \tag{5.2}$$

Table 5.1: Total energies and energies of PTRs for different magnetic ordering for the aggregate of two iron atoms taken from the simulations performed in section 5.2 which are shown in Fig. 5.4.

spin	energy / eV	diff to min / eV	energy of PTR / eV
++	-107.86	0.04	0.49
+−	-107.90	0.00	0.36

Table 5.2: Total energies and energies of PTRs for different magnetic ordering for the aggregate of four iron atoms taken from the simulations performed in section 5.2 and which are shown in Fig. 5.4.

spin	energy / eV	diff to min / eV	energy of PTR / eV
++−−	-165.52	0.04	0.28
+−+−	-165.51	0.05	0.06
+−−+	-165.56	0.00	0.08
+++++	-165.18	0.38	0.04
+++−+	-165.52	0.04	0.28
+−++	-165.51	0.05	0.06
+++−	-165.45	0.11	0.23
−+++	-165.51	0.05	0.08

Only oxygens which are coordinated by at least two iron atoms are used, because PTRs are expected to be facilitated since these atoms are over-coordinated. Moreover, PTR from oxygen atoms which are only single coordinated by an iron atom would lead to an undercoordinated oxygen atom. The educt (before PTR) and product (after PTR) structures are minimized by a conjugate gradient (CG) algorithm as implemented in VASP. The obtained total energies of the aggregate for the different magnetic ordering, as well as ΔE are listed in Table 5.1 and 5.2. In case of the aggregate of two iron atoms, the influence of the magnetic ordering to the total energy and ΔE with differences of 0.04 eV and 0.13 eV are quite small. Nevertheless, the aggregate with +− spin configuration is more stable. The same behavior is shown in case of the aggregate which consists of four iron atoms. The alternate +− spin configurations are slightly more stable than the +−++ spin configurations, with deviations between 0.0 eV and 0.11 eV and much more stable than the +++++ spin configuration with an energy loss of 0.38 eV. This is in perfect agreement with the observed most stable antiferromagnetic ordering in the goethite primitive unit cell [102]. The energy differences for the PTR for the stable spin

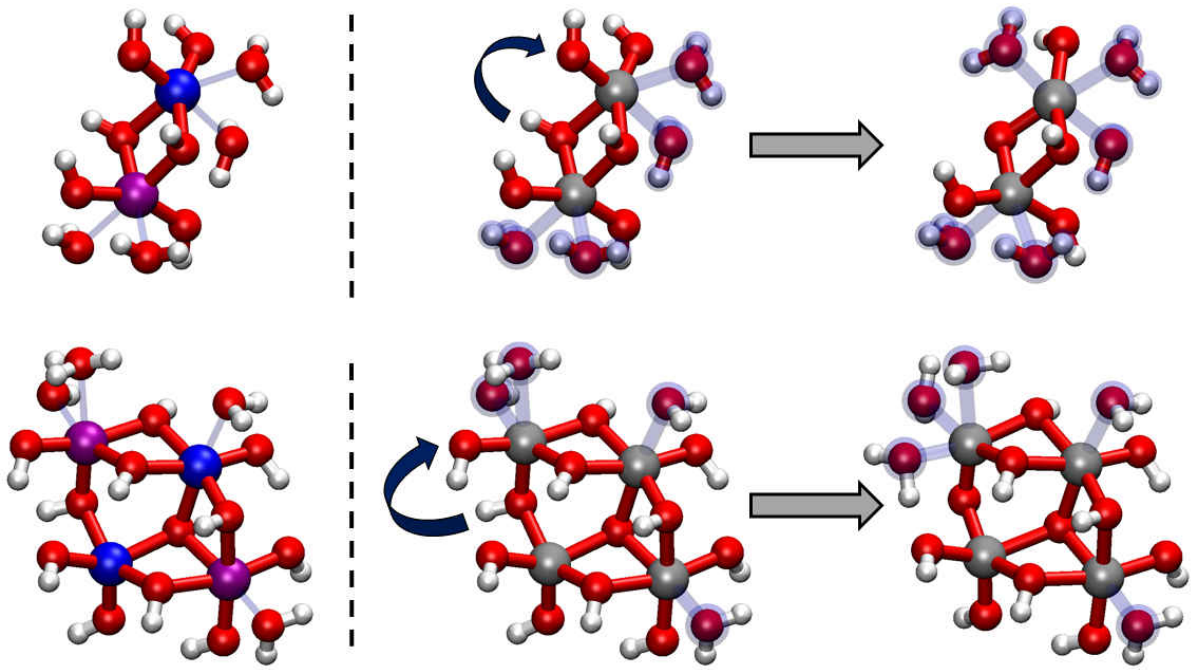

Figure 5.4: Representation of the grown aggregate with two (upper figures) and four (lower figures) iron atoms in the two most stable spin configurations (see Table 5.1 and 5.2). The spin-density isosurfaces (purple: negative, blue: positive) are shown on the left-hand side. The proton transfer reaction is shown on the right-hand side. TIP3P water molecules are highlighted by a blue sphere.

configurations differ between 0.06 eV and 0.28 eV slightly but within the error of DFT. Based on these results and the obtained knowledge that the influence of the magnetic ordering on PTR energy differences are negligibly small, the same PTR are investigated by the parameter set developed in section 4.1.1. For that, the TIP3P parameters are assigned to the created water molecule and the structures are subsequently minimized by the CG algorithm as implemented in LAMMPS. The force-field-based energy difference between products and educts are 1.4 eV and 1.01 eV for the aggregates with two and four iron atoms respectively. In comparison to the DFT based PTR energies, these values are shifted by 1.04 eV and 0.93 eV. This leads to the assumption that the inclusion of a single energy-shift term could enable the developed classical force field to reproduce the DFT based proton transfer reactions energies.

To ascertain a possible energy correction term, five indepentent simulations of the growth process of $Fe(OH)_3$ are performed. Aggregates of different sizes are taken randomly from these simulations, and the DFT and FF based energies of the educt and the

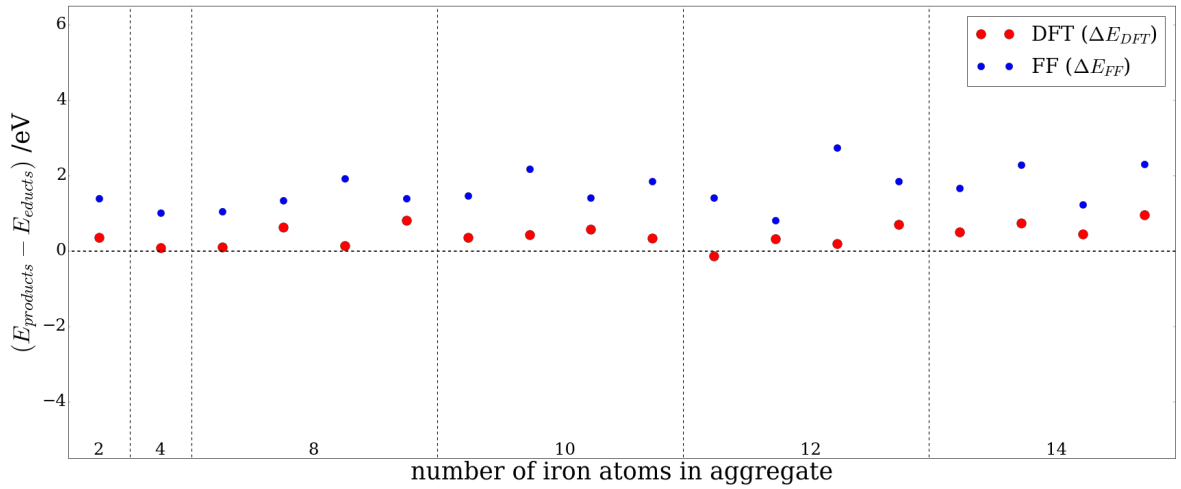

Figure 5.5: DFT and FF based proton transfer reaction energies of different sized $Fe(OH)_3(H_2O)_x$ aggregates.

product of four different proton transfer reactions are calculated. As already mentioned, the energy of each aggregate is calculated by an energy minimization of the educt and product, based on the conjugate gradient algorithm as implemented in the respective code. The reaction energies are then calculated by:

$$\Delta E_{\mathrm{DFT}} = E_{\mathrm{DFT,product}} - E_{\mathrm{DFT,educt}} \tag{5.3}$$

$$\Delta E_{\mathrm{FF}} = E_{\mathrm{FF,product}} - E_{\mathrm{FF,educt}} \tag{5.4}$$

for DFT and FF based calculations. The energy differences which are observed in the DFT based calculations are shown with red spheres and FF based calculations with blue spheres in Fig. 5.5. Based on these results, the energy difference ($\Delta\Delta E$) between the obtained DFT and FF based reaction energies is then calculated by:

$$\Delta\Delta E = \Delta E_{\mathrm{DFT}} - \Delta E_{\mathrm{FF}} \tag{5.5}$$

The average value of these differences is 1.03 eV, where we exclude the two highest positive deviations. These are the third from the left energy differences of the aggregate of 8 and 12 iron atoms. This leads to an overall improvement of the accordance and shift of the FF based energies to more endothermic behavior. Thus the FF based results are forced to be slightly less reactive. By adding this value to the obtained FF based energy differences, an

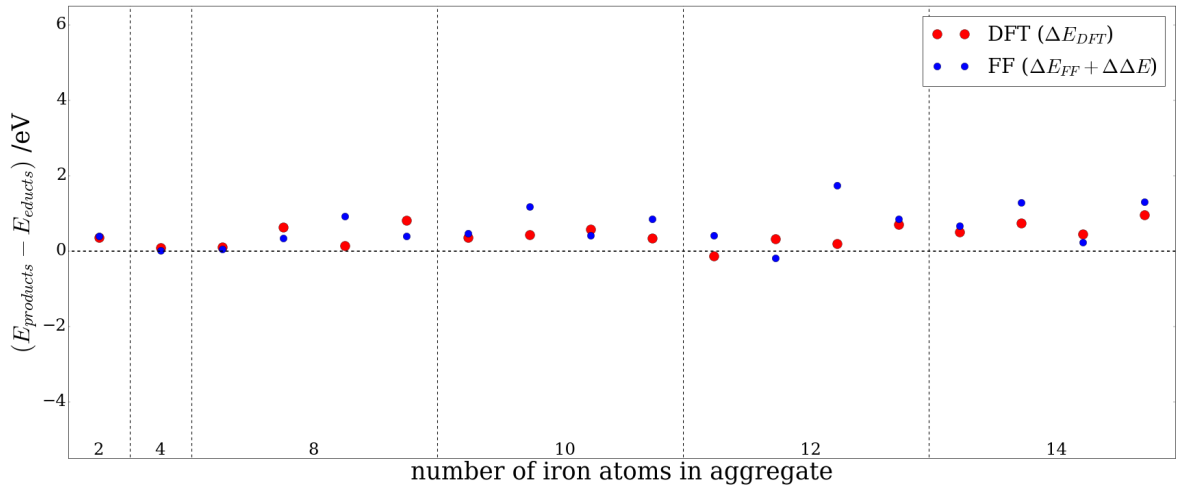

Figure 5.6: DFT and FF based proton transfer reaction energies of different sized $Fe(OH)_3(H_2O)_x$ aggregates. The average value of all differences between DFT and FF based energies ($\Delta\Delta E$) is added to correct the FF based results.

outstanding overlap between DFT and FF based results is obtained as shown in Fig. 5.6. The DFT based energy differences reveal that mostly all PTRs are positive and thus of endothermic nature. Only one PTR is exothermic in case of the aggregate of 12 iron atoms (first from left) with an energy difference between product and educt of -0.13 eV. The same result is observed in case of FF based energies, except one exothermic case with a PTR energy of -0.21 eV, for the aggregate of 12 iron atoms. Based on this overall agreement, and the general correct distinction of endo- and exothermic reactions, this energy correction term will be used in the following simulation. Therefore, PTRs are considered and treated during the simulations based on pure classical force fields, on the basis of the DFT based reaction energies.

Besides this kind of PTR, which will be named in the following as PTR1, other kinds are conceivable. To answer the question of the influence of the type of included proton transfer reaction to the final crystal structure, another type of PTR will be investigated. This second PTR is based on the assumption that supporting experiments, which treat the growth of Fe(III) structures on ferritin, are performed at pH 8. Therefore, proton transfer reactions between the aggregate and OH^- ions in solution are possible, named in the following PTR2. Thus, the educts are the aggregate and an OH^- ion and the products

are the aggregate without the proton and the newly formed TIP3P water molecule.

$$Agg - OH_2 + OH^- \rightarrow Agg - OH^- + H_2O \tag{5.6}$$

Moreover, the proton transfer from a TIP3P water molecule, which is attached to the aggregate, to an OH^- ion in solution will be also considered, named PTR3:

$$Agg - OH + OH^- \rightarrow Agg - O^- + H_2O \tag{5.7}$$

Here, the educts and products are the same as the previous one but with this strategy, a new OH group is formed at the surface of the aggregate.

These two kinds of PTR will create a charged system over time. This charge is compensated by adding a charged complex in the next step. This charged complex is the protonated versions of the complex shown in Fig. 5.2. Thus, the hydroxyl groups of the complex are protonated, resulting in an additional TIP3P water molecule, which can be done three times resulting in a complex with a maximum charge of $+3$. For example the singly protonated version:

$$Fe(OH)_3(OH_2)_3 + H^+ \rightarrow [Fe(OH)_2(OH_2)_4]^+ \tag{5.8}$$

I have to remark that based on the usage of partial charges, this is not a real charge of $+3$ but a charge of $+0.45$ for each proton. Like in the previous part, the energy correction term is obtained by averaging all obtained values for $\Delta\Delta E$ for the respective reaction at different, randomly chosen aggregates of different size. Here, energy correction terms of 0.711 eV and 0.765 eV are obtained for the reaction displayed in Fig. 5.7 on the left and right-hand side respectively. The DFT (red) and FF (blue) based energy differences are shown in Fig. 5.7.

In contrast to PTR1 which is mainly of endothermic nature, the observed energy differences in case of PTR2 and PTR3 are mainly exothermic, which based probably on the instable/reactive OH^- ion. Only for the smallest possible aggregate with only two iron atoms in PTR2 and the aggregate with 12 iron atoms of PTR3 the PTR energies are positive, probably since the removal of the hydrogen from the aggregate leads to an instable rearrangement and an energetically less favorable state. Nevertheless, by adding the energy correction terms to the FF based energy differences, the classical force field is

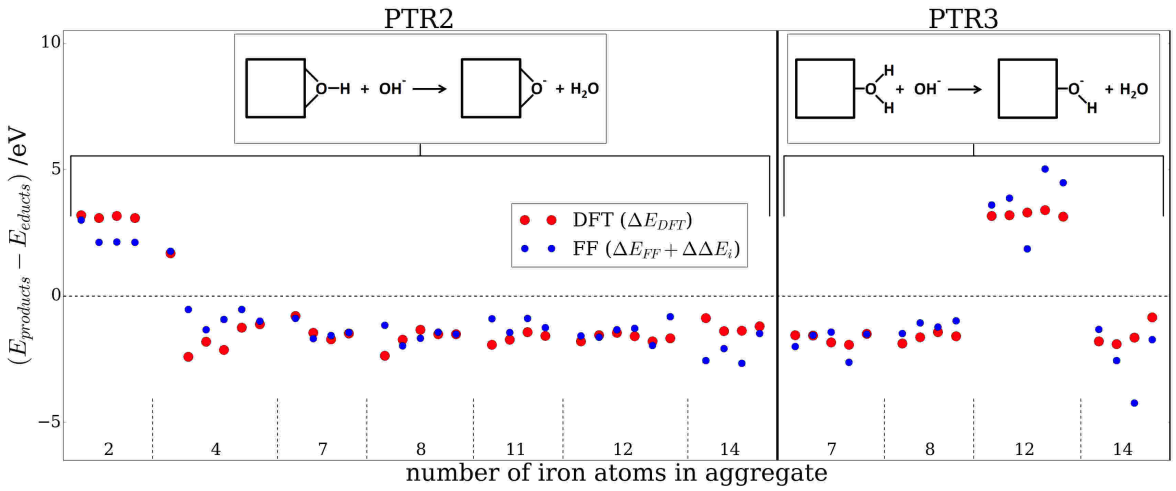

Figure 5.7: DFT and FF based energies for different proton transfer reactions of iron oxyhydroxide aggregates with different size, obtained in crystal growth simulations without any proton transfer.

able to reproduce all these DFT based results.

Based on the obtained knowledge, an additional fourth step is implemented in the iterative scheme (see Fig. 5.8 IV.). Here, the obtained aggregate of the relaxation process in step III is extracted from the system, and the energies of all possible PTRs are calculated. The energy correction term is added, and for all cases in which the jump of the proton leads to an energetically more stable aggregate, means an exothermic reaction, the resulting aggregate is used as new educt for the subsequent calculations of possible PTR. I have to remark that all possible PTRs are checked, independently of the distance between donor and acceptor. This relies on the assumption that protons can be transferred over large distances over the hydrogen bond network of liquid water, via a Grotthus-mechanism. The obtained most stable aggregate is at the end placed back into the system, followed by a short relaxation of the surrounding water to react to changes in spatial dimensions, which may occur due to the PTR. After that, the iterative process starts from the beginning.

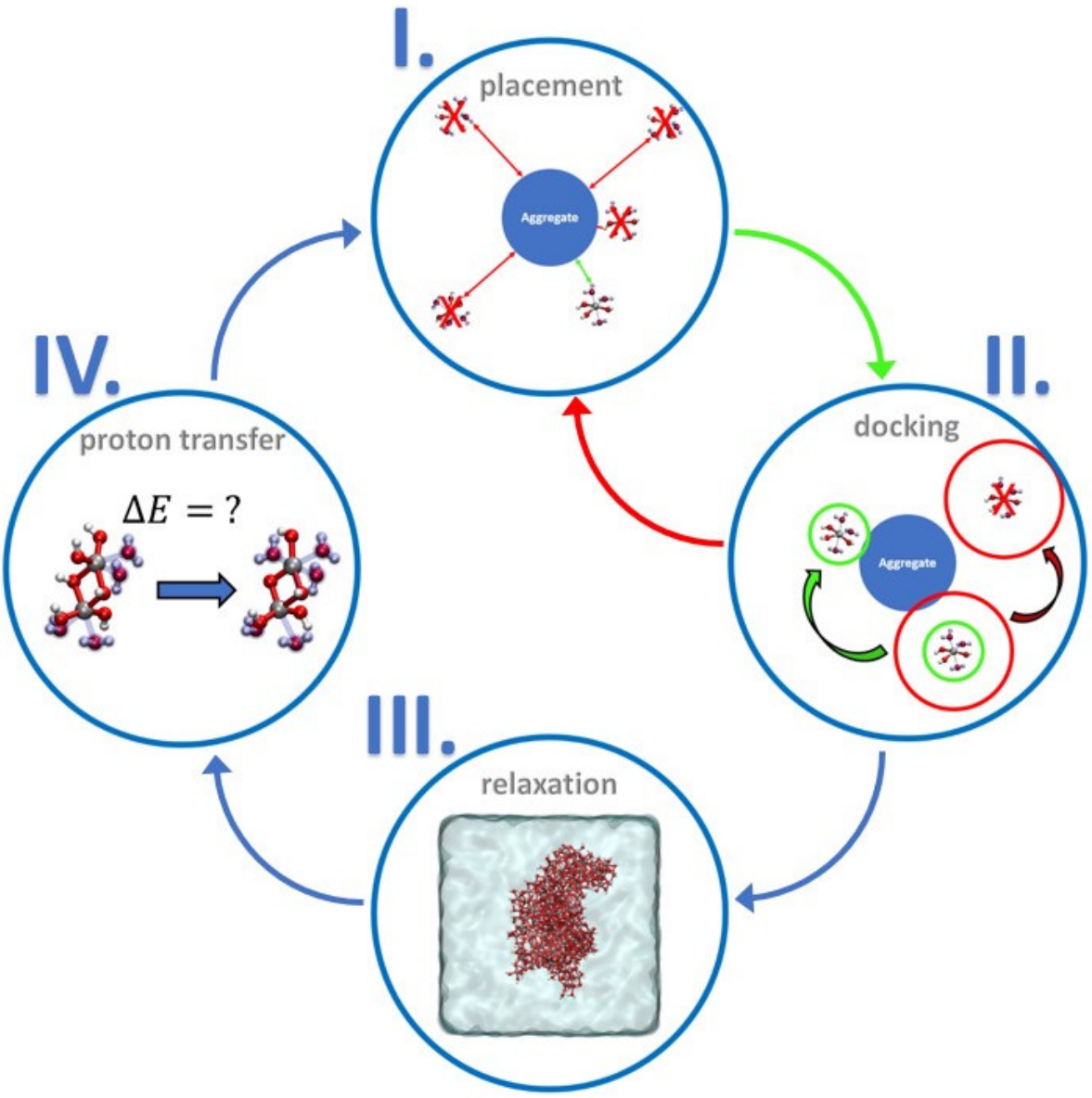

Figure 5.8: Extended iterative scheme for simulation the crystal growth of iron oxyhydroxide based on the Kawska-Zahn-approach [60]. I. Placement of the complex randomly in the box is only succesful if the distance between complex and existing aggregate is in a defined range. II. A docking simulation is performed by checking the distance between complex and aggregate in every step and succeeds if the complex attaches to the aggregate. If the complex moves away from the aggregate, the complex is removed from the system and step I. is repeated. III. Relaxation of the system. IV. The aggregate is checked for possible exothermic proton transfer reactions.

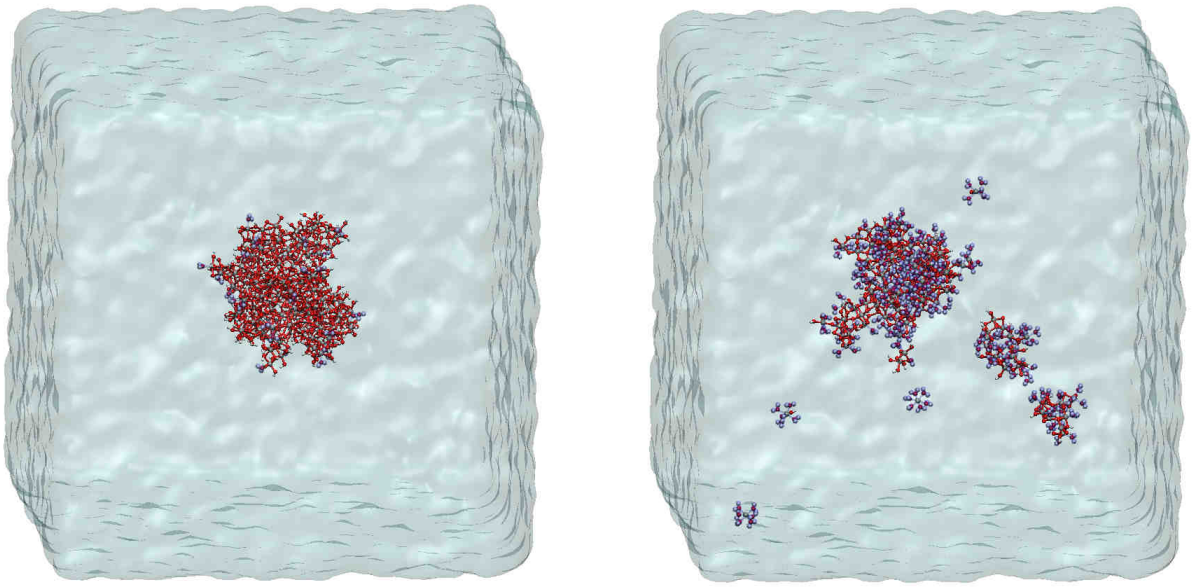

Figure 5.9: One representative result for the single aggregate obtained in systems of PTR1 on the left-hand side, and one representative result for several aggregates which are obtained in systems of PTR2 and PTR3 on the right-hand side. TIP3P water molecules which are directly attached to iron atoms are highlighted by blue spheres.

5.4 Growth of $FeO_x(OH)_y$ in water

To simulate the growth of $FeO_x(OH)_y$ structures from the $Fe(OH)_3$ complexes which are added in every step, the PTR as described in the previous section are included in the iterative process as shown in Fig. 5.8. For that, two different systems are investigated, where in the first one PTRs of type PTR1, and in the second one PTRs of types PTR2 and PTR3 are considered. For both systems, five indepentent simulations are performed.

In every system which include PTR1, only one single aggregate is obtained. In contrast, systems which include PTR2 and PTR3 contain several aggregates, and, in some cases, single iron atoms only stabilized by six TIP3P water molecules. An example of the system of PTR1 is shown on the left-hand side in Fig. 5.9, and of PTR2 and PTR3 on the right hand side in the same figure. Since these single iron atoms and the other aggregates are initially attached to the "main" aggregate, they have to detach during the relaxation. This means, the charged complex which is used to compensate arising charges during the simulation, e.g. $[Fe(OH)(OH_2)_5]^{2+}$, is not as stably attached as the "normal" $Fe(OH)_3(OH_2)_3$ complex. Based on the knowledge obtained in section 5.2, in which the OH groups are found to build the connection between the complexes (see Fig. 5.3),

Table 5.3: Listed are the number of exothermic proton transfer reactions, in the different simulations of systems considering PTR1 and PTR2/PTR3, as well as the observed minimum energy of all exothermic proton transfer reactions in the respective simulation.

system	run	exothermic PTR	min energy / eV
PTR1	1	4	-0.252
	2	1	-0.920
	3	0	0
	4	0	0
	5	3	-0.665
PTR2/PTR3	1	564	-3.329
	2	456	-3.477
	3	530	-3.130
	4	632	-3.501
	5	762	-3.498

the missing OH groups cannot stabilize the resulting aggregates. Therefore, aggregates of systems which includes PTR1 are probably more stable than aggregates obtained in systems with PTR2 and PTR3, due to the higher amount of OH groups.

During the simulations, a huge difference in the number of perfomed PTR between both systems could be observed, as shown in Table 5.3. This behaviour can be explained by the mainly endothermic behaviour of PTR1 and mainly exothermic behaviour of PTR2 and PTR3, as already seen in Fig. 5.7 and 5.6.

The upper aggregate in Fig. 5.10 is one example of the aggregate obtained in the system containing PTR1. The aggregate at the bottom is a resulting aggregate of the system containing PTR2 and PTR3, where here only the biggest aggregate of the system is shown. All other obtained structures are shown in the Appendix in section A1.7. In both cases, 200 iron atoms are added to the system during the iterative process. On the left-hand side of Fig. 5.10 the aggregate is shown and the to Fe iron atom attached TIP3P water molecules are highlighted by blue spheres. On the right-hand side, the TIP3P water molecules which are directly bound to Fe are visualized by transparent blue clouds. It is seen that the aggregate of the system based on PTR1 look like compact particles, while the aggregate based on PTR2 and PTR3 appear more like a scaffold stabilized by water. Here, in case of PTR2 and PTR3 the huge amount of bound water and the scaffold around can be seen, while in the system with PTR1 only a few water molecules are attached on the surface of the aggregate to coordinate the undercoordinated iron atoms.

Despite these quite obvious differences, a detailed structure analysis is missing so far,

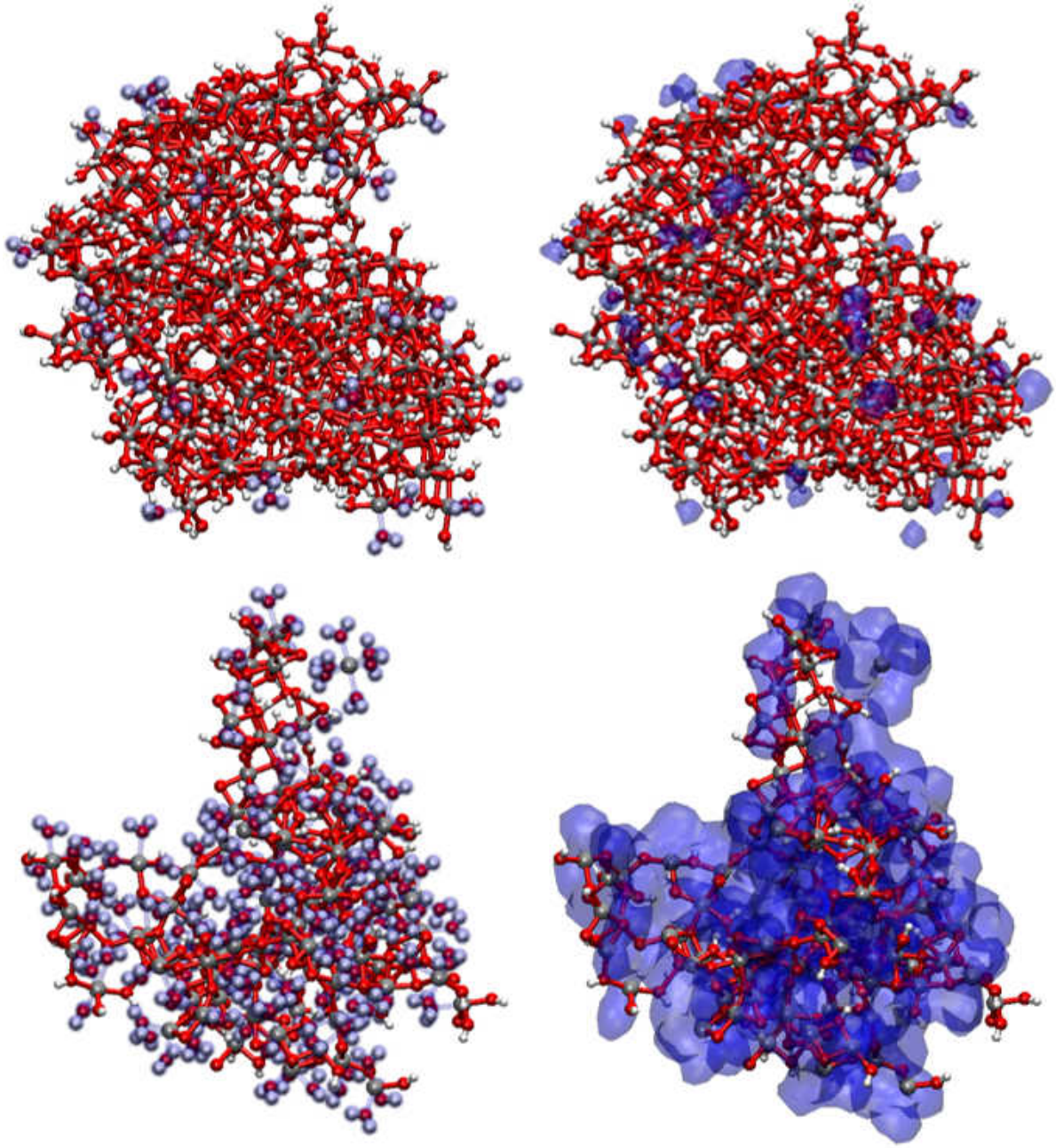

Figure 5.10: The upper aggregate is one example of the system which includes PTR1, while the aggregate on the bottom is one results of the system containing PTR2 and PTR3. On the left-hand side the directly attached TIP3P water molecules are highlighted by a blue sphere and on the right-hand side by transparent blue clouds.

and to determine the crystal structure by visual inspection is, in this case, impossible. Therefore, a robust strategy is necessary to distinguish between the different iron oxyhydroxide structures, and a promising new way is introduced in the following section.

5.5 Structure determination

Standard methods to differentiate between the different crystal phases such as radial distribution function (see section 3.1.1), coordination number [126] or motif recognition [127] are hardly applicable for iron oxyhydroxides structures with highly similar coordination of the iron atoms. A suitable way to overcome this problem, is the inclusion of the second shell of neighbours in the structure recognition. A promising way was introduced by Lechner et. al [248], and based on a modified version of the local bond order parameters as described in the following section.

5.5.1 Steinhardt bond order parameter

The classical bond order parameters, also known as Steinhardt order parameters, are independent of the specific crystal structure and do not require the definition of a reference frame. The algorithm to calculate the parameters based on spherical harmonics [249], where the complex vector $q_{lm}(i)$ of particle i is defined as [250]:

$$q_{lm}(i) = \frac{1}{N_b(i)} \sum_{j=1}^{N_b(i)} Y_{lm}(\vec{r}_{ij}) \tag{5.9}$$

Here, the function $Y_{lm}()$ are the spherical harmonics based on the vector $\vec{r}_{ij}$ from particle i to particle j, with the free integer parameter l and the integer m which runs from $m = -l$ to $m = +l$. The values are summed over all nearest neighbours and then divided by the total number of nearest neighbours $N_b(i)$ of particle i. The averaged form of this vector includes also the second shell of surrounding atoms by the vector $\bar{q}_{lm}(i)$ [248]:

$$\bar{q}_{lm}(i) = \frac{1}{\tilde{N}_b(i)} \sum_{k=0}^{\tilde{N}_b(i)} q_{lm}(k) \tag{5.10}$$

Table 5.4: Different crystal structures of the Fe(III)O_x(OH)$_y$ and Fe_2(III)O_3 phases which are used as references.

Name	structure	space group	structure taken from
Akageneite	$\beta - FeO(OH)$	I 1 2/m 1	[254]
Bernalite	$Fe(OH)_3$	I m m m	[255]
Feroxyhyte	δ-FeO(OH)	P -3 m 1	[256]
Ferrihydrite	$Fe_{10}O_{16}H_2$	$P6_3mc$	[95]
Goethite	α-FeO(OH)	P n m a	[257]
Hematite	α-Fe_2O_3	R -3 c :H	[258]
Lepidocrocite	γ-FeO(OH)	B b m m	[259]
Maghemite	γ-Fe_2O_3	P 41 3 2	[260]

which is the sum of all neighbours $\tilde{N}_b(i)$ of particle i and the particle i itself. Thus, the local orientational vectors $q_{lm}(i)$ are averaged over particle i and its surroundings to calculate $\bar{q}_{lm}$ This vector is not able to discriminate between different crystal structures, thus local bond order parameters, or Steinhardt order parameters are needed. [250] The averaged form of this local bond order parameters is defined as:

$$\bar{q}_l(i) = \sqrt{\frac{4\pi}{2l+1} \sum_{m=-1}^{l} |\bar{q}_{lm}(i)|^2} \tag{5.11}$$

The parameters $\bar{q}_4$ and $\bar{q}_6$ are often used in literature to distinguish between cubic and hexagonal structures [251–253]. Therefore, these values are calculated for iron (oxy) (hydroxides) references structures as listed in Table 5.4 and visualised in Fig. 5.11. Most of these compounds can form and transform in aqueous solutions. The $\bar{q}_4$ and $\bar{q}_6$ values are calculated for all iron atoms of these bulk structures in a classical MD simulations in the NVT ensemble at 300 K. Here, only the iron and oxygen atoms are considered and hydrogens are neglected. The results are shown in Fig. 5.12. Here, Hematite owns a clear area, but parts are widely spread. Maghemite, Goethite, Bernalite are overlying each other, whereby Maghemite is the widest spread. Akageneite is the phase with the clearest data points, but parts are covered likewise of Maghemite. Nevertheless, the crystal phases of Ferrihydrite, Lepidocrocite, and Feroxyhyte are clearly separated from all others and could be clearly determined. Despite the combination of the $\bar{q}_4$ and $\bar{q}_6$ values to separate between the crystal phases, other combinations could lead to separations between phases which are overlying in the case of $\bar{q}_4$ and $\bar{q}_6$. Instead of testing all possible combinations

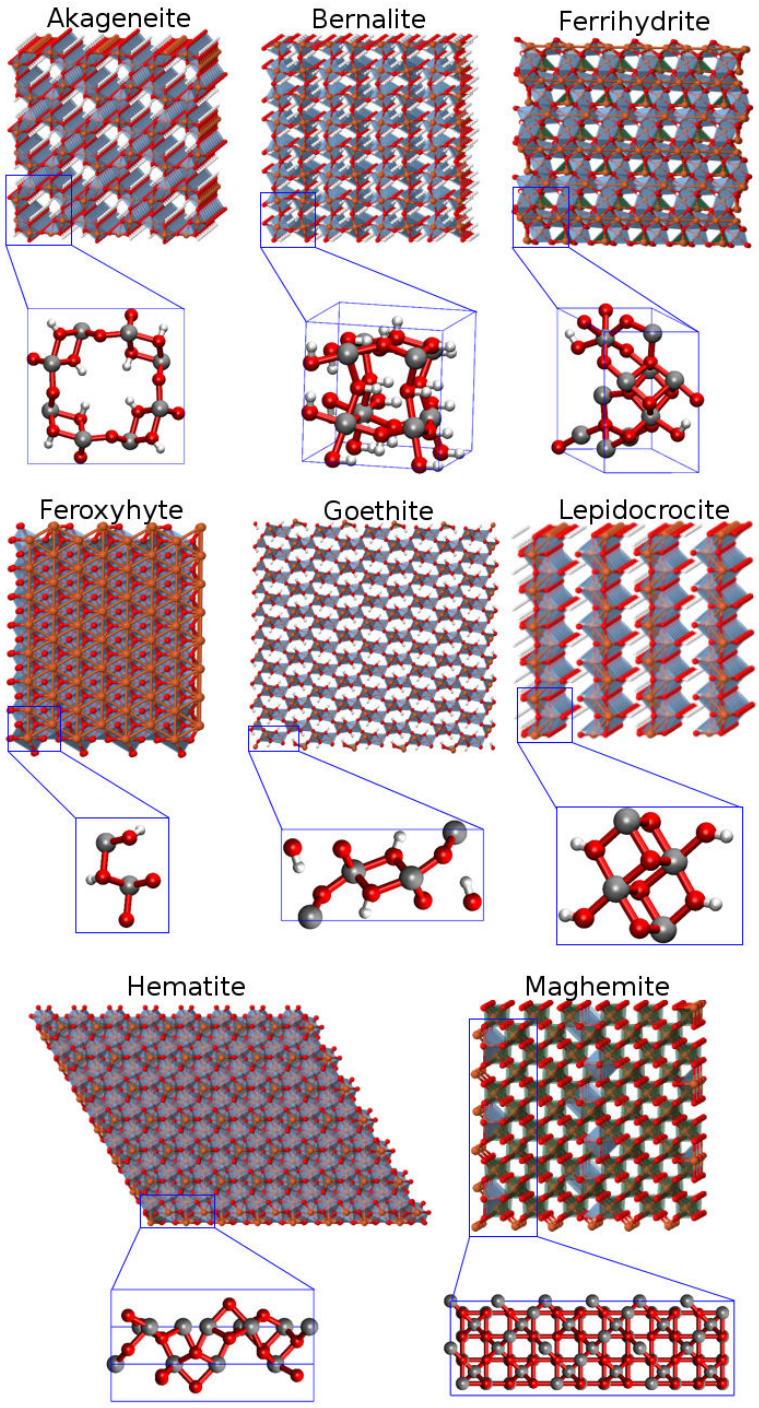

Figure 5.11: Crystal structures and unit cells of $Fe(III)O_x(OH)_y$ and $Fe_2(III)O_3$ phases. Six-fold coordinated iron atoms are highlighted with blue and four times coordinated iron atoms with green polyhedrals.

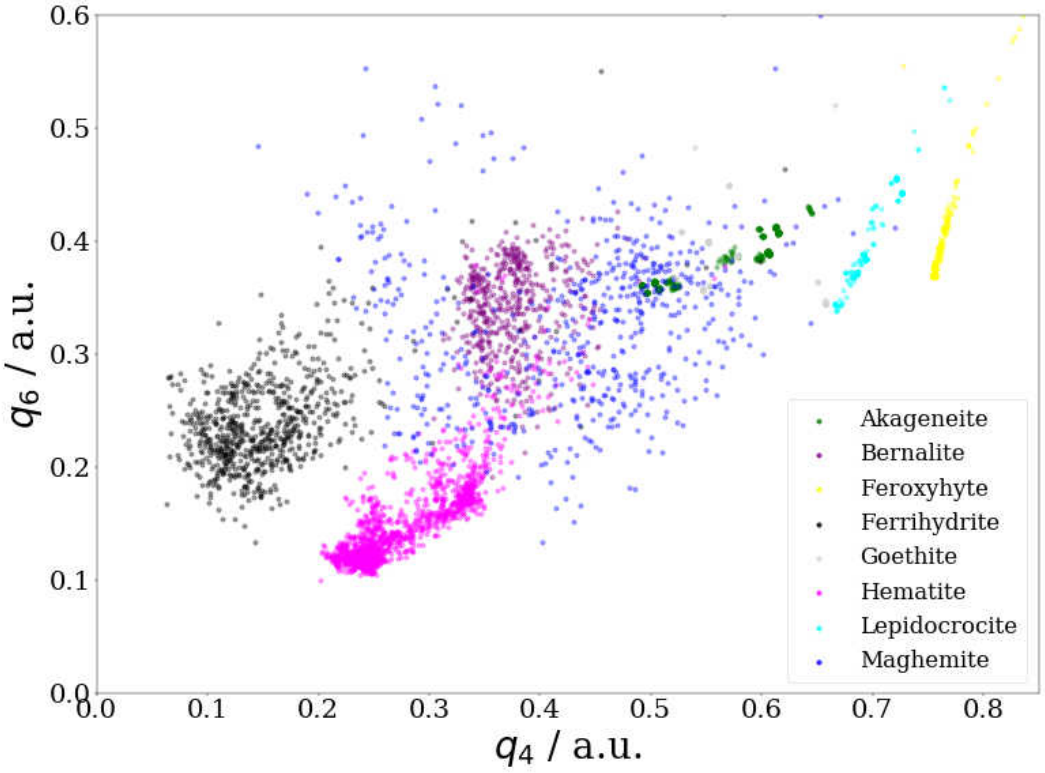

Figure 5.12: $\bar{q}_4$ and $\bar{q}_6$ of all iron (oxy)(hydroxides) references structures as listed in Table 5.4.

and search for the combination, or combination set, which allows to clearly separate between all crystal phases, the whole ten-dimensional parameter set $\bar{q}_3$ to $\bar{q}_{12}$ is used. This allows a more rigorous differentiation of the iron oxyhydroxide structures, obtained in different crystal growth simulations. To handle those ten-dimensional parameter set, a Gaussian Mixture Model is used as introduced in the next section.

5.5.2 Gaussian mixture model

A Gaussian Mixture Model (GMM) is a particularly convenient approach to fit n distributions to a sum of n multivariate Gaussians if the underlying mean μ_i and covariance Σ_i of each distribution are known:

$$\hat{P}(\mathbf{x}) = \sum_{i=1}^{n} p_i G(\mathbf{x}|\mu_i, \widetilde{\Sigma}_i) \tag{5.12}$$

As reference dataset for the GMM, the aforementioned refence structures of the most common iron oxyhydroxide phases are used, as listed in Table. 5.4. The $\bar{q}_3$ to $\bar{q}_{12}$ values are calculated for all iron atoms of these bulk structures in a classical MD simulations in the NVT ensemble at 300 K. Here, the GMM is calculated (trained) for 75 % randomly selected iron oxide atoms from each crystal structure MD trajectory. The associated $\bar{q}_3$ to $\bar{q}_{12}$ values are used to estimate the individual covariance matrix Σ_i and mean position μ_i in the 10-dimensional space spanned by the $\bar{q}_3$ to $\bar{q}_{12}$ descriptors. These calculations are performed together with Prof. Dr.-Ing. Robert Meißner of the Technische Universität Hamburg Harburg. The multivariate Gaussian calculated on each aforementioned crystal structure is then given by

$$G(\mathbf{x}|\mu,\Sigma) = \frac{1}{\sqrt{(2\pi)^D \det\Sigma}} e^{-\frac{1}{2}(x-\mu)^T\Sigma^{-1}(x-\mu)} \tag{5.13}$$

where D is the dimensionality of the descriptor. The probability $\hat{P}_i$ to be assigned to a distinct crystal class i is obtained from

$$\hat{P}_i = \frac{p_i G(x|\mu_i,\widetilde{\Sigma}_i)}{\hat{P}}. \tag{5.14}$$

Since all crystal structures should have the same probability as a classifier, we set the weights p_i in eq. 5.12 to $1/n$.

However, insufficient sampling or highly correlated descriptors can lead to an ill-conditioned covariance matrix Σ and/or eigenvalues that are zero to within machine precision. Thus, we apply a more robust estimator to obtain a less strongly biased covariance matrix $\widetilde{\Sigma}_i$ known as Oracle Approximating Shrinkage (OAS) estimator [261] given by:

$$\widetilde{\mathbf{\Sigma}}_i = (1-\psi_i)\mathbf{\Sigma}_i + \frac{\psi_i \mathrm{Tr}(\mathbf{\Sigma}_i)\mathbf{I}}{D} \tag{5.15}$$

where

$$\psi_i = \min\left[1, \frac{\left(1-\frac{2}{D}\right)\mathrm{Tr}(\mathbf{\Sigma}_i^2) + \mathrm{Tr}^2(\mathbf{\Sigma}_i)}{\left(N_i+1-\frac{2}{D}\right)\mathrm{Tr}(\mathbf{\Sigma}_i^2) - \frac{\mathrm{Tr}^2(\mathbf{\Sigma}_i)}{D}}\right].$$

The remaining 25 % of the data is then used to validate the GMM by assigning each atom to the highest probable classification given by the GMM. The training on crystal structures which have been simulated at 300 K allows a robust and unbiased classification

Table 5.5: Classification accuracy of the GMM using either the full dimensional bond order descriptor or a two-dimensional subset. Training of the GMM was done using 75 % of the data while classification was done on the remaining 25 %

Crystal Phase	Total Samples	q_3-q_{12}	q_4 and q_6
Akaganeite	7197120	94.9 %	89.4 %
Bernalite	5120000	94.5 %	88.0 %
Feroxyhyte	3840000	99.6 %	99.5 %
Ferrihydrite	7200000	95.6 %	96.3 %
Goethite	2800000	97.1 %	27.6 %
Hematite	4032000	95.2 %	95.5 %
Lepidocrocite	3840000	98.7 %	98.5 %
Maghemite	5760000	96.2 %	42.2 %

for unknown iron oxyhydroxide phases at 300 K and yielded an almost perfect agreement with the validation dataset as shown in Table 5.5). Moreover, the GMM has been parameterized as discussed above using the typically in literature used $\bar{q}_4$ and $\bar{q}_6$ values. Here, the differentiation between Feroxyhyte, Ferrihydrite, Hematite and Lepidocrocite is as good as in the ten dimensional descriptor. Huge problems occur in case of the determination of Goethite and Maghemite and the parameter set is in general not as good as the ten-dimensional descriptor. In Fig. 5.13 the two-dimensional GMM for $\bar{q}_4$ and $\bar{q}_6$ is shown. Clearly seen is the strong overlap between Akaganeite, Goethite, Bernalite and Maghemite. This overlap impacts negatively the classification accuracy as shown in Table 5.5.

To validate the accuracy of our approach, the GMM is compared to the GMMs of the Scikit-learn package [262]. Those GMMs have been calculated and tested using full and tied covariances on the same training and test data and the mean position of each crystal structure and the total number of classes have been used as initial parameters. An averaged accuracy of 78.2 % and 87.9 % was achieved with this approach, respectively. This demonstrates the superior quality of predictions using our approach over traditional Expectation-Maximization (EM) algorithms.

Before using the GMM to identify the crystal structures of the grown aggregates, the association of atoms which are in an amorphous structure should be taken into account. For that, models of amorphous FeO(OH) bulk structures are created via the same simulated annealing strategy following the scheme of Chagarov et al. [176] as described in

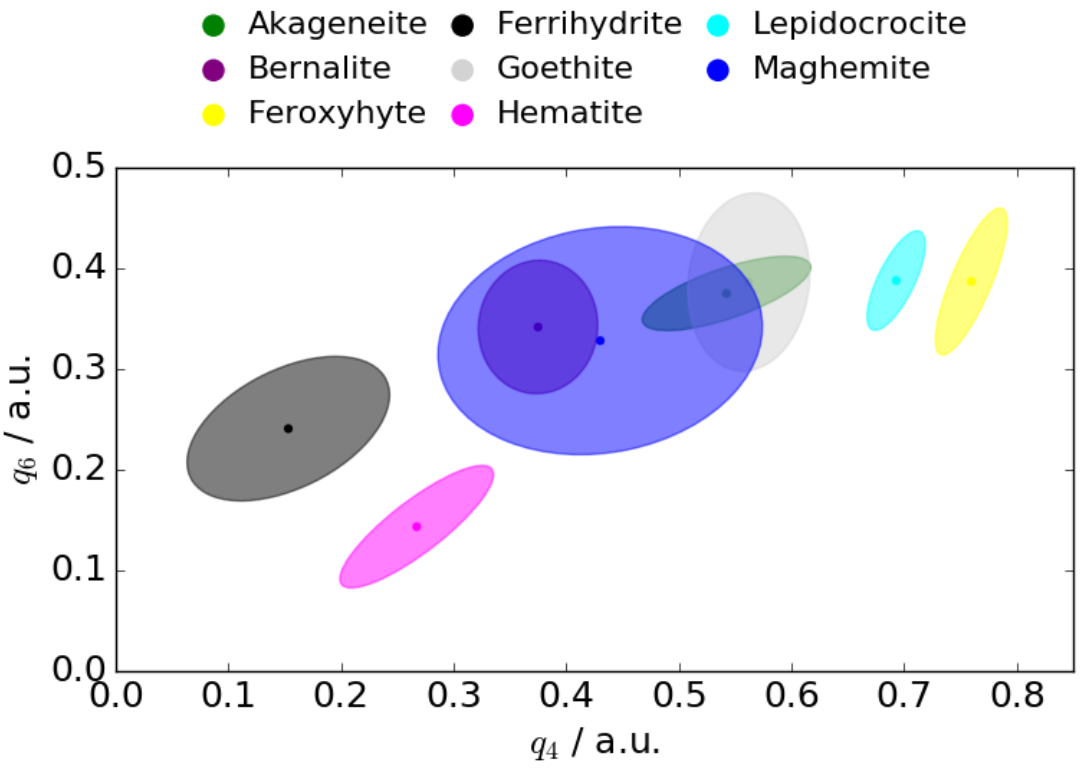

Figure 5.13: Two-dimensional GMM using only $\bar{q}_4$ and $\bar{q}_6$ as descriptors for all $Fe(III)O_x(OH)_y$ and $Fe_2(III)O_3$ reference structures.

detail in section 3.1 to create amorphous models of alumina. 1000 random systems are created containing FeO(OH) with 100 iron atoms and every system is annealed at 5000 K for 500 ps at constant volume with a density of 5 g/cm^3. The density is then gradually decreased to a density of 2.18 g/cm^3 [263] in 100 ps followed by a further 100 ps equilibration. Finally, the system is cooled down to 300 K in 100 ps and further equilibrated for 1 ns. The $\bar{q}_3$ to $\bar{q}_{12}$ values for the last 100 snapshots of each MD trajectory are calculated and included in the training dataset of a new GMM.

To visualize the high dimensional parameter set, the dimensionality reduction "Sketch-map algorithm", as explained in detail in ref. [264], is used. This algorithm reproduces the connectivity between a set of high dimensionality data points in the space of lower dimensionality, by transforming the distances between the points in the low and high-dimensionality space by a sigmoid function. Therefore, data points which are close together in high dimensional space lie close together in the low-dimensionality space,

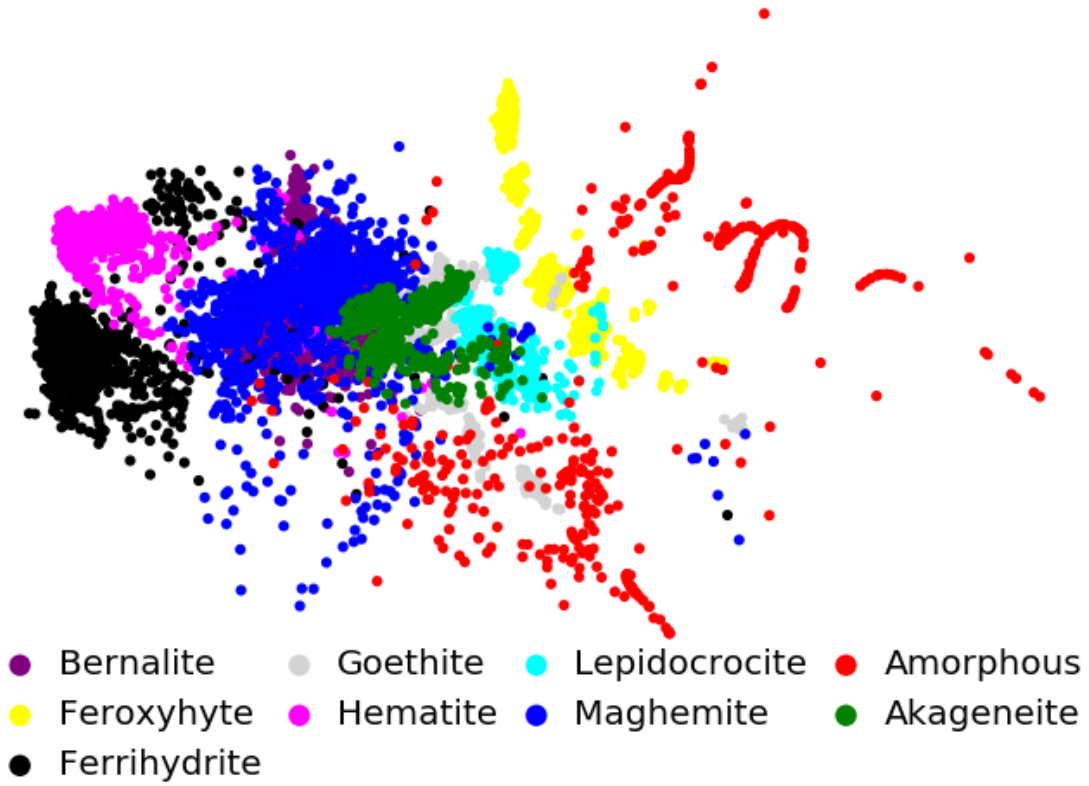

Figure 5.14: Two-dimensional projection of the high-dimensional descriptor of all $\bar{q}_3$ to $\bar{q}_{12}$ values as descriptors for the Fe(III)O_x(OH)$_y$, Fe_2(III)O_3 and amorphous reference structures.

and data points that are far apart. The Sketchmap algorithm is used to create a two-dimensional projection of all references and the amorphous structures and is shown in Fig. 5.14. It can be seen that the amorphous phases are widely spread, but mainly separated from the crystal phases, enabling the differentiation between crystal and amorphous structures.

All the previous investigations and results reveal the quality of the method to differentiate between different crystal phases. Therefore, the GMM is now used to identify the crystal structures of the aggregates obtained in the previous crystal growth simulation (see section 5.4). Table 5.6 contains the average occurence of each species in the five different simulations containing respectively PTR1 or PTR2 and PTR3. It is clearly shown that the systems considering PTR1 mainly consist of Maghemite (around 93%) with a small amount of amorphous parts (around 5%). The same trend is generally shown in the case of systems considering PTR2/TPR3. Nevertheless, the amorphous part is much higher

Table 5.6: Average percentage occurence of each species in the different simulations containing PTR1 or PTR2 and PTR3.

Name	PTR1 / %	PTR2/PTR3 / %
Akageneite	0.11	0.12
Amorphous	4.53	36.35
Bernalite	1.68	0.84
Feroxyhyte	0.10	0.72
Ferrihydrite	0.00	0.00
Goethite	0.94	0.72
Hematite	0.06	0.0
Lepidocrocite	0.02	0.15
Maghemite	92.56	61.10

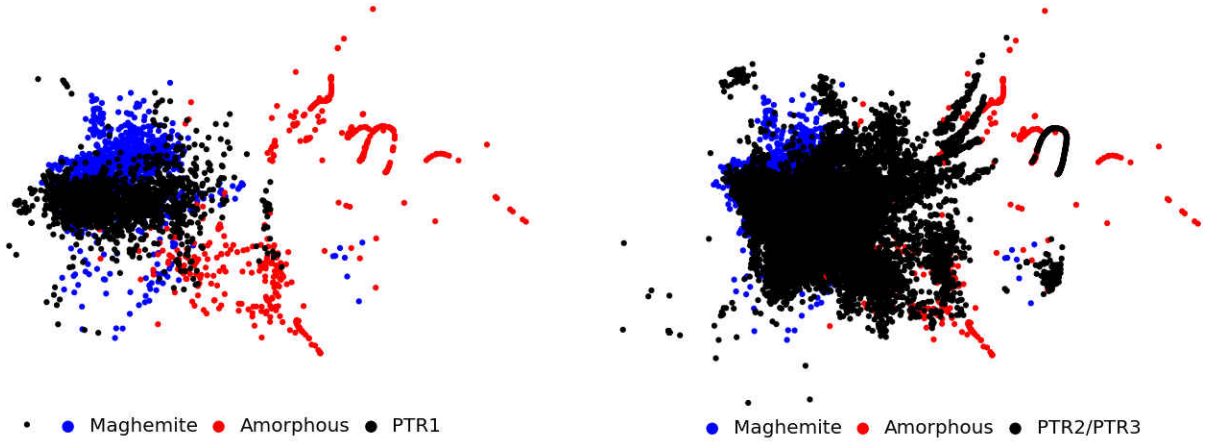

Figure 5.15: Zoom into the two-dimensional projection of the high-dimensional descriptor of amorphous FeO(OH) and Maghemite as shown in Fig. 5.14. The data points of the grown structures in water of the systems considering PTR1 (left-hand side) and PTR2/PTR3 (right-hand side) are shown in black.

(34%). Due to the fact that amorphous FeO(OH) and Maghemite are the main parts of the grown structures, Fig. 5.15 contains a zoom into the previous shown Sketchmap, where only the reference data points of Maghemite and the amorphous structures are shown. The data points of the grown aggregates in water of the systems considering PTR1 and PTR2/PTR3 are added in black. In case of PTR1 (left-hand side) the main part is locally connected in a region above the data points of Maghemite and only single points can be found in the region of the amorphous structure. The data points of the system considering PTR2/PTR3 are much more spread and cover almost the whole region of Maghemite and the amorphous structures.

To visualize the obtained crystal structure determination, Fig. 5.16 contains on the left-hand side the aggregate as shown in Fig 5.10 and on the right-hand side the iron atoms colored by their respective color code. The amorphous parts are mainly found on the surface of the aggregates. In case of PTR2/PTR3, amorphous parts can be found also at the inner side, whereby here TIP3P water molecules form an interface between parts of the crystal. Moreover, parts of Bernalite and other structures are mainly found on the surface of the aggregates, as shown here and in the Appendix A1.7. This leads to the assumption that the attached TIP3P water molecules force the iron atoms on the surface in mainly amorphous or any other structure, where some structures are slightly more probable then others. Therefore, the classical force field tends to create aggregates of Maghemite, and missing neighbors leads obviously to structural rearrangements mainly ending in structures which are amorphous.

Based on the previously obtained knowledge and the ability to differentiate between different iron oxyhydroxide crystal phases, the nucleation behavior and the Fn supported nucleation and growth of $FeO_x(OH)_y$ is investigated in the next section.

5.6 Nucleation and growth of $FeO_x(OH)_y$ on Ferritin

To investigate possible influences of the ferritin protein to the crystal structure of the grown iron oxyhydroxes in comparison to water, first crystal growth simulations supported by Fn subunits are performed in this section. Five independent simulations of the growth on two subunits arrangements of the heavy and the light subunits respectively are performed. In case of the L subunit simulations are performed where 200 iron atoms are added to the system, while in case of H subunits between 50 and 150 iron atoms are added to the system.

Based on the obtained results for the formation in water, we only consider proton transfer reactions of type PTR1 to reduce the amount of the amorphous phase. For the calculation of the energy differences of the educt and product state in the PTR, the atoms of the Fn subunits are fixed during the relaxation process. Additionally, the distances between the new complex and existing aggregates are checked after docking step. The relaxation step and the subsequent check for PTR are only performed if the complex is attached directly or close to an existing aggregate. If the complex is only attached to the Fn subunits, these steps are skipped since no PTRs are expected.

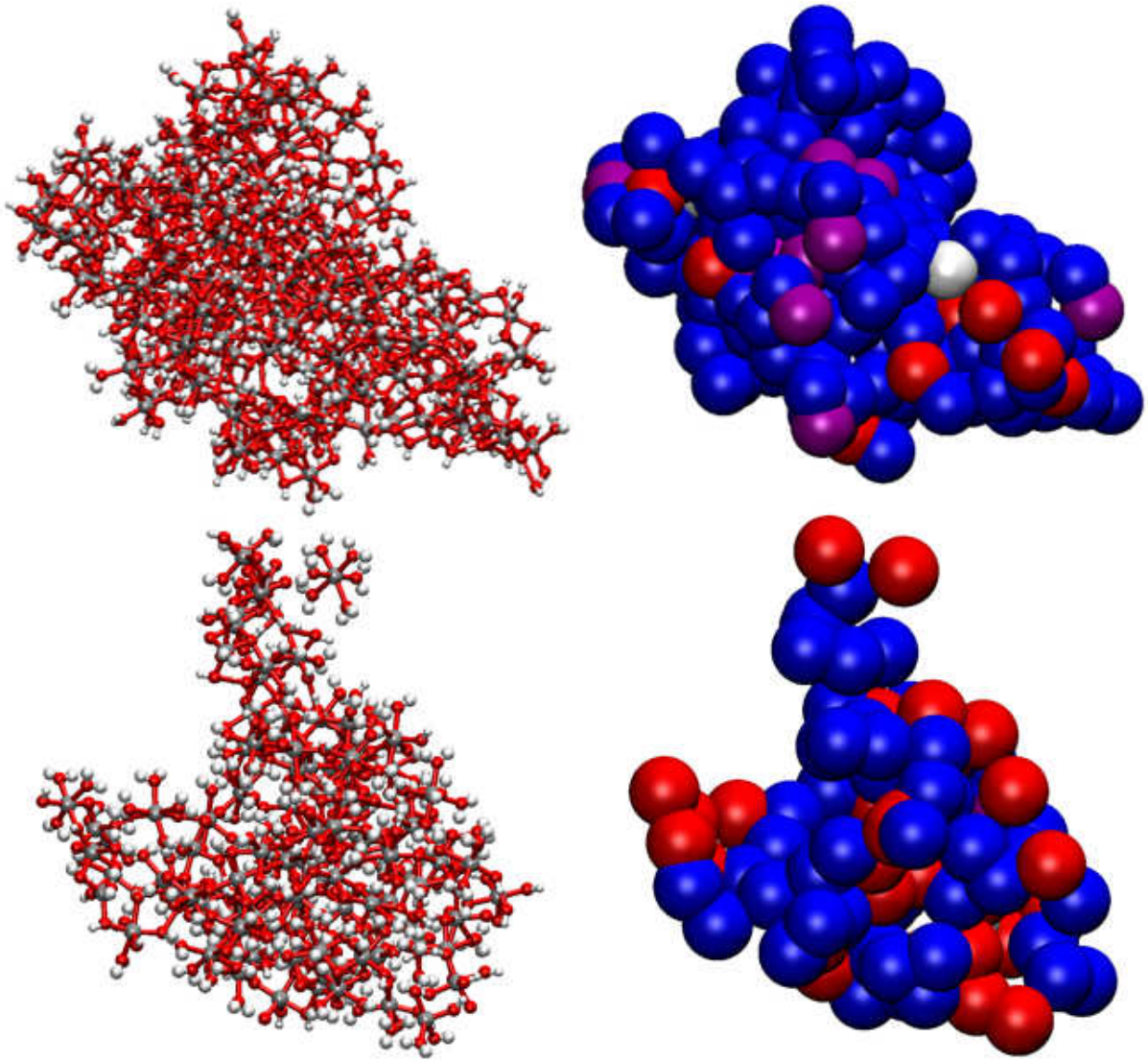

Figure 5.16: On the left-hand side the aggregate as grown based on the in the simulation of PTR1 (upper one) and PTR2/PTR3 (lower one). On the right-hand side all iron atoms are colored corresponding to their identified crystal structure (blue - Maghemite, red - amorphous, purple - Bernalite, white - Goethite).

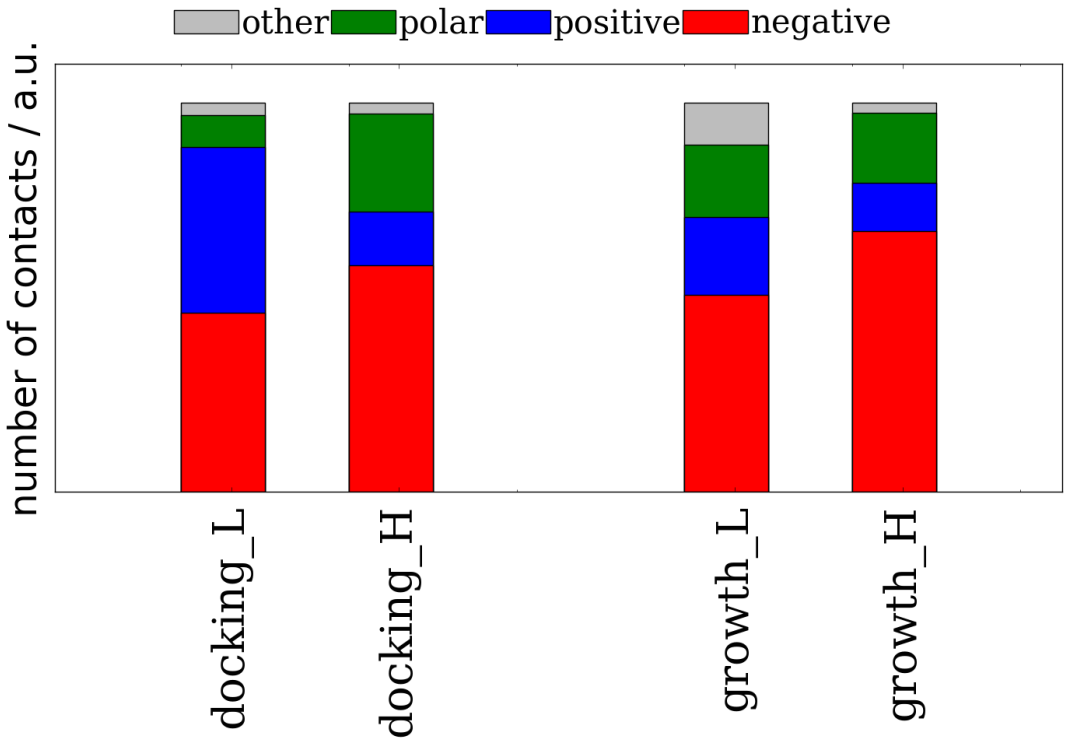

Figure 5.17: On the left hand side the normalized results of the predefined particle as shown in Fig. 4.13 d for the L and H subunit arrangements are shown. The right-hand side shows the averaged and normalized percentage occurrence of polar, positively and negatively charged and all other amino acids as anchor points for aggregates grown in the five different systems containing H and L subunits respectively.

At first, the anchoring points of the grown aggregates at the different subunits are investigated and compared to the results obtained in chapter 4. The percentage occurrence of polar, positively and negatively charged amino acids are ascertained and the results for each system is shown in the Appendix in Fig. A15. The average of all results for the systems containing the L and H subunits are shown on the right-hand side in Fig. 5.17. The values are normalized to compare the systems which contain different numbers of attached aggregates, and atoms within. For comparison, the results are compared with these shown in Fig. 4.13 d, which are reported on the left-hand side in Fig. 5.17. These results contain the sum of all interactions between the predefined particle and the Fn subunit arrangements at the inner and outer side of the subunit, with respect to the whole Fn cage, and are chosen since the grown aggregates are found on all sides of the subunits. The percentage occurrence of negatively charged amino acids are quite similar in case

Table 5.7: Average percentage occurrence of each species in the different simulations of growth on the L and H subunit.

Name	water / %	L subunit/ %	H subunit/ %
Akageneite	0.11	0.54	0.65
Amorphous	4.53	14.96	33.11
Bernalite	1.68	3.27	2.10
Feroxyhyte	0.10	0.4	2.79
Ferrihydrite	0.00	0.02	0.00
Goethite	0.94	1.16	3.05
Hematite	0.06	0.02	0.0
Lepidocrocite	0.02	0.14	1.25
Maghemite	92.56	79.44	57.03

of predefined particles and grown aggregates. In particular, the occurrence of positively charged amino acids as anchor points is higher in the case of L subunits than in the case of H subunits, although the difference is bigger in the case of the predefined particles. Nevertheless, in contrast to the docking of the predefined particles, the attachment on the sides of the subunits is generally possible and observed in the simulations. Due to the slightly varying results of the total amount of different kinds of amino acids as anchor points, observed for different phases and sizes of predefined particles, this overall agreement is acceptable.

To investigate the grown structures, the GMM model is used to identify the respective crystal structure and the average percentage occurrence of each species in the different simulations is shown in Table 5.7. It can be seen that the occurrence of crystal structures follows in general the results obtained in water. Nevertheless, since the aggregate which is grown in water (aggregates which consist each of 200 iron atoms) is bigger then the aggregates grown on the L subunit (200 iron atoms in several aggregates) and on the H subunit (between 50 and 150 iron atoms in several aggregates) it seems that the amorphous part corresponds to the size of the system. This fits perfectly with the previously obtained results that amorphous parts are mainly found on the surface of the aggregates. To proof and visualize this assumption, the percentage occurrence of the different phases for differently sized aggregates, as observed in the different simulations on the L subunit, is shown in Fig. 5.18. It can be seen that the structure of a single complex, only surrounded by oxygen atoms (hydrogens are not considered in the GMM), are mainly amorphous and the structure is only in rare cases assigned to a reference crystal structure in the

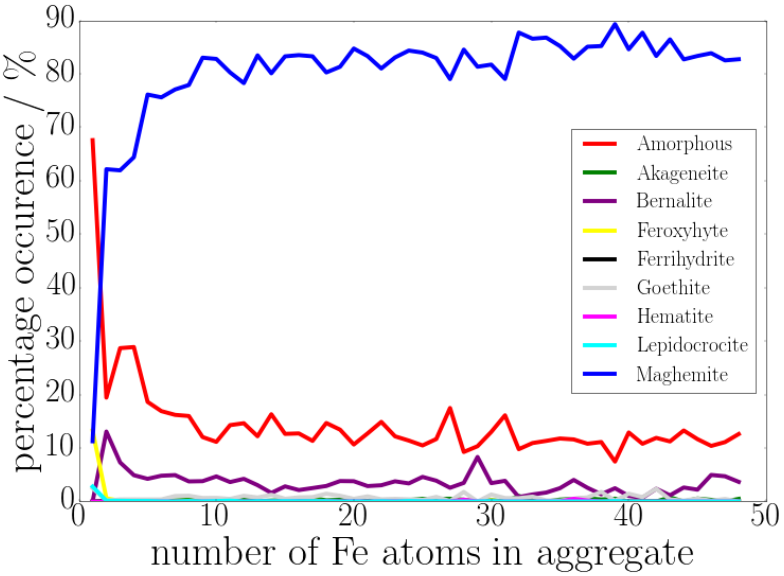

Figure 5.18: Percentage occurrence of the different crystal structures over the size of the aggregates as observed in the simulations of growth on the L subunit.

GMM. Moreover, up to a size of three iron atoms in the aggregate other phases such as Feroxyhyte, Lepidocrocite are visible and only Bernalite is obtained in small amounts over all aggregate sizes. As a general trend, an increasing amount of Maghemite and a decreasing amount of amorphous parts is observed.

Examples of the grown structures are shown in Fig. 5.19. The upper side contains the system of L subunits and the lower part contains the system with H subunits. On the left-hand side the system without water is shown and on the right-hand side the same snapshot is shown, where all iron atoms are colored corresponding to their identified crystal structure. Here, it can be easily seen that, as in case of growth in water, the mainly occurring structure is Maghemite (blue), where atoms at the surface and atoms of small aggregates include amorphous parts (red) and structures of other phases. Therefore, it can be concluded that the obtained structures mainly based on the used force field, and are independent of the presence of the protein as a scaffold.

However, a difference between the simulation of crystal growth in water and on the Fn subunits is observed in case of the number of performed PTR. Table 5.8 contains the number of exothermic proton transfer reactions in the different simulations, as well as the obtained minimum energy of proton transfer reactions in the respective run. The number

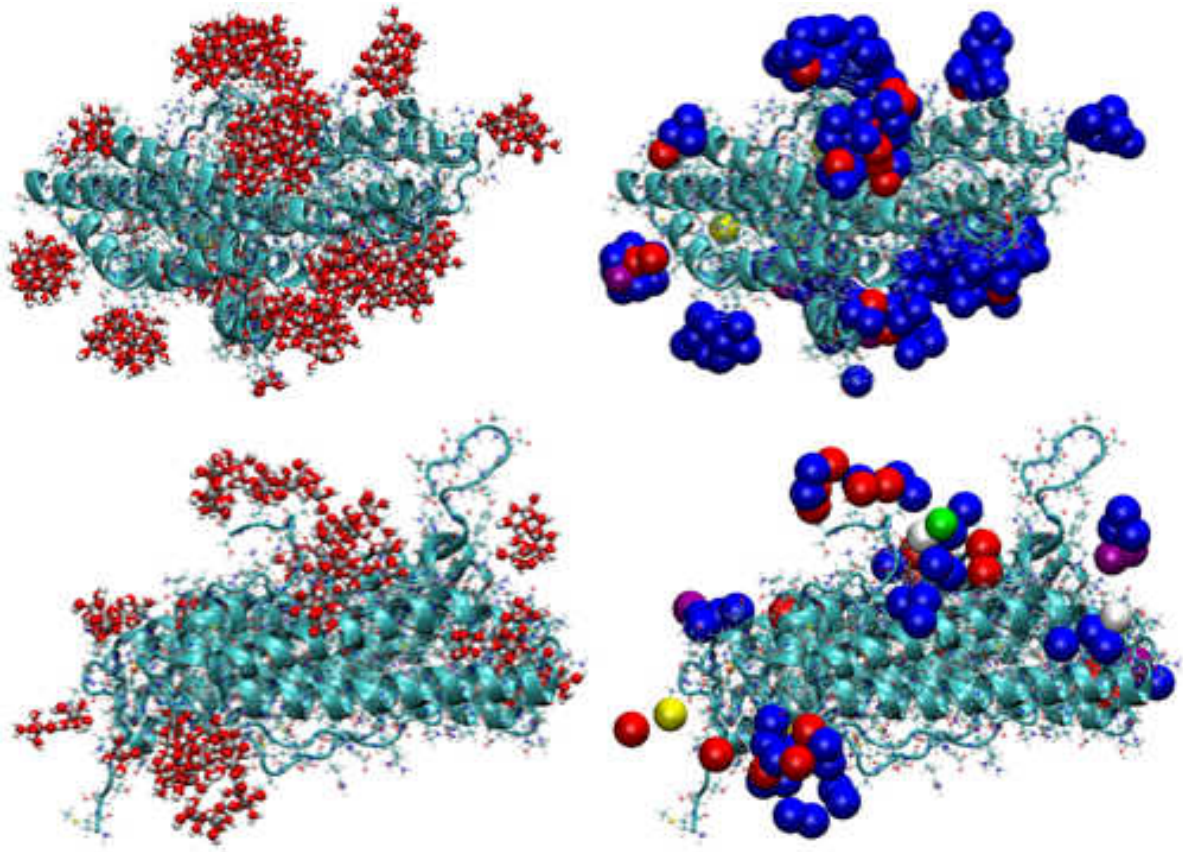

Figure 5.19: On the upper side the system with L subunits are shown and the lower part contain the system with H subunits. On the left-hand side the system without water is shown and on the right-hand side all iron atoms are colored corresponding to their identified crystal structure (blue - Maghemite, red - amorphous, magenta - Hematite, yellow - Feroxyhyte, green - Akageneite, white - Goethite).

Table 5.8: Listed are the number of exothermic proton transfer reactions in the different runs of the growth of iron oxyhydroxide in water, and in water on two H or L subunits of the ferritin protein, as well as the obtained minimum energy of proton transfer reactions (PTR1) in the respective simulation.

system	run	exothermic PTR	min energy
water	1	4	-0.252
	2	1	-0.920
	3	0	0
	4	0	0
	5	3	-0.665
L subunit	1	13	-0.527
	2	14	-1.362
	3	12	-1.409
	4	15	-1.101
	5	31	-1.736
H subunit	1	8	-1.000
	2	12	-0.735
	3	6	-1.076
	4	15	-0.523
	5	13	-0.496

of PTRs is much higher on the H/L subunits than in water. Additionally, the maximum observed energy differences between educt and product system is generally higher than in water. Moreover, the PTRs occur in case of the subunits on much smaller aggregates, since the biggest observed aggregates in case of H and L subunits consists of around 50 iron atoms. In case of the aggregates in water, the first PTR is observed in an aggregate which consists of 116 iron atoms and all other PTRs occur on aggregates with sizes between 172 and 200 iron atoms. In conclusion, the Fn subunits, which acts as fixed scaffolds in the relaxation of the aggregates to compare the energies of the educts and product structures of PTR, leads much more often to an energetically favourable product state than in the case of dissolved aggregates.

Chapter 6

Conclusion and Perspective

6.1 Conclusion

In this thesis, several simulation methods ranging from Density Functional Theory to classical force field based calculations have been used. Thereby, the immobilization of Fn, as well as the process of nucleation and the early stages of ferritin-promoted crystal growth of iron oxyhydroxide at the atomic level have been investigated. The obtained knowledge contributes to a knowledge-based fabrication protocol, where several experimental protocols could already be improved.

Strategies to create realistic structural models and classical force field parameter sets have been shown. Classical and advanced molecular dynamic simulations, based on these models and force fields, were able to predict experimental observables such as the heat of immersion or the adsorption free energies of peptides. Moreover, by adding an ascertained energy shift, the classical force field is able to reproduce energy differences between educts and products of proton transfer reactions.

It has been shown that energy profiles based on DLVO theory of Fn in different orientations above oxide surfaces are a suitable way to identify the protein's preferred adsorption orientation. The surface charge as a function of the pH value is a very important factor since the negative or positive surface charge at different pH values can lead to energetically favorable and unfavorable orientations above the surface. In case of Fn, preferred orientations above silica are found, in which the outer side of the subunits, with respect to the whole cage, faces towards the surface. Instead, in the case of alumina, no preferred orientations are found since the interactions at pH 3 and pH 8 are only repulsive

or attractive. Moreover, the binding forces observed in this simulations are able to predict the possibility to immobilize the protein to the respective surface by physisorption. Here, the necessity to covalently immobilize Ferritin subunits on silica surface is shown and a subsequently changed experimental immobilization protocol led to the successful mineralization of iron oxide.

Possible anchoring sites and their distribution for Fe(III) nuclei in Fn were identified by docking simulations of differently sized iron oxyhydroxide nanoparticles. The results show a much larger availability of anchoring sites at the inner part of the subunits rather than at the outer part (with reference to their assembly in hollow Fn spheres), which is consistent with the evolutionary-driven sequence engineering of the natural protein. Moreover, we have found that positively charged and neutral residues such as arginine and lysine are heavily involved in the anchoring of Fe(III) clusters, making up about 50 % of the total observed contacts for the case of L subunits. The importance of positively charged sites has often been overlooked in the available literature, although consistent with the frequent presence of basic residues in iron oxide binding peptide sequences [123, 124]. Compared to L subunits, H subunits seem to possess a larger number of negatively charged and neutral anchoring sites, which could promote a selectively heterogeneous Fe(III) nucleation after the binding of dissolved Fe^{2+} ions and their initial oxidation to Fe^{3+}. In fact, mineralization experiments including a long activation step, in which H or L subunits are loaded with Fe^{2+} ions before starting the oxidation, have led to the growth of particularly dense and homogeneous mineral films especially for the case of H subunits.

It has been shown that pure classical force field simulations are able to describe the crystal growth of iron oxyhydroxide, as well as included proton transfer reactions. The exclusion of interactions between the solvent and the newly added complex during the docking process is an excellent way to overcome the otherwise necessary long timescales associated with diffusion processes. The performed simulations of iron oxyhydroxide growth in water and on Fn subunits reveal that the resulting crystal structure is probably based on the used classical force field. Especially the surface atoms of the grown aggregates are found to be amorphous in perfect agreement with the crystal growth processes in nature. Thus, the amorphous structure at the surface minimizes the surface energy, since a crystalline surface comprises much higher surface energy.

These results could be revealed by a machine learning based method of phase recognition. The Gaussian Mixture Model of the high-dimensional descriptor, in the form of the

"average local bond order", allows for a rigorous differentiation of the structures obtained in different crystal growth simulations and are therefore a robust way to classify unknown structures.

6.2 Perspective

The consideration of Fe(III)$(OH)_3$ as solitary species in the performed simulations is correct as a start at a pH value of 8. Recent studies have pointed out that a polyphasic model, including ferrihydrite and magnetite (or other iron(II)-containing phases), could describe the nature of the ferritin core more realistically [265]. Therefore, simulations at other pH values which contain Fe(II) could lead to more accurate results, as well as entirely new possibilities in terms of nucleation behavior, reaction kinetics, crystal phases and two and three-dimensional structures. For that, force fields of different Fe^{2+}/Fe^{3+} oxide phases, as well as Fe^{2+}/Fe^{3+}/water interfaces, have to be parameterized. This can be done by following the strategies described in this thesis for other oxides.

An energetical description of the obtained crystal structures is still missing. Thus, the change of energy and therefore stability of the particles over size, as well as the stability in contrast to particles with the same size but different crystal structure is of fundamental interest. The stability of the aggregates over size could be described by the energy ($E_{formation}$) which is obtained by subtracting the chemical potential of every element (μ_i), multiplied with the total number of atoms of this element (N_i), from the total energy of the aggregate ($E_{aggregate}$):

$$\Delta E_{formation} = E_{aggregate} - N_{Fe} \times \mu_{Fe} - N_O \times \mu_O - N_H \times \mu_H \tag{6.1}$$

As a first test, spherical aggregates with different radii are extracted from the respective bulk structures. Iron atoms which are less than five-fold coordinated are removed as artifacts from the slicing process, as well as oxygen and hydrogen atoms which are under-coordinated. The atomic positions of the aggregates are relaxed to obtain the total energy of the aggregate. The energy of formation is calculated for all aggregates by equation 6.1, where chemical potentials for Fe, O, and H are taken from ref. [266], as a first initial guess. First results are shown in Fig. 6.1. As in nature, the classical force field reveals hematite as the most stable phase. Nevertheless, maghemite is the phase which is grown in the

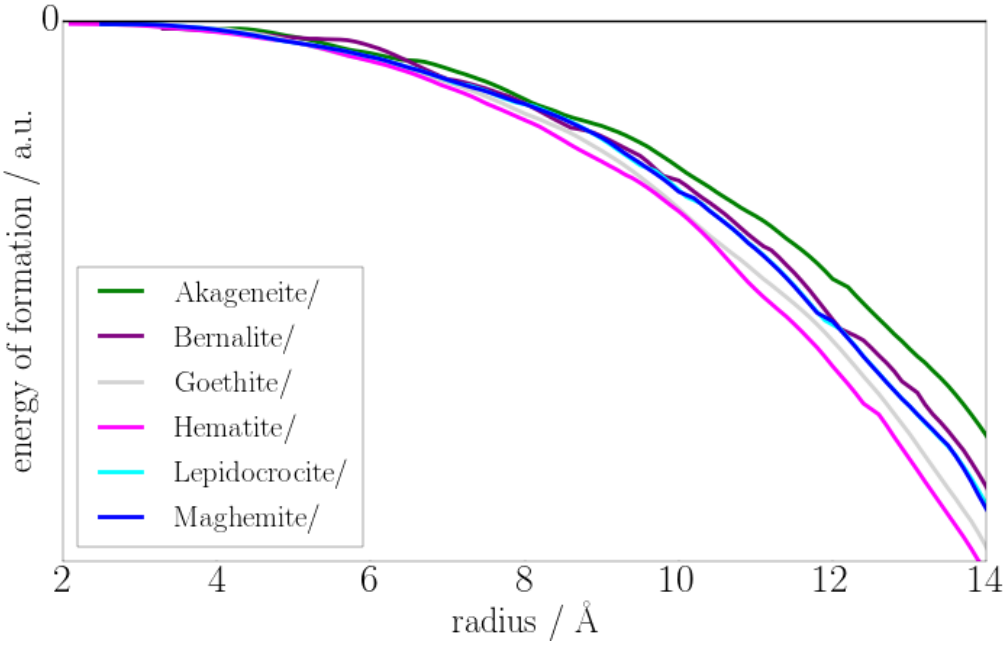

Figure 6.1: The energy of formation for differently sized spherical aggregates of different $FeO_x(OH)_y$ phases.

simulations, which could be explained by the missing coherence to the used classical force field or the missing surface termination. Anyhow, phase transition could be enforced by exposure of the obtained particles to different conditions, such as high temperatures and pressures, to overcome energy barriers or to degas the contained water.

Here, based on the conditions and size of the particles, phase transitions to further ascertain more stable phases could be observed as proposed in the size/energy diagram. First tests for an aggregate grown in water with PTR1 are performed. Here, the whole system is heated up to 1000 K, followed by a cool down phase down to 300 K and a further performed conjugate gradient minimization. The obtained aggregate consists only of ferrihydrite (17.3%) and amorphous parts (82.7%), as shown in Fig. 6.2 b). By heating the aggregate, without the solvent, and creating a sphere around the aggregate (without interactions to the solvent), which ensures that no atom can move away from the aggregate, the amount of ferrihydrite is increased to 35.9% while the amorphous part is reduced to 64.1%, as shown in Fig. 6.2 c). Therefore, it is quite interesting to investigate different setups, as well as the correlation of the resulting phase in comparison to the stability of the different phases as observed in Fig. 6.1.

Based on a developed force field for Fe^{2+}/Fe^{3+}, a suitable way to improve the crystal

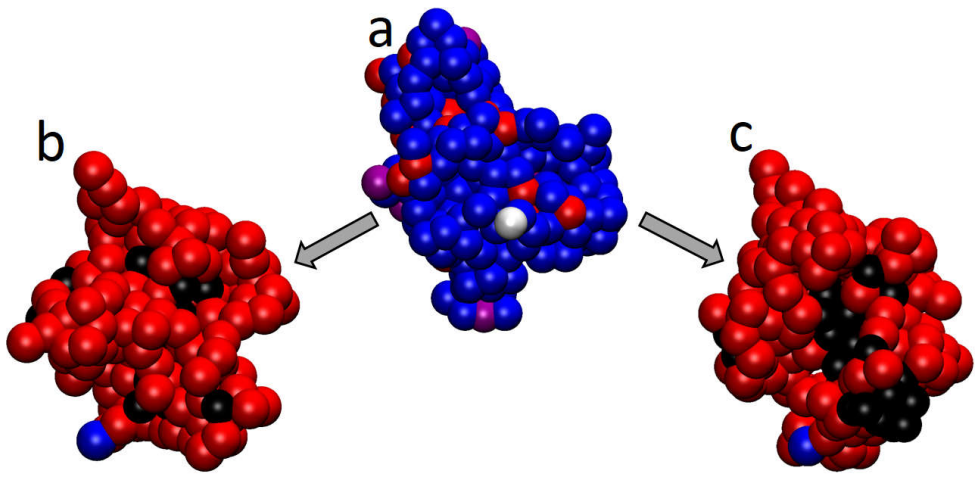

Figure 6.2: (b) Aggregate which is obtained by heating up the (a) initial structure to 1000 K, followed by a cool down phase down to 300 K and a further performed conjugate gradient minimization. (c) Aggregate which is obtained after heating up the (a) initial structure without solvent to 1000 K, followed by a cool down phase down to 300 K and a further performed conjugate gradient minimization. Additionally, a sphere around the aggregate (without interactions to the solvent) is created, which ensures that no atom can move away from the aggregate.

growth simulations could be the inclusion of the oxidation reaction of Fe(II) to Fe(III). This oxidation reaction could be implemented by changing the force field parameter and partial charges after attachment to the Fn subunits or the aggregate. The probabilities of the respective reactions as well as nucleation rates could be included by a Monte-Carlo approach leading to more realistic structures and mineralization behavior. Moreover, proton exchanges between the mineral and the protein, which could (and probably would) happen in reality could be included in the simulations.

A possible strategy to control the growth of specific two and three-dimensional structures could be the presence of inhibitors during the growth, such as small organic molecules, peptides or Fn subunits. For that, simulations should be performed in which inhibitors are introduced at different stages, for instance before the initial binding of the first Fe ions to the protein (see Fig. 6.3 b), or after the initial binding (see Fig. 6.3 c), or after the formation of mineral clusters of different sizes (see Fig. 6.3 d). In doing this, we could understand at which point the inclusion of inhibitors in the experimental protocol could lead to the best results in terms of film uniformity, optimizing the ratio between heterogeneous nucleation density and cluster accretion kinetics. Besides, RESTmetaD simulations of iron oxide binding peptides, such as described in ref. [123, 124] (an examplary peptide is

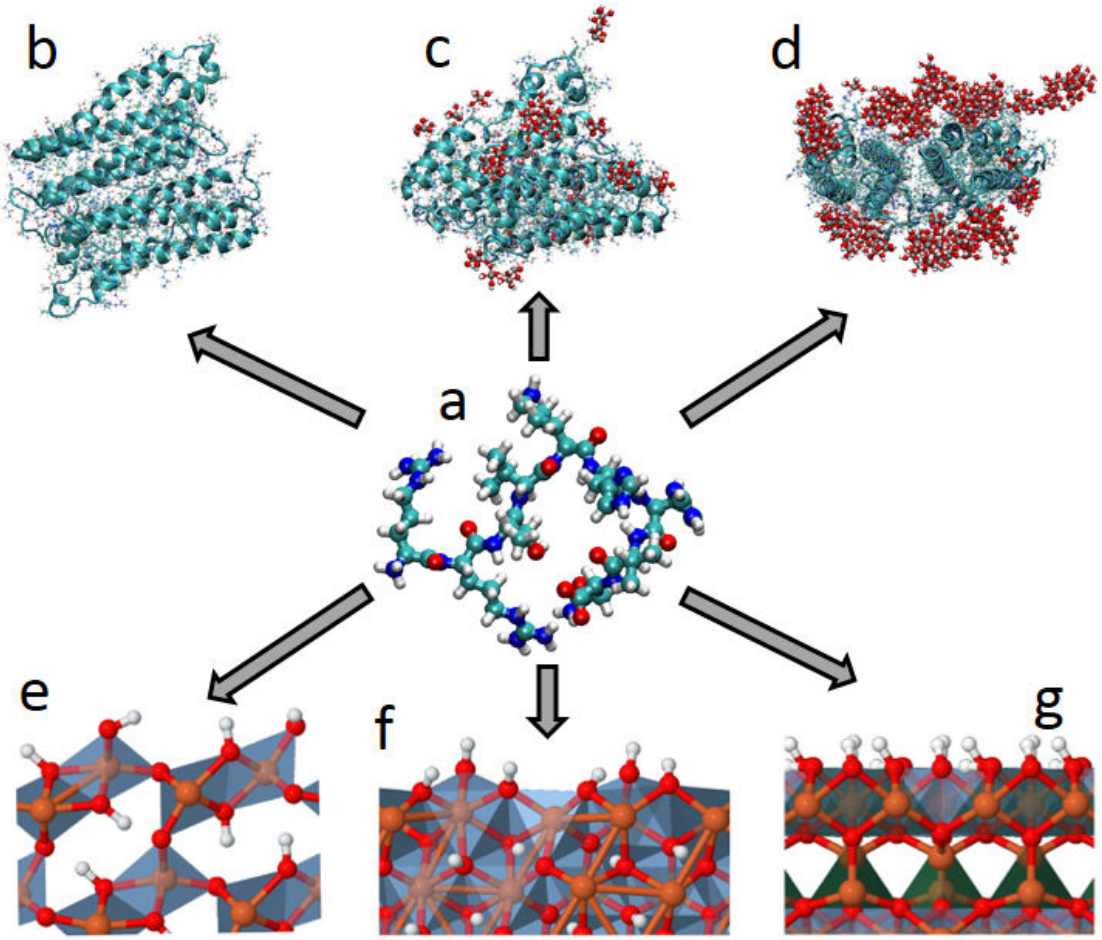

Figure 6.3: (a) Iron binding peptide [123] which could be added before the initial binding of the first Fe ions to the protein, (b) after the initial binding, or (c) after the formation of mineral clusters of different sizes. Moreover RESTmetaD simulations above the (e) goethite (110), (f) goethite (021), or (g) the ferrihydrite surface could reveal preferable iron oxide surfaces.

shown in Fig. 6.3 a), could be used to reveal preferable iron oxide surfaces (see Fig. 6.3 e, f, g). With this knowledge, the inhibitors can be used to exclude further growth of iron oxide on selected surfaces, which enables the control of growth in certain directions and therefore specific three-dimensional structures.

Of course, all presented techniques and methods are applicable to study other bio-/mineralization systems. Moreover, to investigate the crystal structures and growth experimentally, methods such as cryogenic transmission electron microscopy (cryo-TEM), scanning transmission electron microscopy (STEM), X-ray diffraction (XRD), or Mössbauer spectroscopy could be performed.

Chapter 7

Appendix

A1.1 Computational details

The following sections contain the computational details of the performed simulations in this thesis. Deviating settings are mentioned in the respective section and corresponding publication [105, 171, 220].

A1.1.1 Simulations based on DFT

The static, in case of FeO(OH) spin-polarized, DFT based calculations are performed with the Vienna Ab initio Simulation Package (VASP) [267–270]. The gradient-corrected Perdew-Berke-Ernzerhof (PBE GGA) functional [271] is employed to describe the exchange-correlation interactions. The van-der-Waals DF2 correction (vdwDF2) [162] is used to account for van-der-Waals interactions [162]. Based on the work of Cococcioni and de Gironcoli [158], the Hubbard-U correction [272] with a parameter U of 4.3 eV is applied to the iron atoms to handle the strongly correlated d-electrons. The simulations super-cells are sampled with Γ-centered Monkhorst-Pack grids [273] for the integration of the Brillouin Zone, and a Gaussian smearing are applied. The electron-core interactions are described with the projector augmented wave (PAW) method [274], and the plane-wave basis set is expanded up to a kinetic energy cutoff of 400 eV.

The first-principles molecular dynamics simulation of the amorphous alumina surface in contact with water are performed with the Car-Parrinello scheme [165] as implemented in the LAUTREC code [275, 276], using the PW91 [277] GGA functional and a cutoff

of 540 eV. A fictitious electron mass of 300 au and a timestep of 5.0 au, increasing the mass of the hydrogen atoms to 2 amu, are used. This ensures adiabaticity of the electronic system throughout the dynamics, without addition of an electronic thermostat. The temperature of the simulation was progressively increased within 0.5 ps and then maintained constant to about 350 ± 20 K by rescaling the atom velocities through a small adaptive (positive/negative) damping term applied to the motion of the atoms, which was updated every 100 timesteps.

A1.1.2 Simulations based on classical force fields

The Large-scale Atomic/Molecular Massively Parallel Simulator (LAMMPS) [129] code is used for all calculations based on classical force fields (FF). A cut-off value of 8 Å is used in case of the Buckingham potential, and of 12 Å for the Lennard-Jones potential and real-space electrostatic contributions. The Ewald long-range electrostatic contributions in reciprocal space are computed by means of the particle-particle particle-mesh solver [278]. Molecular dynamics simulations are typically performed in the NVT ensemble at 300 K with using an integration timestep of 1 fs and a Nosé-Hoover thermostat with a coupling constant of 0.1 ps. In case of simulations in explicit TIP3P water [279], as many Na^+ or Cl^- counterions as required are added for electrostatic neutrality of each simulated system.

The structures of H and L Fn subunits are taken from the Protein Data Bank (codes 2FHA.pdb and 2FG8.pdb, respectively) and described by the AMBER-99SB [117] force field. The LEaP program of the AmberTools package is used to append to the H chain missing residues which are not present in the X-ray structure. In case of simulations at different pH values, the protonation state of each residue has been adjusted to the respective pH value; otherwise, the protonation state is consistently set to a pH of 8.6, as used in the experiments.

The PLUMED package as a LAMMPS extension [280] is used to perform the metadynamics (metaD) simulations. The well-tempered metaD scheme [234, 281] with a bias factor of 15 is employed, where Gaussian hills with a height of 0.03 eV and a full width at half-maximum of 0.3 Å are added every 0.5 ps. Furthermore, to sample the internal degrees of freedom of the peptide the replica exchange with solute tempering (REST) method [140] is employed. The combined RESTmetaD simulations are performed as described in [143], with 15 replicas in the NVT ensemble with temperatures between 300 K

and 510 K separated uniformly by steps of 15 K, and attempting exchanges between neighboring replicas every 1 ps. The duration of each simulation is 200 ns, and the energies are averaged over the last 100 ns to compute the free energy of adsorption.

A1.2 Classical force field fitting process of Al_2O_3

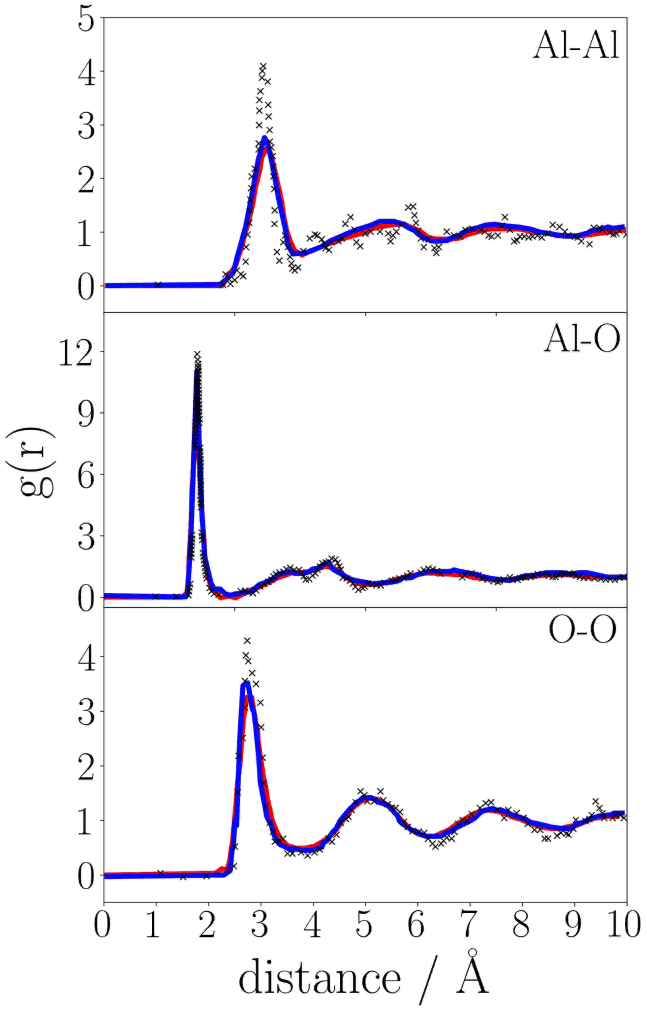

Figure A1: RDF curves of Gutierrez et al. [177] (1800 atoms - red line), Adiga et al. [179] (21375 atoms - blue line) and Chagarov et al.[176] (100 atoms - summarized over 2000 snapshots - black x). As mentioned in the main text, the small deviations of the curve based mainly on the small number of atoms in the system.

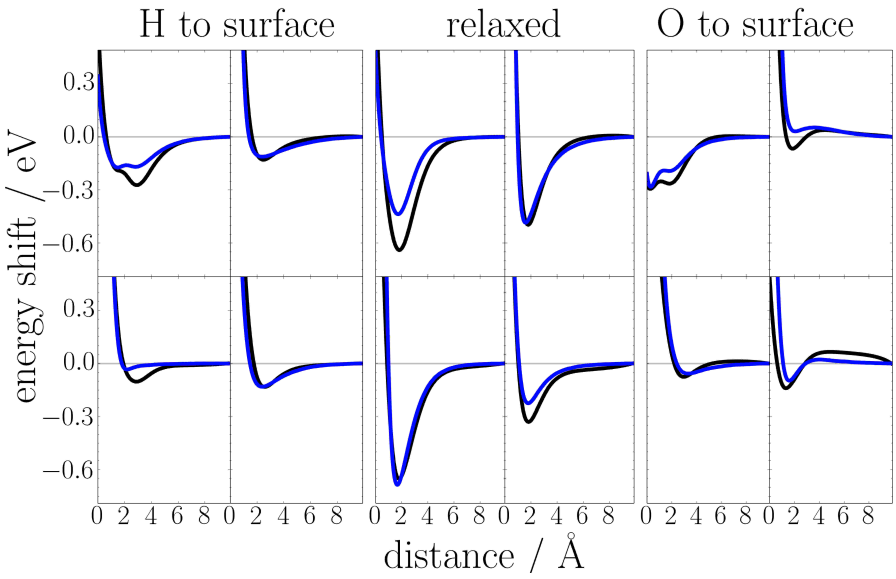

Figure A2: Potential energy profiles of water molecules at different orientations above an amorphous alumina surface (surface 1) computed with DFT (black lines) and our force field (FF, blue lines) with the optimized parameters listed in Table 3.3 in the main text. The height over the surface is relative to an arbitrary initial position at 0 Å.

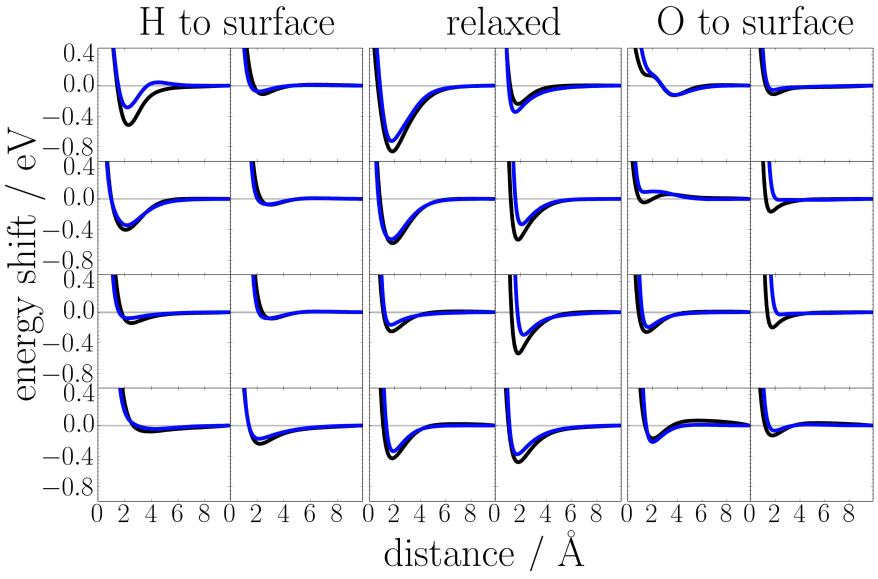

Figure A3: Potential energy profiles of water molecules at different orientations above an amorphous alumina surface (surface 2) computed with DFT (black lines) and our force field (FF, blue lines) with the optimized parameters listed in Table 3.3 in the main text. The height over the surface is relative to an arbitrary initial position at 0 Å.

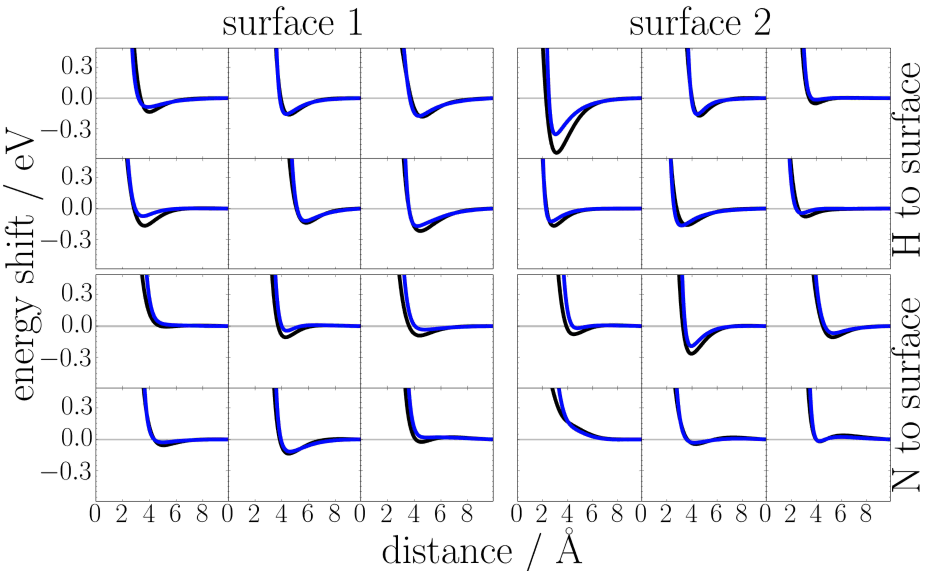

Figure A4: Potential energy profiles of ammonia (NH_3) molecules at different orientations above two different amorphous alumina surface computed with DFT (black lines) and our force field (FF, blue lines) with the optimized parameters listed in the main text in Table 3.3. The height over the surface is relative to an arbitrary initial position at 0 Å.

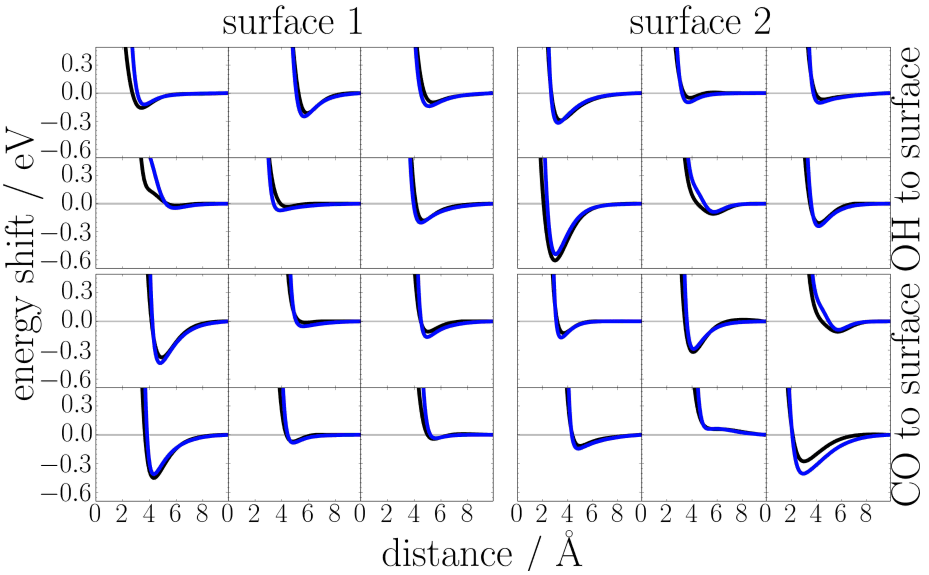

Figure A5: Potential energy profiles of formic acid (HCOOH) molecules at different orientations above two different amorphous alumina surface computed with DFT (black lines) and our force field (FF, blue lines) with the optimized parameters listed in the main text in Table 3.3. The height over the surface is relative to an arbitrary initial position at 0 Å.

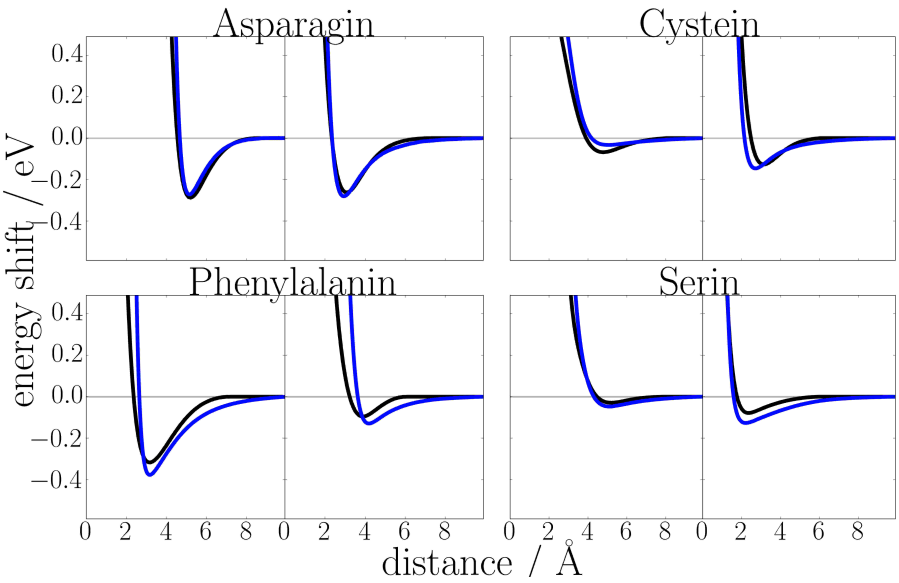

Figure A6: Potential energy profiles of four different amino acid side chains at different orientations above two different amorphous alumina surface computed with DFT (black lines) and our force field (FF, blue lines) with the optimized parameters listed in the main text in Table 3.3. The height over the surface is relative to an arbitrary initial position at 0 Å.

A1.3 Classical force field fitting process of FeO(OH)

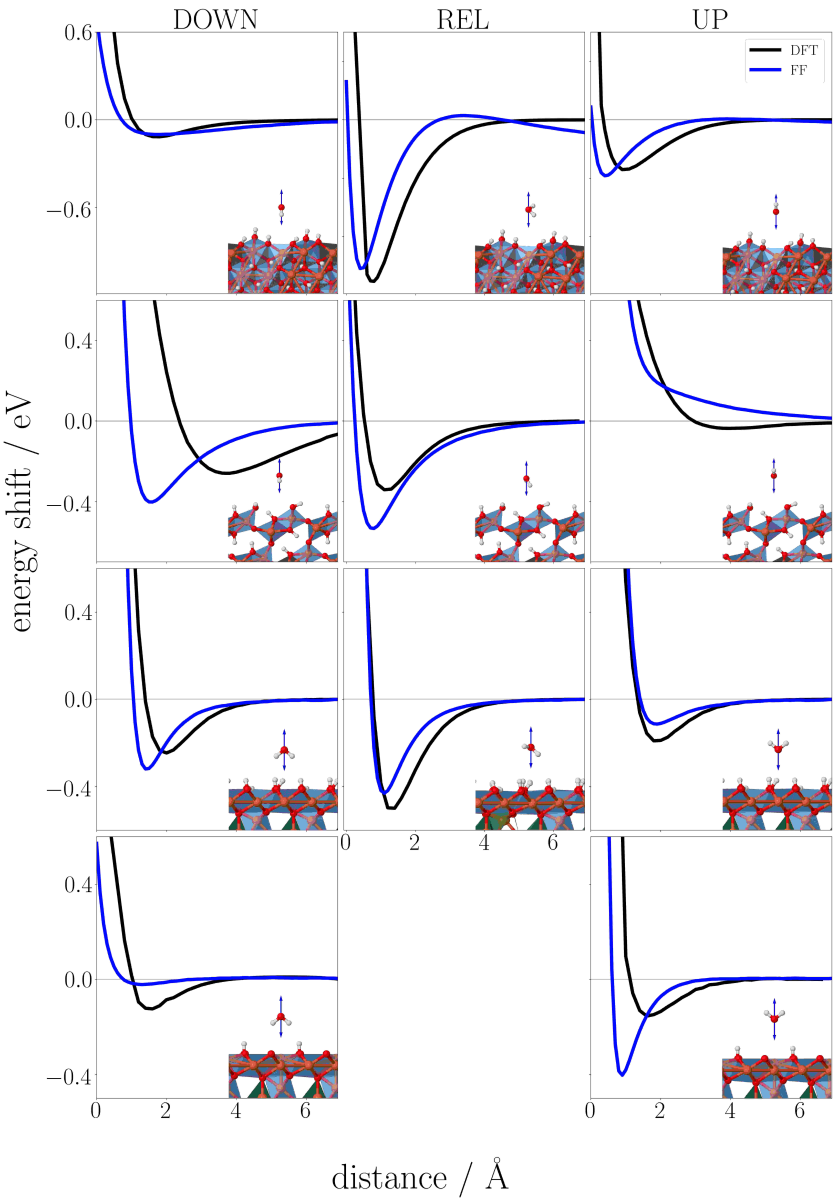

Figure A7: Potential energy profiles of water (TIP3P water model) molecules at different orientations above the (021) and (110) goethite surface as well as the ferrihydrite surface. The profiles are computed with DFT (black lines) and our force field (FF, blue lines) with the optimized parameters listed in the main text in Table 4.3. The height over the surface is relative to an arbitrary initial position at 0 Å.

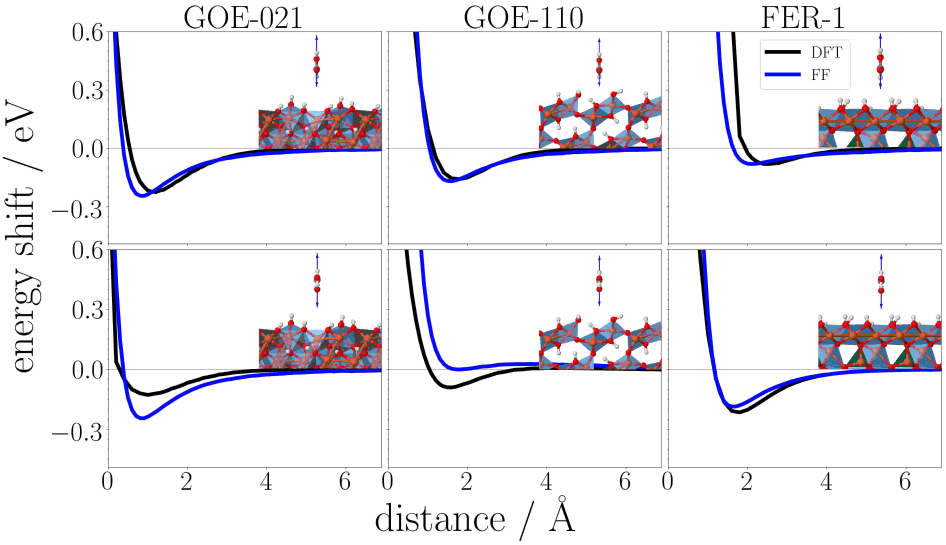

Figure A8: Potential energy profiles of formic acid (HCOOH) molecules at different orientations above the (021) and (110) goethite surface as well as the ferrihydrite surface. The profiles are computed with DFT (black lines) and our force field (FF, blue lines) with the optimized parameters listed in the main text in Table 4.3. The height over the surface is relative to an arbitrary initial position at 0 Å.

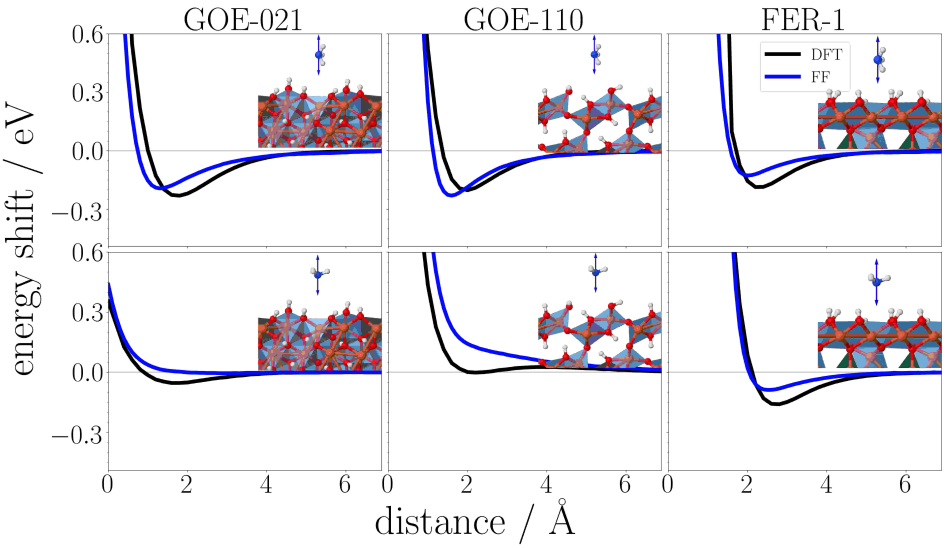

Figure A9: Potential energy profiles of ammonia (NH_3) molecules at different orientations above the (021) and (110) goethite surface as well as the ferrihydrite surface. The profiles are computed with DFT (black lines) and our force field (FF, blue lines) with the optimized parameters listed in the main text in Table 4.3. The height over the surface is relative to an arbitrary initial position at 0 Å.

A1.4 Anchor point analysis of the Ferritin/FeO(OH) interface

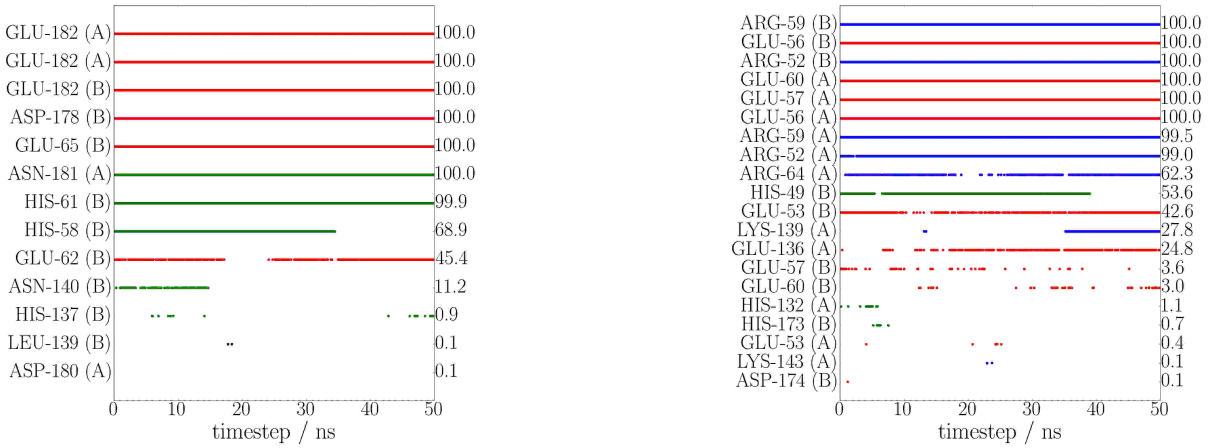

Figure A10: Time evolution of the anchoring sites between the 2-fold symmetric Fn H subunit (left) and L subunit (right) arrangements and the 'goethite big' particle model. Marked are all contacts with distances smaller than 2.7 Å between any atom of the Fn amino acid residues and any atom of the Fe(III) particle. The residues are labeled with their sequence position number and the chain they belong to. The time percentage in which a contact is present is shown on the right in each graphics. Contacts involving amino acids with positively charged side chains are colored blue, with negatively charged side chains red, with uncharged polar side chains green and all others colored grey.

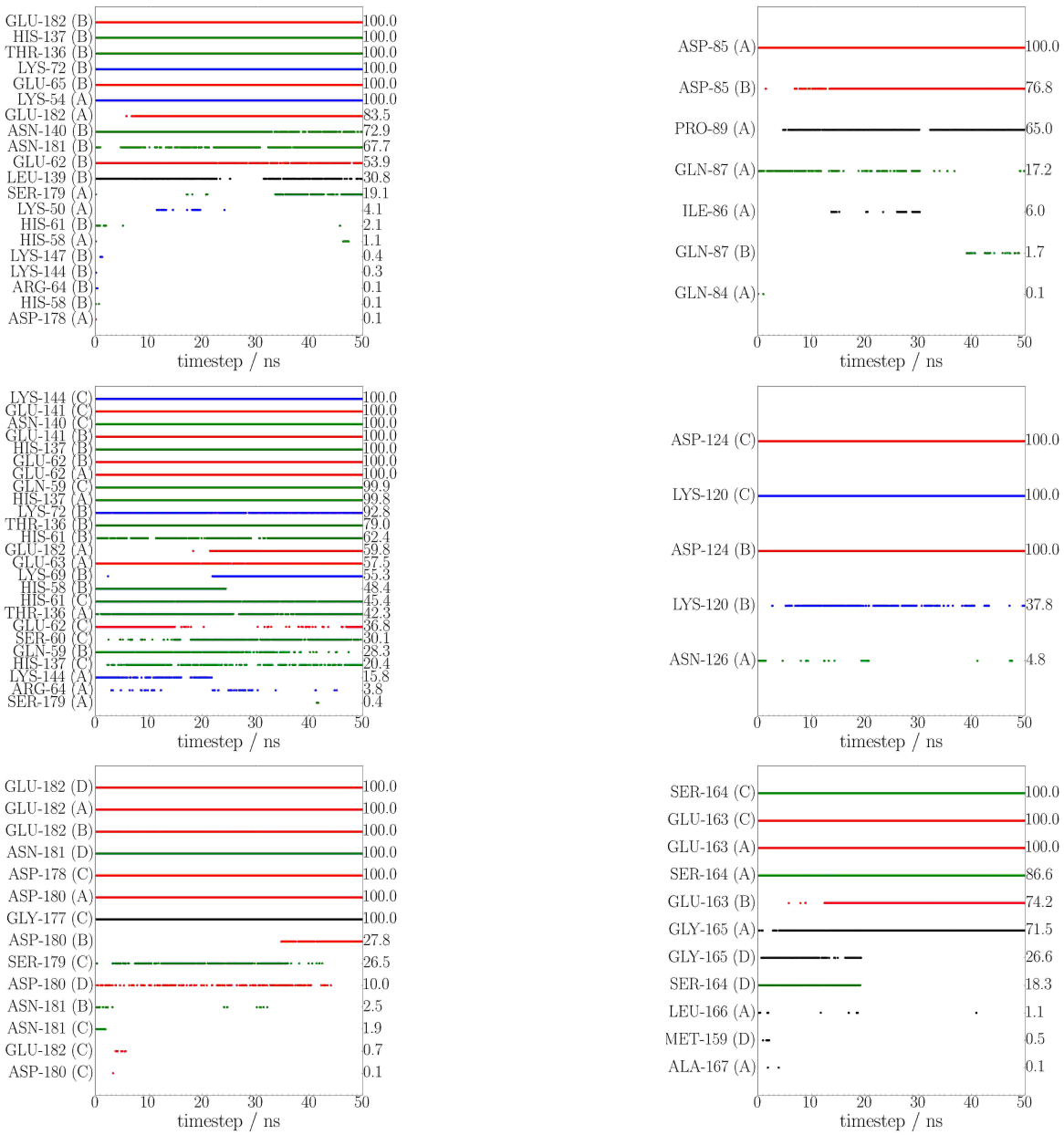

Figure A11: Time evolution of the anchoring sites between Fn **H subunit** arrangements (from top to bottom: two, three, four subunits) and the 'goethite small' particle model, displayed separately for the inner side (left column) and outer side (right column) of the entire shell. Marked are all contacts with distances smaller than 2.7 Å between any atom of the Fn amino acid residues and any atom of the Fe(III) particle. The residues are labeled with their sequence position number and the chain they belong to (A/B, A/B/C, A/B/C/D for the three arrangements). The time percentage in which a contact is present is shown on the right in each graphics. Contacts involving amino acids with positively charged side chains are colored blue, with negatively charged side chains red, with uncharged polar side chains green and all others colored grey.

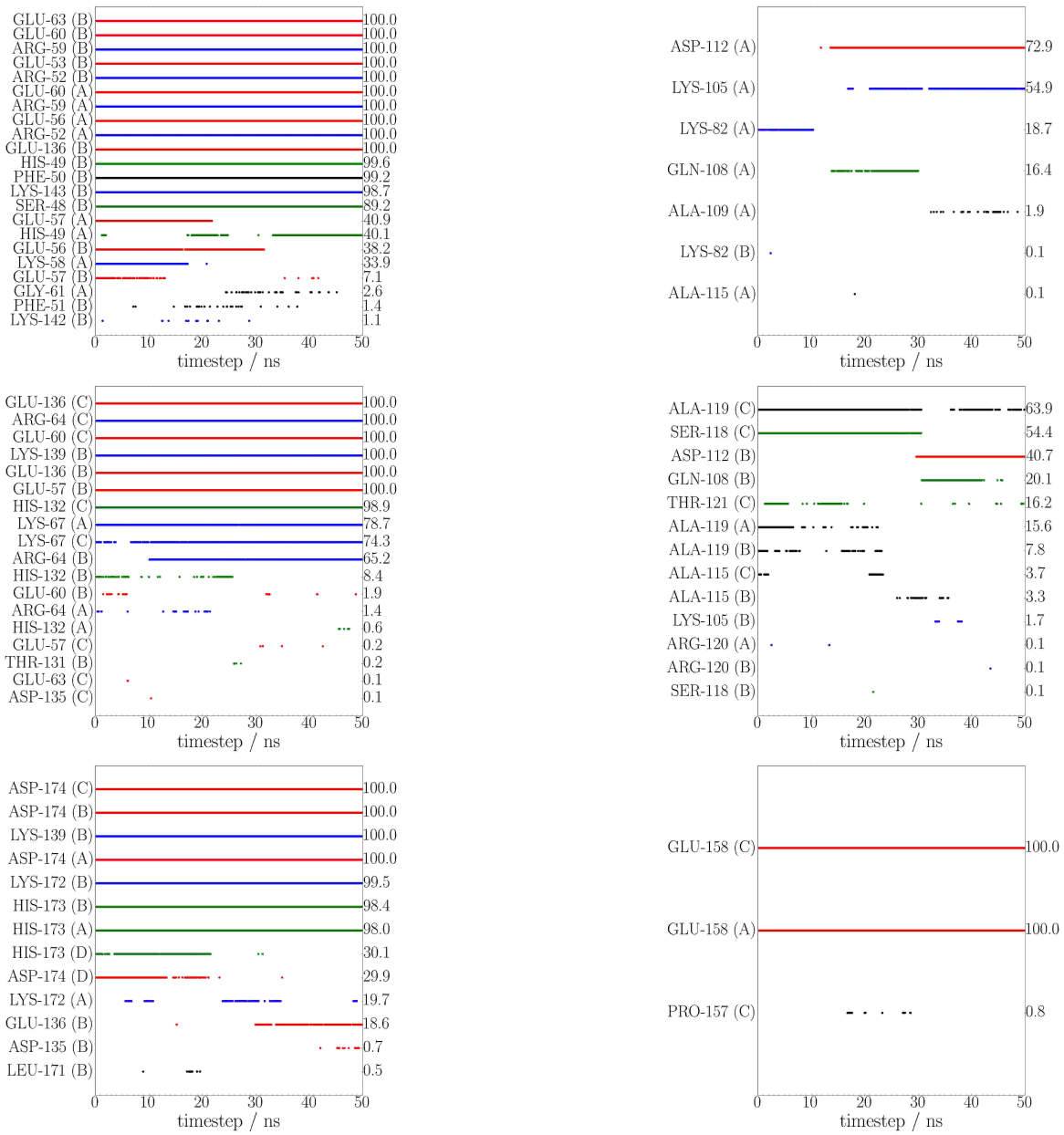

Figure A12: Time evolution of the anchoring sites between Fn **L subunit** arrangements (from top to bottom: two, three, four subunits) and the 'goethite small' particle model, displayed separately for the inner side (left column) and outer side (right column) of the entire shell. Marked are all contacts with distances smaller than 2.7 Å between any atom of the Fn amino acid residues and any atom of the Fe(III) particle. The residues are labeled with their sequence position number and the chain they belong to (A/B, A/B/C, A/B/C/D for the three arrangements). The time percentage in which a contact is present is shown on the right in each graphics. Contacts involving amino acids with positively charged side chains are colored blue, with negatively charged side chains red, with uncharged polar side chains green and all others colored grey.

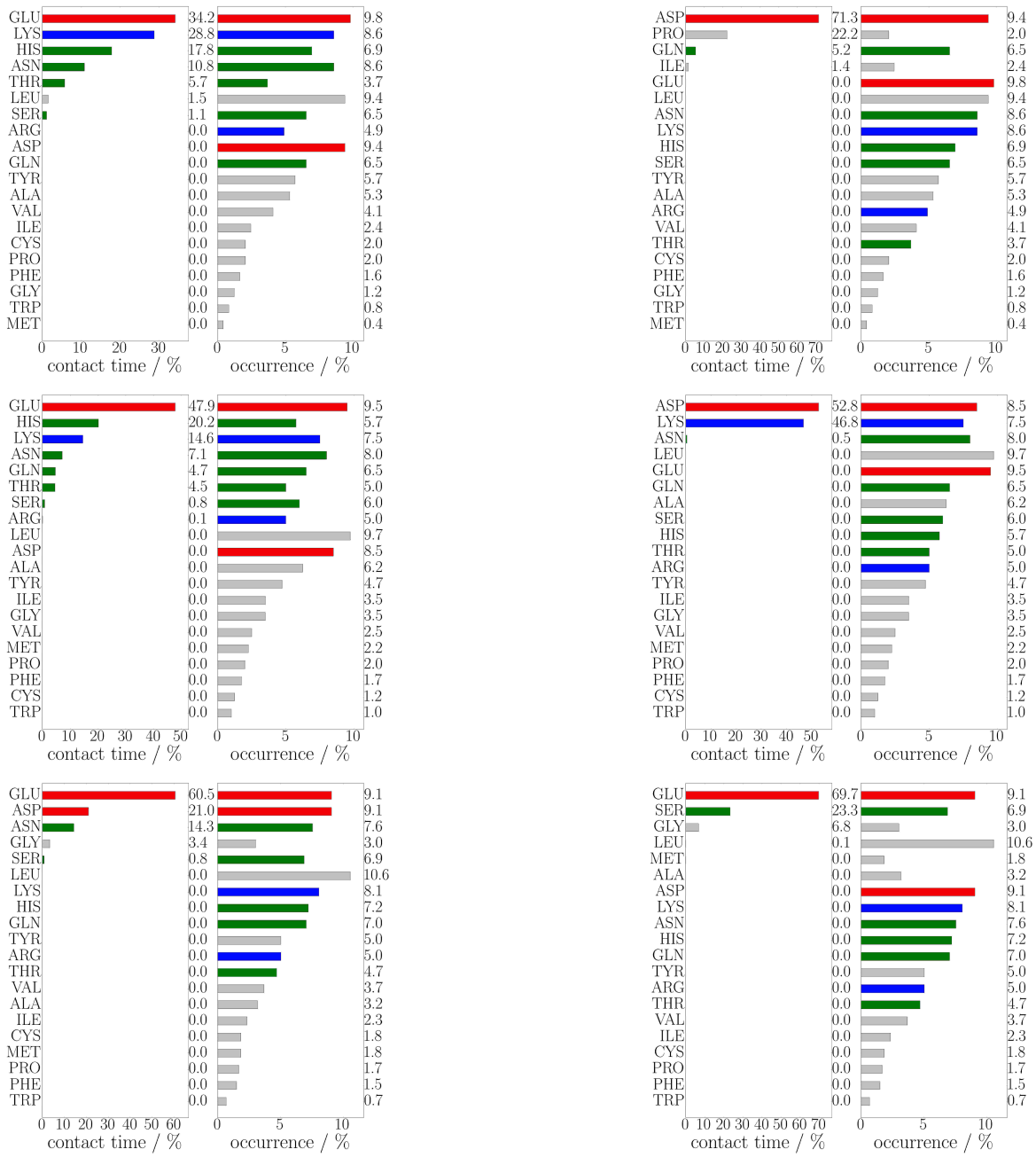

Figure A13: Amino-acid-residue-resolved analysis of the anchoring sites between Fn **H subunit** arrangements (from top to bottom: two, three, four subunits) and the 'goethite small' particle model, displayed separately for the inner side (left column) and the outer side (roght column) of the entire Fn shell. Shown are the percentage of contact time (left panels) and the relative residue occurrence at the solvent accessible surface of the subunits (right panels). The values for each residue type are also reported on the right-hand side of each panel, for better clarity. Contacts involving amino acids with positively charged side chains are colored blue, with negatively charged side chains red, with uncharged polar side chains green and all others colored grey.

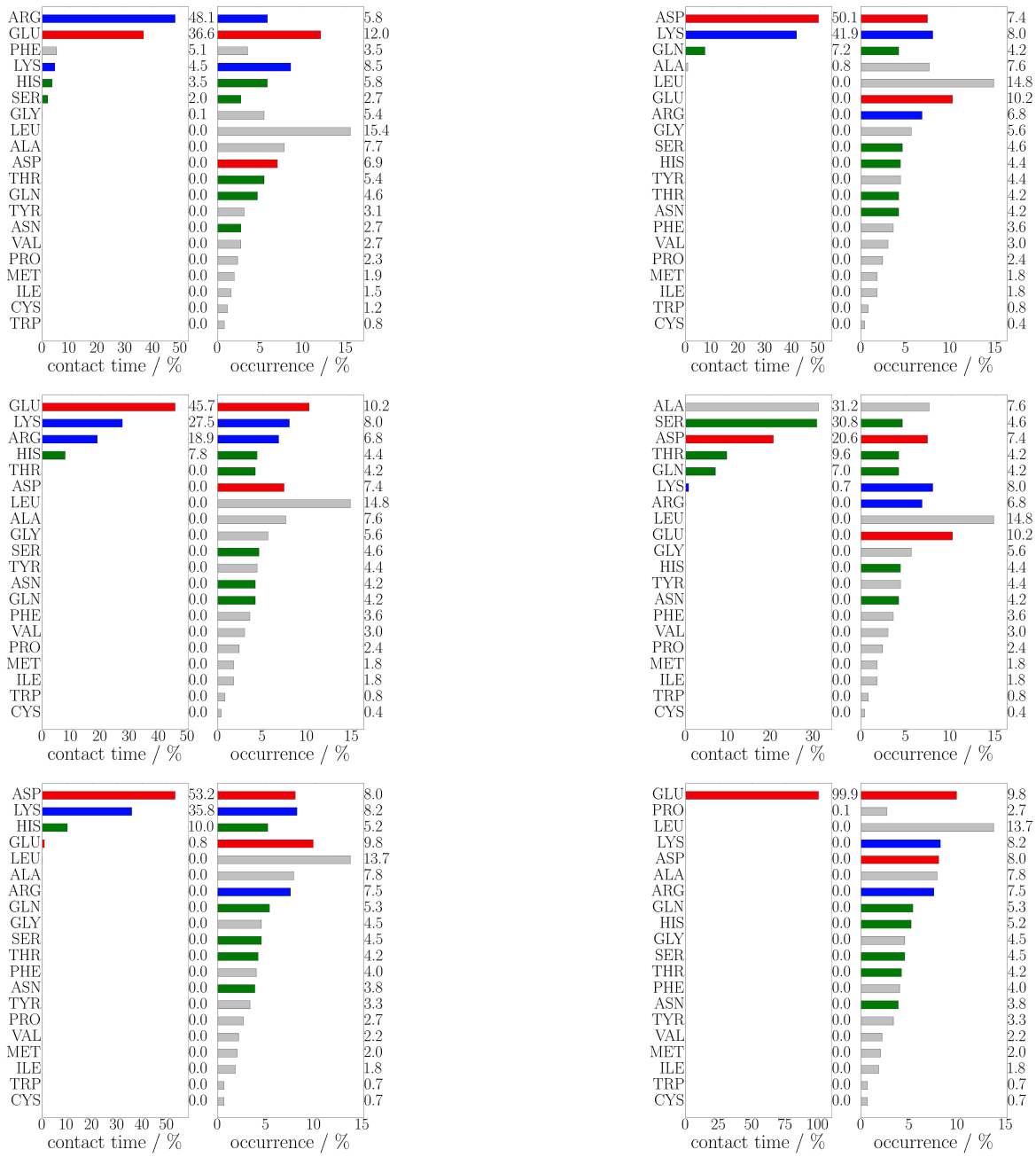

Figure A14: Amino-acid-residue-resolved analysis of the anchoring sites between Fn **L subunit** arrangements (from top to bottom: two, three, four subunits) and the 'goethite small' particle model, displayed separately for the inner side (left column) and the outer side (roght column) of the entire Fn shell. Shown are the percentage of contact time (left panels) and the relative residue occurrence at the solvent accessible surface of the subunits (right panels). The values for each residue type are also reported on the right-hand side of each panel, for better clarity. Contacts involving amino acids with positively charged side chains are colored blue, with negatively charged side chains red, with uncharged polar side chains green and all others colored grey.

A1.5 Source Code of crystal growth simulations

This section contains the most important parts of the LAMMPS input file for the performed crystal growth simulations. For a better overview, all "standard" environment settings are removed. All commands are explained in detail in the LAMMPS documentation.

A1.5.1 Placement of the new complex in the simulation box

To place the new complex in a specific distance range to the already existing atoms of the aggregate or protein, the structure and parameter of the complex, which is added in every step, is read by the molecule command (1). Afterward, groups for the already existing atoms of the aggregate (2) and the atoms of the complex (3) are defined. A loop of maximum 50000 attempts is started (5), in which one (7) new complex is randomly deposited (6) in the simulation box. Afterward, the radial distribution function (9) between the new complex and the aggregate or protein is calculated (12). If the complex is too close (14) to the protein or an aggregate, the new complex is removed from the system and after resetting the system (16/17) the next attempt (18) is started by jumping back (19) to the start of the loop. If the new complex is in an appropriate distance to the protein or aggregate, the docking procedure starts (15).

```
1  molecule F_read_complex feoh3(oh2)3.mol
2  group aggregate type 3 4 5 6
3  group complex type 24 25 26 27 28
4  label place_new_complex
5  variable ii loop 1 50000
6      fix F_deposit new_complex deposit 1 0 1 $random region region_to_place
~      mol F_read_complex near 1.0 attempt 1000
7      run 1
8      group G_check_docking union aggregate new_complex protein
9      compute C_RDF_complex G_check_docking rdf 1 24*28 3*22
10     variable V_RDF_complex equal c_C_RDF_complex[1][3]
11     thermo_style custom c_C_RDF_complex[1][3]
12     run 0
```

```
13    unfix F_deposit
14    if '$V_RDF_cluster > 0' then 'delete_atoms group new_complex'
15    if '$V_RDF_cluster == 0' then 'jump $SELF start_docking_process'
16    uncompute C_RDF_complex
17    variable V_RDF_complex delete
18 next ii
19 jump input.linp.sh place_new_complex
```

A1.5.2 Docking procedure

If the placement of the new complex is successful, the docking procedure is started (1). The group of atoms of the new complex, the aggregate, and the protein is defined (2) and set to the beginning to the internal atom list (3), which is necessary to include only this atoms in the neighbor list (4). By that, all interactions, except between atoms of this group, are switched off. In the next step, all atoms (5) are fixed at their actual position (6), except the new complex which is able to move in the NVT ensemble at 300 K (7). The radial distribution function is used to calculate the current distance between the complex and the aggregate or protein (8). The number of atoms in a selected range to the complex is stored in variable *V_failed* (9). The *halt* function is used to stop the MD simulation (13) if the complex moves closer to the aggregate or protein (11) or away, and therefore outside the selected range, without atoms of the aggregate or protein (12) inside the cutoff range. After the simulation stops, since the complex is moved away from the aggregate or protein (17), the complex is removed (21), the system is reset (18, 19, 20, 22) and the placement of a new complex starts from the beginning (23). If the docking is successful and the complex gets close to the aggregate or protein, additional MD simulation steps are performed (24), followed by the relaxation of the system.

```
1  label start_docking_process
2  group group_min union aggregate new_complex protein
3  atom_modify first group_min
4  neigh_modify every 1 delay 1 include group_min
5  group group_freeze subtract all new_complex
6  fix freeze_system group_freeze setforce 0.0 0.0 0.0
```

```
7  fix F_min new_complex nvt temp 300.0 300.0 20.0
8  compute C_RDF_docked G_check_docking rdf 3 24*28 3*22
9  variable V_docked equal c_C_RDF_docked[1][3]
10 thermo_style custom c_C_RDF_docked[1][3] c_C_RDF_docked[3][3]
11 fix F_halt_docked all halt 100 v_V_docked > 0 error continue
12 fix F_halt_failed all halt 100 v_V_failed == 0 error continue
13 run 100000
14 unfix F_halt_docked
15 unfix F_halt_failed
16 variable V_docked delete
17 if '$V_failed == 0' then &
18    "uncompute C_RDF_docked" &
19    "variable V_failed delete" &
20    "unfix F_min" &
21    "delete_atoms group new_complex" &
22    "neigh_modify every 1 delay 1 include all" &
23    "jump input.linp.sh place_new_complex"
24 run 1000
```

A1.5.3 Relaxation of the system

After the successful docking of the newly added complex, the relaxation of the TIP3P water and afterward the whole system is performed. First, all atoms (1) except the TIP3P water molecules (type 1 and 2) are fixed at their initial position (2). The fire algorithm is used (4) to push the atoms away from each other slowly (6). This is followed by a short nve/limit (10) run (11) to slowly relax the defined bonds, which are not considered in the previous minimization step. Afterward, the timestep (15, 19, 26), as well as the temperature and the coupling constant (16, 20), are slowly increased to relax the whole system. Finally, a simulation in NPT ensemble to adjust the correct density is followed by a long simulation in NVT ensemble.

```
1  group group_freeze type 3 4 5 6 7 8 9 10 11 12 13 14 15 16 17 18 19 20 21 22
23
```

```
2  fix freeze_system group_freeze setforce 0.0 0.0 0.0
3  timestep 10.0
4  min_style fire
5  min_modify dmax 0.1
6  minimize 1.0e-12 1.0e-12 100 100
7  unfix freeze_system
8  group group_freeze delete
9  timestep 1.0
10 fix F_nve all nve/limit 0.1
11 run 10
12 velocity all set 0.0 0.0 0.0 sum no units box
13 unfix F_nve
14 fix F_shake all shake 1.0e-6 500 0 t 2 5 8 10 12 13 15 18 19 20 21 28 a 1 b 1 2
15 timestep 0.1
16 fix F_nvt all nvt temp 30.0 50.0 1.0
17 run 100
18 unfix F_nvt
19 timestep 1.0
20 fix F_nvt all nvt temp 50.0 300.0 10.0
21 run 1000
22 unfix F_nvt
23 fix F_nvt all nvt temp 300.0 300.0 100.0
24 run 1000
25 unfix F_nvt
26 timestep 2.0
27 fix F_npt all npt temp 300.0 300.0 100.0 iso 1.0 1.0 100.0
28 run 25000
29 fix F_nvt all nvt temp 300.0 300.0 100.0
30 run 100000
31 unfix F_nvt
```

A1.6 Anchor point analysis of the grown aggregates

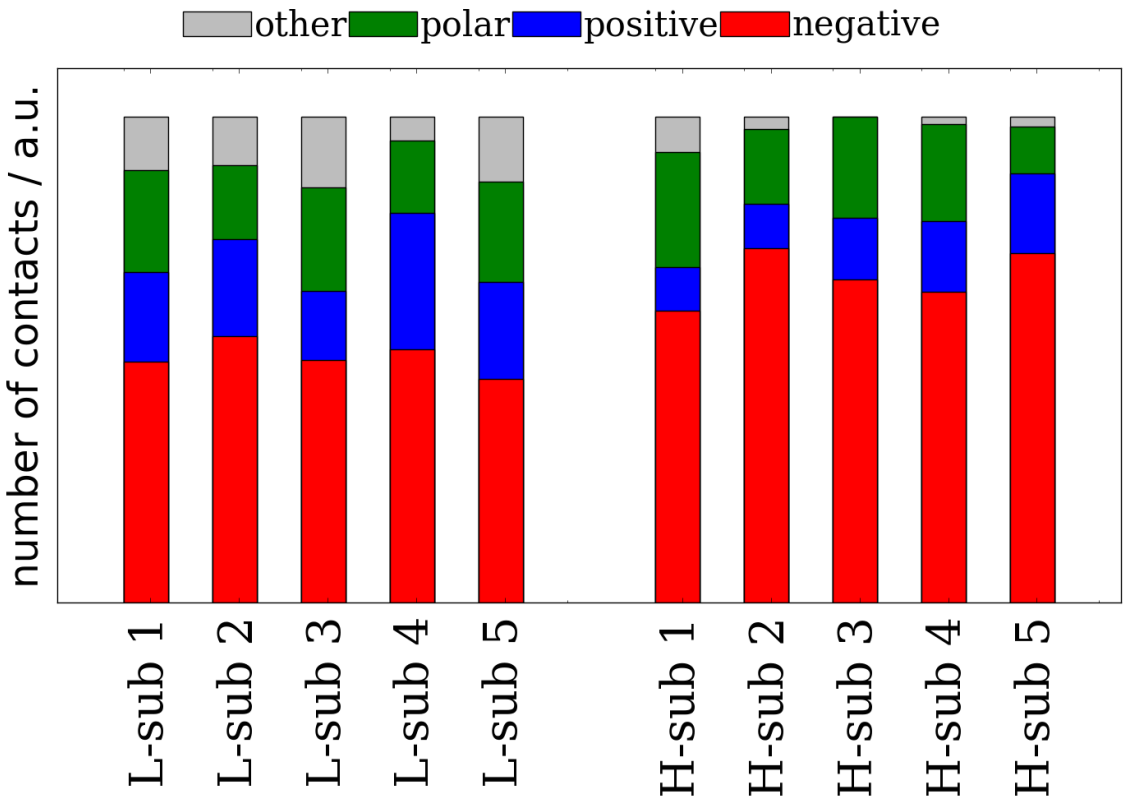

Figure A15: Normalized percentage occurence of polar, positive and negatively charged amin acids as anchor points of aggregates which grow on the L subunits (left-hand side) and H subunits (right-hand side) for all five performed indipendent simulations.

A1.7 Aggregates obtained in crystal growth simulations

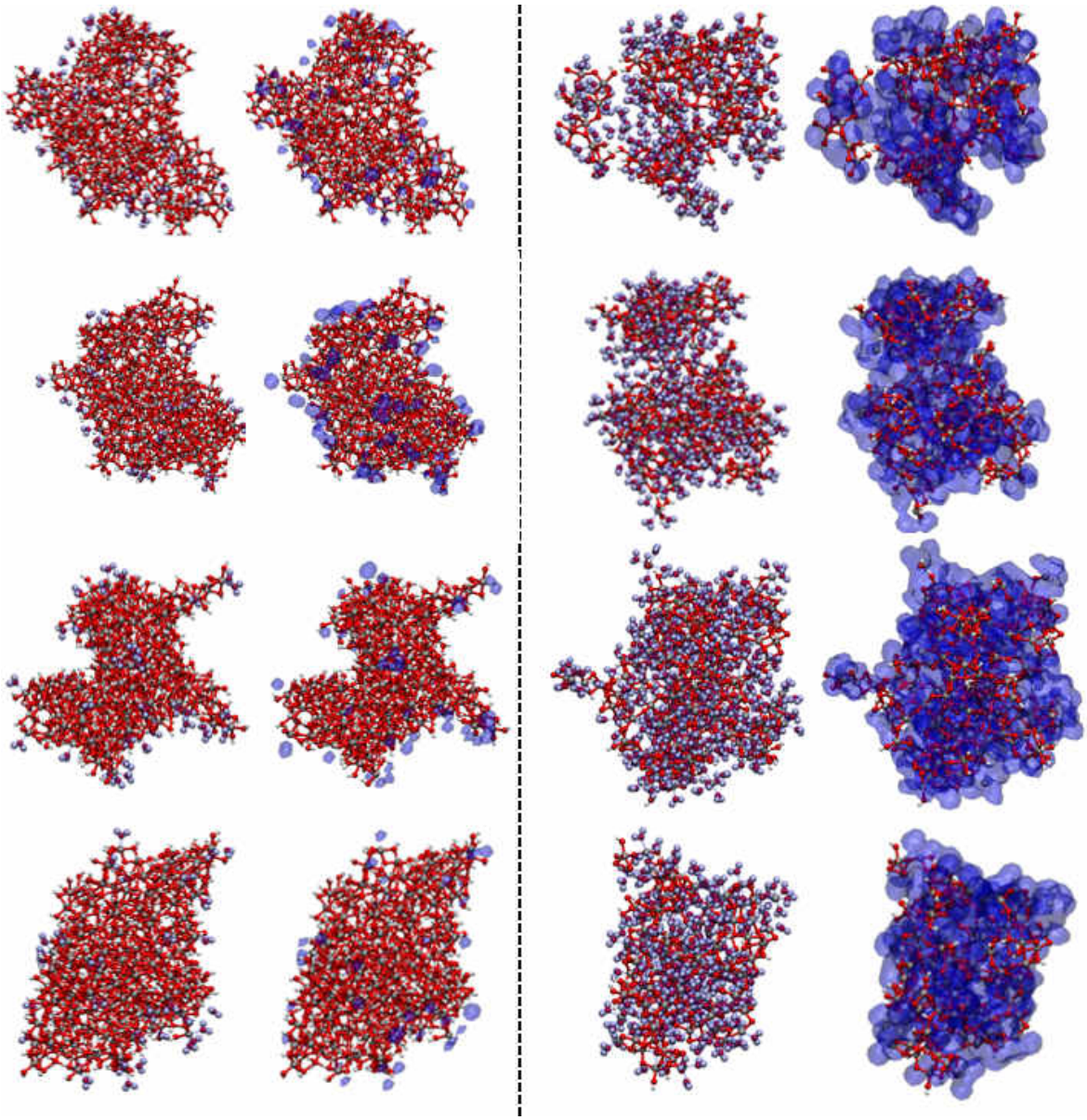

Figure A16: The aggregates in the left half are obtained in the systems which consider PTR1, while the aggregate in the right half are results of the systems which consider PTR2 and PTR3. On the left-hand side, the directly attached TIP3P water molecules are highlighted by a blue sphere and on the right-hand side by transparent blue clouds.

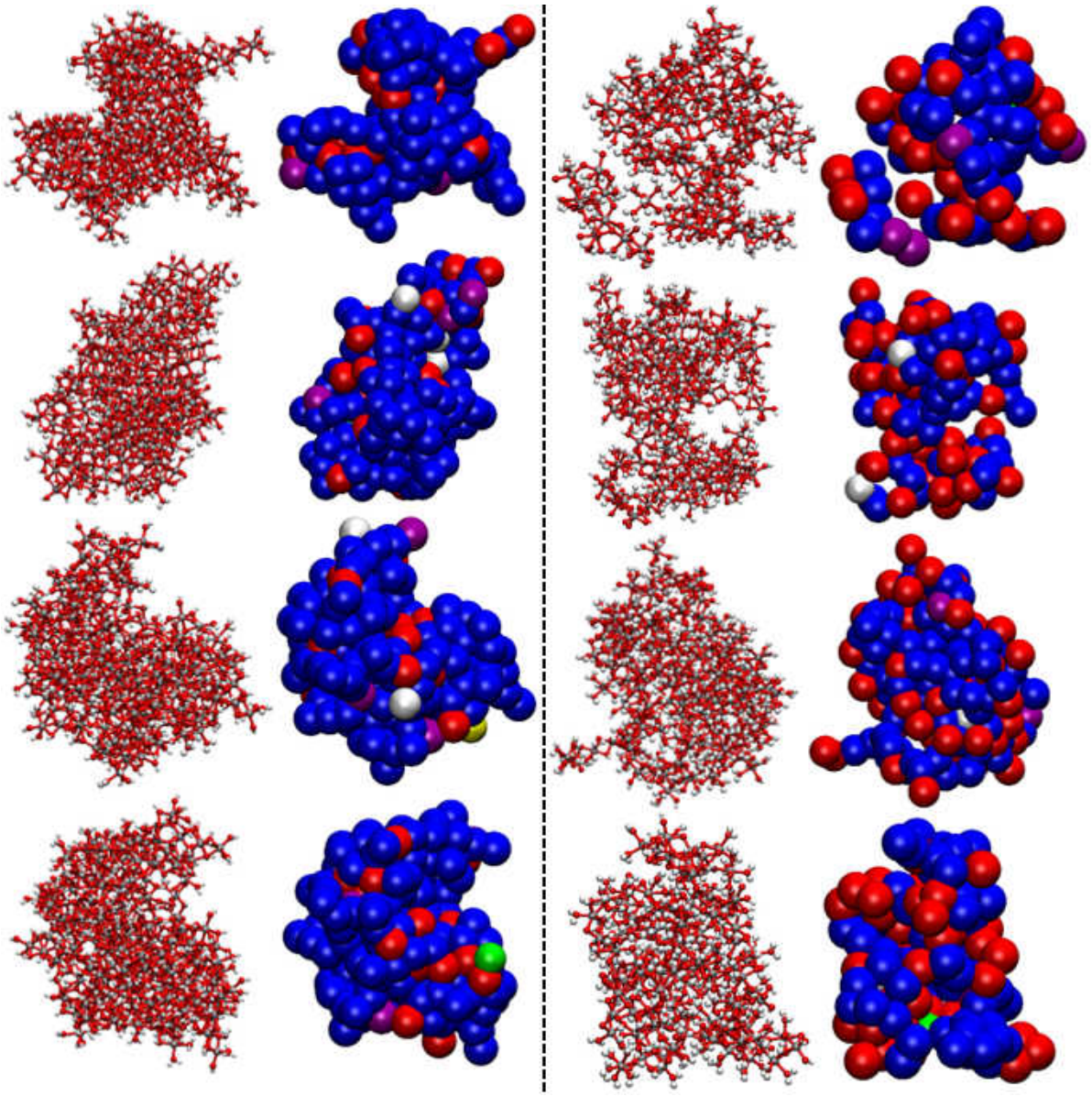

Figure A17: The aggregates in the left half are obtained in the systems which consider PTR1, while the aggregate in the right half are results of the systems which consider PTR2 and PTR3. On the right-hand side, all iron atoms are colored corresponding to their identified crystal structure (blue - Maghemite, red - amorphous, purple - Bernalite, white - Goethite, green - Akageneite).

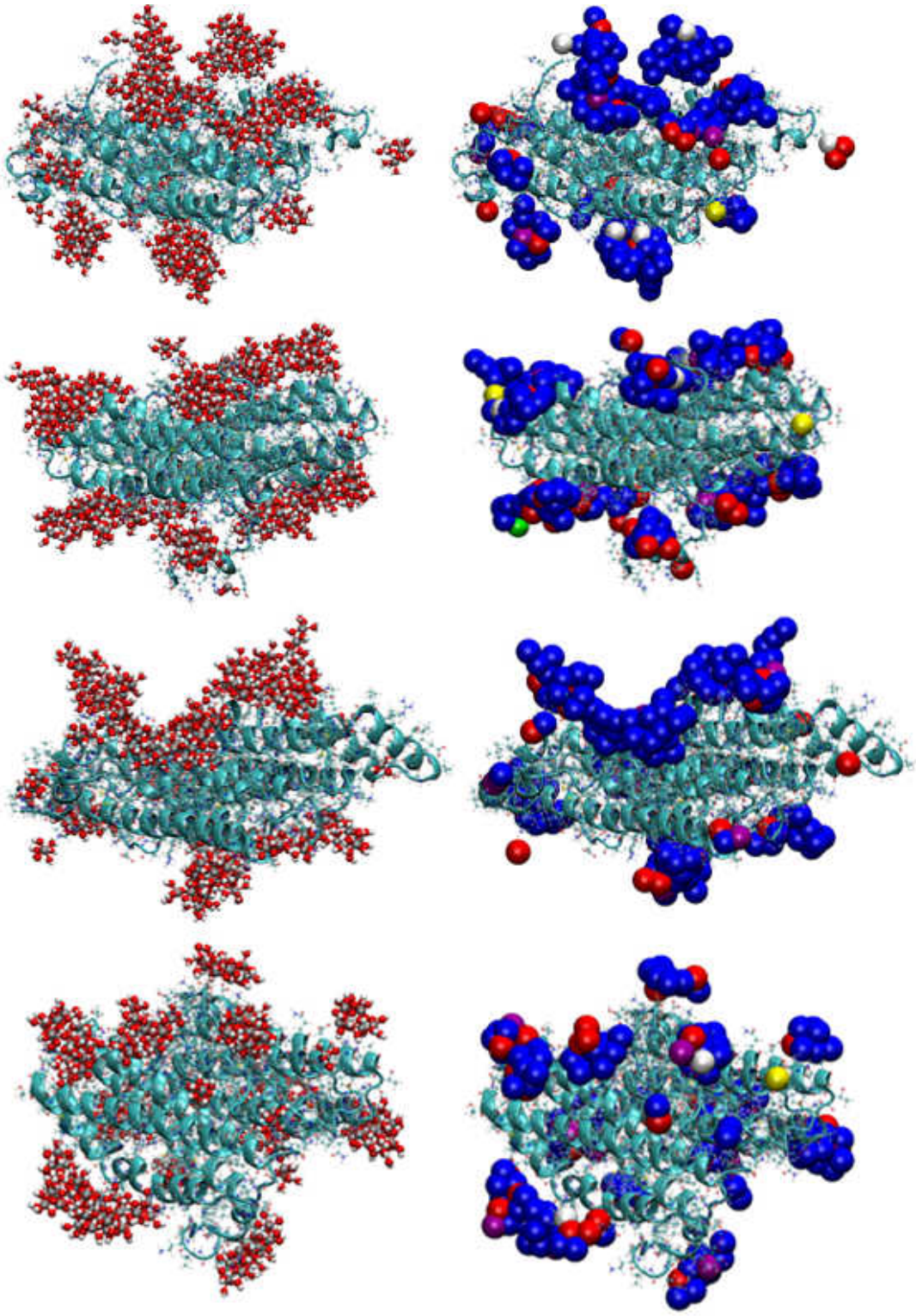

Figure A18: Different systems of crystal growth simulation of $FeO_x(OH)_y$ on the **L subunit**. On the right-hand side, all iron atoms are colored corresponding to their identified crystal structure (blue - Maghemite, red - amorphous, purple - Bernalite, white - Goethite, green - Akageneite, yellow - Feroxyhyte).

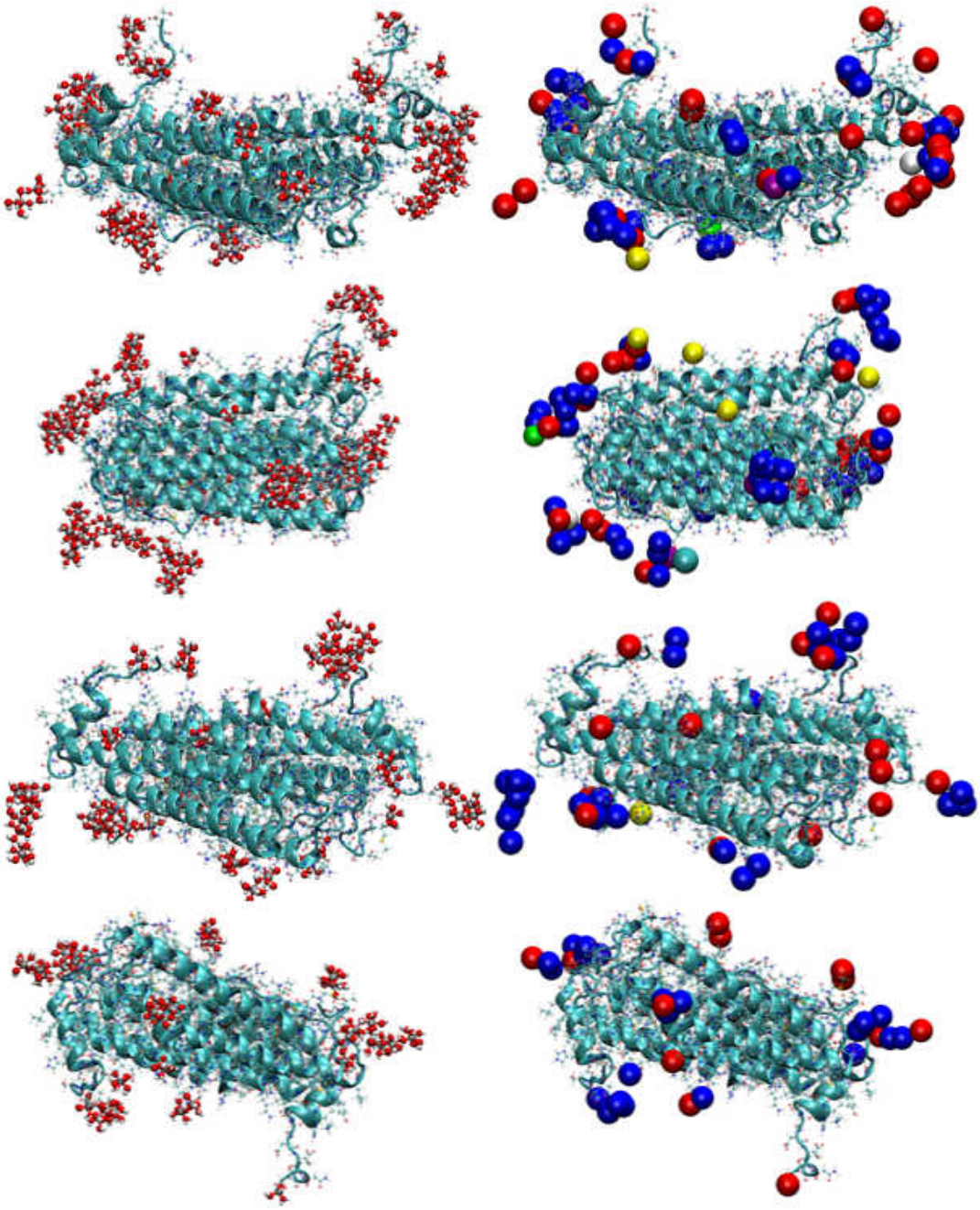

Figure A19: Different systems of crystal growth simulation of $FeO_x(OH)_y$ on the **H subunit**. On the right-hand side, all iron atoms are colored corresponding to their identified crystal structure (blue - Maghemite, red - amorphous, purple - Bernalite, white - Goethite, green - Akageneite, yellow - Feroxyhyte).

Acknowledgements

Thanks Lucio, for all your support and advice in all scientific and personal things.

I want to acknowledge all my former colleagues within the HMI group and the BCCMS. We had a great time together. Thanks, Balint, Gang, Hannah, Ilona, Jens, Jingfeng, Laura, Magdalena, Massimo, Meike, Nils, Oliver, Qing, Robert, Sebastian, Susi, Tatjana, and special thanks to Christian, Monika and Stefan. I had a really great time with all of you.

Thanks to all cooperation partners in the Ferritin project, in particular: Ana Rei, Daniel Carmona, Laura Treccani, Michael Maas, and Torben Halfer. Moreover, I want to thank Dirk Zahn and Tina Kollmann for all their support. It was alway a pleasure to work and discuss with you.

Thanks to Kai, Kira, Massimo, Monika, and Sebastian for proofreading parts of this work.

Thanks to Prof. Dominik Horinek for agreeing to act as the co-examiner.

This work was supported by the Deutsche Forschungsgemeinschaft trough the SPP 1569 (grant CO 1043/4 and KO 3811/3-1) and the Emmy Noether program (grant CI 144/2), and by the European Commission through the FP7-NMP grant 229205 ADGLASS. Allocation of computer resources was provided by the North-German Supercomputing Alliance system (HLRN - Hannover and Berlin), ZIH (Dresden), and the University of Bremen.

Finally, I thank my family and friends for all their support in the last years.

But, most of all, I wish to thank Naina.

Bibliography

[1] Jian Li and Carl Rau. "Fabrication, investigation and modification of magnetic states in nano-scale patterned cobalt films by using scanning ion microscopy with polarization analysis (SIMPA)". In: *Nuclear Instruments and Methods in Physics Research Section B: Beam Interactions with Materials and Atoms* vol. 256. no. 1 (2007), pp. 446–450.

[2] Oxana V Kharissova, HV Rasika Dias, and Boris I Kharisov. "Magnetic adsorbents based on micro-and nano-structured materials". In: *RSC Advances* vol. 5. no. 9 (2015), pp. 6695–6719.

[3] Qiu Yang, Zhiyi Lu, Junfeng Liu, Xiaodong Lei, Zheng Chang, Liang Luo, and Xiaoming Sun. "Metal oxide and hydroxide nanoarrays: Hydrothermal synthesis and applications as supercapacitors and nanocatalysts". In: *Progress in Natural Science: Materials International* vol. 23. no. 4 (2013), pp. 351–366.

[4] Goutam Sheet, Alexandra R Cunliffe, Erik J Offerman, Chad M Folkman, Chang-Beom Eom, and Venkat Chandrasekhar. "dc and high frequency magnetic properties of nanopatterned $CoFe_2O_4$ arrays fabricated using sol-gel precursors". In: *Journal of Applied Physics* vol. 107. no. 10 (2010), p. 104309.

[5] Anthony HB de Vries, Johannes S Kanger, Bea E Krenn, and Roel van Driel. "Patterned electroplating of micrometer scale magnetic structures on glass substrates". In: *Journal of microelectromechanical systems* vol. 13. no. 3 (2004), pp. 391–395.

[6] Majid Hejazian, Weihua Li, and Nam-Trung Nguyen. "Lab on a chip for continuous-flow magnetic cell separation". In: *Lab on a Chip* vol. 15. no. 4 (2015), pp. 959–970.

[7] Roger SM Rikken, Roeland JM Nolte, Jan C Maan, Jan CM van Hest, Daniela A Wilson, and Peter CM Christianen. "Manipulation of micro-and nanostructure motion with magnetic fields". In: *Soft Matter* vol. 10. no. 9 (2014), pp. 1295–1308.

[8] Giuseppe Schiavone, Marc PY Desmulliez, and Anthony J Walton. "Integrated magnetic MEMS relays: Status of the technology". In: *Micromachines* vol. 5. no. 3 (2014), pp. 622–653.

[9] Elena Bellido, Rocío de Miguel, Javier Sesé, Daniel Ruiz-Molina, Anabel Lostao, and Daniel Maspoch. "Nanoscale positioning of inorganic nanoparticles using biological ferritin arrays fabricated by dip-pen nanolithography". In: *Scanning* vol. 32. no. 1 (2010), pp. 35–41.

[10] Ichiro Yamashita, Kenji Iwahori, and Shinya Kumagai. "Ferritin in the field of nanodevices". In: *Biochimica et Biophysica Acta (BBA)-General Subjects* vol. 1800. no. 8 (2010), pp. 846–857.

[11] Atsushi Arakaki, Katsuhiko Shimizu, Mayumi Oda, Takeshi Sakamoto, Tatsuya Nishimura, and Takashi Kato. "Biomineralization-inspired synthesis of functional organic/inorganic hybrid materials: organic molecular control of self-organization of hybrids". In: *Organic & biomolecular chemistry* vol. 13. no. 4 (2015), pp. 974–989.

[12] Pauline M Harrison and Paolo Arosio. "The ferritins: molecular properties, iron storage function and cellular regulation". In: *Biochimica et Biophysica Acta (BBA)-Bioenergetics* vol. 1275. no. 3 (1996), pp. 161–203.

[13] Paolo Arosio, Rosaria Ingrassia, and Patrizia Cavadini. "Ferritins: a family of molecules for iron storage, antioxidation and more". In: *Biochimica et Biophysica Acta (BBA)-General Subjects* vol. 1790. no. 7 (2009), pp. 589–599.

[14] Masaki Uchida, Sebyung Kang, Courtney Reichhardt, Kevin Harlen, and Trevor Douglas. "The ferritin superfamily: Supramolecular templates for materials synthesis". In: *Biochimica et Biophysica Acta (BBA)-General Subjects* vol. 1800. no. 8 (2010), pp. 834–845.

[15] ND Chasteen. "Ferritin. Uptake, storage, and release of iron." In: *Metal ions in biological systems* vol. 35 (1998), p. 479.

[16] Unai Carmona, Le Li, Lianbing Zhang, and Mato Knez. "Ferritin light-chain subunits: key elements for the electron transfer across the protein cage". In: *Chemical Communications* vol. 50. no. 97 (2014), pp. 15358–15361.

[17] Gisele Zandman-Goddard and Yehuda Shoenfeld. "Ferritin in autoimmune diseases". In: *Autoimmunity reviews* vol. 6. no. 7 (2007), pp. 457–463.

[18] Gerald D Watt, Jae-Woo Kim, Bo Zhang, Timothy Miller, John N Harb, Robert C Davis, and Sang H Choi. "A protein-based ferritin bio-nanobattery". In: *Journal of Nanotechnology* vol. 2012 (2012).

[19] Takuro Matsui, Nozomu Matsukawa, Kenji Iwahori, Ken-Ichi Sano, Kiyotaka Shiba, and Ichiro Yamashita. "Realizing a two-dimensional ordered array of ferritin molecules directly on a solid surface utilizing carbonaceous material affinity peptides". In: *Langmuir* vol. 23. no. 4 (2007), pp. 1615–1618.

[20] Yoshitaka Nakagawa, Hiroyuki Kageyama, Yuya Oaki, and Hiroaki Imai. "Direction control of oriented self-assembly for 1D, 2D, and 3D microarrays of anisotropic rectangular nanoblocks". In: *Journal of the American Chemical Society* vol. 136. no. 10 (2013), pp. 3716–3719.

[21] Dong-Hyun Kim, Elena A Rozhkova, Ilya V Ulasov, Samuel D Bader, Tijana Rajh, Maciej S Lesniak, and Valentyn Novosad. "Biofunctionalized magnetic-vortex microdiscs for targeted cancer-cell destruction". In: *Nature materials* vol. 9. no. 2 (2010), p. 165.

[22] Birju Shah, Perry T Yin, Shraboni Ghoshal, and Ki-Bum Lee. "Multimodal Magnetic Core–Shell Nanoparticles for Effective Stem-Cell Differentiation and Imaging". In: *Angewandte Chemie International Edition* vol. 52. no. 24 (2013), pp. 6190–6195.

[23] Heinz Adolf Lowenstam and Stephen Weiner. *On biomineralization*. Oxford University Press on Demand, 1989.

[24] Damien Faivre and Dirk Schuler. "Magnetotactic bacteria and magnetosomes". In: *Chemical Reviews* vol. 108. no. 11 (2008), pp. 4875–4898.

[25] Joanna Aizenberg, Alexei Tkachenko, Steve Weiner, Lia Addadi, and Gordon Hendler. "Calcitic microlenses as part of the photoreceptor system in brittlestars". In: *Nature* vol. 412. no. 6849 (2001), p. 819.

[26] Stephen Mann. *Biomineralization: principles and concepts in bioinorganic materials chemistry*. Vol. 5. Oxford University Press on Demand, 2001.

[27] Elia Beniash, Joanna Aizenberg, Lia Addadi, and Stephen Weiner. "Amorphous calcium carbonate transforms into calcite during sea urchin larval spicule growth". In: *Proceedings of the Royal Society of London B: Biological Sciences* vol. 264. no. 1380 (1997), pp. 461–465.

[28] Yael Politi, Talmon Arad, Eugenia Klein, Steve Weiner, and Lia Addadi. "Sea urchin spine calcite forms via a transient amorphous calcium carbonate phase". In: *Science* vol. 306. no. 5699 (2004), pp. 1161–1164.

[29] Ingrid Maria Weiss, Noreen Tuross, LIA Addadi, and Steve Weiner. "Mollusc larval shell formation: amorphous calcium carbonate is a precursor phase for aragonite". In: *Journal of Experimental Zoology Part A: Ecological Genetics and Physiology* vol. 293. no. 5 (2002), pp. 478–491.

[30] Lia Addadi, Sefi Raz, and Steve Weiner. "Taking advantage of disorder: amorphous calcium carbonate and its roles in biomineralization". In: *Advanced Materials* vol. 15. no. 12 (2003), pp. 959–970.

[31] Stephen Weiner and Lia Addadi. "Design strategies in mineralized biological materials". In: *Journal of Materials Chemistry* vol. 7. no. 5 (1997), pp. 689–702.

[32] L Addadi, J Moradian, E Shay, NG Maroudas, and S Weiner. "A chemical model for the cooperation of sulfates and carboxylates in calcite crystal nucleation: relevance to biomineralization". In: *Proceedings of the national academy of sciences* vol. 84. no. 9 (1987), pp. 2732–2736.

[33] Lia Addadi and S Weiner. "Interactions between acidic proteins and crystals: stereochemical requirements in biomineralization". In: *Proceedings of the National Academy of Sciences* vol. 82. no. 12 (1985), pp. 4110–4114.

[34] Giuseppe Falini, Shira Albeck, Steve Weiner, and Lia Addadi. "Control of aragonite or calcite polymorphism by mollusk shell macromolecules". In: *Science* vol. 271. no. 5245 (1996), pp. 67–69.

[35] Dimo Kashchiev. "Thermodynamically consistent description of the work to form a nucleus of any size". In: *The Journal of chemical physics* vol. 118. no. 4 (2003), pp. 1837–1851.

[36] Douglas H Everett et al. *Basic principles of colloid science*. Royal society of chemistry, 2007.

[37] Denis Gebauer and Helmut Cölfen. "Prenucleation clusters and non-classical nucleation". In: *Nano Today* vol. 6. no. 6 (2011), pp. 564–584.

[38] D Kashchiev and GM Van Rosmalen. "Nucleation in solutions revisited". In: *Crystal Research and Technology* vol. 38. no. 7-8 (2003), pp. 555–574.

[39] Jens Baumgartner and Damien Faivre. "Iron solubility, colloids and their impact on iron (oxyhydr) oxide formation from solution". In: *Earth-science reviews* vol. 150 (2015), pp. 520–530.

[40] Helmut Cölfen, Heimo Schnablegger, Armin Fischer, Friederike C Jentoft, Gisela Weinberg, and Robert Schlögl. "Particle growth kinetics in zirconium sulfate aqueous solutions followed by dynamic light scattering and analytical ultracentrifugation: Implications for thin film deposition". In: *Langmuir* vol. 18. no. 9 (2002), pp. 3500–3509.

[41] Peter G Vekilov. "The two-step mechanism of nucleation of crystals in solution". In: *Nanoscale* vol. 2. no. 11 (2010), pp. 2346–2357.

[42] Denis Gebauer, Antje Völkel, and Helmut Cölfen. "Stable prenucleation calcium carbonate clusters". In: *Science* vol. 322. no. 5909 (2008), pp. 1819–1822.

[43] Andreas Verch. "Pränukleationscluster und ihre Wechselwirkungen mit Additiven". PhD thesis. Universität Potsdam Potsdam, 2010.

[44] Raffaella Demichelis, Paolo Raiteri, Julian D Gale, David Quigley, and Denis Gebauer. "Stable prenucleation mineral clusters are liquid-like ionic polymers". In: *Nature communications* vol. 2 (2011), p. 590.

[45] Helmut Cölfen and Stephen Mann. "Higher-order organization by mesoscale self-assembly and transformation of hybrid nanostructures". In: *Angewandte Chemie International Edition* vol. 42. no. 21 (2003), pp. 2350–2365.

[46] Helmut Cölfen and Markus Antonietti. "Mesocrystals: inorganic superstructures made by highly parallel crystallization and controlled alignment". In: *Angewandte Chemie International Edition* vol. 44. no. 35 (2005), pp. 5576–5591.

[47] Markus Niederberger and Helmut Cölfen. "Oriented attachment and mesocrystals: non-classical crystallization mechanisms based on nanoparticle assembly". In: *Physical chemistry chemical physics* vol. 8. no. 28 (2006), pp. 3271–3287.

[48] Helmut Cöelfen and Markus Antonietti. *Mesocrystals and nonclassical crystallization*. John Wiley & Sons, 2008.

[49] Fiona C Meldrum and Helmut Cölfen. "Controlling mineral morphologies and structures in biological and synthetic systems". In: *Chemical reviews* vol. 108. no. 11 (2008), pp. 4332–4432.

[50] Marthe Rousseau, Evelyne Lopez, Philippe Stempflé, Marcel Brendlé, Loïc Franke, Alain Guette, Roger Naslain, and Xavier Bourrat. "Multiscale structure of sheet nacre". In: *Biomaterials* vol. 26. no. 31 (2005), pp. 6254–6262.

[51] Ingo Sethmann, Ruth Hinrichs, Gert Wörheide, and Andrew Putnis. "Nano-cluster composite structure of calcitic sponge spicules—a case study of basic characteristics of biominerals". In: *Journal of inorganic biochemistry* vol. 100. no. 1 (2006), pp. 88–96.

[52] Yuya Oaki, Akiko Kotachi, Takashi Miura, and Hiroaki Imai. "Bridged nanocrystals in biominerals and their biomimetics: classical yet modern crystal growth on the nanoscale". In: *Advanced Functional Materials* vol. 16. no. 12 (2006), pp. 1633–1639.

[53] PT Cardew and RJ Davey. "The kinetics of solvent-mediated phase transformations". In: *Proc. R. Soc. Lond. A*. Vol. 398. 1815. The Royal Society. 1985, pp. 415–428.

[54] Jamshed Anwar and Papa Kofi Boateng. "Computer simulation of crystallization from solution". In: *Journal of the American Chemical Society* vol. 120. no. 37 (1998), pp. 9600–9604.

[55] PE Bonnett, KJ Carpenter, S Dawson, and RJ Davey. "Solution crystallisation via a submerged liquid–liquid phase boundary: oiling out". In: *Chemical communications* no. 6 (2003), pp. 698–699.

[56] Peter G Vekilov. "Dense liquid precursor for the nucleation of ordered solid phases from solution". In: *Crystal Growth & Design* vol. 4. no. 4 (2004), pp. 671–685.

[57] Tian Hui Zhang and Xiang Yang Liu. "Nucleation: what happens at the initial stage?" In: *Angewandte Chemie International Edition* vol. 48. no. 7 (2009), pp. 1308–1312.

[58] W Ostwald. "The formation and changes of solids". In: *Z. Phys. Chem* vol. 22 (1897), pp. 289–330.

[59] Jens Baumgartner, Archan Dey, Paul HH Bomans, Cécile Le Coadou, Peter Fratzl, Nico AJM Sommerdijk, and Damien Faivre. "Nucleation and growth of magnetite from solution". In: *Nature materials* vol. 12. no. 4 (2013), p. 310.

[60] Agnieszka Kawska, Jürgen Brickmann, Rüdiger Kniep, Oliver Hochrein, and Dirk Zahn. "An atomistic simulation scheme for modeling crystal formation from solution". In: *The Journal of chemical physics* vol. 124. no. 2 (2006), p. 024513.

[61] N Dennis Chasteen and Pauline M Harrison. "Mineralization in ferritin: an efficient means of iron storage". In: *Journal of structural biology* vol. 126. no. 3 (1999), pp. 182–194.

[62] Elizabeth C Theil, Manolis Matzapetakis, and Xiaofeng Liu. "Ferritins: iron/oxygen biominerals in protein nanocages". In: *JBIC Journal of Biological Inorganic Chemistry* vol. 11. no. 7 (2006), pp. 803–810.

[63] RA Grant, DJ Filman, SE Finkel, R Kolter, and JM Hogle. "The crystal structure of Dps, a ferritin homolog that binds and protects DNA". In: *Nature Structural & Molecular Biology* vol. 5. no. 4 (1998), pp. 294–303.

[64] Jelena Pesek, Rita Büchler, Reinhard Albrecht, Wilhelm Boland, and Kornelius Zeth. "Structure and mechanism of iron translocation by a Dps protein from Microbacterium arborescens". In: *Journal of Biological Chemistry* vol. 286. no. 40 (2011), pp. 34872–34882.

[65] Asuncion Martinez and Roberto Kolter. "Protection of DNA during oxidative stress by the nonspecific DNA-binding protein Dps." In: *Journal of bacteriology* vol. 179. no. 16 (1997), pp. 5188–5194.

[66] Felix Frolow, A Joseph Kalb, and Joseph Yariv. "Structure of a unique twofold symmetric haem-binding site". In: *Nature Structural & Molecular Biology* vol. 1. no. 7 (1994), pp. 453–460.

[67] PM Harrison, SC Andrews, PJ Artymiuk, GC Ford, JR Guest, J Hirzmann, DM Lawson, JC Livingstone, JMA Smith, A Treffry, et al. "Probing structure-function relations in ferritin and bacterioferritin". In: *Advances in inorganic chemistry* vol. 36 (1991), pp. 449–486.

[68] Simon C Andrews, Pauline M Harrison, Stephen J Yewdall, Paolo Arosio, Sonia Levi, Werner Bottke, Matthias von Darl, Jean-François Briat, Jean-Pierre Laulhère, and Stephane Lobreaux. "Structure, function, and evolution of ferritins". In: *Journal of inorganic biochemistry* vol. 47. no. 1 (1992), pp. 161–174.

[69] Elizabeth C Theil. "Ferritin: structure, gene regulation, and cellular function in animals, plants, and microorganisms". In: *Annual review of biochemistry* vol. 56. no. 1 (1987), pp. 289–315.

[70] Stephanie Pfaffen, Raz Abdulqadir, Nick E Le Brun, and Michael EP Murphy. "Mechanism of ferrous iron binding and oxidation by ferritin from a pennate diatom". In: *Journal of Biological Chemistry* vol. 288. no. 21 (2013), pp. 14917–14925.

[71] Dustin JE Huard, Kathleen M Kane, and F Akif Tezcan. "Re-engineering protein interfaces yields copper-inducible ferritin cage assembly". In: *Nature chemical biology* vol. 9. no. 3 (2013), pp. 169–176.

[72] Sergey P Martsev, Alexander P Vlasov, and Paolo Arosio. "Distinct stability of recombinant L and H subunits of human ferritin: calorimetric and ANS binding studies." In: *Protein engineering* vol. 11. no. 5 (1998), pp. 377–381.

[73] José M Domínguez-Vera and Enrique Colacio. "Nanoparticles of Prussian blue ferritin: a new route for obtaining nanomaterials". In: *Inorganic chemistry* vol. 42. no. 22 (2003), pp. 6983–6985.

[74] James W Drysdale. "Ferritin phenotypes: structure and metabolism". In: *Ciba Foundation Symposium 51-Iron Metabolism*. Wiley Online Library. 1977, pp. 41–78.

[75] Paul D Hempstead, Stephen J Yewdall, Alisdair R Fernie, David M Lawson, Peter J Artymiuk, David W Rice, Geoffrey C Ford, and Pauline M Harrison. "Comparison of the three-dimensional structures of recombinant human H and horse L ferritins

at high resolution". In: *Journal of molecular biology* vol. 268. no. 2 (1997), pp. 424–448.

[76] S Levi, SJ Yewdall, PM Harrison, P Santambrogio, A Cozzi, E Rovida, A Albertini, and P Arosio. "Evidence of H-and L-chains have co-operative roles in the iron-uptake mechanism of human ferritin". In: *Biochemical Journal* vol. 288. no. 2 (1992), pp. 591–596.

[77] C Bernacchioni, V Ghini, EC Theil, and P Turano. "Modulating the permeability of ferritin channels". In: *RSC Advances* vol. 6. no. 25 (2016), pp. 21219–21227.

[78] Robert R Crichton and Jean-Paul Declercq. "X-ray structures of ferritins and related proteins". In: *Biochimica et Biophysica Acta (BBA)-General Subjects* vol. 1800. no. 8 (2010), pp. 706–718.

[79] GC Ford, PM Harrison, DW Rice, JMA Smith, A Treffry, JL White, and J Yariv. "Ferritin: design and formation of an iron-storage molecule". In: *Philosophical Transactions of the Royal Society of London B: Biological Sciences* vol. 304. no. 1121 (1984), pp. 551–565.

[80] FA Fischbach and JW Anderegg. "An X-ray scattering study of ferritin and apoferritin". In: *Journal of molecular biology* vol. 14. no. 2 (1965), 458IN15–473.

[81] S Pead, E Durrant, B Webb, C Larsen, D Heaton, J Johnson, and GD Watt. "Metal ion binding to apo, holo, and reconstituted horse spleen ferritin". In: *Journal of inorganic biochemistry* vol. 59. no. 1 (1995), pp. 15–27.

[82] Elizabeth C Theil, Rabindra K Behera, and Takehiko Tosha. "Ferritins for chemistry and for life". In: *Coordination chemistry reviews* vol. 257. no. 2 (2013), pp. 579–586.

[83] Daniela Lalli and Paola Turano. "Solution and solid state NMR approaches to draw iron pathways in the ferritin nanocage". In: *Accounts of chemical research* vol. 46. no. 11 (2013), pp. 2676–2685.

[84] Trevor Douglas and Daniel R Ripoll. "Calculated electrostatic gradients in recombinant human H-chain ferritin". In: *Protein Science* vol. 7. no. 5 (1998), pp. 1083–1091.

[85] KJ Hintze and EC Theil. "Cellular regulation and molecular interactions of the ferritins". In: *Cellular and Molecular Life Sciences* vol. 63. no. 5 (2006), pp. 591–600.

[86] Sun-Ah You and Qing Wang. "Ferritin in atherosclerosis". In: *Clinica Chimica Acta* vol. 357. no. 1 (2005), pp. 1–16.

[87] Fadi Bou-Abdallah. "The iron redox and hydrolysis chemistry of the ferritins". In: *Biochimica et Biophysica Acta (BBA)-General Subjects* vol. 1800. no. 8 (2010), pp. 719–731.

[88] Lucio Colombi Ciacchi and Mike C Payne. "The entry pathway of O_2 into human ferritin". In: *Chemical physics letters* vol. 390. no. 4 (2004), pp. 491–495.

[89] Ivano Bertini, Daniela Lalli, Stefano Mangani, Cecilia Pozzi, Camilla Rosa, Elizabeth C Theil, and Paola Turano. "Structural insights into the ferroxidase site of ferritins from higher eukaryotes". In: *Journal of the American Chemical Society* vol. 134. no. 14 (2012), pp. 6169–6176.

[90] Louise Toussaint, Luc Bertrand, Louis Hue, Robert R Crichton, and Jean-Paul Declercq. "High-resolution X-ray structures of human apoferritin H-chain mutants correlated with their activity and metal-binding sites". In: *Journal of molecular biology* vol. 365. no. 2 (2007), pp. 440–452.

[91] Xiaofeng Liu and Elizabeth C Theil. "Ferritins: dynamic management of biological iron and oxygen chemistry". In: *Accounts of chemical research* vol. 38. no. 3 (2005), pp. 167–175.

[92] Craig C Jolley, Masaki Uchida, Courtney Reichhardt, Richard Harrington, Sebyung Kang, Michael T Klem, John B Parise, and Trevor Douglas. "Size and crystallinity in protein-templated inorganic nanoparticles". In: *Chemistry of Materials* vol. 22. no. 16 (2010), pp. 4612–4618.

[93] Nick E Le Brun, Allister Crow, Michael EP Murphy, A Grant Mauk, and Geoffrey R Moore. "Iron core mineralisation in prokaryotic ferritins". In: *Biochimica Et Biophysica Acta (BBA)-General Subjects* vol. 1800. no. 8 (2010), pp. 732–744.

[94] Allison Lewin, Geoffrey R Moore, and Nick E Le Brun. "Formation of protein-coated iron minerals". In: *Dalton transactions* no. 22 (2005), pp. 3597–3610.

[95] F. M. Michel, L. Ehm, S. M. Antao, P. L. Lee, P. J. Chupas, G. Liu, D. R. Strongin, M. A. A. Schoonen, B. L. Phillips, and J. B. Parise. "The Structure of Ferrihydrite, a Nanocrystalline Material". In: *Science* vol. 316. no. 5832 (2007), pp. 1726–1729.

[96] Nan Jian, Miriam Dowle, Richard D Horniblow, Chris Tselepis, and Richard E Palmer. "Morphology of the ferritin iron core by aberration corrected scanning transmission electron microscopy". In: *Nanotechnology* vol. 27. no. 46 (2016), 46LT02.

[97] VA Drits, BA Sakharov, AL Salyn, and A Manceau. "Structural model for ferrihydrite". In: *Clay Minerals* vol. 28 (1993), pp. 185–185.

[98] Lena Mazeina and Alexandra Navrotsky. "Enthalpy of Water Adsorption and Surface Enthalpy of Goethite (α-FeOOH) and Hematite (α-Fe_2O_3)". In: *Chemistry of Materials* vol. 19. no. 4 (2007), pp. 825–833.

[99] Juraj Majzlan, Klaus-Dieter Grevel, and Alexandra Navrotsky. "Thermodynamics of Fe oxides: Part II. Enthalpies of formation and relative stability of goethite (α-FeOOH), lepidocrocite (γ-FeOOH), and maghemite (γ-Fe2O3)". In: *American Mineralogist* vol. 88. no. 5-6 (2003), pp. 855–859.

[100] Claar van der Zee, Darryl R Roberts, Denis G Rancourt, and Caroline P Slomp. "Nanogoethite is the dominant reactive oxyhydroxide phase in lake and marine sediments". In: *Geology* vol. 31. no. 11 (2003), pp. 993–996.

[101] Rochelle M Cornell and Udo Schwertmann. *The iron oxides: structure, properties, reactions, occurrences and uses*. Wiley. com, 2003.

[102] Daniel Tunega. "Theoretical Study of Properties of Goethite (α-FeOOH) at Ambient and High-Pressure Conditions". In: *The Journal of Physical Chemistry C* vol. 116. no. 11 (2012), pp. 6703–6713.

[103] Benedict Russell, Mike Payne, and Lucio Ciacchi. "Density functional theory study of Fe(II) adsorption and oxidation on goethite surfaces". In: *Physical Review B* vol. 79. no. 16 (2009).

[104] Jean-François Boily, Johannes Lützenkirchen, Olivier Balmmés, James Beattie, and Staffan Sjöberg. "Modeling proton binding at the goethite (α-FeOOH)-water interface". In: *Colloids and Surfaces A: Physicochemical and Engineering Aspects* vol. 179. no. 1 (2001), pp. 11–27.

[105] Julen Larrucea, Steffen Lid, and Lucio Colombi Ciacchi. "Parametrization of a classical force field for iron oxyhydroxide/water interfaces based on Density Functional Theory calculations". In: *Computational Materials Science* vol. 92 (2014), pp. 343–352.

[106] Dawn E. Janney, John M. Cowley, and Peter R. Buseck. "Transmission electron microscopy of synthetic 2- and 6-line ferrihydrite". In: *Clays and Clay Minerals* vol. 48. no. 1 (2000), pp. 111–119.

[107] A. Cristina Cismasu, F. Marc Michel, A. Patricia Tcaciuc, Tolek Tyliszczak, and Gordon E. Brown. "Composition and structural aspects of naturally occurring ferrihydrite". In: *Comptes Rendus Geoscience* vol. 343. no. 2-3 (2011), pp. 210–218.

[108] F. Marc Michel, Vidal Barrón, José Torrent, María P. Morales, Carlos J. Serna, Jean-François Boily, Qingsong Liu, Andrea Ambrosini, A. Cristina Cismasu, and Gordon E. Brown. "Ordered ferrimagnetic form of ferrihydrite reveals links among structure, composition, and magnetism". In: *Proceedings of the National Academy of Sciences* vol. 107. no. 7 (2010), pp. 2787–2792.

[109] John L. Jambor and John E. Dutrizac. "Occurrence and Constitution of Natural and Synthetic Ferrihydrite, a Widespread Iron Oxyhydroxide". In: *Chemical Reviews* vol. 98. no. 7 (1998), pp. 2549–2586.

[110] Tjisse Hiemstra. "Surface and mineral structure of ferrihydrite". In: *Geochimica et Cosmochimica Acta* vol. 105 (2013), pp. 316–325.

[111] Nathan Pinney, James D. Kubicki, Derek S. Middlemiss, Clare P. Grey, and Dane Morgan. "Density Functional Theory Study of Ferrihydrite and Related Fe-Oxyhydroxides". In: *Chemistry of Materials* vol. 21. no. 24 (2009), pp. 5727–5742.

[112] T. Hiemstra and W.H. van Riemsdijk. "A surface structural model for ferrihydrite I: Sites related to primary charge, molar mass, and mass density". In: *Geochimica et Cosmochimica Acta* vol. 73. no. 15 (2009), pp. 4423–4436.

[113] Emilie M Pouget, Paul HH Bomans, Jeroen ACM Goos, Peter M Frederik, Nico AJM Sommerdijk, et al. "The initial stages of template-controlled $CaCO_3$ formation revealed by cryo-TEM". In: *Science* vol. 323. no. 5920 (2009), pp. 1455–1458.

[114] Jens Baumgartner, Guillaume Morin, Nicolas Menguy, Teresa Perez Gonzalez, Marc Widdrat, Julie Cosmidis, and Damien Faivre. "Magnetotactic bacteria form magnetite from a phosphate-rich ferric hydroxide via nanometric ferric (oxyhydr) oxide intermediates". In: *Proceedings of the National Academy of Sciences* vol. 110. no. 37 (2013), pp. 14883–14888.

[115] Nils Hildebrand, Susan Köppen, Ludmilla Derr, Kaibo Li, Mohammad Koleini, Kurosch Rezwan, and Lucio Colombi Ciacchi. "Adsorption orientation and binding motifs of lysozyme and chymotrypsin on amorphous silica". In: *The Journal of Physical Chemistry C* vol. 119. no. 13 (2015), pp. 7295–7307.

[116] Anke Butenuth, Gianpietro Moras, Julian Schneider, Mohammad Koleini, Susan Köppen, Robert Meißner, Louise B. Wright, Tiffany R. Walsh, and Lucio Colombi Ciacchi. "Ab initio derived force-field parameters for molecular dynamics simulations of deprotonated amorphous-SiO_2/water interfaces". In: *physica status solidi (b)* vol. 249. no. 2 (2011), pp. 292–305.

[117] D.A. Case, T.A. Darden, T.E. Cheatham, C.L. Simmerling, J. Wang, R.E. Duke, R. Luo, R.C. Walker, W. Zhang, K.M. Merz, B. Roberts, S. Hayik, A. Roitberg, G. Seabra, J. Swails, A.W. Götz, I. Kolossvary, K.F. Wong, F. Paesani, J. Vanicek, R.M. Wolf, J. Liu, X. Wu, S.R. Brozell, T. Steinbrecher, H. Gohlke, Q. Cai, X. Ye, J. Wang, M.-J. Hsieh, G. Cui, D.R. Roe, D.H. Mathews, M.G. Seetin, R. Salomon-Ferrer, C. Sagui, V. Babin, T. Luchko, S. Gusarov, A. Kovalenko, and Kollman P.A. "AMBER 12". In: *University of California: San Francisco, CA* (2012).

[118] Fabian Meder, Timo Daberkow, Laura Treccani, Michaela Wilhelm, Marco Schowalter, Andreas Rosenauer, Lutz Mädler, and Kurosch Rezwan. "Protein adsorption on colloidal alumina particles functionalized with amino, carboxyl, sulfonate and phosphate groups". In: *Acta Biomaterialia* vol. 8. no. 3 (2012), pp. 1221–1229.

[119] PS Wang, SG Malghan, SM Hsu, DC Bartenfelder, and B Hegemann. "Surface chemistry of α-alumina powders treated by aqueous and nonaqueous solvents". In: *Ceram Trans* vol. 22 (1991), pp. 217–225.

[120] Daniel J Cole, Mike C Payne, Gábor Csányi, S Mark Spearing, and Lucio Colombi Ciacchi. "Development of a classical force field for the oxidized Si surface: Application to hydrophilic wafer bonding". In: *The Journal of chemical physics* vol. 127. no. 20 (2007), p. 204704.

[121] Daniel J Cole, Mike C Payne, and Lucio Colombi Ciacchi. "Water structuring and collagen adsorption at hydrophilic and hydrophobic silicon surfaces". In: *Physical Chemistry Chemical Physics* vol. 11. no. 48 (2009), pp. 11395–11399.

[122] Julian Schneider and Lucio Colombi Ciacchi. "A Classical Potential to Model the Adsorption of Biological Molecules on Oxidized Titanium Surfaces". In: *Journal of Chemical Theory and Computation* vol. 7. no. 2 (2011), pp. 473–484.

[123] Brian H Lower, Roberto D Lins, Zachery Oestreicher, Tjerk P Straatsma, Michael F Hochella Jr, Liang Shi, and Steven K Lower. "In vitro evolution of a peptide with a hematite binding motif that may constitute a natural metal-oxide binding archetype". In: *Environmental science & technology* vol. 42. no. 10 (2008), pp. 3821–3827.

[124] Stanley Brown. "Engineered iron oxide-adhesion mutants of the Escherichia coli phage lambda receptor." In: *Proceedings of the National Academy of Sciences* vol. 89. no. 18 (1992), pp. 8651–8655.

[125] PM Harrison, FA Fischbach, TG Hoy, and GH Haggis. "Ferric oxyhydroxide core of ferritin". In: *Nature* vol. 216. no. 5121 (1967), p. 1188.

[126] Dirk Zahn and Stefano Leoni. "Nucleation and growth in pressure-induced phase transitions from molecular dynamics simulations: Mechanism of the reconstructive transformation of NaCl to the CsCl-type structure". In: *Physical review letters* vol. 92. no. 25 (2004), p. 250201.

[127] Theodor Milek, Patrick Duchstein, Gotthard Seifert, and Dirk Zahn. "Motif Reconstruction in Clusters and Layers: Benchmarks for the Kawska–Zahn Approach to Model Crystal Formation". In: *ChemPhysChem* vol. 11. no. 4 (2010), pp. 847–852.

[128] David A. Pearlman, David A. Case, James W. Caldwell, Wilson S. Ross, Thomas E. Cheatham, Steve DeBolt, David Ferguson, George Seibel, and Peter Kollman. "AMBER, a package of computer programs for applying molecular mechanics, normal mode analysis, molecular dynamics and free energy calculations to simulate the structural and energetic properties of molecules". In: *Computer Physics Communications* vol. 91. no. 1-3 (1995), pp. 1–41.

[129] Steve Plimpton. "Fast Parallel Algorithms for Short-Range Molecular Dynamics". In: *Journal of Computational Physics* vol. 117. no. 1 (1995), pp. 1–19.

[130] H. A. Lorentz. "Ueber die Anwendung des Satzes vom Virial in der kinetischen Theorie der Gase". In: *Annalen der Physik* vol. 248. no. 1 (1881), pp. 127–136.

[131] Daniel Berthelot. "Sur le mélange des gaz". In: *Comptes rendus hebdomadaires des séances de l'Académie des Sciences* vol. 1. no. 126 (1898), pp. 1703–1855.

[132] William C Swope, Hans C Andersen, Peter H Berens, and Kent R Wilson. "A computer simulation method for the calculation of equilibrium constants for the formation of physical clusters of molecules: Application to small water clusters". In: *The Journal of Chemical Physics* vol. 76 (1982), p. 637.

[133] Shuichi Nosé. "A unified formulation of the constant temperature molecular dynamics methods". In: *The Journal of Chemical Physics* vol. 81. no. 1 (1984), p. 511.

[134] William Hoover. "Canonical dynamics: Equilibrium phase-space distributions". In: *Physical Review A* vol. 31. no. 3 (1985), pp. 1695–1697.

[135] Gareth A Tribello, Massimiliano Bonomi, Davide Branduardi, Carlo Camilloni, and Giovanni Bussi. "PLUMED 2: New feathers for an old bird". In: *Computer Physics Communications* vol. 185. no. 2 (2014), pp. 604–613.

[136] Alessandro Laio and Michele Parrinello. "Escaping free-energy minima". In: *Proceedings of the National Academy of Sciences* vol. 99. no. 20 (2002), pp. 12562–12566.

[137] Yuji Sugita and Yuko Okamoto. "Replica-exchange molecular dynamics method for protein folding". In: *Chemical physics letters* vol. 314. no. 1 (1999), pp. 141–151.

[138] Koji Hukushima and Koji Nemoto. "Exchange Monte Carlo method and application to spin glass simulations". In: *Journal of the Physical Society of Japan* vol. 65. no. 6 (1996), pp. 1604–1608.

[139] Pu Liu, Byungchan Kim, Richard A Friesner, and BJ Berne. "Replica exchange with solute tempering: A method for sampling biological systems in explicit water". In: *Proceedings of the National Academy of Sciences of the United States of America* vol. 102. no. 39 (2005), pp. 13749–13754.

[140] Hiroaki Fukunishi, Osamu Watanabe, and Shoji Takada. "On the Hamiltonian replica exchange method for efficient sampling of biomolecular systems: Application to protein structure prediction". In: *J. Chem. Phys.* vol. 116. no. 20 (2002), p. 9058.

[141] Giovanni Bussi, Francesco Luigi Gervasio, Alessandro Laio, and Michele Parrinello. "Free-energy landscape for β hairpin folding from combined parallel tempering and metadynamics". In: *Journal of the American Chemical Society* vol. 128. no. 41 (2006), pp. 13435–13441.

[142] Robert H. Meißner, Julian Schneider, Peter Schiffels, and Lucio Colombi Ciacchi. "Computational Prediction of Circular Dichroism Spectra and Quantification of Helicity Loss upon Peptide Adsorption on Silica". In: *Langmuir* vol. 30. no. 12 (2014), pp. 3487–3494.

[143] Julian Schneider and Lucio Colombi Ciacchi. "Specific Material Recognition by Small Peptides Mediated by the Interfacial Solvent Structure". In: *Journal of the American Chemical Society* vol. 134. no. 4 (2012), pp. 2407–2413.

[144] Max Born and Robert Oppenheimer. "Zur Quantentheorie der Moleküle". In: *Annalen der Physik* vol. 389. no. 20 (1927), pp. 457–484.

[145] Pierre Hohenberg and Walter Kohn. "Inhomogeneous electron gas". In: *Physical review* vol. 136. no. 3B (1964), B864.

[146] Walter Kohn and Lu Jeu Sham. "Self-consistent equations including exchange and correlation effects". In: *Physical Review* vol. 140. no. 4A (1965), A1133.

[147] John P Perdew, Kieron Burke, and Matthias Ernzerhof. "Generalized gradient approximation made simple". In: *Physical review letters* vol. 77. no. 18 (1996), p. 3865.

[148] G. Kresse and J. Hafner. "Ab initio molecular dynamics for liquid metals". In: *Physical Review B* vol. 47 (1993), pp. 558–561.

[149] G. Kresse and J. Hafner. "Ab initio molecular-dynamics simulation of the liquid-metal-amorphous-semiconductor transition in germanium". In: *Physical Review B* vol. 49 (1994), pp. 14251–14269.

[150] G. Kresse and J. Furthmüller. "Efficiency of ab-initio total energy calculations for metals and semiconductors using a plane-wave basis set ". In: *Computational Materials Science* vol. 6. no. 1 (1996), pp. 15–50.

[151] G. Kresse. "Efficient iterative schemes for ab initio total-energy calculations using a plane-wave basis set". In: *Physical Review B* vol. 54. no. 16 (1996), pp. 11169–11186.

[152] Peter E Blöchl. "Projector augmented-wave method". In: *Physical Review B* vol. 50. no. 24 (1994), p. 17953.

[153] DJ Chadi and Marvin L Cohen. "Special points in the Brillouin zone". In: *Physical Review B* vol. 8. no. 12 (1973), p. 5747.

[154] Hendrik J. Monkhorst and James D. Pack. "Special points for Brillouin-zone integrations". In: *Physical Review B* vol. 13. no. 12 (1976), pp. 5188–5192.

[155] Vladimir I Anisimov, Jan Zaanen, and Ole K Andersen. "Band theory and Mott insulators: Hubbard U instead of Stoner I". In: *Physical Review B* vol. 44. no. 3 (1991), p. 943.

[156] V. I. Anisimov, I. V. Solovyev, and M. A. Korotin. "Density-functional theory and NiO photoemission spectra". In: *Physical Review B* vol. 48. no. 23 (1993), pp. 16929–16934.

[157] I. V. Solovyev and P. H. Dederichs. "Corrected atomic limit in the local-density approximation and the electronic structure of d impurities in Rb". In: *Physical Review B* vol. 50. no. 23 (1994), pp. 16861–16871.

[158] Matteo Cococcioni and Stefano de Gironcoli. "Linear response approach to the calculation of the effective interaction parameters in the LDA+U method". In: *Physical Review B* vol. 71. no. 3 (2005).

[159] G Rollmann, A Rohrbach, P Entel, and J Hafner. "First-principles calculation of the structure and magnetic phases of hematite". In: *Physical Review B* vol. 69. no. 16 (2004), p. 165107.

[160] Anke Butenuth, Gianpietro Moras, Julian Schneider, Mohammad Koleini, Susan Köppen, Robert Meißner, Writh Louise B., Tiffany R. Walsh, and Lucio Colombi Ciacchi. "Ab initio derived force-field parameters for molecular dynamics simulations of deprotonated amorphous-SiO_2/water interfaces". In: *Physica Status Solidi (b)* vol. 249. no. 2 (2012), pp. 292–305.

[161] Y. Andersson, D. Langreth, and B. Lundqvist. "van der Waals Interactions in Density-Functional Theory". In: *Physical Review Letters* vol. 76. no. 1 (1996), pp. 102–105.

[162] Kyuho Lee, Éamonn D. Murray, Lingzhu Kong, Bengt I. Lundqvist, and David C. Langreth. "Higher-accuracy van der Waals density functional". In: *Physical Review B* vol. 82. no. 8 (2010).

[163] Yingkai Zhang and Weitao Yang. "Comment on "Generalized Gradient Approximation Made Simple"". In: *Phys. Rev. Lett.* vol. 80 (1998), pp. 890–890.

[164] John P Perdew and Wang Yue. "Accurate and simple density functional for the electronic exchange energy: Generalized gradient approximation". In: *Physical Review B* vol. 33. no. 12 (1986), p. 8800.

[165] R. Car and M. Parrinello. "Unified Approach for Molecular Dynamics and Density-Functional Theory". In: *Physical Review Letters* vol. 55. no. 22 (1985), pp. 2471–2474.

[166] Dominik Marx and Jurg Hutter. "Ab initio molecular dynamics: Theory and implementation". In: *Modern methods and algorithms of quantum chemistry* vol. 1. no. 301-449 (2000), p. 141.

[167] Daniel Carmona, Laura Treccani, Monika Michaelis, Steffen Lid, Christian Debus, Lucio Colombi Ciacchi, Kurosch Rezwan, and Michael Maas. "Mineralization of Iron Oxide Induced by Ferritin Subunits Immobilized on Silica Nanoparticles". In: (2018), submitted.

[168] Naiara I. Vazquez, Zoilo González, Begona Ferrari, and Y Castro. "Synthesis of mesoporous silica nanoparticles by sol-gel as nanocontainer for future drug delivery applications". In: vol. 56 (2017).

[169] Stephen Kroll, Christoph Brandes, Julia Wehling, Laura Treccani, Georg Grathwohl, and Kurosch Rezwan. "Highly efficient enzyme-functionalized porous zirconia microtubes for bacteria filtration". In: *Environmental science & technology* vol. 46. no. 16 (2012), pp. 8739–8747.

[170] Laura Treccani, Marcus Maiwald, Volker Zöllmer, Matthias Busse, Georg Grathwohl, and Kurosch Rezwan. "Antibacterial and Abrasion-Resistant Alumina Micropatterns". In: *Advanced Engineering Materials* vol. 11. no. 7 (2009).

[171] Steffen Lid, Susan Köppen, and Lucio Colombi Ciacchi. "Creation of models and parametrization of a classical force field for amorphous Al_2O_3/water interfaces based on Density Functional Theory". In: *Computational Materials Science* vol. 140 (2017), pp. 307–314.

[172] Ralf Dringen, Yvonne Koehler, Ludmilla Derr, Giulia Tomba, Maike M. Schmidt, Laura Treccani, Lucio Colombi Ciacchi, and Kurosch Rezwan. "Adsorption and Reduction of Glutathione Disulfide on α-Al_2O_3 Nanoparticles: Experiments and Modeling". In: *Langmuir* vol. 27. no. 15 (2011), pp. 9449–9457.

[173] Karen Johnston, Claudia R. Herbers, and Nico F. A. van der Vegt. "Development of Classical Molecule-Surface Interaction Potentials Based on Density Functional Theory Calculations: Investigation of Force Field Representability". In: *The Journal of Physical Chemistry C* vol. 116. no. 37 (2012), pp. 19781–19788.

[174] S.P. Adiga, P. Zapol, and L.A. Curtiss. "Structure and Morphology of Hydroxylated Amorphous Alumina Surfaces". In: *Journal of Physical Chemistry C* vol. 111. no. 20 (2007), pp. 7422–7429.

[175] M. Matsui. "A Transferable Interatomic Potential Model for Crystals and Melts in the System CaO-MgO-Al_2O_3-SiO_2". In: *Mineralogical Magazine* vol. 58A. no. 2 (1994), pp. 571–572.

[176] Evgueni Chagarov and Andrew C. Kummel. "Generation of Realistic Amorphous Al_2O_3 and ZrO_2 Samples By Hybrid Classical and First-Principle Molecular Dynamics Simulations". In: *ECS Transactions*. Electrochemical Society, 2008, pp. 773–785.

[177] Gonzalo Gutiérrez and Börje Johansson. "Molecular dynamics study of structural properties of amorphous Al_2O_3". In: *Physical Review B* vol. 65. no. 10 (2002), p. 104202.

[178] P. Lamparter and R. Kniep. "Structure of amorphous Al_2O_3". In: *Physica B: Condensed Matter* vol. 234-236 (1997), pp. 405–406.

[179] S. P. Adiga, P. Zapol, and L. A. Curtiss. "Atomistic simulations of amorphous alumina surfaces". In: *Phys. Rev. B* vol. 74. no. 6 (2006).

[180] K. C. Hass. "The Chemistry of Water on Alumina Surfaces: Reaction Dynamics from First Principles". In: *Science* vol. 282. no. 5387 (1998), pp. 265–268.

[181] K. C. Hass, W. F. Schneider, A. Curioni, and W. Andreoni. "First-Principles Molecular Dynamics Simulations of H_2O on α-Al_2O_3 (0001)". In: *J. Phys. Chem. B* vol. 104. no. 23 (2000), pp. 5527–5540.

[182] H. Knözinger and P. Ratnasamy. "Catalytic Aluminas: Surface Models and Characterization of Surface Sites". In: *Catalysis Reviews* vol. 17. no. 1 (1978), pp. 31–70.

[183] Jizhong Sun, T. Stirner, W.E. Hagston, A. Leyland, and A. Matthews. "A simple transferable interatomic potential model for binary oxides applied to bulk and the (0001) surface". In: *Journal of Crystal Growth* vol. 290. no. 1 (2006), pp. 235–240.

[184] Sandro Jahn, Paul Madden, and Mark Wilson. "Transferable interaction model for Al_2O_3". In: *Physical Review B* vol. 74. no. 2 (2006).

[185] Micael Baudin and Kersti Hermansson. "Metal oxide surface dynamics from molecular dynamics simulations: the α-Al_2O_3(0001) surface". In: *Surface Science* vol. 474. no. 1-3 (2001), pp. 107–113.

[186] F. H. Streitz and J. W. Mintmire. "Electrostatic potentials for metal-oxide surfaces and interfaces". In: *Physical Review B* vol. 50. no. 16 (1994), pp. 11996–12003.

[187] A. K. Rappe, C. J. Casewit, K. S. Colwell, W. A. Goddard, and W. M. Skiff. "UFF, a full periodic table force field for molecular mechanics and molecular dynamics simulations". In: *Journal of the American Chemical Society* vol. 114. no. 25 (1992), pp. 10024–10035.

[188] Kim Bolton, Bosio, William L. Hase, William F. Schneider, and Kenneth C. Hass. "Comparison of Explicit and United Atom Models for Alkane Chains Physisorbed on α-Al_2O_3 (0001)". In: *J. Phys. Chem. B* vol. 103. no. 19 (1999), pp. 3885–3895.

[189] Michael F. Russo, Rong Li, Matthew Mench, and Adri C.T. van Duin. "Molecular dynamic simulation of aluminum-water reactions using the ReaxFF reactive force field". In: *International Journal of Hydrogen Energy* vol. 36. no. 10 (2011), pp. 5828–5835.

[190] A. D. MacKerell, D. Bashford, M. Bellott, R. L. Dunbrack, J. D. Evanseck, M. J. Field, S. Fischer, J. Gao, H. Guo, S. Ha, and et al. "All-Atom Empirical Potential for Molecular Modeling and Dynamics Studies of Proteins". In: *J. Phys. Chem. B* vol. 102. no. 18 (1998), pp. 3586–3616.

[191] William L. Jorgensen and Julian. Tirado-Rives. "The OPLS [optimized potentials for liquid simulations] potential functions for proteins, energy minimizations for crystals of cyclic peptides and crambin". In: *Journal of the American Chemical Society* vol. 110. no. 6 (1988), pp. 1657–1666.

[192] Carlos Campañá, Bastien Mussard, and Tom K. Woo. "Electrostatic Potential Derived Atomic Charges for Periodic Systems Using a Modified Error Functional". In: *Journal of Chemical Theory and Computation* vol. 5. no. 10 (2009), pp. 2866–2878.

[193] Julian D Gale. "GULP: A computer program for the symmetry-adapted simulation of solids". In: *Journal of the Chemical Society, Faraday Transactions* vol. 93. no. 4 (1997), pp. 629–637.

[194] Junmei Wang, Romain M. Wolf, James W. Caldwell, Peter A. Kollman, and David A. Case. "Development and testing of a general amber force field". In: *Journal of Computational Chemistry* vol. 25. no. 9 (2004), pp. 1157–1174.

[195] Marek Kosmulski. *Chemical properties of material surfaces*. Vol. 102. CRC press, 2001.

[196] Justin W. Ntalikwa. "Determination of surface charge density of α-alumina by Acid-base titration". In: *Bull. Chem. Soc. Eth.* vol. 21. no. 1 (2007).

[197] David van der Spoel, Paul J. van Maaren, and Herman J. C. Berendsen. "A systematic study of water models for molecular simulation: Derivation of water models optimized for use with a reaction field". In: *J. Chem. Phys.* vol. 108. no. 24 (1998), p. 10220.

[198] Raymond L. Venable, William H. Wade, and Norman Hackerman. "Heats of Immersion. VIII. Differential Heats of Adsorption as a Function of Particle Size for the Alumina-Water System". In: *J. Phys. Chem.* vol. 69. no. 1 (1965), pp. 317–321.

[199] W. H. Wade and Norman Hackerman. "HEATS OF IMMERSION. IV. THE ALUMINA-WATER SYSTEM—VARIATIONS WITH PARTICLE SIZE AND OUTGASSING TEMPERATURE". In: *J. Phys. Chem.* vol. 64. no. 9 (1960), pp. 1196–1199.

[200] A. C. Makrides and Norman Hackerman. "Heats of Immersion. I. The System Silica-water". In: *J. Phys. Chem.* vol. 63. no. 4 (1959), pp. 594–598.

[201] Tetsuo Morimoto, Koichi Shiomi, and Hiroshi Tanaka. "The Heat of Immersion of Aluminum Oxide in Water". In: *Bull. Chem. Soc. Jpn.* vol. 37. no. 3 (1964), pp. 392–395.

[202] Fabian Meder, Henrik Hintz, Yvonne Koehler, Maike M. Schmidt, Laura Treccani, Ralf Dringen, and Kurosch Rezwan. "Adsorption and Orientation of the Physiological Extracellular Peptide Glutathione Disulfide on Surface Functionalized Colloidal Alumina Particles". In: *Journal of the American Chemical Society* vol. 135. no. 16 (2013), pp. 6307–6316.

[203] William Humphrey, Andrew Dalke, and Klaus Schulten. "VMD – Visual Molecular Dynamics". In: *Journal of Molecular Graphics* vol. 14 (1996), pp. 33–38.

[204] BV Derjaguin, L Landau, et al. "Theory of the stability of strongly charged lyophobic sols and of the adhesion of strongly charged particles in solutions of electrolytes". In: *Acta physicochim. URSS* vol. 14. no. 6 (1941), pp. 633–662.

[205] EJW Verwey. "Theory of the stability of lyophobic colloids." In: *The Journal of Physical Chemistry* vol. 51. no. 3 (1947), pp. 631–636.

[206] J. Sonnefeld. "Surface charge density on spherical silica particles in aqueous alkali chloride solutions". In: *Colloid and Polymer Science* vol. 273. no. 10 (1995), pp. 932–938.

[207] Patricia M Dove and Colin M Craven. "Surface charge density on silica in alkali and alkaline earth chloride electrolyte solutions". In: *Geochimica et Cosmochimica Acta* vol. 69. no. 21 (2005), pp. 4963–4970.

[208] Motoyoshi Kobayashi, Frédéric Juillerat, Paolo Galletto, Paul Bowen, and Michal Borkovec. "Aggregation and charging of colloidal silica particles: effect of particle size". In: *Langmuir* vol. 21. no. 13 (2005), pp. 5761–5769.

[209] Fiona C Meldrum, Brigid R Heywood, and Stephen Mann. "Magnetoferritin: in vitro synthesis of a novel magnetic protein". In: *Science* vol. 257. no. 5069 (1992), pp. 522–524.

[210] Fiona C Meldrum, Trevor Douglas, Sonia Levi, Paolo Arosio, and Stephen Mann. "Reconstitution of manganese oxide cores in horse spleen and recombinant ferritins". In: *Journal of inorganic biochemistry* vol. 58. no. 1 (1995), pp. 59–68.

[211] Kim KW Wong, Trevor Douglas, Savas Gider, David D Awschalom, and Stephen Mann. "Biomimetic synthesis and characterization of magnetic proteins (magnetoferritin)". In: *Chemistry of materials* vol. 10. no. 1 (1998), pp. 279–285.

[212] Julian Schneider and Lucio Colombi Ciacchi. "First principles and classical modeling of the oxidized titanium (0001) surface". In: *Surface Science* vol. 604. no. 13 (2010), pp. 1105–1115.

[213] FD Murnaghan. "The compressibility of media under extreme pressures". In: *Proceedings of the national academy of sciences of the United States of America* vol. 30. no. 9 (1944), p. 244.

[214] Arianna E Gleason, Raymond Jeanloz, and Martin Kunz. "Pressure-temperature stability studies of FeOOH using X-ray diffraction". In: *American Mineralogist* vol. 93. no. 11-12 (2008), pp. 1882–1885.

[215] P.F. Rossi. "Heats of immersion of iron oxide pigments in water: Geothite and hematite". In: *Materials Chemistry* vol. 3. no. 1 (1978), pp. 7–15.

[216] Mihee Kim, Yecheol Rho, Kyeong Sik Jin, Byungcheol Ahn, Sungmin Jung, Heesoo Kim, and Moonhor Ree. "pH-Dependent Structures of Ferritin and Apoferritin in Solution: Disassembly and Reassembly". In: *Biomacromolecules* vol. 12. no. 5 (2011), pp. 1629–1640.

[217] Cecilia Pozzi, Silvia Ciambellotti, Caterina Bernacchioni, Flavio Di Pisa, Stefano Mangani, and Paola Turano. "Chemistry at the protein–mineral interface in L-ferritin assists the assembly of a functional (μ3-oxo) Tris [(μ2-peroxo)] triiron (III) cluster". In: *Proceedings of the National Academy of Sciences* (2017), p. 201614302.

[218] Paola Turano, Daniela Lalli, Isabella C Felli, Elizabeth C Theil, and Ivano Bertini. "NMR reveals pathway for ferric mineral precursors to the central cavity of ferritin". In: *Proceedings of the National Academy of Sciences* vol. 107. no. 2 (2010), pp. 545–550.

[219] Michael Mertig, Lucio Colombi Ciacchi, Ralf Seidel, Wolfgang Pompe, and Alessandro De Vita. "DNA as a selective metallization template". In: *Nano Letters* vol. 2. no. 8 (2002), pp. 841–844.

[220] Steffen Lid, Daniel Carmona, Michael Maas, Laura Treccani, and Lucio Colombi Ciacchi. "Anchoring of Iron Oxyhydroxide Clusters at H and L Ferritin Subunits". In: *ACS Biomaterials Science & Engineering* (2018).

[221] Yiying Wu and Peidong Yang. "Direct observation of vapor- liquid- solid nanowire growth". In: *Journal of the American Chemical Society* vol. 123. no. 13 (2001), pp. 3165–3166.

[222] Urs Gasser, Eric R Weeks, Andrew Schofield, PN Pusey, and DA Weitz. "Real-space imaging of nucleation and growth in colloidal crystallization". In: *Science* vol. 292. no. 5515 (2001), pp. 258–262.

[223] U Kaiser, DA Muller, JL Grazul, A Chuvilin, and M Kawasaki. "Direct observation of defect-mediated cluster nucleation". In: *Nature Materials* vol. 1. no. 2 (2002), p. 102.

[224] Yan Liang, David G Lynn, and Keith M Berland. "Direct observation of nucleation and growth in amyloid self-assembly". In: *Journal of the American Chemical Society* vol. 132. no. 18 (2010), pp. 6306–6308.

[225] Koji Harano, Tatsuya Homma, Yoshiko Niimi, Masanori Koshino, Kazu Suenaga, Ludwik Leibler, and Eiichi Nakamura. "Heterogeneous nucleation of organic crystals mediated by single-molecule templates". In: *Nature materials* vol. 11. no. 10 (2012), p. 877.

[226] Thomas Huber, Andrew E Torda, and Wilfred F van Gunsteren. "Local elevation: a method for improving the searching properties of molecular dynamics simulation". In: *Journal of computer-aided molecular design* vol. 8. no. 6 (1994), pp. 695–708.

[227] Glenn M Torrie and John P Valleau. "Nonphysical sampling distributions in Monte Carlo free-energy estimation: Umbrella sampling". In: *Journal of Computational Physics* vol. 23. no. 2 (1977), pp. 187–199.

[228] Stefan Auer and Daan Frenkel. "Prediction of absolute crystal-nucleation rate in hard-sphere colloids". In: *Nature* vol. 409. no. 6823 (2001), p. 1020.

[229] C Dellago, PG Bolhuis, and PL Geissler. "Adv. Chem. Phys." In: no. 123 (2002), pp. 1–78.

[230] Dorothy M Duffy and John H Harding. "Simulation of organic monolayers as templates for the nucleation of calcite crystals". In: *Langmuir* vol. 20. no. 18 (2004), pp. 7630–7636.

[231] JH Harding and DM Duffy. "The challenge of biominerals to simulations". In: *Journal of Materials Chemistry* vol. 16. no. 12 (2006), pp. 1105–1112.

[232] Simone Marsili, Alessandro Barducci, Riccardo Chelli, Piero Procacci, and Vincenzo Schettino. "Self-healing umbrella sampling: a non-equilibrium approach for quantitative free energy calculations". In: *The Journal of Physical Chemistry B* vol. 110. no. 29 (2006), pp. 14011–14013.

[233] Richard P Sear. "Nucleation: theory and applications to protein solutions and colloidal suspensions". In: *Journal of Physics: Condensed Matter* vol. 19. no. 3 (2007), p. 033101.

[234] Alessandro Barducci, Giovanni Bussi, and Michele Parrinello. "Well-Tempered Metadynamics: A Smoothly Converging and Tunable Free-Energy Method". In: *Physical Review Letters* vol. 100. no. 2 (2008).

[235] Rosalind J Allen, Chantal Valeriani, and Pieter Rein ten Wolde. "Forward flux sampling for rare event simulations". In: *Journal of physics: Condensed matter* vol. 21. no. 46 (2009), p. 463102.

[236] Baron Peters. "Competing nucleation pathways in a mixture of oppositely charged colloids: Out-of-equilibrium nucleation revisited". In: *The Journal of chemical physics* vol. 131. no. 24 (2009), p. 244103.

[237] Jamshed Anwar and Dirk Zahn. "Uncovering molecular processes in crystal nucleation and growth by using molecular simulation". In: *Angewandte Chemie International Edition* vol. 50. no. 9 (2011), pp. 1996–2013.

[238] Wolfgang Lechner, Christoph Dellago, and Peter G Bolhuis. "Role of the prestructured surface cloud in crystal nucleation". In: *Physical review letters* vol. 106. no. 8 (2011), p. 085701.

[239] Dominik Marx and Jürg Hutter. *Ab initio molecular dynamics: basic theory and advanced methods*. Cambridge University Press, 2009.

[240] David Chandler. "Introduction to modern statistical mechanics". In: *Oxford University Press* (1987), p. 288.

[241] Daan Frenkel and Berend Smit. *Understanding molecular simulation: from algorithms to applications*. Vol. 1. Elsevier, 2001.

[242] Steve Plimpton. "Fast Parallel Algorithms for Short-Range Molecular Dynamics". In: *Journal of Computational Physics* vol. 117. no. 1 (1995), pp. 1–19.

[243] Frank Millero and D Pierrot. "Speciation of metals in natural waters". In: *Chemistry of Marine Water and Sediments*. Springer, 2002, pp. 193–220.

[244] Isabelli N Dias, Bruno S Souza, João HOS Pereira, Francisca C Moreira, Márcia Dezotti, Rui AR Boaventura, and Vítor JP Vilar. "Enhancement of the photo-Fenton reaction at near neutral pH through the use of ferrioxalate complexes: a case study on trimethoprim and sulfamethoxazole antibiotics removal from aqueous solutions". In: *Chemical Engineering Journal* vol. 247 (2014), pp. 302–313.

[245] Agnieszka Kawska, Patrick Duchstein, Oliver Hochrein, and Dirk Zahn. "Atomistic mechanisms of ZnO aggregation from ethanolic solution: ion association, proton transfer, and self-organization". In: *Nano letters* vol. 8. no. 8 (2008), pp. 2336–2340.

[246] M Walther and D Zahn. "From bismuth oxide/hydroxide precursor clusters towards stable oxides: Proton transfer reactions and structural reorganization govern the stability of $[Bi_{18}O_{13}(OH)_{10}]$-nitrate clusters". In: *Chemical Physics Letters* vol. 691 (2018), pp. 87–90.

[247] Mengqiang Zhu, Cathrine Frandsen, Adam F Wallace, Benjamin Legg, Syed Khalid, Hengzhong Zhang, Steen Mørup, Jillian F Banfield, and Glenn A Waychunas. "Precipitation pathways for ferrihydrite formation in acidic solutions". In: *Geochimica et Cosmochimica Acta* vol. 172 (2016), pp. 247–264.

[248] Wolfgang Lechner and Christoph Dellago. "Accurate determination of crystal structures based on averaged local bond order parameters". In: *The Journal of chemical physics* vol. 129. no. 11 (2008), p. 114707.

[249] Stefan Auer and Daan Frenkel. "Numerical simulation of crystal nucleation in colloids". In: *Advanced Computer Simulation* (2005), pp. 130–130.

[250] Paul J Steinhardt, David R Nelson, and Marco Ronchetti. "Bond-orientational order in liquids and glasses". In: *Physical Review B* vol. 28. no. 2 (1983), p. 784.

[251] Daniele Moroni, Pieter Rein Ten Wolde, and Peter G Bolhuis. "Interplay between structure and size in a critical crystal nucleus". In: *Physical review letters* vol. 94. no. 23 (2005), p. 235703.

[252] Benoit Coasne, Surendra K Jain, Linda Naamar, and Keith E Gubbins. "Freezing of argon in ordered and disordered porous carbon". In: *Physical Review B* vol. 76. no. 8 (2007), p. 085416.

[253] Shuji Ogata. "Monte Carlo simulation study of crystallization in rapidly supercooled one-component plasmas". In: *Physical Review A* vol. 45. no. 2 (1992), p. 1122.

[254] Jeffrey E Post, Peter J Heaney, Robert B Von Dreele, and Jonathan C Hanson. "Neutron and temperature-resolved synchrotron X-ray powder diffraction study of akaganéite". In: *American Mineralogist* vol. 88. no. 5-6 (2003), pp. 782–788.

[255] William D Birch, Allan Pring, Armin Reller, and Helmut W Schmalle. "Bernalite, $Fe(OH)_3$, a new mineral from Broken Hill, New South Wales; description and structure". In: *American Mineralogist* vol. 78. no. 7-8 (1993), pp. 827–834.

[256] G Patrat, F De Bergevin, M Pernet, and JC Joubert. "Structure locale de δ-FeOOH". In: *Acta Crystallographica Section B: Structural Science* vol. 39. no. 2 (1983), pp. 165–170.

[257] Alessandro F Gualtieri and Paolo Venturelli. "In situ study of the goethite-hematite phase transformation by real time synchrotron powder diffraction". In: *American Mineralogist* vol. 84. no. 5-6 (1999), pp. 895–904.

[258] Larry W Finger and Robert M Hazen. "Crystal structure and isothermal compression of Fe_2O_3, Cr_2O_3, and V_2O_3 to 50 kbars". In: *Journal of Applied Physics* vol. 51. no. 10 (1980), pp. 5362–5367.

[259] RW Wyckoff. *Crystal Structures-2; Inorg. Compounds*. Wiley, 1964.

[260] Carlos Pecharromán, T Gonzalez-Carreno, and Juan E Iglesias. "The infrared dielectric properties of maghemite, γ-Fe_2O_3, from reflectance measurement on pressed powders". In: *Physics and Chemistry of Minerals* vol. 22. no. 1 (1995), pp. 21–29.

[261] Yilun Chen, Ami Wiesel, Yonina C Eldar, and Alfred O Hero. "Shrinkage algorithms for MMSE covariance estimation". In: *IEEE Transactions on Signal Processing* vol. 58. no. 10 (2010), pp. 5016–5029.

[262] F. Pedregosa, G. Varoquaux, A. Gramfort, V. Michel, B. Thirion, O. Grisel, M. Blondel, P. Prettenhofer, R. Weiss, V. Dubourg, J. Vanderplas, A. Passos, D. Cournapeau, M. Brucher, M. Perrot, and E. Duchesnay. "Scikit-learn: Machine Learning in Python". In: *Journal of Machine Learning Research* vol. 12 (2011), pp. 2825–2830.

[263] JW Anthony, RA Bideaux, KW Bladh, and MC Nichols. "Handbook of Mineralogy. V. II-Silicates. Mineralogical Society of America". In: (2001).

[264] Michele Ceriotti, Gareth A Tribello, and Michele Parrinello. "Simplifying the representation of complex free-energy landscapes using sketch-map". In: *Proceedings of the National Academy of Sciences* vol. 108. no. 32 (2011), pp. 13023–13028.

[265] Natividad Gálvez, Belén Fernández, Purificación Sánchez, Rafael Cuesta, Marcelo Ceolín, Miguel Clemente-León, Susana Trasobares, Miguel López-Haro, Jose J Calvino, Odile Stéphan, et al. "Comparative structural and chemical studies of ferritin cores with gradual removal of their iron contents". In: *Journal of the American Chemical Society* vol. 130. no. 25 (2008), pp. 8062–8068.

[266] *Eduard-Job-Foundation for Thermo- and Matterdynamics*. `https://www.job-stiftung.de/index.php?data-collection`. Accessed: 2018-03-05.

[267] G. Kresse and J. Hafner. "Ab initio molecular dynamics for liquid metals". In: *Phys. Rev. B* vol. 47. no. 1 (1993), pp. 558–561.

[268] G. Kresse and J. Hafner. "Ab initio molecular-dynamics simulation of the liquid-metal-amorphous-semiconductor transition in germanium". In: *Phys. Rev. B* vol. 49. no. 20 (1994), pp. 14251–14269.

[269] G. Kresse. "Efficient iterative schemes for ab initio total-energy calculations using a plane-wave basis set". In: *Phys. Rev. B* vol. 54. no. 16 (1996), pp. 11169–11186.

[270] Georg Kresse and Jürgen Furthmüller. "Efficiency of ab-initio total energy calculations for metals and semiconductors using a plane-wave basis set". In: *Computational Materials Science* vol. 6. no. 1 (1996), pp. 15–50.

[271] John P Perdew, Kieron Burke, and Matthias Ernzerhof. "Generalized gradient approximation made simple". In: *Physical review letters* vol. 77. no. 18 (1996), p. 3865.

[272] SL Dudarev, GA Botton, SY Savrasov, CJ Humphreys, and AP Sutton. "Electron-energy-loss spectra and the structural stability of nickel oxide: An LSDA+U study". In: *Physical Review B* vol. 57. no. 3 (1998), p. 1505.

[273] Hendrik J. Monkhorst and James D. Pack. "Special points for Brillouin-zone integrations". In: *Phys. Rev. B* vol. 13. no. 12 (1976), pp. 5188–5192.

[274] P. E. Blöchl. "Projector augmented-wave method". In: *Physical Review B* vol. 50. no. 24 (1994), pp. 17953–17979.

[275] A De Vita, A Canning, G Galli, F Gygi, F Mauri, and R Car. "Quantum molecular dynamics on massively parallel computers". In: *EPFL Supercomputing Review* vol. 6 (1994).

[276] Massimiliano Stengel and Alessandro De Vita. "First-principles molecular dynamics of metals: A Lagrangian formulation". In: *Physical Review B* vol. 62. no. 23 (2000), p. 15283.

[277] John P. Perdew and Yue Wang. "Accurate and simple analytic representation of the electron-gas correlation energy". In: *Physical Review B* vol. 45. no. 23 (1992), pp. 13244–13249.

[278] RW Hockney and JW Eastwood. "Computer simulation using particles, 1988". In: *Hilger, Bristol* (1988).

[279] William L. Jorgensen, Jayaraman Chandrasekhar, Jeffry D. Madura, Roger W. Impey, and Michael L. Klein. "Comparison of simple potential functions for simulating liquid water". In: *J. Chem. Phys.* vol. 79. no. 2 (1983), p. 926.

[280] Massimiliano Bonomi, Davide Branduardi, Giovanni Bussi, Carlo Camilloni, Davide Provasi, Paolo Raiteri, Davide Donadio, Fabrizio Marinelli, Fabio Pietrucci, Ricardo A. Broglia, and et al. "PLUMED: A portable plugin for free-energy calculations with molecular dynamics". In: *Computer Physics Communications* vol. 180. no. 10 (2009), pp. 1961–1972.

[281] Alessandro Laio and Francesco L Gervasio. "Metadynamics: a method to simulate rare events and reconstruct the free energy in biophysics, chemistry and material science". In: *Reports on Progress in Physics* vol. 71. no. 12 (2008), p. 126601.

Erklärung

Hiermit erkläre ich, dass ich

- *die Arbeit ohne unerlaubte fremde Hilfe angefertigt habe;*
- *keine anderen als die von mir angefertigten Quellen und Hilfsmittel benutzt habe;*
- *die den benutzten Werken wörtlich oder inhaltlich entnommenen Stellen als solche kenntlich gemacht habe.*

Bremen, den 18.04.2018

Steffen Lid